Dielectrophoretic assembly of carbon nanotube devices

Dimaki, Maria; Bøggild, Peter

Publication date:
2004

Document Version
Publisher's PDF, also known as Version of record

Dielectrophoretic Assembly of Carbon Nanotube Devices

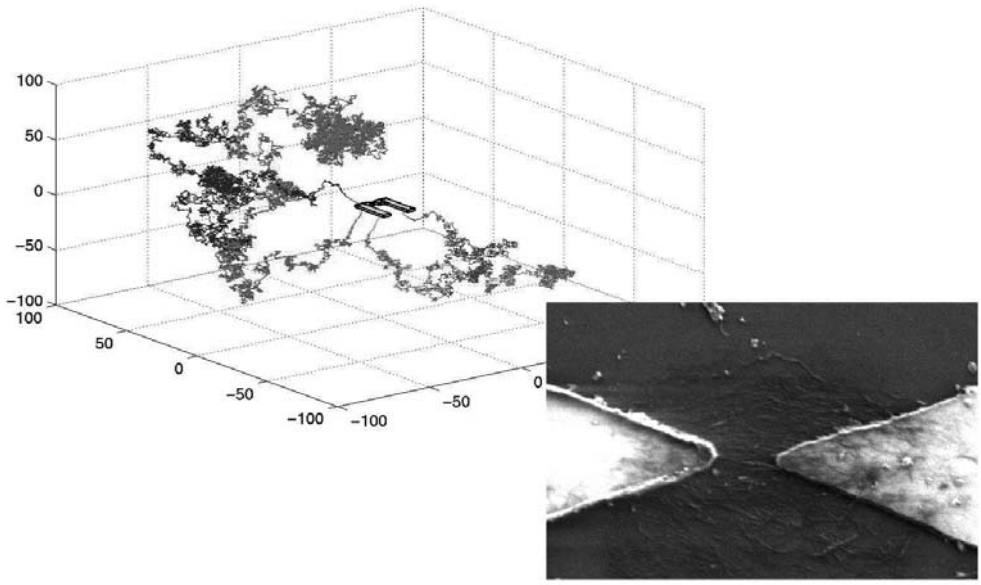

Ph.D. Thesis

Maria Dimaki

MIC - Department of Micro and Nanotechnology

December 2004

Abstract

The purpose of this project has been to assemble single-walled carbon nanotubes on electrodes at the tip of a biocompatible cantilever and use these for chemical species sensing in air and liquid, for example in order to measure the local activity from ion channels in the cell membrane. The electrical resistance of carbon nanotubes has been shown to be extremely sensitive to gas molecules.

Dielectrophoresis is a method capable of quickly attracting nanotubes on microelectrodes by using an electric field, thus enabling nanotube integration in microsystems. Dielectrophoresis offers also the potential of distinguishing between nanotubes of different electrical properties, which is very important for the optimisation of the properties of the carbon nanotube sensors.

Various cantilever and planar structures were designed, fabricated and tested both with multi-walled and single-walled carbon nanotubes dispersed in a number of different liquids. As a result of these test experiments a cantilever probe was designed specifically for the dielectrophoretic assembly of carbon nanotubes and a prototype was fabricated in the MIC (now Danchip) cleanroom. The prototype is not yet fully operational.

A model for the dielectrophoretic assembly of carbon nanotubes on microelectrodes was developed and several simulations were conducted using values from the available literature for the various key parameters. The model can give qualitative results regarding the parameters dominating the dielectrophoretic process and assist in the design of future experiments.

Based on the literature and the simulation results, several of the parameters governing the dielectrophoretic assembly of carbon nanotubes were investigated and the results generally agree with the theory. During heating and cooling of the nanotube networks their resistance changes following a pattern that could be explained by oxygen desorption and adsorption. Moreover, the resistance of the networks is generally unstable, which could indicate that the networks are responding to normal changes in the environmental conditions. The response of the assembled carbon nanotube networks to heat, nitrogen, humidity and light was also investigated and the results point once again to oxygen desorption and adsorption as important factors in determining the conductance of a nanotube.

Finally an attempt was made to sort carbon nanotubes into metallic and semiconducting. Raman spectra taken from samples assembled at different frequencies directly contradicted theoretical predictions as well as previously published experimental results.

Resumé (in Danish)

Formålet med dette projekt har været at opsamle enkeltvæggede kulstof-nanorør på elektroder placeret i spidsen af en biokompatibel bjælke, med henblik på at anvende nanorørene til detektion af kemiske stoffer i luft og i væske - for eksempel for at måle aktiviteten af ionkanaler i celler lokalt. Den elektriske ledningsevne af kulstof-nanorør har vist sig at være yderst følsom overfor molekyler på gasform.

Dielektroforese er en metode til hurtigt at trække nanorør ned til elektroder ved hjælp af et elektrisk felt og dermed integrere disse med mikrosystemer. Herudover potentiale til at kunne skelne mellem nanorør med forskellige elektriske egenskaber, hvilket er meget vigtigt for at kunne optimere nanorørernes sensor egenskaber.

Forskellige bjælke- og planarstrukturer blev designet, fremstillet og undersøgt ud fra forskellige opløsninger med såvel multi- som enkeltvæggede nanorør. Ud fra disse indledende eksperimenter blev en bjælke-probe designet specielt til dielektroforese-baseret integration af nanorør. En prototype fremstillet i MICs renrum (nu Danchip) har vist sig at fungere delvist.

En model for dielektroforese-baseret opsamling af nanorør på mikroelektroder blev udviklet, og adskillige simuleringer blev gennemført med forskellige værdier af nøgleparametre hentet fra den tilgængelige litteratur. Modellen giver et kvalitativt billede af hvilke parametre der har størst indflydelse på dielektroforese-processen, og kan derved bistå i designet af fremtidige eksperimenter.

På grundlag af litteraturen samt simuleringsresultaterne blev adskillige af de parametre, der styrer den dielektroforesebaserede opsamling af nanorør, undersøgt eksperimentelt, og resultaterne er generelt i overensstemmelse med teorien. Under opvarmning og nedkøling af nanorør-netværkene følger deres resistans et mønster, som kan forklares med desorption og adsorption af ilt. Derudover er netværkenes resistans generelt ustabil, hvilket tyder på at netværkene er følsomme overfor naturlige forandringer i deres miljø. De opsamlede netværks respons på varme, kvælstof, fugtighed og lys undersøgtes også, og igen synes resultaterne at pege på desorption og adsorption af ilt som en vigtig, bestemmende faktor for nanorørenes konduktans.

Endelig blev det forsøgt at sortere metalliske og halvledende nanorør, som det er vist tidligere i literaturen. Raman-spektre taget fra prøver integreret ved forskellige frekvenser er i direkte modstrid med de teoretiske forudsigelser og tidligere publicerede, eksperimentelle resultater.

Preface

This thesis is submitted as a partial fulfillment of the requirements for obtaining the Ph.D. degree from the Technical University of Denmark (DTU). The research reported has been conducted at the Department of Micro- and Nanotechnology (MIC) at DTU in the period from October 2001 to December 2004. The project has been supervised by Associate Professor Peter Bøggild and financed by a grant from DTU.

This project would not have been possible without the help from numerous people, whom I would like to take the opportunity to thank here.

The initial work on this project involving the characterisation of a multi-point probe for ion channel measurements was done under the main supervision of Emmanuelle Boubour, now at Rice University, whom I would like to thank for her great enthusiasm and her guidance.

For the ion channel model simulations as well as for hands on experience with patch clamping measurements and valuable discussions I would like to thank Jonatan Kutchinsky from Sophion Bioscience A/S.

During the last three years I supervised a large number of students and would like to particularly thank Rasmus Haugstrup Pedersen, Dan Mario Johansen and Peter Schultz for never giving up and M.Sc. student René Nyberg for working as hard as humanly possible.

Raman spectroscopy was initially done at DTU with the help of Prof. Rolf Berg, whom I would like to thank for fitting me in to his very busy schedule. Raman spectra were also taken at Cambridge University by Andrea Ferrari and Vittorio Scardaci, who deserve a big thank you for scanning a really large number of samples for me.

A special thanks goes to all laboratory technicians whom I have been plaguing with questions at one point in time or another, but especially to Helle V. Jensen, who has offered invaluable help with all the fabrication processes and contributed to a great atmosphere in the cleanroom, to Lis Nielsen for her help during a difficult 3-week course and to Conny Hougaard for fabricating wafers in record-breaking time during the very last stages of this project.

From the Nanointegration group I would like to thank all former and current members, who have helped at one point in time or another. Particularly, Kristian Mølhave for always having another idea and for always making sure that there were enough carbon nanotubes around, Jakob Kjelstrup-Hansen for building the

heating oven used in the experiments and participating in the measurements, Rong Lin for the cell measurements and for providing input that lead to the improvement of the experimental setup, Ramona Mateiu for letting me borrow her process for some new cantilever probes, my long-time office-mate Dorte Nørgaard Madsen for her guidance and a great atmosphere in the office, Kjetil Gjerde for valuable discussions and of course my supervisor Peter Bøggild for teaching me how to think like a scientist, for our countless discussions and for his excellent comments and corrections for all written material produced during this project.

Several other MIC people deserve mentioning: Associate Professor Ole Hansen for never failing to answer a question, Søren Jensen, whom I have consulted several times on mask design issues, lithography and ASE etching, Associate Professors Henrik Bruus and Anders Wolff for valuable discussions, Rodolphe Marie and Zhenyu Wang for their help with the sorting setup, Rasmus Sandberg for his help with the measurements in a N_2 atmosphere and Process Specialist Jonas Michael Jensen for teaching me some nice tricks with the SEM.

Many thanks to Professor Hywel Morgan and Dr. Nicolas Green from the University of Southampton for hosting me there for a week and for helping with the dielectrophoresis modeling and simulations. Some fundamental problems regarding the choice of parameters and equations were solved during that visit. The simulations described in section 3.3 and in appendix B were done in Southampton.

Of course, nothing would have ever been completed without the support of my family and friends. I would like to particularly thank my parents and my brother, who have called me practically every day to find out how I was doing, despite bitter knowledge of how high their phone bill would be. Many thanks also to my second family, Lars, Lis and Erik Andersson for always being there for me.

Finally I would like to mention that some work was done during this project that is not presented in this thesis. That involves the characterisation of biocompatible multipoint probes fabricated at MIC by René Fléron and Helle Ruseng and measurements in salt solutions with these, silicon nanowire placement on a cantilever and welding using a laser beam, insertion of silicon nanowires in yeast cells and nanotube solution droplet levitation for dielectrophoretic experiments in air. These experiments, though promising, were never seriously pursued.

Lyngby, 22.12.2004

Maria Dimaki

Contents

Chapter 1

Introduction

In the last few decades the world has seen some truly remarkable technological advances taking place, things we nowadays take for granted. Everyday appliances, whether it is a television, a computer or a mobile phone, keep getting better, smaller and easier to use, and in the case of the chosen examples, even integrated into one device with roughly all the functionality of each one of its components separately.

To achieve this, technology has not only had to improve on well-known fabrication techniques and instrumentation but also to invest in research of new materials and technologies. One of the fastest growing fields is nanotechnology, dealing with structures of nanometer dimensions. One of the most studied nanomaterials is the carbon nanotube, a cylindrical molecule consisting of carbon atoms arranged in a hexagonal lattice with amazing mechanical and electrical properties.

As the work carried out during this project involves the use of carbon nanotubes as sensors, with the ultimate goal of detecting ionic current from cellular ion channels, this introduction will present a brief overview of carbon nanotubes and their applications, followed by a presentation of probe-like structures fabricated in the past for measurements on nerve cells.

1.1 Carbon nanotubes

Amongst nanomaterials carbon nanotubes and later nanowires have received the most attention ever since Iijima [1] reported the discovery of "Helical microtubules of graphitic carbon", or multi-walled carbon nanotubes as they are known today, in one of the most cited papers in the scientific literature in 1991. Two years later the single-walled carbon nanotubes were discovered [2, 3].

A vast amount of scientific papers have appeared in the literature ever since, dealing with every aspect of the carbon nanotube, ranging from fabrication methods over mechanical and electrical properties investigation to a vast amount of possible and real applications. Here I will focus mostly on work related to this project.

1.1.1 Structure and properties

A more detailed description of the carbon nanotube structure and properties follows in section 2.1. However, a very brief mention is necessary at this point.

A carbon nanotube is essentially a long and thin hollow rod made of carbon atoms arranged in a hexagonal lattice (see Figure 1.1). The way these atoms are arranged, referred to as chirality, determines the electrical properties of the nanotube, so that approximately 2/3 of possible configurations exhibit semiconducting behaviour and 1/3 metallic behaviour. Those nanotubes formed by more than one hollow cylinder one inside the other are called multi-walled nanotubes, otherwise the nanotubes are called single-walled.

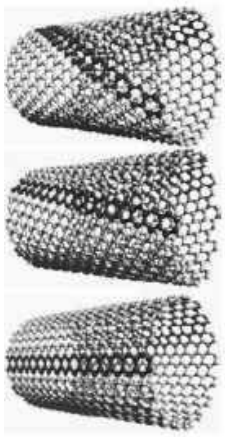

Figure 1.1: The carbon nanotube. The carbon atoms can be arranged in many different ways on the cylinder surface, referred to as chirality, giving the different nanotubes different electrical properties. Reproduced from [4].

1.1.2 Fabrication methods

Nowadays nanotubes are fabricated mainly in four ways [5, 6] :

- Arc discharge method
- Laser ablation method
- Chemical Vapor deposition method (CVD)
- High Pressure Conversion of Carbon Monoxide (HiPCO)

Both multi-walled and single-walled carbon nanotubes can be fabricated using the arc discharge method, which involves two carbon rods in close proximity and a high current of 50-120 A flowing between them, causing the graphite to vaporise into atomic carbon. Multi-walled nanotubes form this way, while by using a proper catalyst single-walled carbon nanotubes of various diameters can be synthesized in gram quantities [7, 8].

Using the laser vaporisation of a graphite target bundles of single-walled carbon nanotubes with yields as high as 70-90% [9] have been reported. The diameters of the single-walled nanotubes are distributed around 1.38 ± 0.02 nm.

The vapor growth method produces both multi-walled and single-walled carbon nanotubes, and is based on using catalyst particles of certain diameter in a relatively low temperature oven (500 - 1000 ^{o}C) with a flow of a hydrocarbon gas. The advantage of this method is that it allows the growth of carbon nanotubes at controllable locations and with desired orientations. An excellent review of this method is presented in [10].

Finally, the HiPCO process is capable of producing large quantities of high purity single-walled carbon nanotubes by flowing CO at a high temperature and pressure [6]. The method has been commercialized by Carbon Nanotechnologies Inc.

1.1.3 Assembling methods

If nanotubes are to be used as building blocks for electronic devices then a way has to be found to easily assemble the nanotubes onto microstructures with high yields. Several methods for nanotube handling, manipulation and positioning exist:

- Direct manipulation using Scanning Probe Microscopy
- Surface patterning
- Direct Growth
- Electric field assisted manipulation

Using the tip of a Scanning Probe Microscope like an Atomic Force Microscope (AFM) in order to push a nanotube around on a surface is a rather straightforward way to position nanotubes on predefined locations. The method has been used extensively in the literature [11, 12, 13, 14, 15, 16], not only for the positioning of the nanotubes but also for studying their mechanical properties. Splitting of bundles into individual nanotubes has also been reported [17].

Surface patterning is a very promising method for the control of the positioning of carbon nanotubes on a surface. In [18] the authors demonstrate how the combination of a patterned surface and flow allows the controlled positioning of nanowires and the fabrication of complex geometries of nanowire networks (see Figure 1.2(a)). Surface patterning for multi-walled and single-walled carbon nanotubes has also been reported in [19, 20, 21, 22]. The method involves the assembly of a monolayer of mostly aminopropyltriethoxysilane (APTS) on PMMA patterned surfaces by an electron-beam. Nanotubes prefer to deposit on APTS layers than on a clean SiO_2 surface (see Figure 1.2(b)). This method was used in [23] for the fabrication of carbon nanotube field effect transistors.

Direct growth of carbon nanotubes on the desired sites is possible with the catalytic CVD growth method. Nanotubes can grow vertically on a substrate

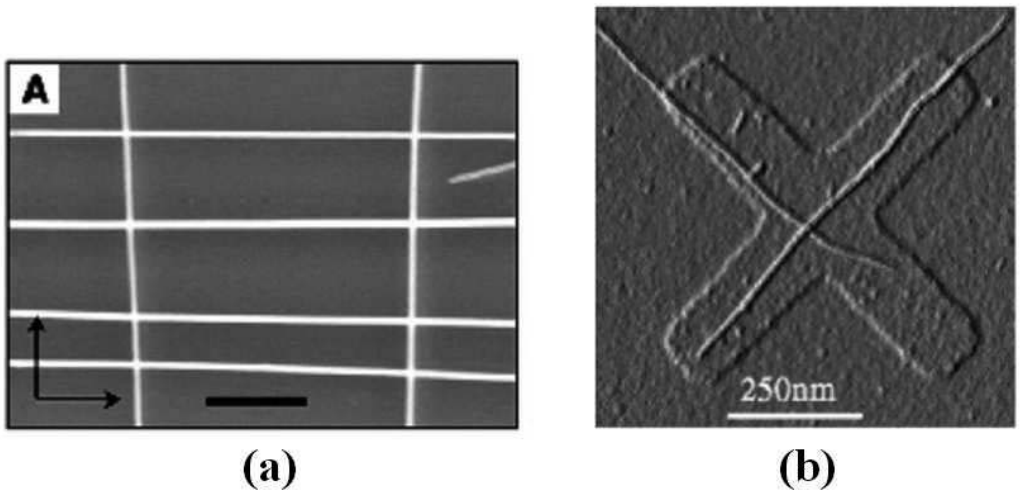

Figure 1.2: **(a)** Complex geometries formed by nanowires by a combined flow/surface patterning method. Reproduced from [18] **(b)** Assembly of nanotubes on a pre-patterned APTS monolayer. Reproduced from [22].

forming pillars of complex patterns [24, 25, 26] or even bridge sites with catalyst islands [27, 28, 29, 30, 31], growing parallel to the substrate. The control of position achieved this way is very high and nanotubes have been grown on a full wafer in this way [30]. Examples of carbon nanotubes grown by this method are shown in Figure 1.3.

Electric field assisted manipulation is a very attractive method for the controlled positioning of carbon nanotubes directly onto pre-fabricated microelectronic devices. Already in 1997 it was shown that a DC voltage across a narrow gap would trap single-walled carbon nanotubes [32] and the method became increasingly popular thereafter. In [33] and later in [34] the alignment with the electrical field of multi-walled and single-walled carbon nanotubes, respectively, was demonstrated. Here the alignment was more pronounced at higher frequencies of the alternating electric field. Most assembly experiments have been conducted with multi-walled carbon nanotubes using either DC or AC voltage [35, 36, 37, 38, 39, 40], although recently the simultaneous deposition of single-walled carbon nanotube bundles on several microelectrodes was demonstrated [41]. Characteristic of this method is the fact that usually more than one nanotube, or even more than one bundle of nanotubes, is trapped on a single electrode pair. It has been shown [42, 43] that a combination of a DC and an AC field can result in controlled deposition of a single multi-walled nanotube or a single bundle between a gap. In [40] the authors also observe that the number of deposited bundles depends on the electrode material, while in [44] the authors find that there is also a dependence on the field application time. Examples of this method are shown in Figure 1.4.

1.1.4 Applications

Carbon nanotubes have a wide range of applications that take advantage of the

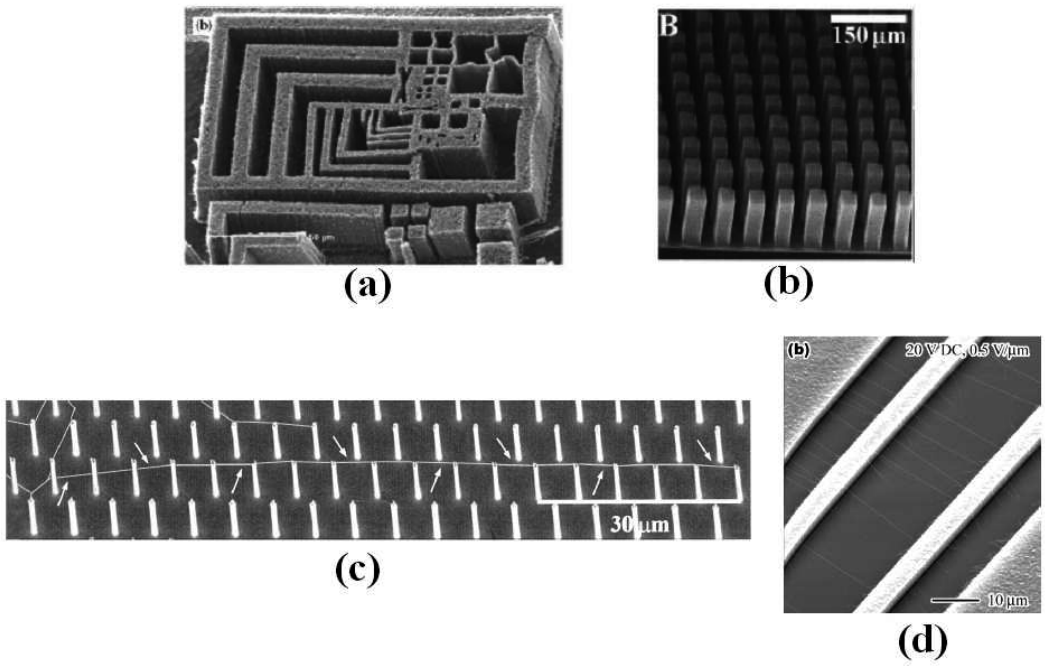

Figure 1.3: **(a)** Complex geometries formed by multi-walled nanotubes. Reproduced from [25] **(b)** Pillars of multi-walled carbon nanotubes. Reproduced from [26]. **(c)** A long single-walled carbon nanotube growing parallel to the substrate on patterned pillars. Reproduced from [31]. **(d)** Aligned single-walled carbon nanotubes growing between electrodes using the electric field generated by them. Reproduced from [30].

unique mechanical and electrical properties of the material.

Perhaps one of the most important applications of nanotubes based on their mechanical properties is their use as reinforcements in composite materials in order to make high strength composites. Polymer, metal and ceramic-matrix composites have been investigated, though the polymer composites are mostly in focus [45]. Generally, experiments show a tendency towards improvement of the mechanical properties of the matrix, however, several problems related to nanotube sliding in the matrix remain to be solved.

Composite nanotube materials also show improvements in the conductivity and thermal conductivity of the matrix [46, 47].

Carbon nanotubes have also been used as tips for atomic force (AFM) and scanning tunneling (STM) microscopes due to their well defined shape, their flexibility and robustness [48] and, for the case of the STM, their conducting properties. The first CNT probe tips were realised in 1996 [49] and showed that a nanotube tip greatly improves the imaging of deep trenches, as well as imaging in water. The fabrication of AFM tips with CVD grown carbon nanotubes was done in wafer scale in [50], while in [51] the nanotube is attached on the probe tip by an electric field.

Nanotubes became even more attractive to researchers when it was discovered that they can function as field effect transistors (FET) at room temperature [52, 53]. Even in the first examples presented the nanotube FETs showed properties close

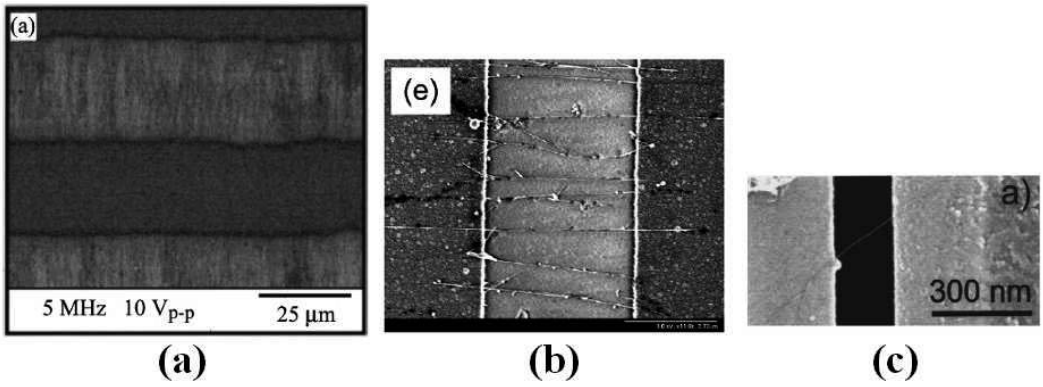

Figure 1.4: (a) Alignment of single-walled carbon nanotubes with the electric field lines. Reproduced from [34]. **(b)** Multi-walled nanotubes deposited across electrodes using a combination of DC and AC voltage. Reproduced from [43]. **(c)** A single single-walled carbon nanotube bundle (diameter 6 nm). Reproduced from [32].

to those of silicon-based transistors. Ever since several CNT FETs and Single-Electron Transistors (SETs) have been built, using different gate and electrode materials and shapes, different gate insulator thicknesses, top or bottom gate electrodes and a variety of nanotube types, dimensions and assembly methods [54, 55, 56, 57, 58, 59]. The transistors can be p-type, n-type or ambipolar depending on the contacts and post-assembly treatment [60]. Logic gates have been fabricated using CNT FETs [60, 61, 57], opening the way for carbon nanotubes to the electronics market. In all cases the conductance of the carbon nanotube could be regulated by several orders of magnitude [52, 53].

As carbon nanotubes have a very large surface area and are able to change their electrical properties dramatically at room temperature as a response to environmental conditions, they are promising candidates for gas and chemical species detection applications. An abundance of scientific papers exist demonstrating the ability of individual single-walled nanotubes and bundles, networks or thin films of single- or multi-walled nanotubes to sense different gas or chemical species before or after a specific treatment.

In [62] the authors exposed a single semiconducting single-walled carbon nanotube to NO_2 and NH_3 at room temperature and observed how the conductance of the nanotube changed by up to 3 orders of magnitude with a response time of a few seconds, comparable to present day sensors, which have to operate at much higher temperatures. In [63] the sensitivity of films of SWCNTs to oxygen was demonstrated, while in [64] the sensitivity of thin films of SWCNTs to NO_2, NH_3, ethanol and humidity was studied (see also Figure 1.5). Sensitivities down to 10 ppb are demonstrated. In [65] the sensitivity of a thin film of SWCNTs to CO and C_6H_6 is also demonstrated. In [66] the response of a network of multi-walled carbon nanotubes to various gases is described. A glucose sensor was demonstrated in [67] by modifying the surface of vertically aligned nanotubes and in [68] the detection of specific proteins in solution by a CNTFET was presented. In [69] sensitivity of sub ppb concentrations of a nerve agent by a network of single-walled carbon nanotubes is demonstrated.

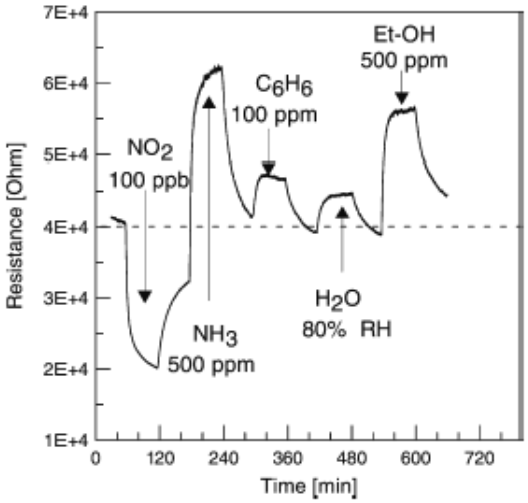

Figure 1.5: The response of a thin film of SWCNTs to various gases. The operating temperature of the sensor is 165 ^{o}C. Reproduced from [64].

Vertically grown carbon nanotubes have been used for field emission [24, 70] with the obvious application of their use as flat panel displays [71].

1.1.5 Issues

For most applications involving carbon nanotubes, semiconducting nanotubes are needed. Therefore sorting semiconducting from metallic nanotubes is important. Several approaches to nanotube sorting exist. Direct growth of nanotubes of specific properties would be the ideal solution. However, no method exists at present for the reliable separation of metallic or semiconducting nanotubes by selective synthesis [72].

Recently [73] sorting of carbon nanotubes was reported using dielectrophoresis, an electric field based assembly method. 80% of the collected nanotubes on the electrodes were metallic, however only 1 out 1000 nanotubes in the experiment was caught.

Another promising method was described in [74], where specific strands of DNA were shown to wrap themselves around nanotubes of specific diameters and chirality, thus enabling separation by anion exchange chromatography.

Finally, removing the unwanted nanotubes by destruction is also a separation method. In [75] the metallic nanotubes in a rope of single-walled carbon nanotubes are selectively burned by high current, while the semiconducting nanotubes remain unaffected as they are already depleted by an electrostatic backgate. In [76] application of monochromatic light pulses during oxidation of the single-walled carbon nanotubes preferentially removes the semiconducting nanotubes whose band gap corresponds to the light wavelength, so that nanotubes with a specific chirality can be achieved.

1.2 Measuring on neurons

Electrophysiological recording from neurons has been the object of research since the beginning of the 20th century because of the importance of neuronal activity for our everyday life. Neurons control all body functions both voluntary (like walking) and automatic (like breathing). A signal is generated somewhere in the body and then propagates via neurons to the brain. If the signal never reaches the brain, no response to the signal information will occur. For many years scientists have only been able to record the signal at one place in the neuron due to the sizes of electrodes. No propagation data could be recorded and studied. With the development of microfabrication techniques the possibility of multiple site recording became available.

There are several problems associated with recording from neurons. One of the most important ones is to make sure that the measuring device does not react with the biological specimen thus causing contamination and possibly death of the cell. Therefore the parts of the device that are in contact with the cell must be covered with an inert material and the actual measuring tip should be made with biocompatible metals such as gold or platinum. The shape of the device should be such so that the measurement can be made within 100 μm from the neuron, otherwise the signal will be lost [77].

In 1993 Frazier et al [78] described in detail how they fabricated a biocompatible multipoint probe using standard microfabrication procedures. The device is shown in Figure 1.6(a). The size of each finger is 25 μm and the distance between the fingers is 75 μm. The authors have been using several different metals as the conducting material like e.g. gold, silver, nickel, copper, platinum and palladium. For releasing the tips and the bonding pads from the silicon nitride the authors use a mask to pattern the areas they want to free and employ standard lift-off techniques. Though the authors report having successfully inserted their devices into biological matter with no mechanical damage to the device or injury to the organism, they do not report on any results obtained during a recording.

Another design of a multipoint probe has appeared in the literature as early as 1988 and at least 4 publications have concerned it until 1992 [79, 80, 81, 82]. An improved modern version of the same probe has appeared as recently as 2000 [83]. This design went one step further and considered a second problem related to the measurement of biological signals, namely that of the low amplitude of these signals. Typical recording sites in the study of neurons are associated with large impedance levels, typically in the area of 1-10 MΩ. The signals are therefore extremely sensitive to any sort of noise. Being able to embed the signal processing electronics in the probe itself could therefore be important, since decreasing the distance between signal and electronics reduces the noise.

In this design (see Figure 1.6(b)) the probe has 16 recording sites with a spacing of 100 μm. Measurements with this probe were successfully carried out on a nerve cell.

Several planar geometries of chips containing multiple recording sites exist, but

these have the disadvantage of having to sustain a culture of cells on them, while probe like structures can just be placed in proximity to the nerve cell in question and reused on several other cells.

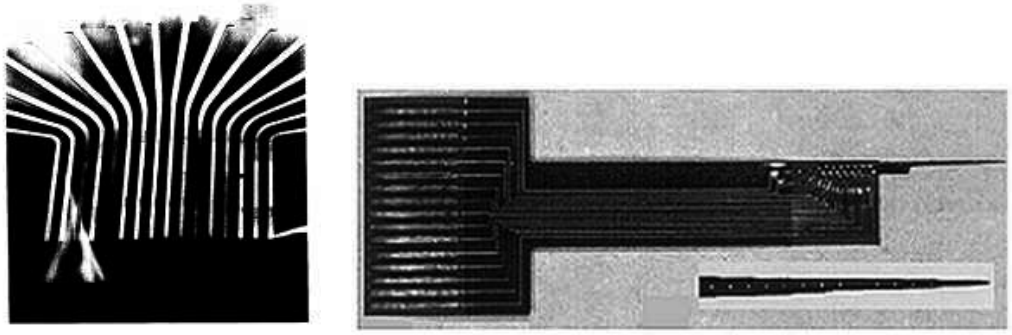

(a) Reproduced from [78] (b) Reproduced from [83]

Figure 1.6: Two biocompatible probes for the recording of signals from neurons. The inset in (b) shows a detail of the needle containing the recording sites.

1.3 Project goal and approach

The purpose of this project has been to assemble single-walled carbon nanotubes on electrodes at the tip of a biocompatible cantilever and use these for chemical species sensing in air and liquid, the latter primarily in order to measure the activity from a single ion channel.

The chosen method for the assembly of the nanotubes is dielectrophoresis, because of its potential to be scaled up to wafer level and to sort semiconducting from metallic nanotubes. A cantilever platform for the assembly was chosen, since the same cantilever can contain in principle a large number of electrodes and is free to move on a surface of a cell, thus mapping the ion channel activity on a neuron.

Initial tests were performed to evaluate the feasibility of the method on cantilever structures. For these experiments multi-walled carbon nanotubes were used because they are easily dispersed in solvents and large enough to be observed by a Scanning Electron Microscope (SEM). Once the feasibility of the method was established, test structures were fabricated in order to optimise the various parameters controlling the dielectrophoretic assembly of single-walled carbon nanotubes. A theoretical model was also developed to assist in the choice of parameters.

The assembled nanotubes on the test structures were also tested in terms of their response to common environmental conditions, such as temperature and humidity variations, in order to evaluate the possibility of using these as sensor components.

Based on these initial results from the test structures, a special probe structure was designed, fabricated and tested.

During the course of the project a number of milestones were set:

- The dielectrophoretic assembly of nanotubes should be controlled so that yields higher than 85% can be achieved.
- Nanotube networks should be assembled both on planar as well as cantilever structures. The process should be refined until single bundles of a few nanotubes and ultimately only one nanotube are assembled by dielectrophoresis.
- The resistance of the assembled networks should be controlled by a backgate indicating the presence of semiconducting nanotubes in the networks.
- The nanotube reaction to temperature and humidity variations should be measured, so that the posiibility of using the dielectrophoretically assembled nanotubes as sensors can be established.
- A prototype cantilever probe specially designed for dielectrophoretic assembly of carbon nanotubes should be realised and tested in terms of structural and electrical performance and its ability to function as a platform for dielectrophoretic assembly and electrical measurements of nanotubes.
- Measurements of gas species in air and ion concentration in liquid should be done.

1.4 Organisation of the thesis

This thesis is divided into nine chapters and four appendices.

In chapter two a basic theoretical background for the structure and electrical properties of the carbon nanotube is given, along with an introduction to carbon nanotube Raman spectra interpretation, needed later in this work. Moreover, we present a simple model of an ion channel and argue that a carbon nanotube could be suitable for sensing ion channel activity.

In chapter three a model of the dielectrophoretic assembly of carbon nanotubes onto microelectrodes is presented. Three simulation results are described, showing how the model can give remarkably different results depending on the various parameters controlling it.

In chapter four a description of the nanotubes, solutions, microelectrodes and experimental setups used in this project is presented.

In chapter five the various parameters controlling the dielectrophoretic assembly of carbon nanotubes on microelectrodes are extensively investigated in order to optimise the process. Moreover, the effects of low temperature heating, of an electron beam and of electrical measurements on the assembled networks are presented.

In chapter six the response of assembled networks to common environmental conditions, such as heating, white light illumination and humidity are presented.

In chapter seven our attempts to use cantilever structures for the dielectrophoretic assembly of carbon nanotubes as well as the design, fabrication and characterisation of a cantilever probe optimised for dielectrophoretic experiments with carbon nanotubes are described .

In chapter eight our attempts to incorporate microfluidics in the assembly process are presented, along with studies of the ability of dielectrophoresis to separate metallic from semiconducting carbon nanotubes.

Finally, in chapter nine a brief summary of the project is given along with future work and perspectives.

Appendix A contains the publications, conference proceedings, and conferences attended during the course of this project.

Appendix B contains results of ongoing calculations at the University of Southampton aiming to investigate the influence of the temperature gradients and the resulting fluid flow on the dielectrophoretic process.

Appendix C contains a calculation of the ideal carbon nanotube solution concentration based on the desired number of nanotubes in a certain volume of solution.

Appendix D contains the process sequences for two of the fabrication processes I carried out in the cleanroom but which were developed by other people.

Chapter 2

Theory

In this chapter we will present some general information on carbon nanotubes and their potential for use as sensing components for various chemical species and ultimately for ion channel activity. A simple model of an ion channel has been considered for the purpose. We will also extensively discuss dielectrophoresis, the method used to assemble nanotubes on microstructures in this work.

2.1 Carbon nanotubes

A detailed description of carbon nanotubes is beyond the scope of this report, however, in this section we will present basic information on the structure and electronic properties of this relatively new material and concentrate especially on their dielectric and conducting properties, which are relevant for the remainder of this report.

2.1.1 Structure and Electronic Properties

A carbon nanotube (CNT) can be thought of as a single graphene sheet rolled up into a cylinder. The graphene sheet is one atomic layer of crystalline graphite and on it the carbon atoms are arranged in an open honeycomb network containing two atoms per unit cell. The carbon atoms are connected with very strong covalent bonds. Being the sixth element in the periodic table, carbon has 6 electrons occupying the $1s^2$, $2s^2$ and $2p^2$ atomic orbitals. In a graphene sheet each carbon atom has to connect to three other carbon atoms and for the bonds to be equivalent, hybridization must occur. One of the 2s electrons is promoted to a 2p orbital and the 2s electron remaining along with the now 3 2p orbitals form three new sp^2 orbitals lying on a plane with and angle of 120^o between them. The p orbital that does not participate in the new sp^2 orbitals arranges itself perpendicular to the plane of the three sp^2 orbitals and is free to move between the carbon atoms. Figure 2.1 shows the carbon-carbon bond found in nanotubes. The curvature of the nanotube gives rise to a small amount of sp^3 bonding so that the bonds in the circumferential direction are slightly weaker than along the

nanotube axis.

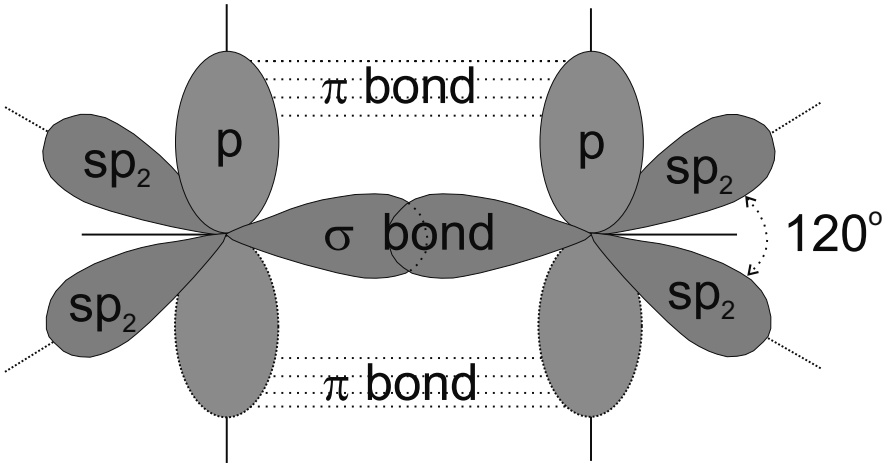

Figure 2.1: The carbon-carbon bond found in carbon nanotubes. Each sp^2 orbital forms a σ bond with each one of the 3 carbon atoms that it is connects to. The electron of the p orbital can be on either side of the nanotube surface but due to the curvature there is an increased probability of it being on the outside, thus creating an amount of sp^3 bonding.

As already mentioned the carbon nanotube is essentially a rolled-up graphene sheet. The circumference of any carbon nanotube can thus be expressed in terms of the chiral vector $\mathbf{C} = n\hat{\mathbf{a}}_\mathbf{1} + m\hat{\mathbf{a}}_\mathbf{2}$ which connects two crystallographically equivalent sites on a 2D graphene sheet (Figure 2.2). The structure of the nanotube depends uniquely on the pair of integers (m, n) which comprise the chiral vector. $\hat{\mathbf{a}}_\mathbf{1}$ and $\hat{\mathbf{a}}_\mathbf{2}$ are the unit vectors of the hexagonal honeycomb lattice of the graphene sheet, shown in Figure 2.2. A chiral angle θ can also be defined by considering $\theta = 0$ in the direction of the unit vector $\hat{\mathbf{a}}_\mathbf{1}$. Three distinct types of nanotubes can now be generated by rolling up the graphene sheet into a cylinder:

- the zigzag nanotubes, corresponding to a chiral angle of $\theta = 0$ or to $(m, n) = (m, 0)$ or $(m, n) = (0, n)$,
- the armchair nanotubes, corresponding to a chiral angle of $\theta = 30^o$ or to $(m, n) = (n, n)$,
- the chiral nanotubes, corresponding to chiral angles of $0 < \theta < 30^o$ or to all other combinations of (m, n).

The cylinder is formed by superimposing the two ends of the chiral vector $\mathbf{C}$. The nanotube diameter is given by equation 2.1,

$$d_t = \sqrt{3}\alpha_{C-C} \cdot (m^2 + mn + n^2)^{1/2}/\pi \tag{2.1}$$

where α_{C-C} is the carbon-carbon bond length (1.42 Å). The chiral angle θ is given by equation 2.2.

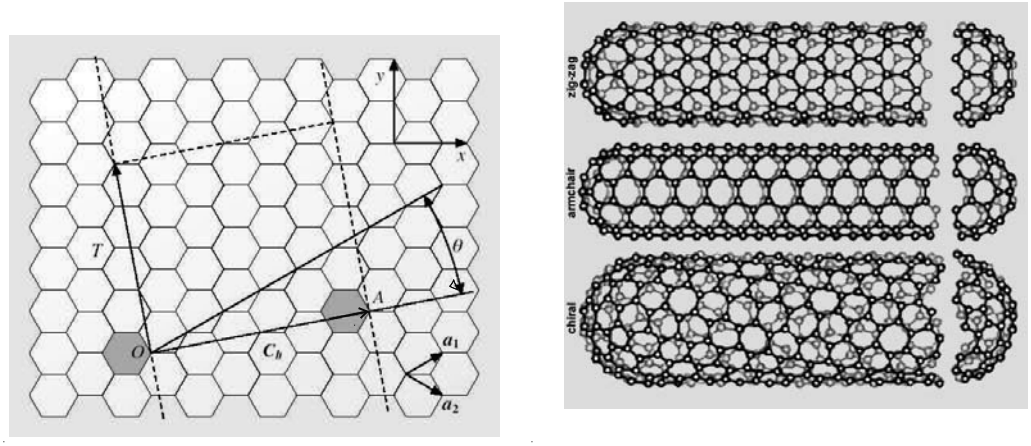

(a) The chiral vector (b) The three types of carbon nanotubes

Figure 2.2: The honeycomb lattice of the graphene sheet and the chiral vector used to describe carbon nanotubes. Figure reproduced from [84]

$$\theta = \arctan\left[\frac{\sqrt{3}n}{2m+n}\right] \tag{2.2}$$

From equation 2.2 it can be seen that the $(n, 0)$ nanotubes would have a chiral angle of $\theta = 60^o$, however, if we limit θ to be between 0 and 30^o, then by symmetry $\theta = 0^o$ for a $(n, 0)$ zig-zag nanotube.

The structural differences give rise to differences in the properties of the various nanotubes. The band structure and the hexagonal shape of the first Brillouin zone of graphene are shown in figure 2.3. The valence and conduction bands meet at six points (K-points) at the Fermi energy. In most directions in k-space the electrons encounter a semiconductor-like band gap but in the directions that pass through the K-points the electrons have free motion and the graphene behaves as a metal. In carbon nanotubes one needs to take into account the confinement of the electrons around the circumference of the nanotube. Only a certain set of states are allowed depending on the nanotube diameter and helicity, namely those that satisfy the equation $\mathbf{k_C C} = 2\pi j$, where $\mathbf{C}$ is the chiral vector, $\mathbf{k_C}$ is the wavevector in the circumferential direction and j is an integer. Those are shown with the black lines in figure 2.3 which are spaced by $\Delta k = 2\pi/|\mathbf{C}| = 2/d_{CNT}$, where d_{CNT} is the nanotube diameter. If these lines pass through a K-point the tube is metallic, otherwise it is semiconducting (Figure 2.4). It can be shown that all (n, n) nanotubes (armchair) are metallic, nanotubes with $n - m = 3i$, where i is an integer are small-gap semiconductors and all other nanotubes are large-gap semiconductors.

The band gap in semiconducting nanotubes is given by [72]

$$E_{GAP} = \frac{4hv_F}{6\pi d_{CNT}} \tag{2.3}$$

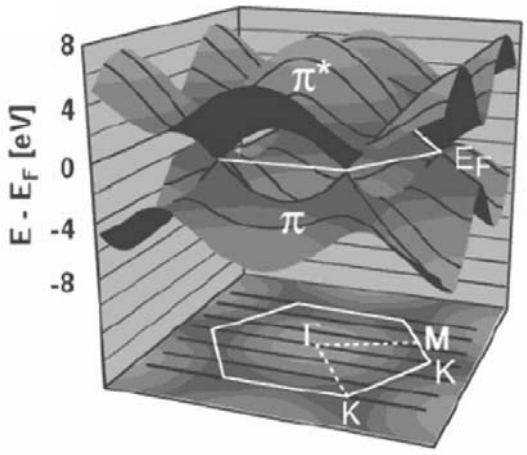

Figure 2.3: Band structure of the 2D graphene sheet. The valence and conduction bands meet at 6 points at the Fermi energy. The black lines represent the allowed states for a (3,3) nanotube. Figure reproduced from [85]

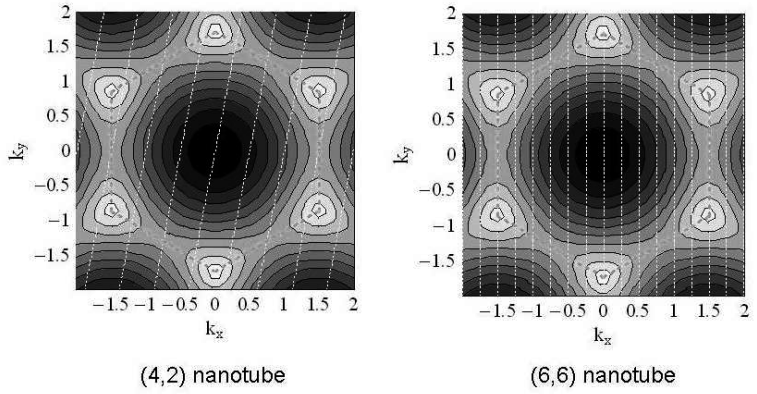

Figure 2.4: The allowed states of a (4,2) and a (6,6) nanotube plotted with white lines. The lines pass through the K-points for the (6,6) nanotube giving it a metallic character. The figure was done using a Mathematica program written by Mads Brandbyge.

where v_F is the Fermi velocity, d_{CNT} is the nanotube diameter and h is the Planck constant.

In [86] the chirality of the nanotube is also taken into account yielding the band gap of a nanotube (neglecting higher order terms) to be:

$$E_{GAP} = \frac{2\gamma_0 \cdot a_{C-C}}{d_{CNT} cos(\theta)} \tag{2.4}$$

where $a_{C-C} = 1.42$ Å is the distance between two neighboring carbon atoms and γ_0 is the interaction energy between neighboring carbon atoms.

2.1.2 Conducting Properties

Carbon nanotubes have been reported to be capable of carrying enormous current densities, up to 10^9 A/cm^2 without being destroyed. This value is 2-3 orders of magnitude higher than is possible in metals such as Al and Cu and can be explained by considering that the motion of the electrons in carbon nanotubes is possible only in the two directions along the tube axis. Along with the constraints for energy and momentum conservation this means that the electrons moving inside a metallic nanotube in principle do not experience scattering.

In the absence of scattering, transport is ballistic and the two-terminal conductance of the metallic nanotube can be expressed by the Landauer equation:

$$G = \frac{2e^2}{h} \sum_{i}^{N} T_i \tag{2.5}$$

In equation (2.5) $2e^2/h$ is referred to as the conductance quantum, T_i is the transmission of each contributing conducting channel produced by the confinement of the electrons along the circumference of the carbon nanotube and $N = 2$. This gives a resistance for a perfect metallic carbon nanotube of $\sim$ 6.5 kΩ. This resistance is a contact resistance arising from the mismatch of the number of conduction channels in the CNT and the macroscopic metal leads.

2.1.3 Dielectric Properties

Theoretical values for the permittivity ranging from unity to infinity ([87], [88] and [86]) have been reported in literature, depending on the tube being metallic or semiconducting. In the case of a semiconducting nanotube with band gap E_g it is shown in [87] that the permittivity is given by:

$$\varepsilon = 1 + \frac{\hbar\omega_p}{5.4E_g} \tag{2.6}$$

where $\hbar\omega_p$ is the energy of the plasma oscillation along the nanotube axis [89].

Metallic nanotubes have been predicted to have infinite permittivity [87], however, the finite length and the presence of defects effectively lead to a finite permittivity.

No measurements or calculations in the sub-GHz regime for the permittivity of m-SWCNT have been reported, however, Martens and co-workers [90] investigated the dielectric function of disordered single-walled carbon nanotubes experimentally in the 8 GHz - 800 GHz regime, and found the permittivity to approach $-10000\varepsilon_0$ at 8 GHz. This value does not correspond to the dielectric constant of the nanotube but is rather a measure of the refractive index of the nanotubes. A negative permittivity does not have any physical meaning.

A good approximation would be to use the permittivity of graphite, which is about $3\varepsilon_0$. As it will be shown later, the permittivity value of the nanotubes does not play such a large role in the dielectrophoretic force apart from the high frequencies (> 50 MHz).

2.1.4 Single- versus multi-walled nanotubes

As mentioned earlier, a nanotube can be considered as a rolled-up sheet of graphite. If more than one layer of graphite participates in the rolling then a multi-walled carbon nanotube is formed. A multi-walled carbon nanotube is thus a collection of concentric cylinders held together by van der Waals forces with a shell spacing of about 0.34 nm, slightly larger than the spacing between the individual graphene sheets in graphite. Each different concentric cylinder is an individual single-walled carbon nanotube and can therefore be either metallic or semiconducting.

Single-walled carbon nanotubes (SWCNTs) have typical diameters between 1 nm and 2 nm although nanotubes with diameters from 0.6 nm to 4 nm have been seen [6, 91]. Multi-walled carbon nanotubes (MWCNTs) have diameters between 4 nm and 100 nm and can have anything from 2 to even hundreds of layers. The diameter of the inner hole varies, depending on the tube's outer diameter and the number of layers. All tubes are closed on both ends when produced, in the case of the single-walled nanotubes with a semispherical buckyball.

While single-walled carbon nanotubes can either be metallic or semiconducting according to their chirality, multi-walled carbon nanotubes exhibit almost always metallic behaviour at room temperature regardless the chirality of the various layers. Researchers generally agree that the current flows through the outer layer at low bias but the barriers to the inner layers can be overcome when the bias voltage across the nanotube is increased.

2.1.5 Sensor Potential

As a direct result of their electrical properties and unusual structure carbon nanotubes are good candidates for various applications. Sensing applications in particular have attracted the interest of a large number of researchers. Semiconducting carbon nanotubes are ideal for use as sensors. As was shown as early as 1998 a Carbon NanoTube based Field Effect Transistor (CNTFET) performs better than state-of-the-art silicon FETs in terms of switching speed and transconductance. For certain values of the backgate voltage the nanotube is very sensitive to even small changes of the electrical field, changes that could arise if the CNTFET is present in a buffer containing charged species to be sensed. Indeed, in [92], an electrochemical gate is used on a nanotube FET and a change in the resistance of the nanotube is measured, though issues of contact deterioration by electrochemical reactions on the electrodes exist.

A nanotube in air is normally behaving like a p-type semiconductor, meaning that

the charge carriers are holes. When annealed the nanotube turns into n-type, as was shown in [85], which has led the researchers to believe that oxygen atoms sitting on the nanotube surface cause the p-type behaviour. Others believe the p-type behaviour is related to doping from the metal contacts (in most cases Au) [93], while there are also those that believe that processing of the nanotubes after production, for example oxidation and purification, could be the reason [53]. The conductance of a single semiconducting nanotube can be modulated several orders of magnitude [53] when the gate voltage is changed only a few Volts.

2.1.6 Raman spectroscopy of carbon nanotubes

Perhaps the easiest method to determine the diameter of a carbon nanotube is Raman spectroscopy. A typical carbon nanotube Raman spectra is shown in Figure 2.5. There are three distinct regions visible in the spectra. The Radial Breathing Mode (RBM) in the low energy region (100-300 cm^{-1}), the disorder induced mode (D-mode) and the high energy mode (G-band).

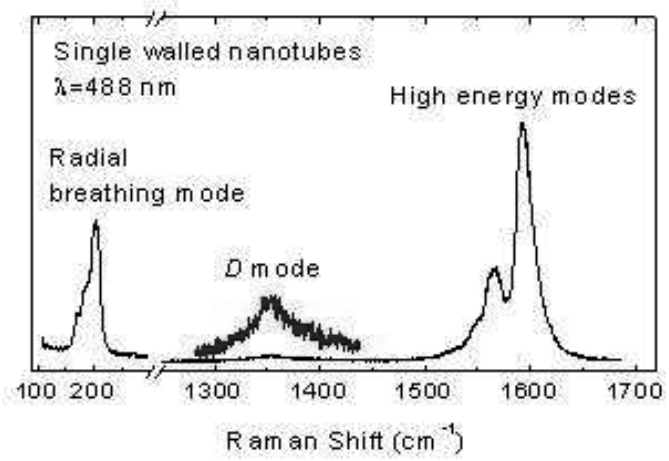

Figure 2.5: A typical carbon nanotube Raman spectra showing the three distinct modes: RBM, D-mode and the G-mode. Reproduced from [94]

It is the RBM mode that allows the evaluation of the diameter of a carbon nanotube. It is generally agreed that the diameter of a carbon nanotube is inversely proportional to the RBM frequency. In [95] the authors calculated the relationship to be $\overline{v}_{RBM}(\text{cm}^{-1}) = 223.75/d(\text{nm})$. However, single-walled nanotubes are never individual but form bundles. The interactions between the various nanotubes in the bundle shift the RBM frequency of particular nanotubes and the relationship becomes $\overline{v}_{RBM}(\text{cm}^{-1}) = 223.5/d(\text{nm})+12.5$ as was determined by Raman and fluorescence studies in [96]. A theoretical calculation of the same effect was done in [97] where the relationship was determined to be $\overline{v}_{RBM}(\text{cm}^{-1}) = 232/d(\text{nm}) + 6.5$. The latter two equations give results with a difference of about 1%.

Figure 2.6 shows how the Raman spectra correspond to nanotubes of particular diameters depending on the laser used for taking the spectra [97]. The Figure

shows that particular lasers can only "see" nanotubes of particular diameters.

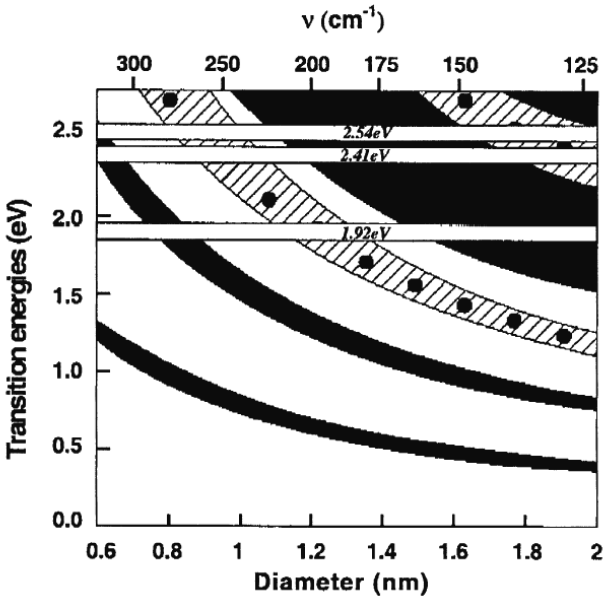

Figure 2.6: The ranges of energies where resonance is expected to occur. Black regions show semiconducting nanotubes while dashed regions show metallic nanotubes. Reproduced from [97]

The intensity of the Raman peaks depends greatly on the polarisation of the light relevant to the nanotube's long axis as was shown in [98] with the strongest signal obtained when the laser light is polarised along the nanotube axis.

Raman spectroscopy can also distinguish between metallic and semiconducting nanotubes. The lower G band (also called G- band) is slightly broadened and shifted to smaller energies for the metallic nanotubes, while the semiconducting nanotubes show a peak in the higher G band (also called the G+ band) much larger than the G- band peak [99].

Raman spectroscopy can also be used for deriving mechanical properties of carbon nanotubes as well as doping levels and defect concentration.

2.2 Sensing Cellular Ion Channels using CNTs

One of the most interesting applications for carbon nanotube sensors is their use for mapping the activity of ion channels in nerve cells. One of the most common methods for the recording of ion channel activity is patch clamping, involving punching a hole in the cell in order to insert a glass pipette in the cell interior. Since the function of an ion channel involves the release from inside the cell of some charged species at a region close to the ion channel, the charge balance will temporarily be disrupted, giving rise to a net positive or negative charge that can act as a local backgate for a nanotube FET in the vicinity. In the following I will present a model of an ion channel and estimate the expected concentration of a

charged species when an ion channel opens, as well as the ion current and the induced voltage due to a local charge distribution.

2.2.1 An ion channel model

When an ion channel opens, ions will move out of or into the cell through the ion channel due to a concentration gradient (diffusion) and an electrical gradient.

In order to model the ion channel the following assumptions will be made:

- The effects of the electrical gradient are neglected
- The ion channel is a point source in space containing initially C_0 ions
- The radial diffusion equation will be solved in the $z > 0$ space, i.e. for $\varphi \epsilon (0, 2\pi)$, $\theta \epsilon (0, \pi/2)$

Figure 2.7 shows a schematic of an ion channel.

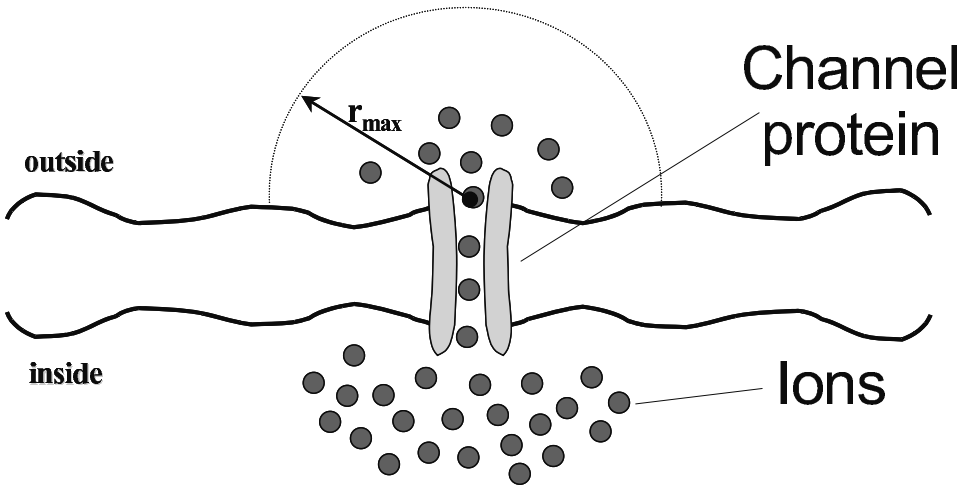

Figure 2.7: A simplified model of an ion channel. The ions will diffuse out of the channel into the region outside of the cell and the concentration change will practically be zero at distance r_{max} from the channel entrance.

2.2.2 The diffusion equation

We will use the diffusion equation to calculate the concentration of an ion species in space and time.

The equation to be solved is:

$$\frac{\partial c(r,t)}{\partial t} = D \cdot \frac{\partial^2 c(r,t)}{\partial r^2} + \frac{2D}{r} \cdot \frac{\partial c(r,t)}{\partial r} \tag{2.7}$$

where D is the diffusion coefficient of the ion under investigation and c is the change in ion concentration due to the ion channel operation as a function of radial distance r from the channel and time t.

Based on the one dimensional solution for this problem we will try solutions of the form

$$c(r,t) = \frac{A}{t^b} \cdot \exp(-\frac{r^2}{4Dt}) \tag{2.8}$$

where A and b are constants to be resolved.

The candidate solution of equation 2.8 is substituted into the diffusion equation 2.7 in order to define constant b. We thus have:

$$\frac{\partial c(r,t)}{\partial t} = \frac{A \cdot e^{-\frac{r^2}{4Dt}} \cdot r^2 \cdot t^{-2-b}}{4D} - A \cdot b \cdot e^{\frac{-r^2}{4Dt}} \cdot t^{-1-b} \tag{2.9}$$

$$\frac{\partial c(r,t)}{\partial r} = -\frac{A \cdot e^{-\frac{r^2}{4Dt}} \cdot r \cdot t^{-1-b}}{2D} \tag{2.10}$$

$$\frac{\partial^2 c(r,t)}{\partial r^2} = A \cdot [\frac{e^{-\frac{r^2}{4Dt}} \cdot r^2}{4D^2 \cdot t^2} - \frac{e^{-\frac{r^2}{4Dt}}}{2Dt}] \cdot t^{-b} \tag{2.11}$$

And by substituting equations 2.9, 2.10 and 2.11 into equation 2.7 we have:

$$\frac{A \cdot e^{-\frac{r^2}{4Dt}} \cdot r^2 \cdot t^{-2-b}}{4D} - A \cdot b \cdot e^{\frac{-r^2}{4Dt}} \cdot t^{-1-b} =$$
$$= D \cdot A \cdot [\frac{e^{-\frac{r^2}{4Dt}} \cdot r^2}{4D^2 \cdot t^2} - \frac{e^{-\frac{r^2}{4Dt}}}{2Dt}] \cdot t^{-b} + \frac{2D}{r} \cdot (-\frac{A \cdot e^{-\frac{r^2}{4Dt}} \cdot r \cdot t^{-1-b}}{2D}) \Longrightarrow$$

$$b \cdot t^{-1-b} = \frac{3}{2} \cdot t^{-1-b} \Longrightarrow b = \frac{3}{2}$$

Therefore:

$$c(r,t) = \frac{A}{t^{\frac{3}{2}}} \cdot \exp(-\frac{r^2}{4Dt}) \tag{2.12}$$

In order to calculate the constant A we will use the fact that the amount of ions diffusing cannot be different from the initial amount of ions C_0 (mols) available at the source. The concentration of equation 2.12 must then obey the equation:

$$\int_V c(r,t)dV = C_0 \tag{2.13}$$

where V is the volume that the ions occupy. To express dV in spherical coordinates the Jacobian is used to transform dV from the cartesian coordinates. The equation:

$$dV = |\frac{\partial(x,y,z)}{\partial(u_1,u_2,u_3)}|du_1du_2du_3 \tag{2.14}$$

will be used, where $u_1 = r$, $u_2 = \theta$ and $u_3 = \varphi$ and

$$|\frac{\partial(x,y,z)}{\partial(u_1,u_2,u_3)}| = \begin{vmatrix} \frac{\partial x}{\partial u_1} & \frac{\partial x}{\partial u_2} & \frac{\partial x}{\partial u_3} \\ \frac{\partial y}{\partial u_1} & \frac{\partial y}{\partial u_2} & \frac{\partial y}{\partial u_3} \\ \frac{\partial z}{\partial u_1} & \frac{\partial z}{\partial u_2} & \frac{\partial z}{\partial u_3} \end{vmatrix} \tag{2.15}$$

The relationship between cartesian and spherical coordinates is given by the equations:

$$x = r\sin\theta\cos\varphi, \quad y = r\sin\theta\sin\varphi, \quad z = r\cos\varphi \tag{2.16}$$

Substituting equations 2.16 and 2.15 into 2.14 gives:

$$dV = r^2\sin\theta dr d\theta d\varphi \tag{2.17}$$

Therefore equation 2.13 becomes:

$$\begin{aligned} &\int_0^{2\pi}\int_0^{\pi/2}\int_0^{\infty} c(r,t)r^2\sin\theta dr d\theta d\varphi = C_0 \Rightarrow \\ &\int_0^{2\pi} d\varphi \int_0^{\pi/2}\sin\theta d\theta \int_0^{\infty} c(r,t)r^2 dr = C_0 \Rightarrow \\ &\frac{2\pi A}{t^{3/2}}\int_0^{\infty} r^2\exp(-\frac{r^2}{4Dt})dr = C_0 \end{aligned} \tag{2.18}$$

From tables we know that

$$\int_0^\infty x^m e^{-\alpha x^2} dx = \frac{\Gamma[(m+1)/2]}{2\alpha^{(m+1)/2}} \tag{2.19}$$

$$\Gamma(n+1) = n! \quad , \quad n = 0, 1, 2, ... \tag{2.20}$$

$$\Gamma(k + \frac{1}{2}) = \frac{1 \cdot 3 \cdot 5 \cdot ... \cdot (2k-1)\sqrt{\pi}}{2^k} \tag{2.21}$$

So, for $m = 2$, $k = 1$ and $\alpha = \frac{1}{4Dt}$ from equations 2.19, 2.20, 2.21 and 2.18 we have that:

$$\begin{aligned}
&\frac{2\pi A}{t^{3/2}} \int_0^\infty r^2 \exp(-\frac{r^2}{4Dt}) dr = C_0 \Rightarrow \\
&\frac{2\pi A}{t^{3/2}} \cdot \frac{\Gamma(3/2)}{2(4Dt)^{-3/2}} = C_0 \Rightarrow \\
&\frac{\pi A \cdot \frac{\sqrt{\pi}}{2}}{(4D)^{-3/2}} = C_0 \Rightarrow \\
&A = \frac{2C_0}{(4\pi D)^{3/2}}
\end{aligned} \tag{2.22}$$

Substituting equation 2.22 into 2.12 the final solution for the concentration is obtained:

$$c(r,t) = \frac{2C_0}{(4\pi Dt)^{3/2}} \exp(-\frac{r^2}{4Dt}) \tag{2.23}$$

2.2.3 Ion concentration

For specific ions we need to determine the diffusion coefficient D and the initial concentration C_0 of equation 2.23. The diffusion coefficient D can be found from tables or calculated from the ion mobility using the Nernst-Einstein law:

$$\mu_i = |z_i| \frac{F}{RT} D_i \tag{2.24}$$

where μ_i is the mobility of ion i, z_i is the charge number of ion i, D_i is the ion's diffusion coefficient, F is the Faraday constant, R is the gas constant and T is the temperature in Kelvin.

Three different ions were examined:

- K^+
  For K^+ the mobility in water is $\mu_{K^+} = 76.2 \cdot 10^{-9}$ m^2/Vs, so from equation 2.24 and for temperature at 25 ^{o}C we find that $D_{K^+} = 1.96 \cdot 10^{-9}$ m^2/s
- Na^+
  For Na^+ the mobility in water is $\mu_{Na^+} = 51.9 \cdot 10^{-9}$ m^2/Vs, so from equation 2.24 and for temperature at 25 ^{o}C we find that $D_{Na^+} = 1.33 \cdot 10^{-9}$ m^2/s
- Ca^{2+}
  From tables it can be obtained that $D_{Ca^{2+}} = 0.6 \cdot 10^{-9}$ m^2/s in water

To determine C_0 we used known values for ion flux through ion channels as well as the time the channels remain open (known as gating time). The latter varies between 1 ms - 2 ms. In this investigation it is set equal to 1 ms.

A literature search was done to obtain the ion flux for the three different ions used. This resulted in a flux ranging between $10^6 - 10^8$ ions/s for all ion channels. Although it was difficult to obtain individual values for each ion channel there seems to be a trend that K^+ channels are the fastest, followed by Na^+ channels, which are in turn followed by Ca^{2+} channels. Therefore for K^+ the flux is taken to be $\sim 10^8$ ions/s. For Na^+ it is taken to be $\sim 10^7$ ions/s and for Ca^{2+} it is taken to be $\sim 10^6$ ions/s. Most results will be presented here in units of C_0 so that this uncertainty will not play a huge role.

If t_g is the gating time and j is the flux then:

$$C_0 = \frac{j t_g}{N_A} \tag{2.25}$$

where N_A is Avogadro's number.

For the above mentioned values for t_g and j we have:

$$C_0^{K^+} = 1.66 \cdot 10^{-19} \ \texttt{mol} \tag{2.26}$$
$$C_0^{Na^+} = 1.66 \cdot 10^{-20} \ \texttt{mol} \tag{2.27}$$
$$C_0^{Ca^{2+}} = 1.66 \cdot 10^{-21} \ \texttt{mol} \tag{2.28}$$

The results for the concentration as a function of radial distance from the channel opening and time after closing for all three ion channels investigated here are plotted in figure 2.8 in units of C_0/m^3.

2.2.4 Ion current

From the solution for the concentration we can also calculate the ion current from the ion movement. This will be given by the equation:

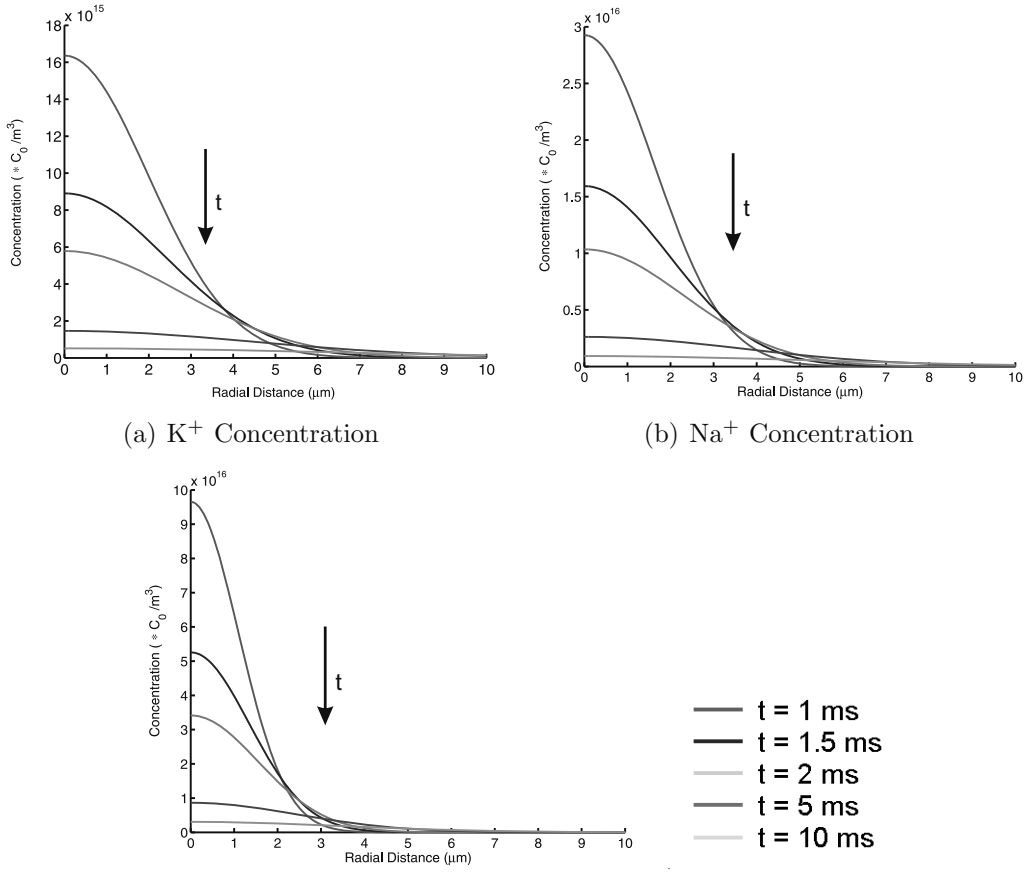

(a) K^+ Concentration (b) Na^+ Concentration

(c) Ca^{2+} Concentration (d)

Figure 2.8: The concentration of the ions after the ion channel opens as a function of time and radial distance from the channel. The concentration is given in units of C_0/m^3.

$$I(r,t) = \frac{\partial}{\partial t}[(\int_{\Delta V} c(r^{'},t)dV) \cdot N_A \cdot |z| \cdot q_e] \tag{2.29}$$

where N_A is Avogadro's number ($= 6.022 \cdot 10^{23}$ mol^{-1}), z is the charge number of the ion and q_e is the charge of one electron ($= 1.602 \cdot 10^{-19}$ Cb) and the integral is evaluated from $r^{'} = 0$ to a distance r, where we want to know the current.

By use of the program Mathematica it was possible to plot the current as a function of distance from the source for time values ranging between $1 - 10$ ms without obtaining an analytical expression. Such an expression is possible to obtain but it will be very complicated because of the nature of the integral of equation 2.29.

The results for the three ions are displayed in figure 2.9 in units of C_0 A/mol.

2.2.5 Induced Voltage

The fact that there is a distribution of charges in our system means that an

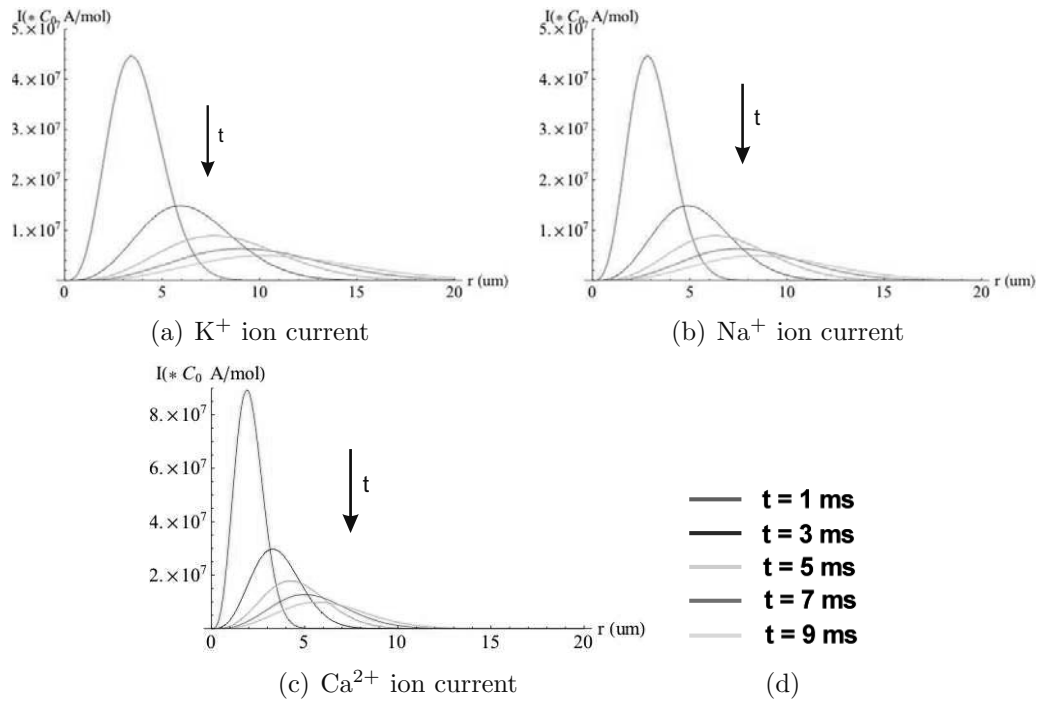

(a) K^+ ion current (b) Na^+ ion current

(c) Ca^{2+} ion current (d)

Figure 2.9: The ion current of the ions after the ion channel opens as a function of time and radial distance from the channel. The current is given in units of C_0 A/mol.

electrode placed inside the system will pick up a voltage with respect to a reference electrode away from the ion channel dependent on the distance from the source that the electrode is placed and the time of measurement after the channel has opened. Poisson's equation will be used to calculate the voltage:

$$\nabla^2 V = -\frac{\rho}{\varepsilon} \tag{2.30}$$

where ρ is the charge density and ε is the permittivity of the solution.

In our symmetrical system the left part of equation 2.30 will be expressed in spherical-radial coordinates. This will give:

$$\nabla^2 V = \frac{1}{r^2}\frac{\partial}{\partial r}(r^2\frac{\partial V}{\partial r}) = -\frac{\rho}{\varepsilon} \tag{2.31}$$

The charge density can easily be calculated from the concentration (equation 2.23) by multiplying with Avogadro's number, the charge number and the electron charge:

$$\begin{aligned} &\rho(r,t) = c(r,t) \cdot N_A \cdot |z| \cdot q_e \Rightarrow \\ &\rho(r,t) = \frac{2C_0 N_A |z| q_e}{(4\pi D t)^{3/2}} \exp(-\frac{r^2}{4Dt}) \end{aligned} \tag{2.32}$$

Combining equations 2.31 and 2.32 it follows that we need to solve the equation:

$$\frac{1}{r^2}\frac{\partial}{\partial r}(r^2\frac{\partial V}{\partial r}) = -\frac{2C_0N_A|z|q_e}{\varepsilon(4\pi Dt)^{3/2}}\exp(-\frac{r^2}{4Dt}) \tag{2.33}$$

Using the program Mathematica for the integration we get the analytical expression:

$$V(r,t) = \frac{C_0N_A|z|q_e}{2\varepsilon r\pi}\cdot Erf(\frac{r}{2\sqrt{Dt}}) \tag{2.34}$$

Figure 2.10 shows the voltage distribution as a function of radial distance from the source and time in units of C_0 Volts/mol.

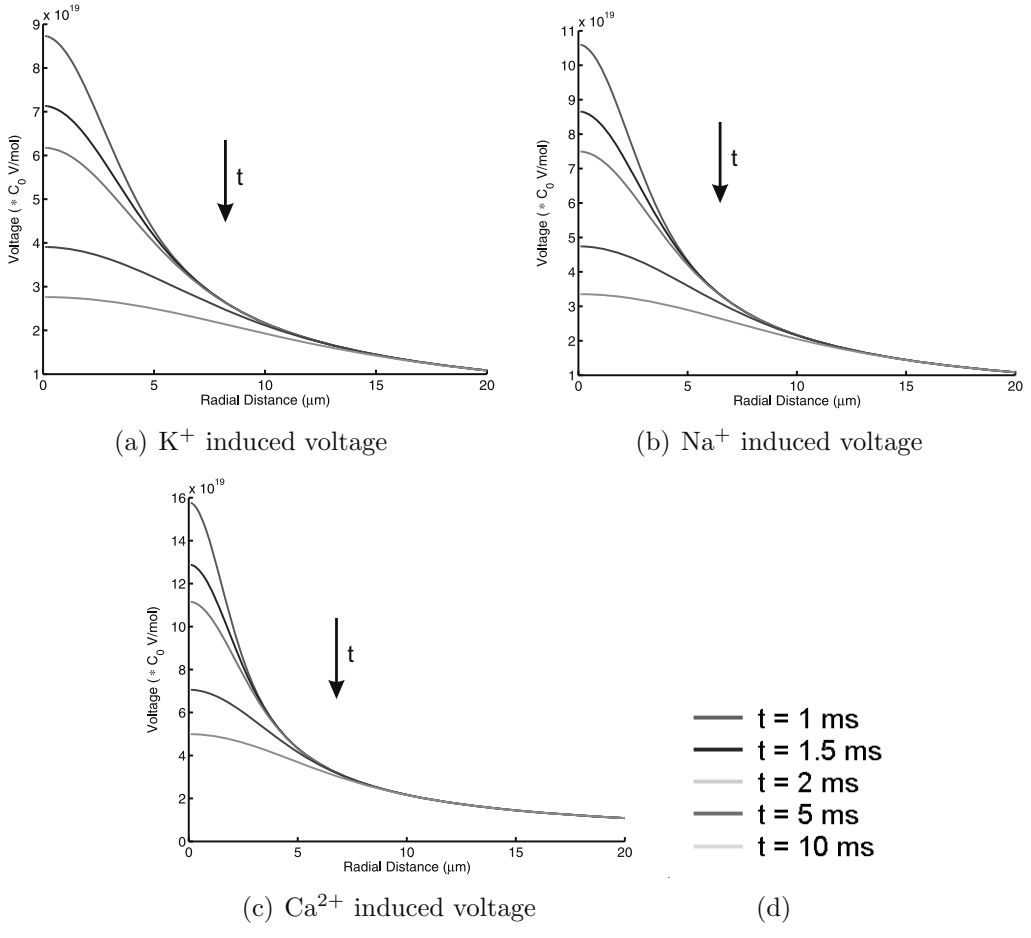

(a) K^+ induced voltage (b) Na^+ induced voltage

(c) Ca^{2+} induced voltage (d)

Figure 2.10: The voltage induced from the charge distribution after the channel opens as a function of time and distance from the channel. The voltage is given in units of C_0 V/mol.

2.2.6 Carbon Nanotubes as sensors

By using the values of the initial concentration for the ions of equations 2.26, 2.27 and 2.28 we find that the maximum change in concentration occurs 1 ms

Table 2.1: The maximum values for the concentration, current and voltage for each of the three ions at 1 ms after the channel has opened.

	Concentration (μM)	**Current (pA)**	**Voltage (V)**
K^+	2.72	7.5	1.47
Na^+	0.49	0.75	0.180
Ca^+	0.16	0.15	0.052

after the channel opens close to the source and is of the order of $1-3$ μM. The maximum current and voltage also occur at the same time and location and are between $1-10$ pA and $0.05-1.4$ V with respect to the voltage far away from the ion channel, respectively. Table 2.1 summarizes the maximum values for the concentration, current and voltage for each ion investigated.

Based on the above calculations there are two ways that the ion channel activity could be measured. The principle described in [78] is one of them. A multi-point probe but with much smaller electrode spacing and a reference electrode isolated from the rest could pick up the local voltage change at several points around the ion channel, always with respect to the potential away from the channel. Such a probe was in fact fabricated and tested with salt solutions early in the project, but several fabrication errors prevented it from functioning properly.

The local charge distribution will change the electric field around the ion channel. A CNTFET tuned at a point of maximum sensitivity would perhaps be able to respond to this local change of the electric field. The calculated concentration changes around an ion channel are very small (a few μM). However, ppb concentrations have been sensed by nanotubes in air. If their sensitivity in liquid is even a 1000 times smaller than that, there is a real chance that they can be used for ion channel activity detection.

2.3 Dielectrophoresis on cylindrical particles

Dielectrophoresis is the motion of a polarisable particle in an inhomogeneous electric field. The keyword in this definition is the *inhomogeneous* field. In such a case the field strength and thus the force acting on each side of the particle will be different, causing the particle to move with respect to the medium. Depending on the polarisability of the particle compared to that of the medium, the force could push the particle towards regions of high or low electric field, termed positive and negative dielectrophoresis, respectively. This is illustrated in figure 2.11 for a cylindrical particle, which is immediately aligned with the field lines [100] and moves perpendicular to the field lines along the gradient. In the case of an alternating electric field (ac) the direction of the force and thus the direction of motion will remain the same even upon field reversal, because the dipole moment will be inverted as well.

The force exerted by an electric field $\mathbf{E}$ on a dipole with dipole moment $\mathbf{p}$ is given

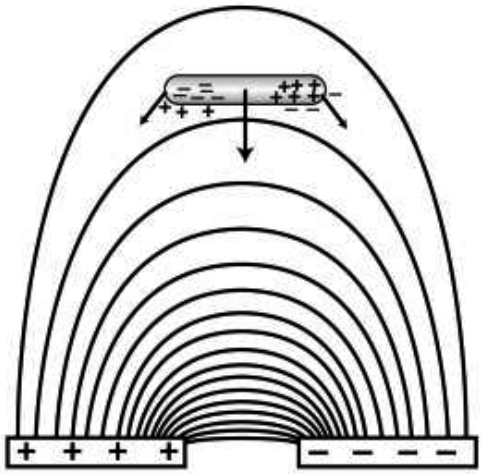

Figure 2.11: Sketch illustrating a carbon nanotube subjected to dielectrophoresis. The nanotube immediately aligns with the field lines and experiences a net force from the ac-field. This force may be directed towards the high field region (down) in the case of positive dielectrophoresis (shown), and towards the low field region (up) for negative dielectrophoresis (not shown).

by

$$\mathbf{F} = (\mathbf{p} \cdot \nabla)\mathbf{E} \tag{2.35}$$

Here the higher order terms of the force are omitted [101]. Thus, the expression is only accurate if the magnitude of the electric field does not vary significantly across the dipole. In an ac-field the time-averaged force on a particle will be given by

$$\mathbf{F_{DEP}} = \mathbf{\Gamma} \cdot \varepsilon_\mathbf{m} \mathbf{Re}\{\mathbf{K_f}\} \nabla |\mathbf{E^2}| \tag{2.36}$$

where Γ is a factor depending on geometry, ε_m the real part of the permittivity of the suspending medium and $\mathbf{E}$ is the amplitude of the electric field. The factor K_f depends on the complex permittivities of both the particle and the medium. In the case of a spherical particle this factor is referred to as the Claussius-Mossotti factor. For an elongated object with the long axis aligned with the field, K_f is given by

$$K_f = \frac{\varepsilon_p^* - \varepsilon_m^*}{\varepsilon_m^* + A_L \cdot (\varepsilon_p^* - \varepsilon_m^*)}, \quad \varepsilon^* = \varepsilon - i \cdot \frac{\sigma}{\omega} \tag{2.37}$$

where the indices p and m refer to the particle and the medium, respectively. Here σ is the conductivity, ε the real permittivity and ω the angular frequency of the applied electric field. A_L is the depolarising factor in the direction of the long

axis. In the case of a prolate ellipsoid, as a carbon nanotube can be considered for this purpose, the geometrical factor Γ and the depolarising factor A_L are given by

$$\Gamma = \frac{\pi}{6} r^2 \ell \tag{2.38}$$

$$A_L = -\frac{2r^2}{\ell^2 \cdot e^3} \cdot \left(2e - ln(\frac{1+e}{1-e}) \right) \tag{2.39}$$

where e is the eccentricity of the prolate ellipsoid, given by $e = \sqrt{1-(2r/\ell)^2}$, r is the radius and ℓ the length of the cylinder.

If $r << \ell$ equation 2.37 can be simplified to:

$$K_f = \frac{\varepsilon_p^* - \varepsilon_m^*}{\varepsilon_m^*} \tag{2.40}$$

and in the high and low frequency limits:

$$K_f = \begin{cases} \frac{\sigma_p - \sigma_m}{\sigma_m}, & \omega \to 0 \\ \frac{\varepsilon_p - \varepsilon_m}{\varepsilon_m}, & \omega \to \infty \end{cases} \tag{2.41}$$

However, as we will show in the next chapter, one should be careful with using this expression, as the term containing the depolarising factor becomes quite important when the particle conductivity is much larger compared to that of the medium so that the approximation of equations 2.40 and 2.41 is no longer valid.

2.4 Summary

A brief introduction to the theory of carbon nanotubes and to dielectrophoresis was presented in this chapter along with a model for an ion channel developed for investigating the potential of using a carbon nanotube as a sensor of ion channel activity in neurons. The model shows that a single ion channel induces a local concentration change of a few μM close to the channel opening, giving rise to a local electric field that could gate a nanotube on a CNTFET provided that the nanotube was tuned to a point of high sensitivity. Alternatively a multi-electrode cantilever structure could be used in order to measure the induced voltage difference between regions close to the ion channel and a reference electrode placed away from the channel.

Chapter 3

Simulations

In the following we will present a simple model for calculating the motion of a carbon nanotube under the influence of an inhomogeneous electric field generated by microelectrodes. The model is crucial for the design of experiments that aim to trap or sort carbon nanotubes. Three simulations have been conducted, two incorporating a microfluidic channel with the nanotube solution flowing with a homogeneous velocity inside and one where the probe is just placed inside a volume of the solution.

3.1 General assumptions

As a crude approximation a carbon nanotube can be considered as a cylinder with a certain conductivity and permittivity. Thus the theory presented in section 2.3 can be applied easily to a carbon nanotube in order to estimate the dielectrophoretic force. However, a carbon nanotube is not an ordinary conductor. We have described how a single-walled carbon nanotube ideally is a perfect ballistic conductor in section 2.1.2. For such a conductor the concept of conductivity does not apply. Regardless of the length of the nanotube the resistance is always the same and equal to 6.5 kΩ. In practice, this is indeed the case for high quality carbon nanotubes of relatively small lengths, i.e. micron size or smaller.

SWNT with transport properties ranging from ballistic to diffusive have been reported in literature [53, 102, 103]. A nanotube is said to be ballistic if the electron elastic mean free path is greater than the length of the nanotube. This is valid for relatively short pieces of near-perfect nanotubes with a very low number of defects. We here consider nanotubes with lengths of several micrometres or more. In this regime most metallic and semiconducting nanotubes can be considered to be diffusive, although they consist of small piece-wise ballistic segments. Thus, the calculations presented here are based on the assumption that the conductivity is a relevant material property, and that standard formulae for dielectrophoresis may be applied, such as described in the previous section.

For the "conductivity" σ of diffusive semiconducting SWCNTs (s-SWCNTs) we

consider a value of 10^5 S/m and for metallic SWCNTs (m-SWCNTs) a value of 10^8 S/m. These values are estimated from electrical measurements of the resistance of single-walled nanotubes at zero gate voltage [53, 104, 105, 106] using the relation $\sigma \equiv G \cdot \ell/\pi(r_{out}^2 - r_{in}^2)$, where G is the measured conductance, ℓ is the length of the nanotube and $r_{out} - r_{in}$ refers to the thickness of the SWCNT wall. These values for the conductivity can be considered at most as characteristic. To see how our results depend on these values we have also made calculations with other values for the conductivity. See section 3.4.4 for details.

As was discussed in section 2.1.3 it is difficult to make any sort of accurate prediction for the permittivity of single-walled carbon nanotubes. In the following calculations we will assume a permittivity of $2.5\varepsilon_0$ for s-SWCNTs tubes, in accordance with [73]. We will return to the permittivity of metallic nanotubes at a later point.

Nanotubes are typically dispersed in a solvent with the aid of ultrasonication. In the following, we will assume that the final solution consists of individually separated tubes in 2-propanol (IPA) or in an 1% aqueous solution of Sodium Dodecyl Sulphate (SDS), two chemicals widely used as a dispersing medium for carbon nanotubes in experiments [73, 33]. IPA has a permittivity of $\varepsilon_{IPA} = 18.6\varepsilon_0$ and a conductivity of $\sigma_{IPA} = 6$ μS/m while a 1% water solution of SDS has a permittivity of $\varepsilon_{SDS} = 80\varepsilon_0$ and a conductivity of $\sigma_{SDS} = 0.125$ S/m [107]. Popular alternatives are dimethylformamide (DMF), $\varepsilon_{DMF} = 38.8\varepsilon_0$, ethanol, $\varepsilon_{ethanol} = 20\varepsilon_0$ and 1,2 dichloroethane (DCE), $\varepsilon_{DCE} = 2.5\varepsilon_0$.

For the calculations we are considering nanotubes 2 nm in diameter and 3 (termed "long") and 0.3 μm (termed "short") in length.

Since equation 2.35 neglects high-order terms, the DEP force on SWCNT near electrodes, where the field gradient is largest, is not well described by the model. In the calculations we found that capturing of nanotubes occurs on a scale significantly larger than the electrode spacing, and thus the characteristic spatial scale of variation of the field. Hence, we do not expect high-order terms to be of critical importance.

We will consider three forces acting on the nanotube: The dielectrophoretic force, the viscous force opposing movement from the solution and the random thermal force. The heating effects that also occur particularly close to the electrodes will not be taken into account in the movement calculation but will be examined separately.

3.2 Microfluidics simulation

In order to plot the trajectory of a carbon nanotube as a result of a force acting on it we will use Newton's 2nd law of motion $\mathbf{F} = m\mathbf{a}$. Here $\mathbf{F}$ is the total force acting on the nanotube, m is the mass and $\mathbf{a}$ is the acceleration of the nanotube, $\mathbf{a} = \frac{d\mathbf{v}}{dt}$, where $\mathbf{v}$ is the velocity of the nanotube. If we ignore the random thermal force at this point, the total force is comprised from the DEP force, $\mathbf{F_{DEP}}$ given

by equation 2.36 and the viscous force, $\mathbf{F_v} = f \cdot (\mathbf{u} - \mathbf{v})$, where f is the friction factor and $\mathbf{u}$ is the velocity of the fluid. Therefore we have:

$$\begin{aligned}
&\mathbf{F} = m\frac{d\mathbf{v}}{dt} \Rightarrow \\
&\mathbf{F_{DEP}} + \mathbf{F_v} = m\frac{d\mathbf{v}}{dt} \Rightarrow \\
&\mathbf{F_{DEP}} + f \cdot (\mathbf{u} - \mathbf{v}) = m\frac{d\mathbf{v}}{dt} \Rightarrow \\
&\frac{d\mathbf{v}}{dt} + \frac{f}{m}\mathbf{v} = \frac{\mathbf{F_{DEP}}}{m} + \frac{f \cdot \mathbf{u}}{m} \Rightarrow \\
&\mathbf{v} = (\frac{\mathbf{F_{DEP}}}{f} + \mathbf{u})(1 - e^{-\frac{f}{m}t}) + \mathbf{v_0} \cdot e^{-\frac{f}{m}t}
\end{aligned} \tag{3.1}$$

Equation 3.1 applies for a nanotube with initial velocity $\mathbf{v_0}$ and is valid for times greater than zero. The exponential term describes the acceleration phase of the nanotube motion and has a time constant of $\tau = m/f$, i.e. for times greater than τ the nanotube will be moving with the terminal velocity:

$$\mathbf{v_T} = \frac{\mathbf{F_{DEP}}}{f} + \mathbf{u}, \tag{3.2}$$

regardless of the initial velocity. For a randomly moving prolate ellipsoid with length ℓ and radius r, the friction factor f in a liquid of viscosity η is:

$$f = \frac{3\pi\eta\ell}{\ln(\ell/r)} \tag{3.3}$$

For isopropanol the viscosity is $\cong$ 2.3 mPa·s at 20 ^{o}C , while for a 1% aqueous SDS solution the viscosity is taken to be the same as to that of water at 20^{o}C, that is $\cong$ 1 mPa·s. According to the Einstein relation this should be within 5% of the true value of the viscosity, an accuracy which is sufficient for our calculations.

For this simulation we use real electrode structures and therefore an analytical expression of the electric field cannot be obtained. Instead we use the finite element modeling laboratory FEMLAB (now known as Comsol Multiphysics) to numerically calculate the electric field generated from these electrodes. The electrodes used for the calculations as well as the generated electric field in a plane in the middle of the electrodes are shown in figure 3.1. The electric field simulation uses a voltage of 5 V_{RMS} applied on the electrodes.

In order to continue with the calculations the solution for the field has to be exported to the mathematical laboratory MATLAB. As a result of this the field and thus the force values are only known in a number of points around the electrodes. The number of grid points is chosen as a compromise of spatial resolution, spatial range and computational time and in this case we have chosen a 200×200×200 grid with one grid point per μm.

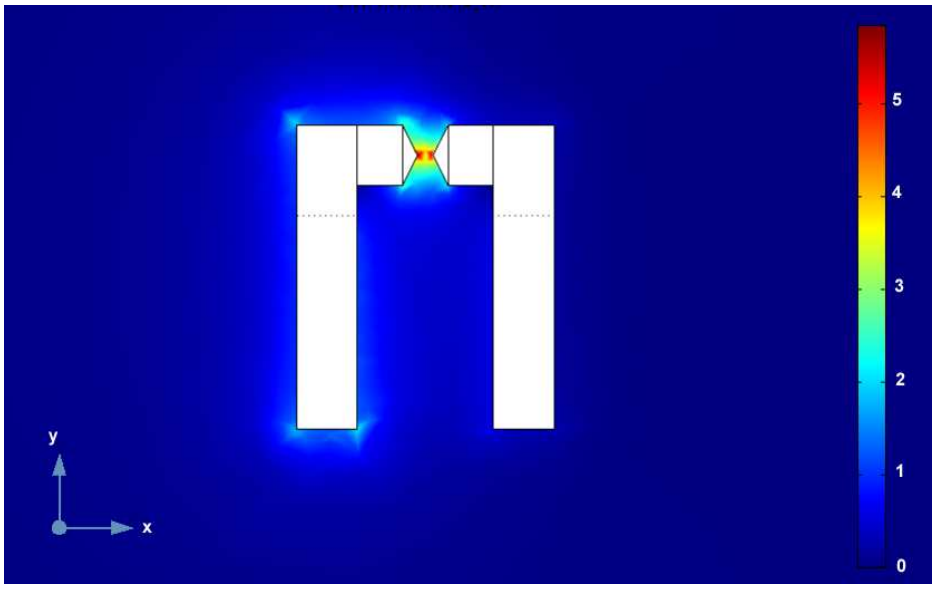

Figure 3.1: A close up of the electric field as calculated by FEMLAB in a plane passing from the middle of the electrodes. The gap between the electrodes is 1μm.

3.2.1 The motion algorithm

The algorithm used for the motion calculation is based on keeping a constant spatial step for the nanotube and evaluate the time it will take to cover this spatial step based on the value of the DEP force at the point of origin. This means that the time-step is effectively reduced near regions of high fields, to avoid accumulation of numerical errors. In our case the time step varies from 1 nsec to 1 sec depending on the nanotube velocity.

As was already mentioned in section 3.2 for times greater than the time constant τ the nanotube will be moving with the terminal velocity of equation 3.2. This time constant in the case of a nanotube is very small, typically smaller than the smallest time interval used in the algorithm (10^{-9} s) and therefore equation 3.2 is applicable at all times.

The electric field has been calculated with FEMLAB and exported as a $201\times201\times201$ array in MATLAB, where the rest of the calculation is taking place. Using equation 2.36 for a given frequency and given nanotube dimensions we can calculate the three components of the dielectrophoretic force in the three cartesian axes and from these the three components of the dielectrophoretic velocity using equation 3.2.

The spatial step employed is equal to 0.1 μm. Since the values for the velocity are known only on the grid points, an interpolation step is necessary in order to get the value of the velocity at the point where the nanotube is situated. The value of the velocity at a point in space is calculated from the values of the 8 nearest grid points using the linear and bilinear interpolation methods.

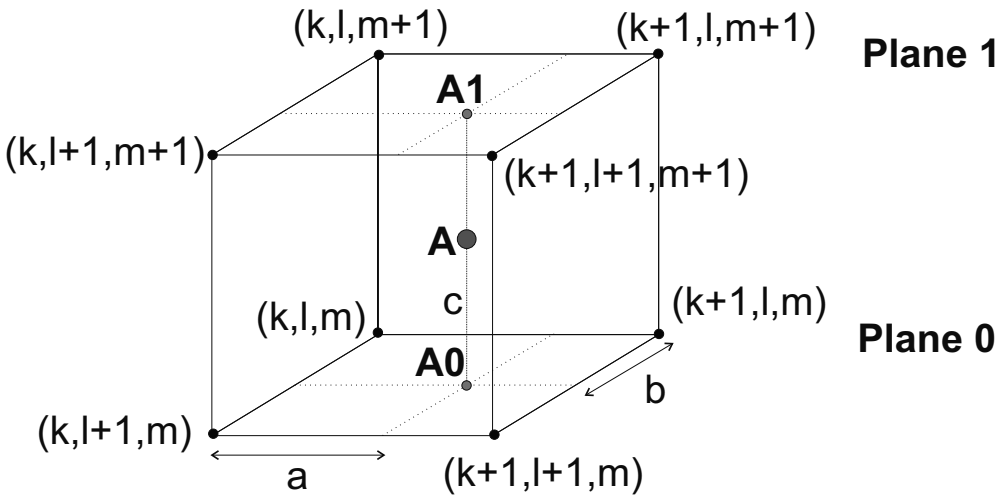

Figure 3.2: The method used to find the value of the velocity in point **A**. **A0** and **A1** are the projections of point **A** on plane 0 and 1 respectively.

First the projections of the point (point **A** in figure 3.2) on planes 0 (point **A0**) and 1 (point **A1**) are found. Then the value of the velocity will be given by:

$$\mathbf{V}(\mathbf{A}) = (1-c)\mathbf{V}(\mathbf{A0}) + c\mathbf{V}(\mathbf{A1}) \tag{3.4}$$

Using the bilinear interpolation method on each plane it can easily be shown that:

$$\begin{aligned}\mathbf{V}(\mathbf{A0}) &= (1-a)(1-b)\mathbf{V}(k,l,m) + (1-a)b\mathbf{V}(k,l+1,m) + \\ &+ (1-b)a\mathbf{V}(k+1,l,m) + ab\mathbf{V}(k+1,l+1,m)\end{aligned} \tag{3.5}$$

$$\begin{aligned}\mathbf{V}(\mathbf{A1}) &= (1-a)(1-b)\mathbf{V}(k,l,m+1) + \\ &+ (1-a)b\mathbf{V}(k,l+1,m+1) + \\ &+ (1-b)a\mathbf{V}(k+1,l,m+1) + ab\mathbf{V}(k+1,l+1,m+1)\end{aligned} \tag{3.6}$$

Combining equations 3.5 and 3.6 with equation 3.4 gives the desired value of the velocity.

With the velocity of the nanotube known, the time step t_s is calculated by the equation:

$$t_s = \frac{0.1 \cdot 10^{-6}}{\sqrt{v_x^2 + v_y^2 + v_z^2}} \tag{3.7}$$

where v_x, v_y and v_z are the three cartesian components of the velocity. If we ignore the thermal motion, the nanotube displacement would then simply be the area under the curve of the velocity vs time (Figure 3.3). In order to reduce the numerical errors we use a linear prediction for the velocity:

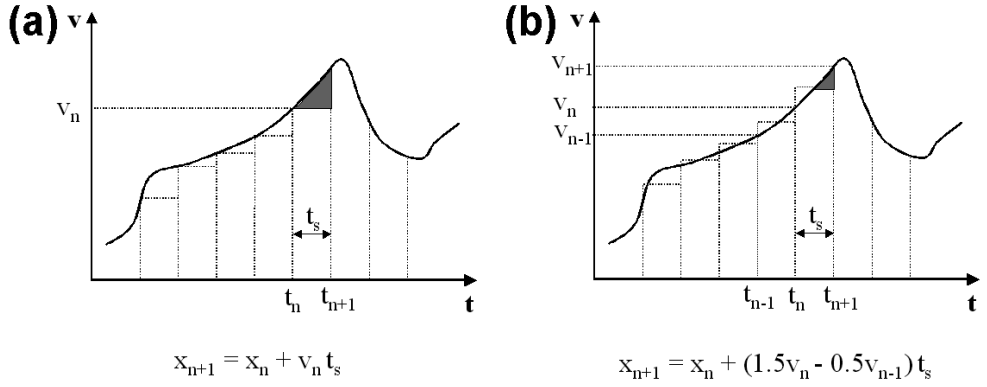

Figure 3.3: The two different methods for finding the position of the nanotube. **(a)** The Euler integration method. The error in the value of the velocity is shown with red. If we use the linear prediction method as shown in **(b)** the error is reduced.

$$\mathbf{v_{n+1}} - \mathbf{v_n} = \mathbf{v_n} - \mathbf{v_{n-1}} \Rightarrow \ \mathbf{v_{n+1}} = 2\mathbf{v_n} - \mathbf{v_{n-1}} \tag{3.8}$$

Therefore:

$$\begin{aligned} \mathbf{x_{n+1}} &= \mathbf{x_n} + (\mathbf{v_n} + \frac{\mathbf{v_{n+1}} - \mathbf{v_n}}{2}) \cdot t_s \Rightarrow^{(3.8)} \\ \mathbf{x_{n+1}} &= \mathbf{x_n} + (\frac{3}{2}\mathbf{v_n} - \frac{1}{2}\mathbf{v_{n-1}}) \cdot t_s \end{aligned} \tag{3.9}$$

Because of the random thermal motion the position $\mathbf{x_n}$ of the nanotube at each point will be unknown by a factor depending on the nanotube's diffusion coefficient $D_{nano} = 3k_bT/f$, where k_b is the Boltzman constant, T is the absolute temperature and f is the friction factor. The thermal displacement (also referred to as Brownian displacement) is then given by $d_B = \sqrt{6D_{nano}t_s}$. Note that the Brownian displacement is only dependent on the time-step t_s, which is in turn dependent on the nanotube velocity. Figure 3.4 shows the expected Brownian displacement for short and long nanotubes dispersed in IPA and SDS for the different time steps used in the algorithm. It can be seen that the Brownian motion affects the short nanotubes more.

The actual position of the nanotube at step n can therefore be anywhere within a sphere with center $\mathbf{x_n}$ and radius d_B. As the worst case scenario, we use the sphere radius as the Brownian displacement. Using MATLAB's random number generator we generate the spherical coordinates θ and φ, which together with d_B provide the magnitude and direction of the Brownian displacement. Then use the known spherical to cartesian conversions to find the cartesian random displacements. The resulting displacements in the cartesian coordinate system are added to the calculated displacement from equation 3.9 (Figure 3.5).

This process is repeated until such time as one of the end requirements are satisfied:

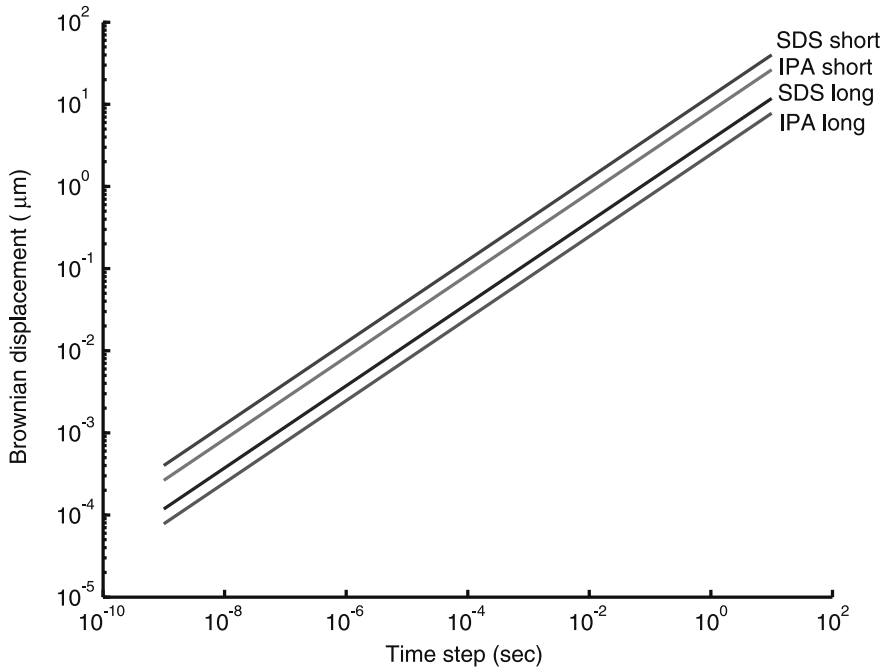

Figure 3.4: The random displacement for short ($\ell = 0.3$ μm) and long ($\ell = 3$ μm) nanotubes dispersed in IPA and SDS as a function of the time step. For the time steps used in the calculations the brownian displacement ranges between a few nanometers up to about 10 μm far away from the electrodes.

- The nanotube has reached the electrodes. The program terminates and the trajectory and the "time-of-arrival" of the nanotube are returned. A flag variable indicates that the electrodes have been reached.
- The nanotube has reached the boundaries of the grid. The program terminates returning the trajectory of the nanotube and the flag variable indicates that the nanotube was out of the grid.
- After a large number of iterations none of the previous stopping conditions have been satisfied. The program returns a flag variable indicating algorithm failure.

Figure 3.6 summarizes the algorithm used.

Two simulations were conducted with different parameters, summarized in table 3.1.

3.2.2 Simulation 1

In this simulation we consider the permittivity of metallic single-walled carbon nanotubes to be $10000\varepsilon_0$. This number is chosen somewhat arbitrarily, based on the theoretical prediction of an infinite permittivity by [87]. However, as it will be shown, the choice of permittivity plays little role in the simulations for most frequencies investigated.

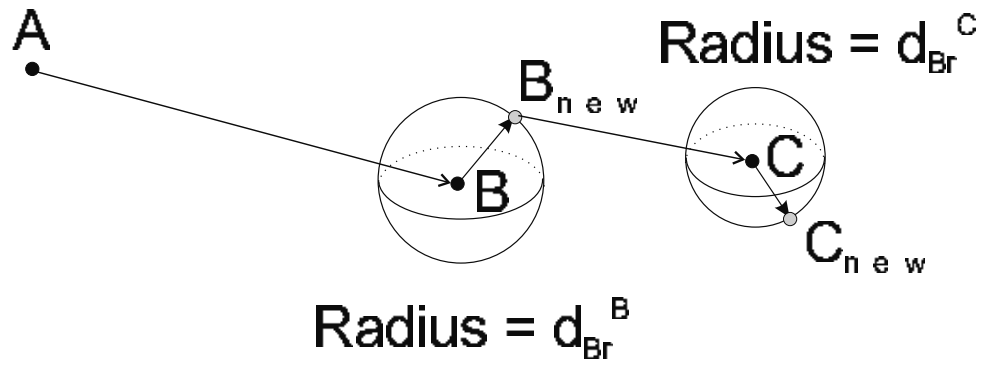

Figure 3.5: The process of adding a random thermal displacement to the DEP displacement. The nanotube starts from point A and goes to point B. There a new random coordinate is assigned to it, based on the expected thermal displacement d_B. From the new position B_{new} the nanotube moves to position C due to DEP forces and is assigned another position C_{new} again.

Table 3.1: The parameters used in each one of the two simulations

Parameter	Simulation 1	Simulation 2
Voltage	10 Vp-p	5.78 Vp-p
ε_{mSWCNT}	$10000\varepsilon_0$	$2.5\varepsilon_0$
Depolarisation factor	no	yes
Brownian motion	time interval up to 1 s	time interval up to 0.01 s

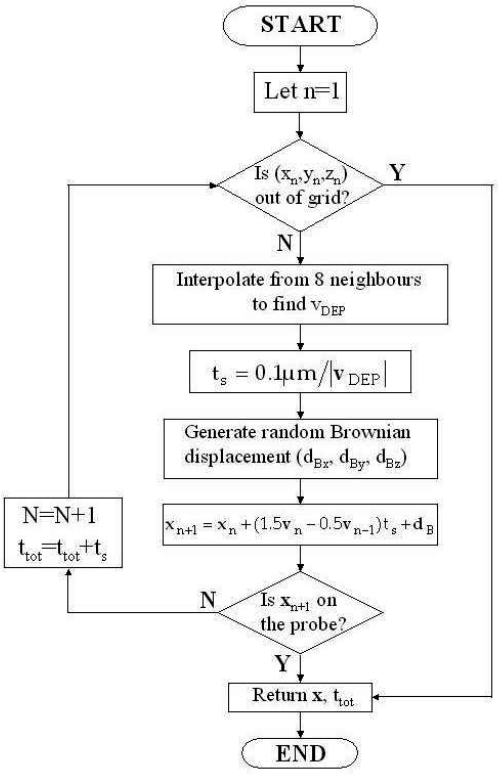

Figure 3.6: A schematic of the algorithm used in this investigation.

Also, for this simulation equation 2.40 has been used for the frequency dependent factor K_f, since the carbon nanotube radius is roughly 1000 times smaller than the length giving an eccentricity value of 0.999999778.

Finally, the results apply for a voltage of 10 V p-p applied between the electrodes.

3.2.2.1 Selection of parameters

Based on the assumptions made in section 3.1 and equations 2.36 and 3.2 we can plot factor $P \equiv \frac{\Gamma \cdot \varepsilon_m \cdot K_f}{f}$ as a function of frequency f for metallic and semiconducting single-walled nanotubes dispersed in IPA and SDS, the two dispersing media used in this theoretical investigation. Figure 3.7 shows the result for a nanotube of 2 nm in diameter and 3 μm in length. Curves s/IPA and s/SDS refer to s-SWCNTs with a permittivity of $2.5\varepsilon_0$ and a conductivity of 10^5 S/m in IPA and SDS respectively, while curves m/IPA and m/SDS refer to m-SWCNTs with a permittivity of $10000\varepsilon_0$ and a conductivity of 10^8 S/m in IPA and SDS respectively.

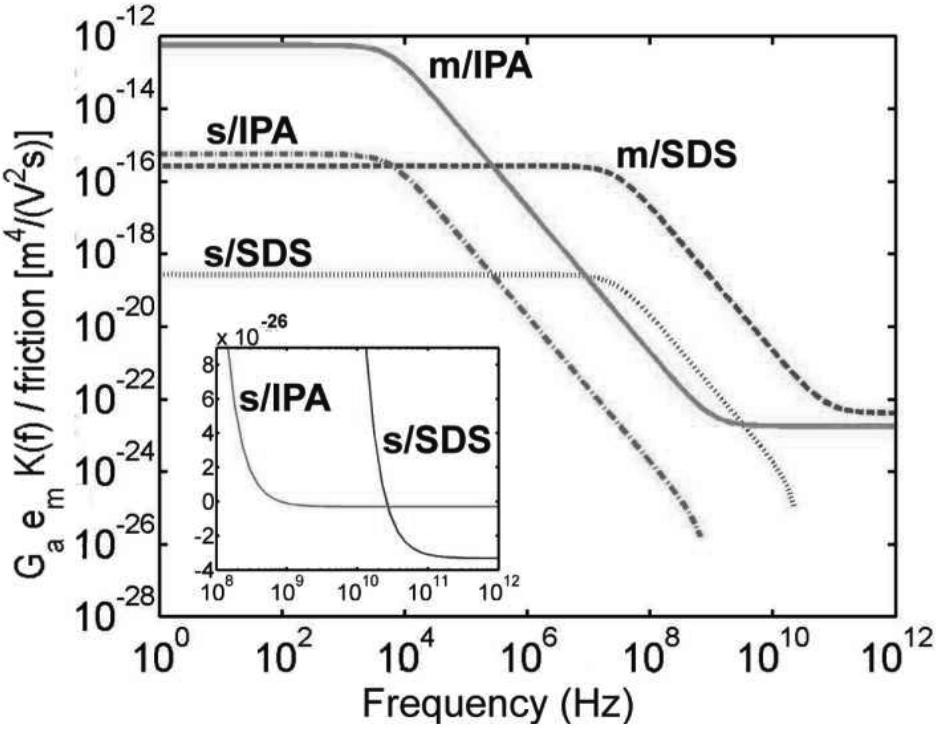

Figure 3.7: A plot of $\frac{\Gamma \cdot \varepsilon_m \cdot K_f}{f}$ as a function of frequency for a nanotube of 3 μm length and 2 nm diameter. The inset shows the value of $\frac{\Gamma \cdot \varepsilon_m \cdot K_f}{f}$ in the high frequency region for SWCNT experiencing negative DEP.

The main reason for the difference in the turnover frequency between IPA and SDS dispersed s-SWCNTs is the conductivity and permittivity of the nanotube with respect to the conductivity of the medium. IPA has a low conductivity compared to the metallic nanotubes resulting in a large positive DEP force, and thus velocity, particularly at low frequencies. The aqueous SDS solution has a much larger

conductivity than IPA leading to a smaller force at low frequencies. In the high frequency region the force is mostly determined by the difference in permittivity of the nanotube and the medium. Since the permittivity of SDS is much larger than of IPA, the force quickly becomes larger for the nanotubes dispersed in SDS. Semiconducting tubes (curves s/IPA and s/SDS) experience negative DEP at a relatively high ($\sim$ 200 MHz), but experimentally achievable frequency and metallic tubes (curves m/IPA and m/SDS) never experience negative DEP. M-SWCNTs also have much larger values of the DEP force and velocity at low frequencies. From the inset in Figure 3.7 one can notice that the value of P for the semiconducting nanotubes is of the order of 10^{-23} $\mathrm{m}^4/\mathrm{V}^2\mathrm{s}$. For a typical set of electrodes used in our calculations the maximum square field gradient is of the order of 10^{19} $\mathrm{V}^2/\mathrm{m}^3$ (see Figure 3.8). From this it follows from Figure 3.7 that the maximum negative DEP velocity would be just a few micrometers per second and only for nanotubes within 10 μm of the electrode gap. In a microfluidic channel with the liquid flowing with a velocity of the same order of magnitude, most nanotubes in the high frequencies would simply be carried away with the flow.

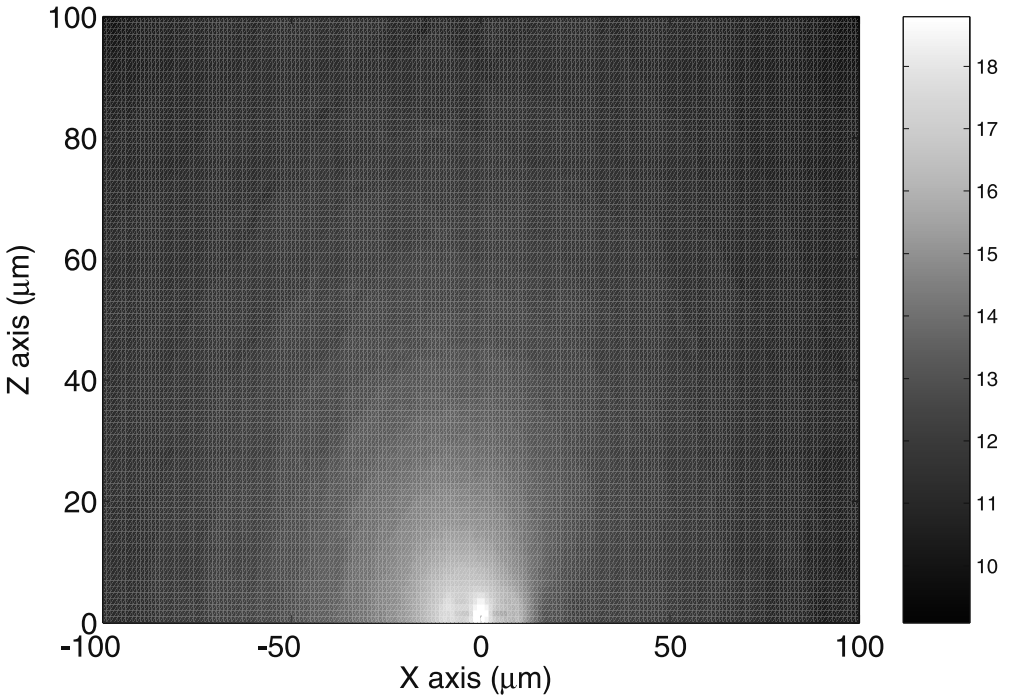

Figure 3.8: A plot of the logarithm of the field gradient at a plane passing from the middle of the electrodes in the y axis (corresponding to $y = 4$ μm).

It should be noted that the corresponding curves plotted for the shorter nanotubes with a length of 0.3 μm (not shown) give a change of less than an order of magnitude, indicating that although the DEP forces will be smaller for the shorter nanotubes, that change is not very significant.

The virtual assembly experiments were conducted by considering that the nanotubes entered the simulation space in 350 positions distributed randomly across the $x = -80$ μm, z>0 plane. At each position 100 nanotube trajectories

were initiated to account for trajectory variations due to the random thermal forces. The solution containing the nanotubes is considered to be flowing towards the positive x direction and the flow is taken to be uniform inside the 3D grid.

Based on Figure 3.7 we have chosed to do the simulations for the frequencies 10 kHz, 1 MHz, 10 MHz and 1 GHz. The fluid velocity was taken in the range $1-32$ μm/s, which for a 200 μm $\times$ 100 μm channel corresponds to $1.2-38$ nl/min, which is a low velocity but possible to achieve with modern microinjection pumps. In this range of velocities most m-SWCNTs will be only slightly affected by the fluid velocity at the experimentally achievable frequencies, while s-SWCNTs will mostly be carried away by the liquid since their velocities are primarily of the same order of magnitude or smaller.

3.2.2.2 Assembly calculations

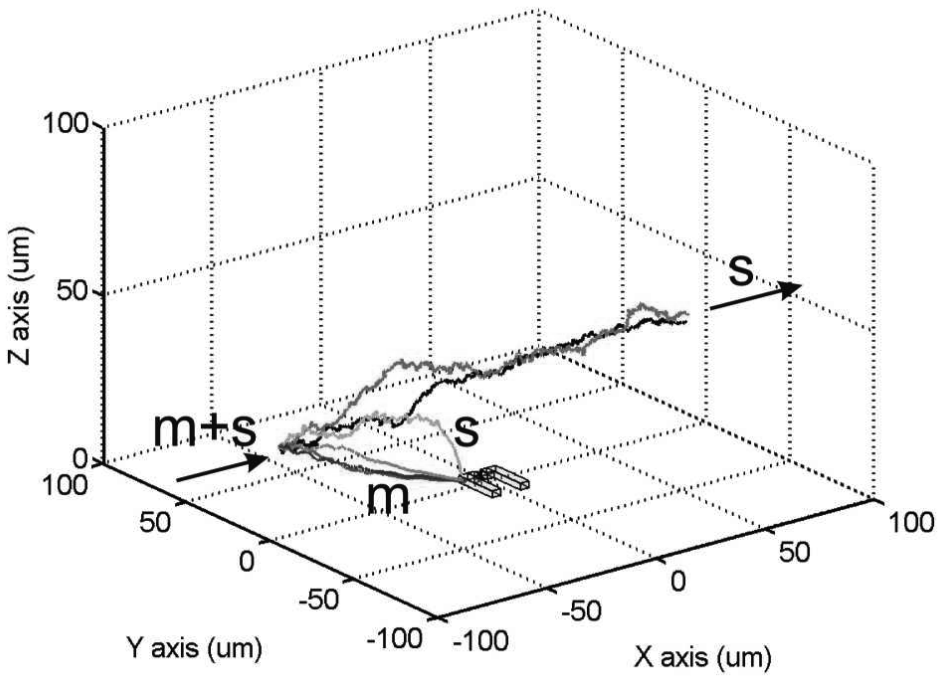

Figure 3.9: The trajectories followed by metallic and semiconducting nanotubes carried by a fluid flow with a velocity of 8 μm/sec along the x-axis. Although all trajectories are initiated from the same point in the YZ plane, (-80, 20, 20), thermal motion make the trajectories different.

Figure 3.9 shows an electrode pair with a voltage drop of 10 V p-p across the gap. The curves illustrate the trajectories followed by a single-walled nanotube with a diameter of 2 nm and a length of 3 μm when starting at a point 80 μm away from the center of the electrodes, while the solution is moving with a velocity of 8 μm/sec in the direction of the arrow. We see that all the m-SWCNTs and just a few s-SWCTNs reach the electrodes. Most of the s-SWCNTs are carried past the electrodes by the fluid flow. This is due to the DEP force being far smaller for

semiconducting nanotubes so that the fluid flow and in part also Brownian motion plays a greater role in their movement. The simulation is done for an isopropanol solution at a frequency of 1 MHz.

Figure 3.10 shows the fraction of SWCNTs caught by the electrodes (trapping efficiency) for the seven fluid velocities used in the calculations, of an ensemble starting on the $x = -80$ μm, z>0 plane for the different frequencies and solutions used in the calculations. The efficiency has been calculated only taking into consideration the trajectories where the algorithm did not fail. As seen in Figure 3.10, the efficiency decreases with the frequency of the applied electric field and with fluid velocity, unless, as for the m/SDS 1 MHz curve, the DEP force is stronger than the fluid drag force at all fluid velocities.

The graphs in Figure 3.11 show the probability of a nanotube trajectory terminating on the electrodes as a function of the starting (y,z)-position on the $x = -80$ μm, z>0 plane with respect to the electrodes, simulated for a range of possible experimental conditions. Unless otherwise indicated all graphs are plotted for the long nanotubes (3 μm). The columns compare metallic to semiconducting tubes, and IPA to SDS. The rows compare a reference fluid velocity and frequency (5 μm/sec, 1 MHz) to series with a higher fluid velocity (32 μm/sec, 1 MHz), larger frequency (5 μm/sec, 1 GHz) and finally short nanotubes at the same fluid velocity and frequency (5 μm/sec, 1 MHz).

The frequency is seen to be a dominating factor compared to fluid flow for the parameter space investigated here. The point where the fluid velocity becomes a dominant factor depends on the frequency used for the experiments and the liquid that the nanotubes are dispersed in. For example in IPA at 1 MHz the efficiency of the DEP drops by 30 % when the fluid velocity increases from 1 to 32 μm/sec, while for SDS the trapping efficiency is largely unaffected by fluid velocity. While the dimensions of the nanotubes play a role as well, these are however not easily controlled experimentally, except by choosing batches of SWCNTs with dimensions in a known range [95, 108]. Longer nanotubes are more likely to be trapped than shorter nanotubes, but as mentioned in section 3.2.1 this is mainly due to Brownian motion affecting shorter particles more.

From the simulations we calculate the time-of-arrival (TOA) from the starting plane at $x = -80$ μm to the electrodes. In figure 3.12 we show the TOA-plots for the same parameters as shown in figure 3.11. Here each graph contains data for both metallic and semiconducting nanotubes. The probe is positioned parallel to the xy-plane at (x,y,z)=(0.5, 4, 1) μm, illustrated with two vertical bars on the Y-axis of each graph in figure 3.12. The time of arrival increases with the distance from the incoming flow axis to the electrodes. With a higher downstream fluid flow velocity, it obviously takes shorter time for the nanotubes to reach the electrodes. For high flow velocities, however, the nanotubes have to be on a flow axis closer to the electrodes to become trapped. There is almost no difference in the TOA depending on tube size, although the tendency is that it takes slightly longer time for the longer tubes to reach the probe. At 1 MHz the time is reduced by up to 80 % for IPA and up to 43 % for SDS dispersed metallic nanotubes when the fluid velocity increases from 5 μm/sec to 32 μm/sec.

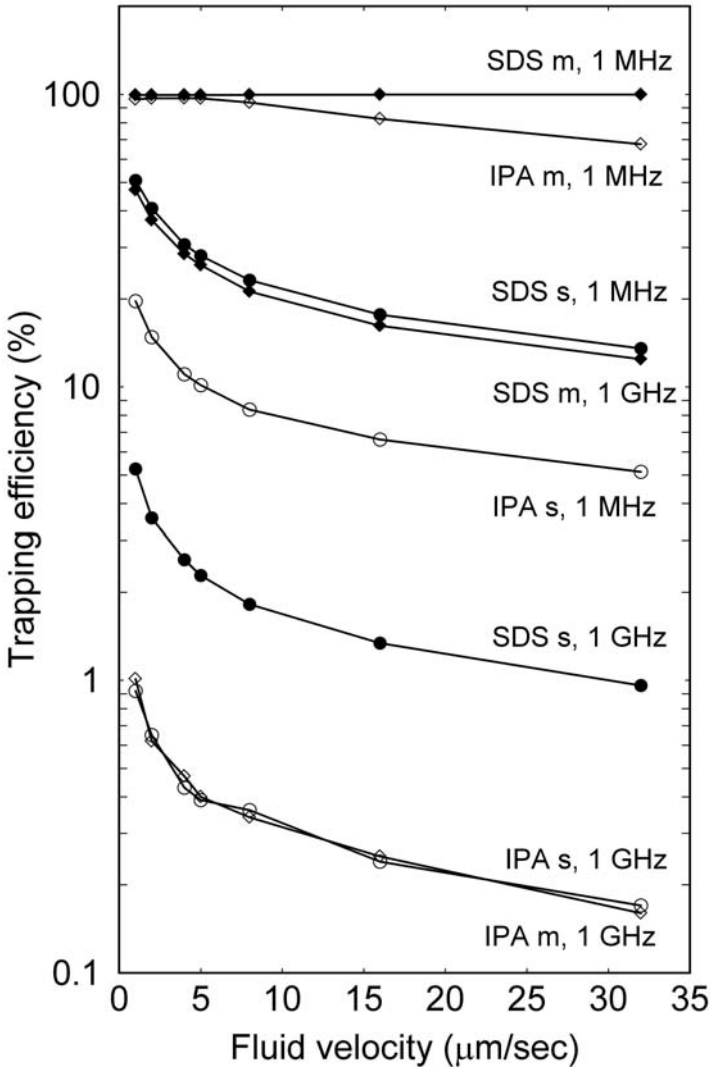

Figure 3.10: Trapping efficiency at 7 different fluid velocities for two frequencies and for two different dispersing mediums. The letter m and the markers ◊ and ♦ denote m-SWCNT in IPA and SDS respectively while s and the markers ○ and • denote s-SWCNT in IPA and SDS respectively. The efficiency generally drops with increasing velocity with the exception of the line referring to m-SWCNT in SDS at 1 MHz. The results plotted here refer only to the long (2 nm diameter, 3 μm length) nanotubes. The short nanotubes exhibit similar behaviour but the trapping efficiency is mostly lower than that of the long nanotubes.

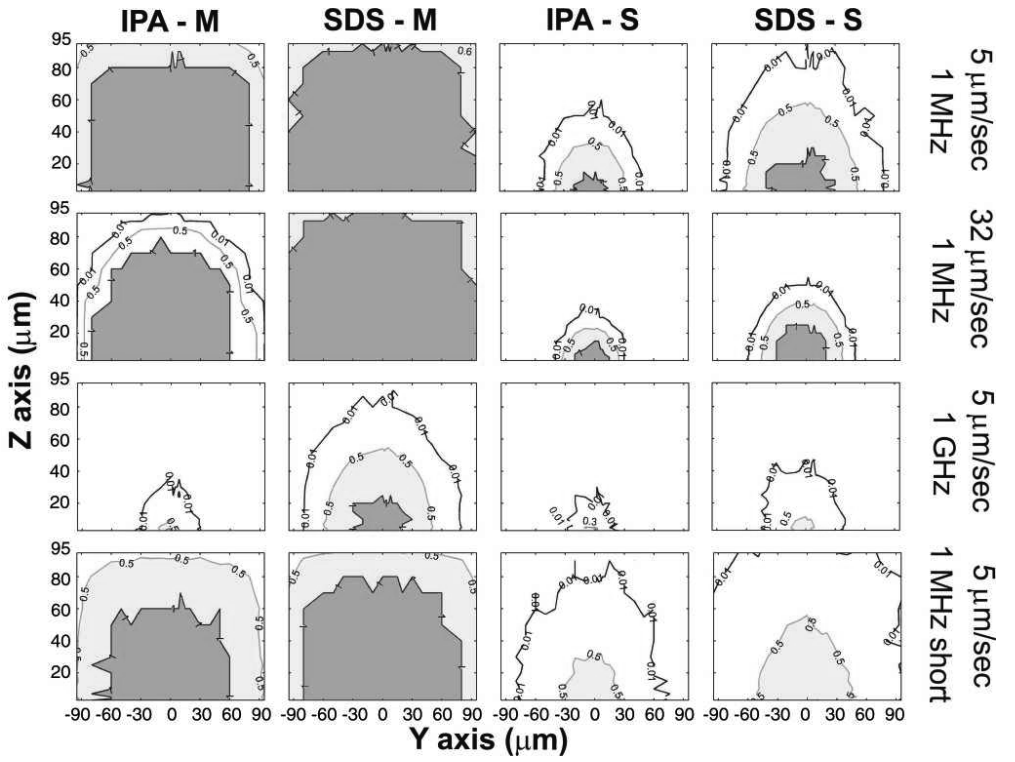

Figure 3.11: Equi-probability curves for a SWNT trajectory terminating on the electrodes as a function of the starting point of the trajectory in the $x = -80$ μm plane. The text indications refer to all graphs in a certain column and row. The three upper rows are calculated for long nanotubes (3 μm in length) while the bottom row refers to the short nanotubes (0.3 μm in length).

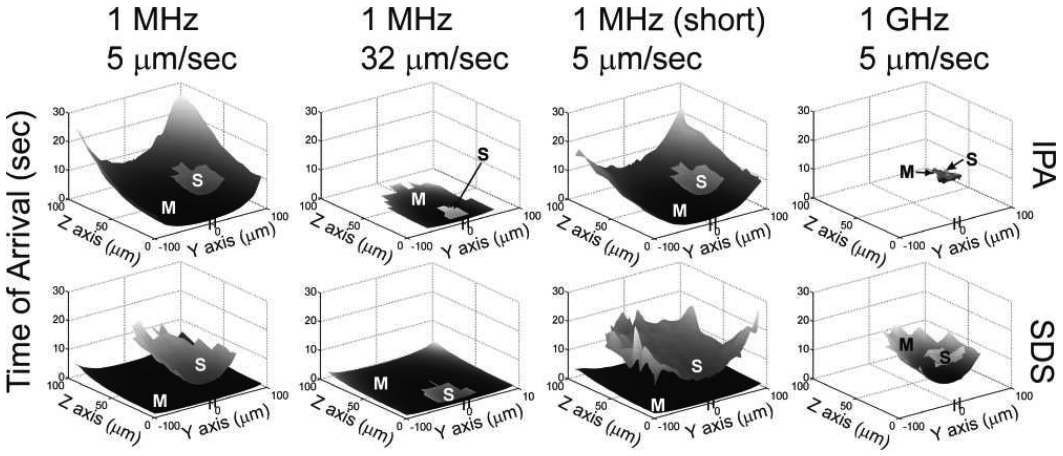

Figure 3.12: The time it takes for a tube to reach the probe as a function of starting position in the zy plane. The text indications refer to all graphs in a certain column and row. The two black lines at 0,0,0 illustrate the position and orientation of the electrodes. The bottom surfaces (M) are for metallic nanotubes while the top surfaces (S) are for semiconducting nanotubes. It should be noted that the lines are placed there only as guide to the eye.

3.2.2.3 Sorting calculations

We can now use the calculations presented in section 3.2.2.2 to consider qualitatively an experiment involving a dispersion of nanotubes being cycled n times past a set of microelectrodes in a microfluidic channel of similar dimensions (200×100 μm^2). By each pass the distribution of semiconducting and metallic nanotubes should change. Letting p_s and p_m denote the fraction of carbon nanotubes trapped on the electrodes, for semiconducting and metallic types respectively, the number of semiconducting nanotubes $N_{S,n}$ remaining in the solution after n passes may be written as $N_{S,n} = (1-p_s)^n \cdot N_{S,0}$, while the number of s-SWCNT on the electrodes is simply $N^*_{S,n} = N_{S,0} - N_{S,n}$. $N_{M,n}$ and $N^*_{M,n}$ are defined correspondingly for metallic nanotubes.

We assume that the starting solution contains 33 % metallic nanotubes and 67 % semiconducting nanotubes, i.e. that there is equal distribution of coordination numbers (n,m) [109].

The efficiency of the sorting E_n and the yield Y_n of s-SWCNT in the remaining solution after n cycles compared to the original quantity may be defined as:

$$E_n = \frac{N_{S,n}}{N_{S,n} + N_{M,n}} \tag{3.10}$$

$$Y_n = \frac{N_{S,n}}{N_{S,0}} \tag{3.11}$$

Figure 3.13 shows the efficiency of the sorting and the yield of s-SWCNT as a function of the number of times that the solution is cycled through the channel for the same cases used in figures 3.11 and 3.12.

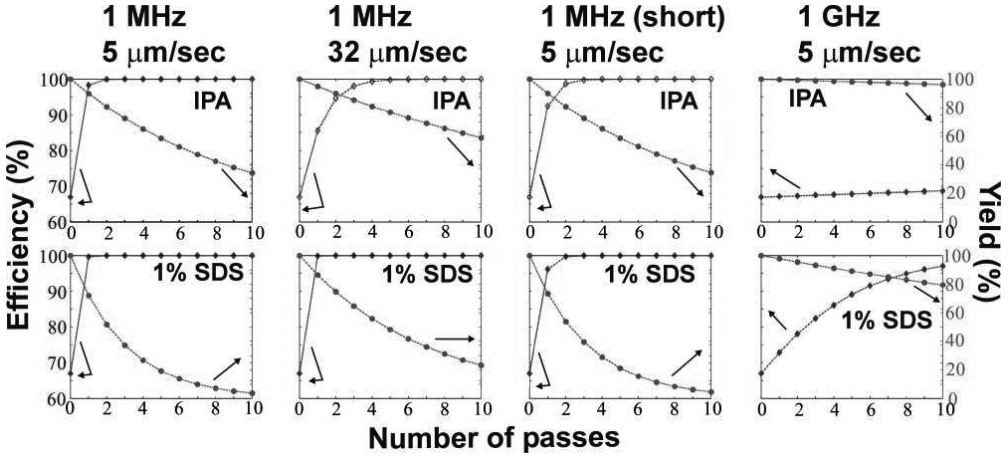

Figure 3.13: The efficiency (left y-axis) and yield (right y-axis) as a function of the number of passes through the channel.

Figure 3.13 gives some interesting results. In Figure 3.7 it is seen that s-SWCNTs dispersed in IPA experience negative DEP at 1 GHz, however Figure 3.13 shows

that a small fraction of the s-SWCNTs in each pass are trapped even at this high frequency. This can be attributed to the fluid flow carrying the semiconducting nanotubes towards the electrodes and to the random thermal motion.

At a frequency of 1 GHz and a flow of 5 μm/sec, corresponding to about 6 nl/min, the efficiency of the sorting changes very little even after 10 passes. At 1 GHz the semiconducting nanotubes are repelled from the electrodes, but on the other hand, the removal of metallic nanotubes is also very inefficient at this frequency.

Despite the fact that both metallic and semiconducting nanotubes experience positive DEP at 1 MHz both in IPA and SDS, the sorting at this frequency is much more efficient in terms of predominantly removing metallic nanotubes from the solution. Indeed, at 1 MHz and after cycling the dispersion only a few times past the electrodes, the resulting solution should have very few or no metallic nanotubes, while the yield is still acceptable, above 20 %. The considerable amount of semiconducting nanotubes that will be trapped on the electrodes is less of a problem, as the primary goal is to obtain a solution free of m-SWCNTs. After obtaining such a solution DEP at low frequencies could be used to assemble single s-SWCNTs or networks onto sensor arrays with a yield close to 100 %, using a more narrow liquid channel to compensate for the smaller range (see Figure 3.11). Furthermore, if a small amount (such as 1 ppm) of metallic nanotubes in the final solution can be tolerated, the yield of semiconducting nanotubes increases by 150-300 % at the expense of a slightly increased probability of device failure.

From Figure 3.13 we also see that SDS increases the efficiency significantly but gives lower yields.

3.2.3 Simulation 2

In this simulation we consider the permittivity of metallic single-walled carbon nanotubes to be $2.5\varepsilon_0$, close to that of graphite. Also, equation 2.37 has been used for the frequency dependent factor K_f, since the previous simulation gives unrealistically high values for it.

The motion algorithm is the same for this simulation as for simulation 1, with two exceptions: 1) The thermal motion calculation has been changed so that the time-step is made equal to 0.01 seconds for all cases where the calculation yields values larger than this. This value was chosen from Figure 3.4, where it can be seen that the brownian step will thus be smaller than 1 μm, the grid spacing in our field simulation. This will have an effect in the movement of the nanotube far away from the electrodes.

Finally, these simulations are assuming a voltage of 5.78 V p-p applied between the electrodes and are conducted on the long nanotubes.

3.2.3.1 Selection of parameters

If we plot factor $P \equiv \frac{\Gamma \cdot \varepsilon_m \cdot K_f}{f}$ (s. Figure 3.14) we note immediately that the values obtained are much smaller than the ones plotted in Figure 3.7. As was

already mentioned in section 2.3, the small value of A_L (of the order of 10^{-6}) compensates for the large difference between the conductivity of the nanotube and that of the medium and therefore the depolarising factor cannot be ignored. The factor P is now 3-4 orders of magnitude smaller and quite similar for metallic and semiconducting nanotubes for the given assumptions, at least for frequencies up to 100 MHz.

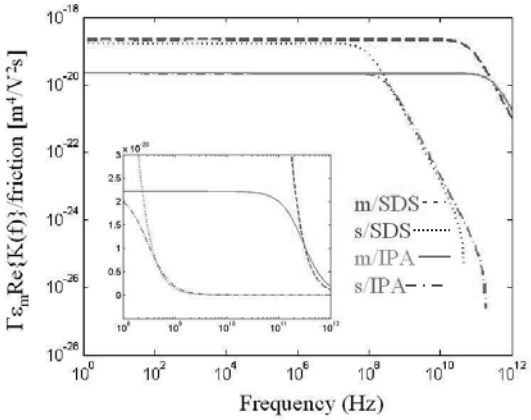

Figure 3.14: A plot of $\frac{\Gamma \cdot \varepsilon_m \cdot K_f}{f}$ as a function of frequency for a nanotube of 3 μm length and 2 nm diameter when the depolarising factor is taken into account. The inset shows the value of $\frac{\Gamma \cdot \varepsilon_m \cdot K_f}{f}$ in the high frequency region.

Based on Figure 3.14 only one simulation is needed for the metallic nanotubes, which would be valid for all frequencies of interest. For the semiconducting nanotubes the frequency region between 1 MHz and 1 GHz is interesting. Simulations were carried out at 1 MHz, 100 MHz and 300 MHz, which is what we can hope to achieve experimentally, and for fluid velocities from $1 - 50$ μm/s.

3.2.3.2 Assembly calculations

Figure 3.15 shows a few trajectories calculated in this second simulation at a frequency of 10 MHz and a velocity of 5 μm/s for metallic nanotubes dispersed in SDS. The random thermal motion is now very prominent, as is the influence of the fluid motion. Only very few nanotubes end up on the electrodes.

Figure 3.16 shows the fraction of the SWCNTs caught by the electrodes for the different frequencies, solutions and fluid velocities simulated. The trapping efficiency decreases with velocity in all cases, closely following a double exponential decay. Comparing this result to that of Figure 3.10 it can be seen that the trapping efficiencies are now much lower. The fact that the voltage is lower in this simulation than it was in the first could play a small role: The force on the nanotubes when the voltage is 10 V p-p would be about 3 times bigger, a difference that would give a small increase in the trapping efficiency. Figure 3.16 also shows that nanotubes dispersed in IPA are essentially unaffected by the change in frequency up to 100 MHz, while nanotubes dispersed in SDS show clear differences in the trapping efficiencies between metallic and semiconducting nanotubes for all frequencies.

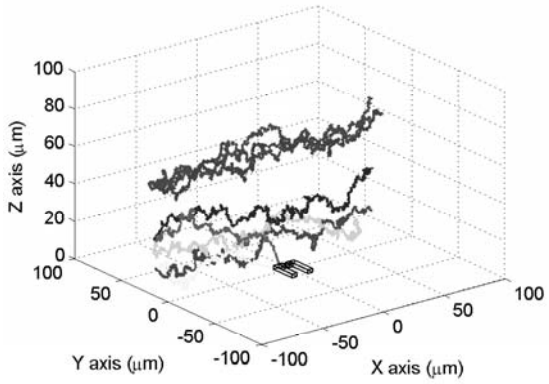

Figure 3.15: Several calculated nanotube trajectories starting on points along the $x = -80$ μm, $y = 40$ μm line. The fluid velocity and the thermal motion is seen to play an important role in the nanotube movement. The simulation is done for metallic nanotubes dispersed in SDS at a frequency of 10 MHz and a fluid velocity of 5 μm/sec.

Figure 3.17 shows the probability of a nanotube trajectory terminating on the electrodes as a function of the starting (y,z)-position on the $x = -80$ μm, $z > 0$ plane with respect to the electrodes for some selected velocities. The columns compare metallic to semiconducting tubes, and IPA to SDS. The rows compare a reference (5 μm/sec, 1 MHz) to series with a higher fluid velocity (50 μm/sec, 1 MHz) and larger frequency (5 μm/sec, 100 MHz).

As was the case in simulation 1, the range of DEP is reduced as the fluid velocity increases, however, in this simulation there is always a region where all nanotubes end up on the electrodes, regardless of the velocity. The area of that region seems to be increasing with the velocity. It is quite likely that this is due to the nanotubes simply colliding with the electrodes as they are carried away by the fluid flow. Figure 3.16 also shows that the differences between metallic and semiconducting nanotubes are very small.

Finally, Figure 3.18 plots the spatial distribution of the time of arrival to the electrodes as a function of the starting position on the $x = -80$ μm plane. Comparing to Figure 3.12 it is clear that the time has increased in this simulation. When the velocity is 50 μm/sec the time to reach the probe (TOA) drops to about $1 - 2$ seconds, almost exactly 10 times smaller than the TOA at a velocity of 5 μm/sec. This time also corresponds to the time it takes for the fluid to reach the probe with this velocity, strengthening our assumption that at this high velocity the nanotubes reach the probe not as much by DEP but as a consequence of the fluid motion.

3.2.3.3 Sorting calculations

We can now repeat the virtual experiment presented in section 3.2.2.3 for the results of simulation 2. The result is presented in Figure 3.19.

It is clear that the sorting is not working as efficient as in simulation 1, at least

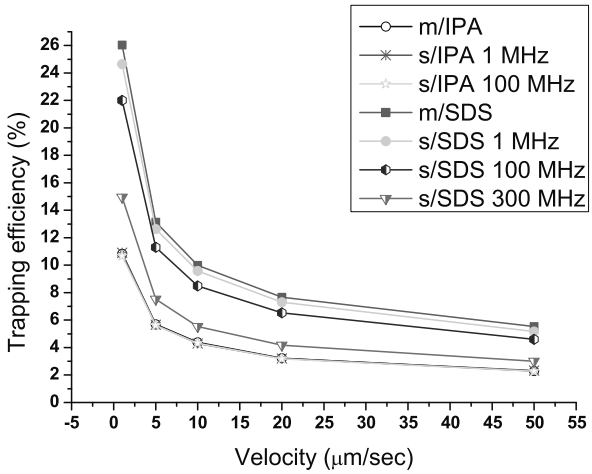

Figure 3.16: The trapping efficiency for a variety of parameters. Compared to Figure 3.10 these values are much lower and the difference between metallic and semiconducting tubes smaller.

not for the investigated frequencies. In order to achieve a solution completely clear of nanotubes we would need to cycle it through the electrodes over 200 times. And in that case the yield would be very small, less than 10^{-10}, which in practice means that no semiconducting nanotube would be left behind. If we could perform the experiment at a frequency of 300 MHz then it would be possible to completely clear the solution of metallic nanotubes while still having 0.5% of the semiconducting nanotubes left.

3.3 Static fluid

For these simulations the solution was not moving in a channel, as we were trying to model an experimental procedure often used in our experiments, where a droplet of the solution is placed on top of the electrodes. The electrode modelled was a realistic electrode such as the one shown in Figure 4.9(b). Due to symmetry only one half of one electrode needed to be modelled while the boundary conditions were mirroring the force in order to create a realistic field. The field was calculated using FlexPDE and the results were exported into Matlab for the simulation. A voltage of 14.5 V p-p was applied on the electrodes. 140 nanotubes were placed uniformly in a $50\times17.5\times200$ μm^3 box where the field was calculated. Their position was further randomly altered using a normally distributed random number generator within a box equal to the length of the nanotubes. Nanotubes of 1 nm radius and 1 μm length were considered.

Three values of the frequency dependent factor were examined and the results in Figure 3.20 show the collected percentage of nanotubes on the electrode as a function of time. The calculated values all fit to double exponential functions, while the fit to a simple exponential is not good.

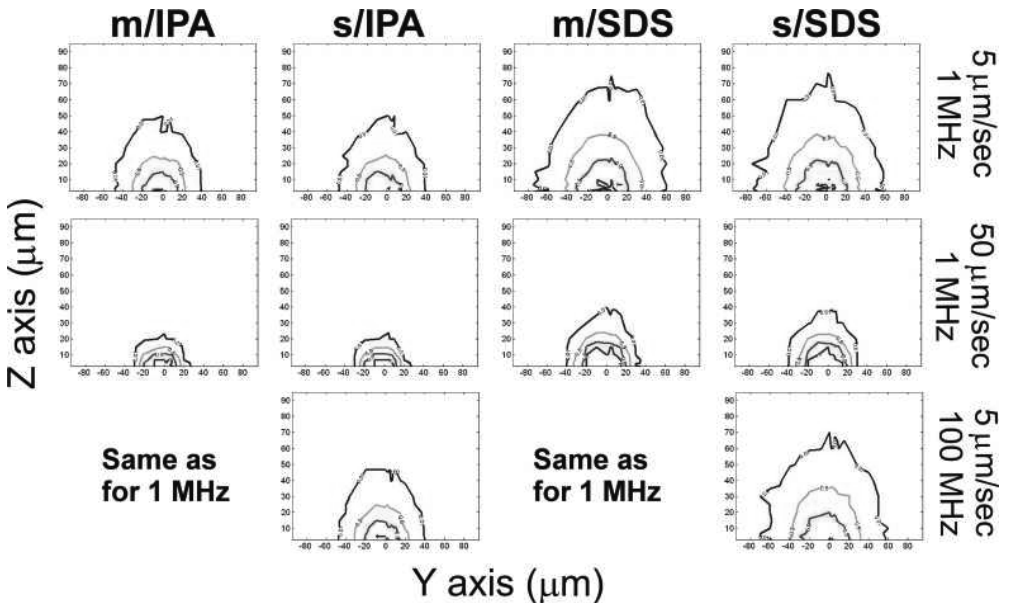

Figure 3.17: The spatial distribution of the probability of a nanotube terminating on the electrodes as a function of the starting position for selected simulated parameters.

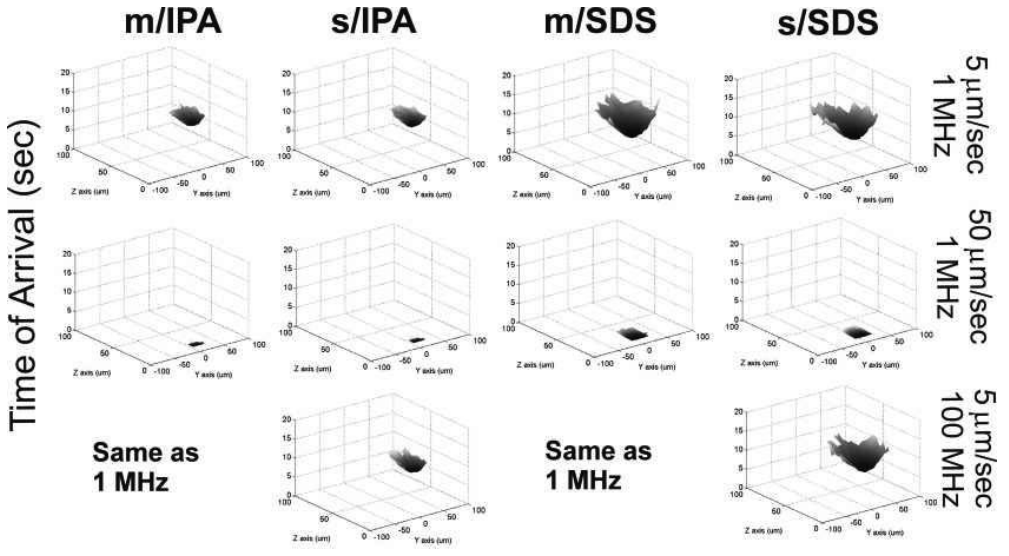

Figure 3.18: The spatial distribution and magnitude of the time-of-arrival (TOA) of the nanotubes on the probe for a selected range of parameters. This figure should be compared to Figure 3.12.

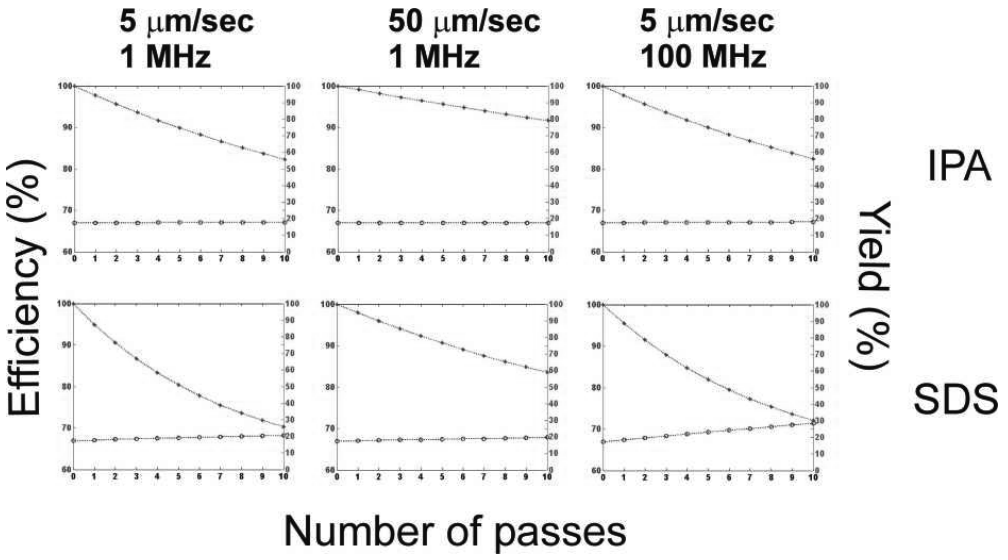

Figure 3.19: The efficiency and yield for the sorting experiment according to the results of simulation 2. The efficiency is very low for most cases.

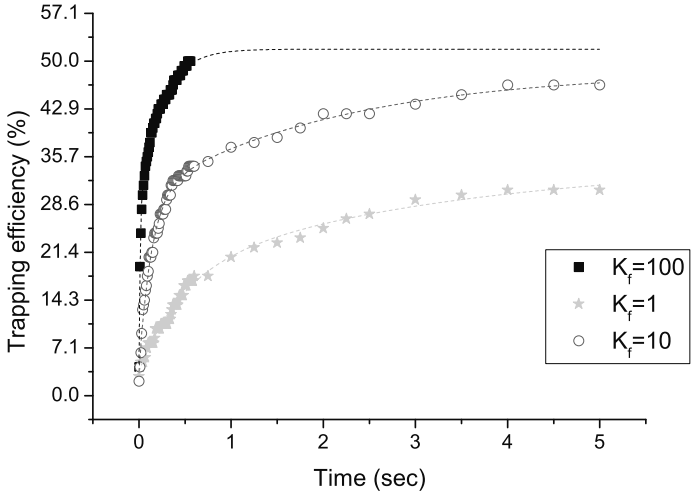

Figure 3.20: The percentage of the nanotubes caught as a function of time for three different values of the frequency dependent factor K_f. The symbols show the calculated cases while the line plots a fit to the calculated data.

Figure 3.21 shows the initial distribution of the nanotubes in the simulation space as well as their distribution after 3.62 seconds of field application time for the K_f=10 case. It can be seen that dielectrophoresis cleans the immediate space above the electrodes of nanotubes.

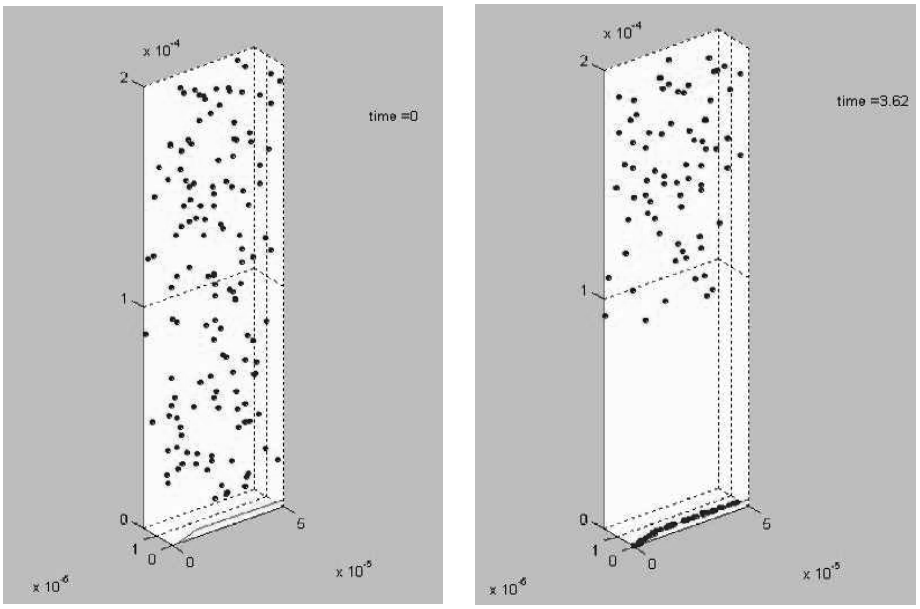

(a) Time = 0 sec (b) Time = 3.62 sec

Figure 3.21: The initial distribution of the nanotubes and their distribution after 3.62 seconds from the voltage application. The dielectrophoretic process clears out the space immediately above the electrodes.

The geometry and selected slice plots of the electric field for this simulation are shown in appendix B.

3.4 Other forces

In the previous discussion we have only considered the DEP force, the viscous drag force and the thermal random force acting on the nanotube. We have not considered any forces acting on the fluid itself. Though these are not directly applied on the nanotube, they will inevitably affect the trajectories and are therefore important to consider.

In a microelectrode system used for the manipulation of small particles or nanotubes the electrical fields generated are quite large and the power dissipation in the fluid is also bound to be rather large, too. The power generation per unit volume is given by

$$W = \sigma_m \mathbf{E}^2 \ (W/m^3) \tag{3.12}$$

where σ_m is the conductivity of the medium. For the system we have presented

in the previous sections (simulations 1 and 2) the maximum value of the field is approximately $5.5 \cdot 10^6$ V/m which means that the power dissipation for the two liquids examined are $W_{IPA} = 1.8 \cdot 10^8$ W/m^3 and $W_{SDS} = 3.8 \cdot 10^{12}$ W/m^3. The volume in which this heat is generated is really small. In our simulation space this would be $V = (200\ \mu\text{m})^3 = 8 \cdot 10^{-12}$ m^3 giving an average power dissipation of $W^V_{IPA} = 1.4$ mW and $W^V_{SDS} = 30$ W.

Especially in the case of the SDS solution the temperature rise could be noticeable when a large power is dissipated in such a small volume. Ramos et al. in [110] have done an order of magnitude estimate of the temperature increase in a fluid and have found it to be given by

$$\Delta T = \frac{\sigma_m V^2_{rms}}{k} \tag{3.13}$$

where k is the thermal conductivity of the medium. For $k_{IPA} = 0.14$ W/mK and $k_{SDS} = k_{water} = 0.6$ W/mK we get that $\Delta T_{IPA} \simeq 0.001^o$C and $\Delta T_{SDS} \simeq 5.4\,^o$C. It should be noted that these values depend greatly on the system geometry and should therefore be treated as an order of magnitude estimate.

Since the electric field is highly non-uniform the power density and thus the temperature rise is also non-uniform. Variation in the temperature of the liquid causes local gradients in the density, viscosity, permittivity and conductivity of the medium and these give rise to forces on the fluid. Three main categories of external forces exist: (a) The electrothermal forces, caused by gradients in the permittivity and conductivity, (b) The buoyancy force, caused by density gradients, giving rise to natural convection and (c)The electro-osmotic forces, where the electric field acts on the free charge in the electrical double layer.

Given the very small mass of these structures and the fact that we are assuming that the nanotubes in our solution are individual (i.e. there are no bundles present) gravity does not play any role.

3.4.1 Electrothermal forces

The conductivity gradient gives rise to free volume charge and hence the Coulomb forces while the permittivity gradient leads to the dielectric force. The general expression for the electrical force per unit volume is [110]

$$\mathbf{F_e} = \rho_q \mathbf{E} - \frac{1}{2}\mathbf{E}^2 \nabla \varepsilon + \frac{1}{2}\nabla(\rho_m \frac{\partial \varepsilon}{\partial \rho_m}\mathbf{E}^2) \tag{3.14}$$

where ρ_q is the volume charge density, ε is the permittivity of the medium and ρ_m is the mass density of the medium. The last term of equation 3.14 can be ignored for an incompressible fluid such as the one we have in our microfluidic channel. For small temperature rises the gradients in permittivity and conductivity can be written as:

$$\nabla\varepsilon = \frac{\partial\varepsilon}{\partial T}\nabla T \tag{3.15}$$

$$\nabla\sigma = \frac{\partial\sigma}{\partial T}\nabla T \tag{3.16}$$

$$\tag{3.17}$$

Again Ramos et al. [110] showed that for a typical microfluidic system containing parallel metal plate electrodes generating the field (s. Figure 3.22) the time averaged electrical force is given by

$$\langle \mathbf{F_e} \rangle = -M(\omega, T)\left(\frac{\varepsilon\sigma V_{rms}^4}{2k\pi^3 r^3 T}\right)\left(1 - \frac{2\theta}{\pi}\right)\hat{\mathbf{n}}_\theta \quad (N/m^3) \tag{3.18}$$

where

$$M(\omega, T) = \left[\frac{\frac{T}{\sigma}\frac{\partial\sigma}{\partial T} - \frac{T}{\varepsilon}\frac{\partial\varepsilon}{\partial T}}{1 + (\omega\tau)^2} + \frac{1}{2}\frac{T}{\varepsilon}\frac{\partial\varepsilon}{\partial T}\right] \tag{3.19}$$

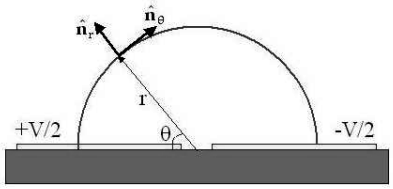

Figure 3.22: A parallel plate electrode geometry used for deriving the analytical expression for the electrical force by Ramos et al. [110]. The plates are placed in a dielectric and a potential of V is applied across the gap.

$M(\omega, T)$ is a dimensionless factor giving the variation of the force as a function of frequency. τ is given by $\tau = \varepsilon/\sigma$ and is the charge relaxation time of the liquid. From equation 3.19 it can be seen that for certain frequencies either the Coulomb force or the dielectric force dominate. The transition occurs at the frequency f_c given by

$$f_c \approx \frac{1}{2\pi\tau}\left(2\frac{\frac{\partial\sigma}{\sigma\partial T}}{\frac{\partial\varepsilon}{\varepsilon\partial T}}\right)^{1/2} \tag{3.20}$$

For IPA it can be found in tables that $\frac{\partial\sigma}{\sigma\partial T} = 2\%/\mathrm{K}$ and we can calculate that $\frac{\partial\varepsilon}{\varepsilon\partial T} = 1.75\%/\mathrm{K}$ (from values of the permittivity at two different temperatures)

while for the 1% aqueous SDS solution we can use the values for water, so $\frac{\partial \sigma}{\sigma \partial T} = 2\%/\mathrm{K}$ and $\frac{\partial \varepsilon}{\varepsilon \partial T} = -0.4\%/\mathrm{K}$.

From equation 3.18 it can be seen that the maximum electrical force on the liquid will be at $\theta = 0$. From Ramos et al. [110] the velocity of the fluid due to the electrical force is given by

$$v_{fluid} \approx |\mathbf{F_e}| \frac{l^2}{\eta} \tag{3.21}$$

where l is the characteristic length of the system and η is the viscosity of the fluid. This equation has been derived as an order of magnitude approximation from the Navier-Stokes equation and is also valid for other volumetric forces.

We can now compare the two velocities, namely the maximum velocity of the fluid and the velocity of the nanotube due to DEP and viscous forces. The latter can be estimated using the numerical results from FEMLAB and equations 2.36 and 3.2. The electrical force can be calculated by combining equations 3.18, 3.19 and 3.21.

Figure 3.23 shows the two calculated velocities as a function of radial distance from the center of the electrodes for a semiconducting nanotube 3 μm in length and 2 nm in diameter at a frequency of 1 MHz. The semiconducting nanotube was selected as it will experience the smallest DEP force according to Figure 3.7 and thus will give an impression of a worst case scenario. The results of simulation 2 have been used for the DEP force.

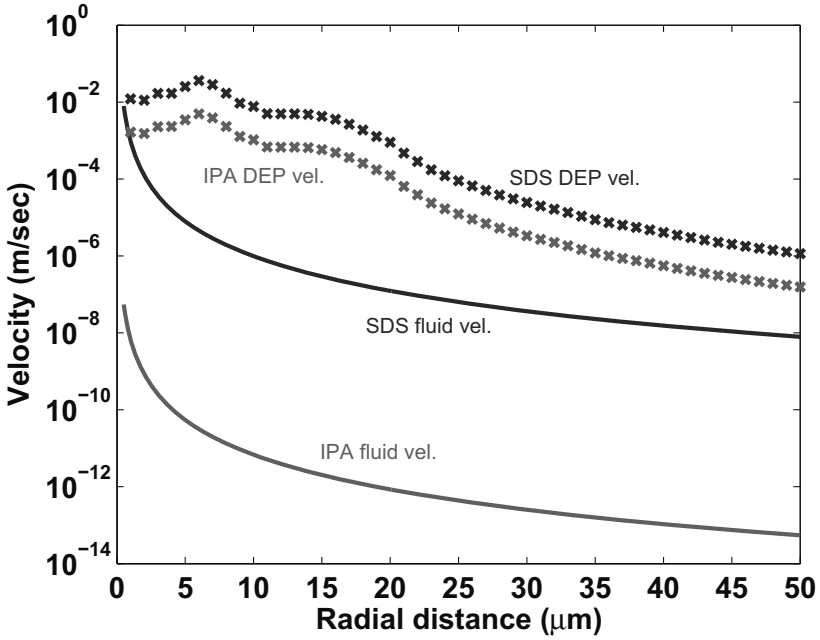

Figure 3.23: The velocity due to DEP and viscous forces on a semiconducting nanotube at 1 MHz compared to the velocity of the fluid due to electrical forces.

Figure 3.23 shows that in general the fluid velocity will not constitute a problem for

the nanotube movement except maybe in the case of the SDS solution and that at distances very close to the electrodes. One should take into account that the fluid flow plotted here is the maximum flow for $\theta = 0$ and that it has direction towards the electrodes because factor $M(\omega, T)$ is positive at this frequency. Consequently these forces can be ignored in this model.

3.4.2 Natural convection

The existence of temperature gradients in the fluid gives rise to changes in fluid density which in turn lead to natural convection. During non-uniform heating the lighter (hotter) parts of the fluid rise while the denser (cooler) parts fall. The buoyancy body force that causes this movement is given by

$$\mathbf{F_g} = \Delta\rho_m \mathbf{g} = \frac{\partial \rho_m}{\partial T} \Delta T \mathbf{g} \quad (N/m^3) \tag{3.22}$$

where T is the temperature, ρ_m is the mass density and $\mathbf{g}$ is the acceleration due to gravity.

Ramos et al [110] have calculated the maximum temperature rise to be $\frac{\sigma V_{rms}^2}{8k}$ at $\theta = 90^o$. Assuming that $(1/\rho_m)(\partial\rho_m/\partial T) = -0.0011$ per degree for isopropanol and $(1/\rho_m)(\partial\rho_m/\partial T) = -0.0001$ per degree for water we get that the maximum velocity due to the buoyancy force is 0.5 pm/s upwards for IPA and 0.8 nm/s downwards for SDS. Comparing with figure 3.23 we can see that these velocities are insignificant compared to the DEP velocities and can therefore be ignored.

3.4.3 Electroosmosis

Electroosmosis is another effect that could disturb the movement of the nanotube. It arises as a result of forces acting on the electrical double layer that forms in the electrode/electrolyte interface. For the planar electrode geometry shown in figure 3.22 the fluid flow at the surface of the electrodes will be given by [111]

$$\mathbf{U} = -\frac{\varepsilon}{4\eta} \Lambda \nabla_{\mathbf{s}} (|\Delta V|^2) \tag{3.23}$$

where $\Lambda = \frac{1}{1+\frac{h}{\varepsilon_c}}$ is a term describing the contribution of the Stern layer (height h and permittivity ε_c) and $\Delta V = \frac{V_0}{2(1+i\Omega)}$ is the potential drop across the double layer,($\Omega = (1/2)\pi\kappa(\varepsilon/\sigma)\omega$, where κ is the inverse thickness of the Debye layer and ω is the angular frequency).

A simpler formula has been used in the following calculations, ignoring the Stern layer. Moreover, the thickness of the Debye layer has been calculated by finding the diffusion coefficients of OH^{-1} (for IPA) and Na^{+} (for SDS), and using the equation $\kappa = \sqrt{\frac{D \cdot \varepsilon}{\sigma}}$.

Figure 3.24 shows the velocity in the x-direction as a function of frequency and distance from the center of the electrodes. It is seen that for IPA the maximum fluid velocity is of the order of 50 mm/s mm/sec at the electrode edge while for SDS the maximum fluid flow is larger, of the order of 50 cm/s at the electrode edge. Both velocities decrease rapidly with increasing distance from the electrode edge. Moreover, the electroosmotic effect is present only at particular frequencies. For IPA these are from 100 Hz up to 10 kHz while for SDS they are higher, from 1 kHz to 1 MHz. Effectively that means that our calculations involving nanotubes in IPA solutions are not seriously affected by this effect. However, the calculations involving SDS could be affected for the 1 MHz frequency. A closer look at figures 3.23 and 3.24(b) shows that the electroosmotic velocity at a frequency of 1 MHz is about 5-12 mm/s, a value of the same order of magnitude than the DEP velocity for a semiconducting nanotube. Therefore, ac electroosmosis could be playing a large role near the electrodes for nanotubes dispersed in SDS.

It should be noted that the calculations for the electroosmotic velocity are based on various assumptions and tend to overestimate the velocity. Equation 3.23 gives the velocity at a distance of κ^{-1} over the electrode surface. According to Scott et al. [112] the flow is observed much further away from the surface, at about 1 μm. Their results predict that the electroosmotic velocity would be reduced for fluids of higher conductivity and is in agreement with other experimental data [101]. Generally experiments done using latex spheres indicate that the electroosmotic velocity for a small applied voltage (1.25 Volts) over electrodes of 25 μm spacing is of the order of 0.5 mm/sec when measured close to the electrode edge for a medium of conductivity of the order of mS/m. For our calculation we use a higher voltage, which means that the electroosmotic velocity will be higher. It is observed that the velocity scales with the square of the voltage [113], which would mean that for a solution of the same conductivity we would expect a maximum elecroosmotic velocity of about 2 mm/sec.

3.4.4 Other considerations

In a real solution carbon nanotubes are rarely perfectly separated. They tend to cluster together in bundles of up to hundreds of nanotubes. In such a system the gravitational force will inevitably start playing a role in the dielectrophoretic process.

Bundles of nanotubes can contain both metallic and semiconducting nanotubes. Since the force on m-SWCNTs is much larger than that on s-SWCNTs bundles containing even just one metallic nanotube will behave as a m-SWCNT with a larger diameter with respect to drag forces. Moreover, there exist no solution containing carbon nanotubes with particular diameters and lengths. Even though batches of nanotubes with certain length and diameter distributions can be achieved, post-processing of the samples done for dispersing them in a solvent, will inevitably change the length distribution, either because ultrasonication tends to cut the nanotubes into pieces or simply because the nanotubes will form ropes of different lengths when in solution.

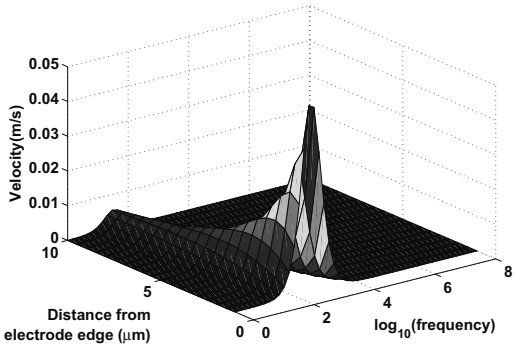

(a) Electroosmotic flow in IPA

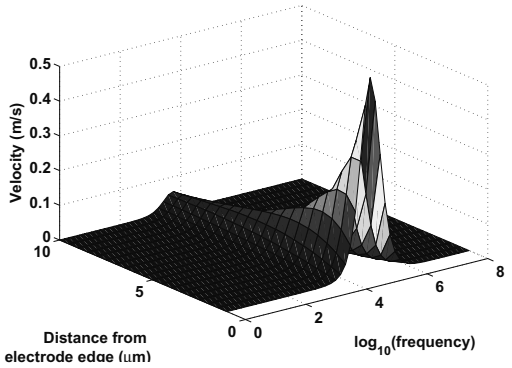

(b) Electroosmotic flow in SDS

Figure 3.24: The electroosmotic velocity as a function of the frequency of the applied field and the distance from the electrode edge.

Because of these two reasons a real sorting experiment will almost certainly differ from the results presented in section 3.2.2.3 and 3.2.3.3. However, if the distribution of length and diameter for a solution of nanotubes is known then the individual results for each dimension can be combined to give an estimate of experimental parameters for optimal sorting.

Another issue is that of nanotube-nanotube interaction. Even in the case of single SWCNTs these will interact together because of electrical or van der Waals forces. It has been shown that particle particle interactions are responsible for the forming of chains of particles using DEP [101], so it might very well be that nanotubes form chains or more complex structures and thereby bridge gaps much larger than the length of a single nanotube.

When nanotubes are dispersed in SDS solutions, the SDS molecules form micelles around the nanotubes, thus increasing the effective diameter of the tube. This has not been taken into account in the calculations. A crude estimate using equation 3.3 with a diameter increase corresponding to a monolayer of SDS around the SWNT gives a 15 % increase of the friction factor f, and a corresponding decrease of the diffusion coefficient. Because of the decrease of the friction factor f, an increase of the DEP velocity is expected. Trapping will therefore become more efficient than what our algorithm predicts.

As mentioned in section 3.1, the values assumed for the conductivity of the nanotubes are to be taken with caution. Figure 3.25 shows how the frequency dependent factor depends on the conductivity of the nanotubes, when the depolarising factor is taken into account. The two upper curves are those for which the simulations were conducted and it is clear that the difference is minimal. However, as the conductivity of the nanotubes decreases so does the dielectrophoretic force and therefore the trapping efficiency. In simulations performed in a static fluid for conductivities of 1, 1000 and 10^8 S/m the trapping efficiencies were 1.86%, 8.71% and 23.03% respectively.

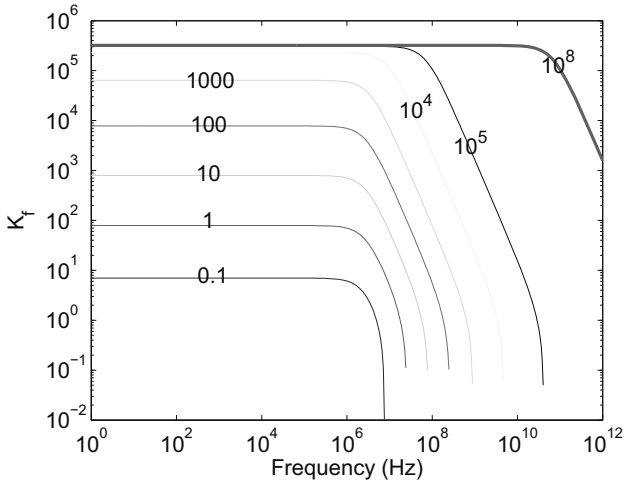

Figure 3.25: The frequency dependent factor K_f plotted for different nanotube conductivities (given on the various curves in S/m).

3.5 Summary

In this section a model of the dielectrophoretic process has been presented. The motion of carbon nanotubes under the influence of an electric field in a liquid has been studied as a function of several parameters and the results were used for a virtual sorting experiment. It was shown that the use of intermediate frequencies, where both m-SWCNTs and s-SWCNTs are attracted towards the electrode, gives the best sorting results in the shortest time, while still leaving a fair amount ($\sim 20\%$) of s-SWCNTs in the remaining solution.

Finally, an order of magnitude estimate of the other forces present in a microliquid system was made. It was shown that these forces are not likely to play a dominating role in the assembly of the nanotubes on the electrodes, except perhaps in the case of an SDS solution at regions very close to the electrode gap.

Chapter 4

Materials and methods

In this chapter an overview of the experimental procedure will be presented. Initially an investigation of the solutions used is going to be described. This will be followed by a description of the various microstructures on which the nanotubes were assembled and the fabrication process followed. Finally the experimental setup will be described.

4.1 CNT solutions

Four samples of carbon nanotubes were used in the experiments. The multiwalled nanotubes used came from Haldor Topsøe (HT) and Wake Forest University whereas the single-walled carbon nanotubes came from HT and Tubes@Rice.

For the purposes of this research the nanotubes had to be dispersed in a liquid. Although it seems trivial, making a carbon nanotube solution can be very difficult. Moreover, the solutions are often stable for a limited period of time only, meaning that the nanotubes tend to sedimentate at the bottom of the container. For the same reason it is also difficult to twice produce a solution of the same concentration, even though the procedure followed and the amount of nanotubes used is the same every time.

The procedure used for producing a carbon nanotube solution is the following: A small quantity of carbon nanotube soot is placed in a container with a certain amount of solvent. The solution is ultrasonicated for a period of time ranging from 30 minutes to 4 hours until it acquires a grayish color. Some solutions were diluted and some centrifuged for better results.

In appendix C a theoretical calculation of an ideal nanotube solution in terms of expected nanotube concentration in a certain volume of solution is described. However, achieving a solution with an ideal concentration such as described in appendix C is not easy. A first problem is weighing the amount of nanotubes used. Very precise scales are needed. A second problem is diluting the solution. Although theoretically the best results should be achieved with having the smallest number of nanotubes available, experimentally dielectrophoretic assembly did not

work well unless the solution had a certain concentration, much higher than the theoretically calculated one. Diluted solutions have been used in the experiments but dilution over 20 times the original usually resulted in no depositions.

Depending on the type of nanotubes (single-walled or multi-walled) various solvents were used. For the multi-walled nanotubes we found that the use of isopropanol was adequate and could disperse the tubes after only 30 minutes of ultrasonication in a 30 W ultrasonic bath. After longer ultrasonication and initial sedimentation the solutions generally remain stable for months at a time. An interesting observation was that when the volume of the solvent was small (5 ml) the nanotubes did not disperse at all and were merely concentrated at the top of the liquid. As soon as more solvent was added (usually up to 10 ml) the nanotubes would disperse after only a few minutes of ultrasonication.

Unfortunately isopropanol was incapable of producing a good stable solution of single-walled carbon nanotubes for more than 5 minutes. Therefore a number of other solvents and substances were tried. The surfactant Sodium Dodecyl Sulphate (SDS) was one of the most popular ones. SDS is a molecule with a hydrophilic head and a hydrophobic tail. When in solution it prefers to form micelles in order to protect its hydrophobic part from the water. That essentially means that in a solution containing carbon nanotubes, SDS will cover the nanotube surface creating a micelle around it. The nanotubes exist therefore in the solution with a coating of SDS, although the exact form of the coating is not well known or studied. For dispersing the nanotubes in SDS we used a 150 W ultrasonic disintegrator for 15 minutes followed by a 3 hour ultrasonication in the 30 W ultrasonic bath.

Most of the experiments in this research were conducted using this SDS solution of single-walled carbon nanotubes. However, the greatest disadvantage of the SDS solution is the fact that the micelle coating of the nanotubes cannot easily be removed. It will be shown that this does not have an effect to the behaviour and properties of the assembled nanotubes. We will also show how it is possible to destroy the SDS coating or even remove it with the use of acetone, isopropanol or water washing, heating, SEM imaging and even by electrical measurements with a low current.

Another solvent tried was 1,2 Dichlorobenzene (DCB). This solvent is also extremely good in dispersing single-walled carbon nanotubes using just the low power ultrasonic bath for 1-3 hours. The solutions are generally stable for at least a month. The presence of the two Cl atoms in the DCB molecule is responsible for the good dispersing properties of DCB, as the molecule adsorbs on the surface of the nanotubes preventing the nanotubes from clustering together in bigger bundles and thus sedimentate. Experiments with single-walled nanotubes dispersed in DCB will also be presented.

A number of other solvents was also tried, like ethanol, dimethylformamide (DMF), chloroform and an SDS/Chloroform composite. Most of these turned out to be unstable. The SDS/Chloroform composite resulted in the separation of the solution in 3 phases, a bottom phase containing only SDS, a middle phase containing concentrated nanotubes and a top phase, which had the distinct grayish

color of nanotube solutions. It is believed that the top phase contains nanotubes in both SDS and chloroform since the solution has the characteristics of a pure SDS solution but consistently forms networks of higher resistance than a pure SDS solution, as will be shown in chapter 5.

4.1.1 Isopropanol solutions of MWCNTs

In order to examine the solutions we deposit a small (2 μl) volume of the solution on a conducting substrate so that we can image it using the Scanning Electron Microscope (SEM). Figure 4.1 shows a solution of MWCNTs in isopropanol as seen in the SEM. The two batches of MWCNTs showed distinct differences, namely that the HT sample contained mainly short nanotubes, 0.5 μm - 3 μm in length, while the Clemson sample contained much longer nanotubes, 2 μm - 30 μm in length.

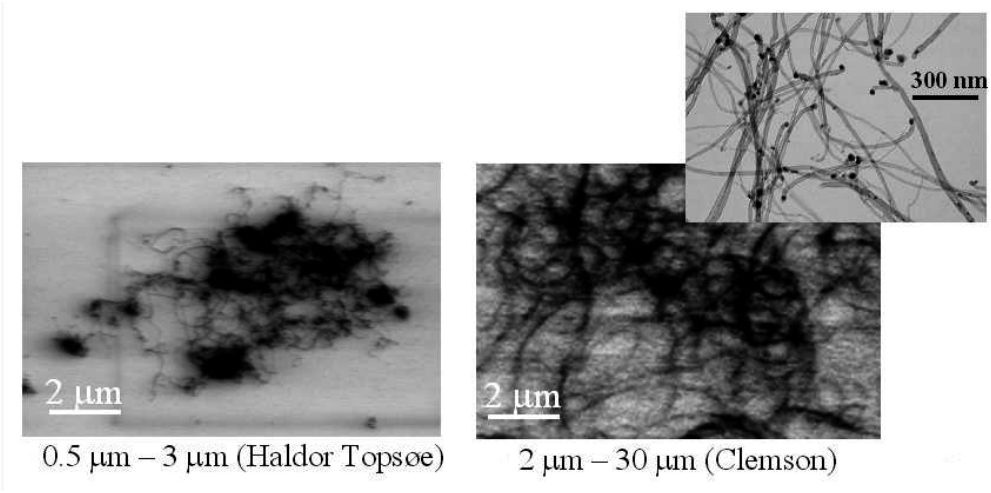

Figure 4.1: Scanning electron microscope images of the multi-walled nanotubes used in the experiments. The inset shows a Transmission Electron Microscope image of the Clemson nanotubes.

The time of ultrasonication had a small effect on these nanotubes. Figure 4.2 shows the diameters of the nanotubes after 2 and 4 hours of ultrasonication. It can be seen that the nanotubes exposed to 4 hours of ultrasound have smaller diameters than the ones exposed to only 2 hours of ultrasound. The nanotubes examined come from different positions on the substrate surface. The larger nanotubes generally came from areas close to the edges while the smaller ones came from central areas of the substrate. The diameters of the nanotubes fit a log-normal distribution with a mean value of 37.4 nm and 24.5 nm for the 2 hour and 4 hour ultrasonicated solutions respectively (Figure 4.2).

4.1.2 SDS solutions of SWCNTs

SDS is a solid substance that is dissolved in water. Therefore, when the water is evaporated from the solution a thick layer of SDS is left on the surface where

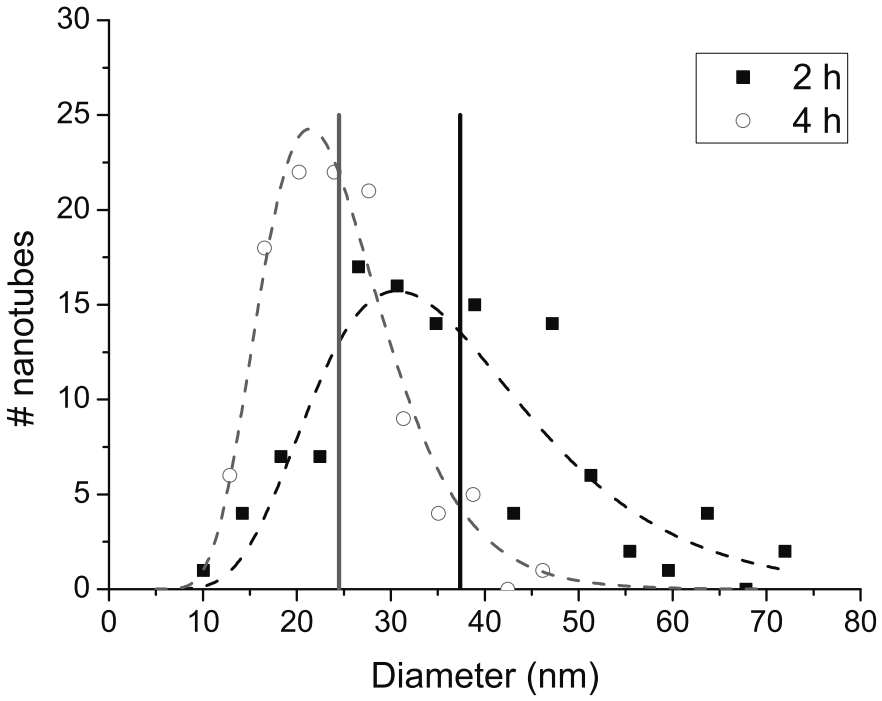

Figure 4.2: Measured diameters for the multi-walled carbon nanotubes after 2 and 4 hours of ultrasonication. The thick lines correspond to the mean values and the dashed lines to the fit with the log normal distribution.

the solution is deposited for imaging purposes. This makes it impossible to image the nanotubes as is shown in figure 4.3. One way to obtain a cleaner solution is to place a droplet on the substrate and then gently blow it off with a stream of nitrogen. Although this method removes most of the SDS solution, there is no guarantee that there are any nanotubes left for imaging purposes. The best way to get an idea of the dimensions of the dispersed nanotubes is by SEM inspection after the assembly process. Most experiments result in bundles of 15 to 30 nm in diameter, though bundles as small as 8 nm have also been observed.

An interesting observation was made during imaging of SDS solutions of carbon nanotubes in agreement with [114]. When a droplet is placed on a substrate it will obtain a circular shape and start evaporating from the edge to the center. Once the water has evaporated from the droplet the sample can be examined using an optical microscope as well as a Scanning Electron Microscope. Even under the optical microscope one notices some cracks in the dark surface of the dried SDS. The cracks are radially aligned following the lines that the droplet itself follows when expanding. Closer inspection with the SEM reveals the presence of carbon nanotubes aligned perpendicular to the cracks, i.e. parallel with the air/liquid surface during drying (for a schematic of the process, see Figure 4.4). Moreover, the cracks become wider as the scanning takes place, showing that the electron beam in itself is a means to remove the SDS coating from the nanotubes.

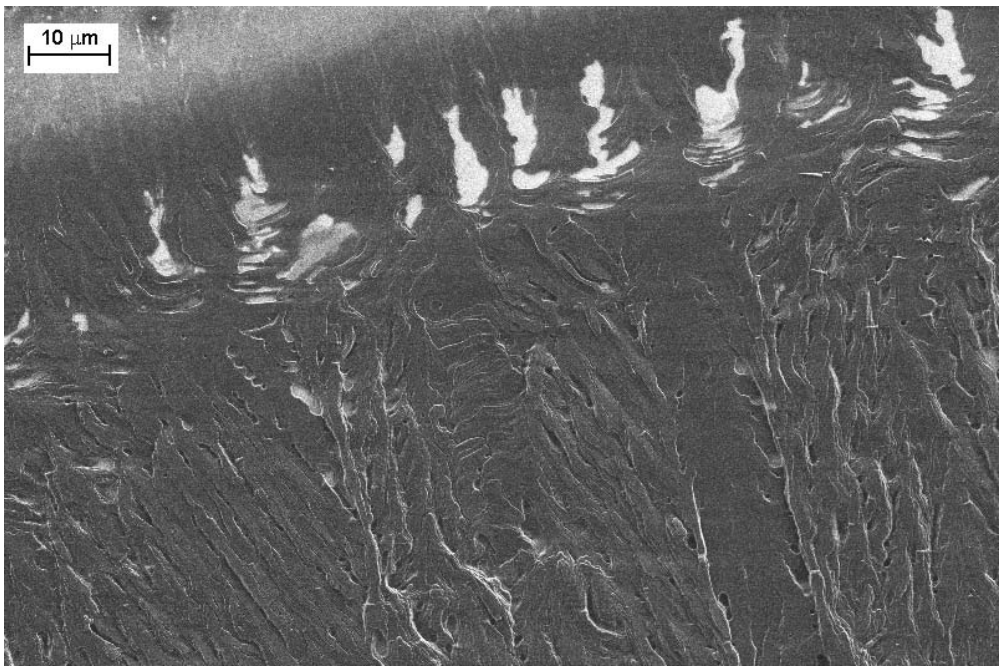

Figure 4.3: A SEM image of a dried SDS solution on a Au substrate. The SDS forms a thick dark layer on the substrate which contains the carbon nanotubes, making it impossible to image them.

The above observation could be used in order to align the nanotubes in a particular direction. To test this idea we placed a rectangular piece of gold-covered silicon vertically in a container with 1.5 ml SDS and let the solution slowly evaporate over the course of 2 days. The sample was then imaged with a SEM at a low voltage of 2 kV. The SEM inspection revealed 3 distinct regions on the sample, as shown in Figure 4.5. The first was about 8 μm long and contained densely packed carbon nanotubes. The second area was about 1 mm long and contained few nanotubes and some half-cylindrical objects. The third area was 2 mm long and was covered with a thick layer of SDS with cracks containing nanotubes. In between the thick SDS layers there were small patches with no surfactant on them, which though contained nanotubes.

We would normally expect the nanotubes to align at the air/liquid interface because of the large surface forces. From the SEM pictures it is generally difficult to draw any conclusions, but it seems like there is a preferred orientation in that direction. This result does not completely agree with the results presented in [114], where the alignment of the nanotubes was very pronounced. This could be attributed to the solution containing larger bundles of nanotubes that may not easily be affected by the surface forces.

The effect of heating and an electron beam on SDS can be seen in Figure 4.6. A droplet of an SDS nanotube solution was placed on a silicon substrate and the solution was spread on the entire substrate surface (2×1 cm^2) using a gentle stream of nitrogen. The sample was imaged with a SEM and it was found that it consisted of areas of dried SDS with the regular crack pattern. Then the sample was placed in an air oven at 200 degrees Celcius and left there for approximately

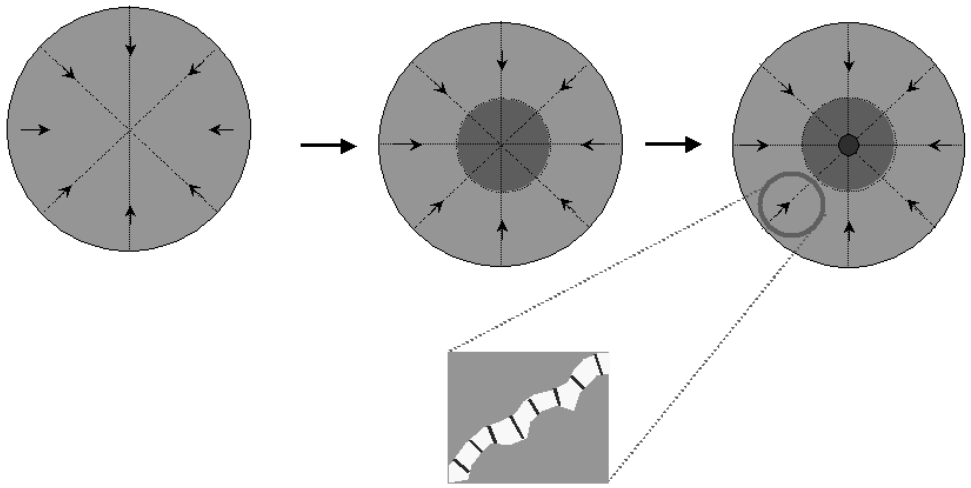

Figure 4.4: Schematic of the drying SDS process that creates radially aligned cracks on the surface. The darker circles indicate the places that dry last. The blue lines in the cracks indicate the carbon nanotubes.

15 hours. After that the sample was imaged again in the SEM. This time the picture had changed completely. Instead of the cracks the sample now consisted of particles of all shapes and sizes, however, mostly rounded particles of up to a few μm in diameter. Since the melting temperature of SDS is about 200 degrees [115] it is reasonable to conclude that the thin layer of SDS covering the surface has melted into these spherical particles, much in the same way that thin layer of metals form particles when warmed up at a high temperature.

It should be noted that it is not necessary to leave the sample in the oven for 15 hours. Samples left at 200 degrees only for 1.5 hours show the same behaviour.

The heating method was used to make sure that the long thin threads between the cracks were indeed nanotubes and not stretched SDS. The sample was heated for one hour at 200 degrees Celcius and imaged afterwards. The SDS had partially retreated into particles leaving behind exposed areas of nanotubes and areas where these threads were now more pronounced, so that we could indeed identify them as nanotubes.

When imaging some of these particle areas with the SEM it was observed that while the beam was exposing the particles, they kept changing appearance: the rounded particles were disappearing from the substrate either leaving behind the substrate or giving rise to much smaller particles (see Figure 4.6(b)). A voltage of 2 kV was used for these experiments, since at higher voltages the surface appeared clean of particles due to the larger penetration depth of the electron beam into the silicon substrate. Each area was scanned for approximately 2 minutes.

When a small quantity of DI water, isopropanol or ethanol is added to an otherwise stable and functional 1% SDS in DI water carbon nanotube solution, the nanotubes in the solution begin to sedimentate immediately and are gathered at the bottom of the container after only a few minutes. A possible explanation is that these liquids break up the micelle structure surrounding the nanotubes,

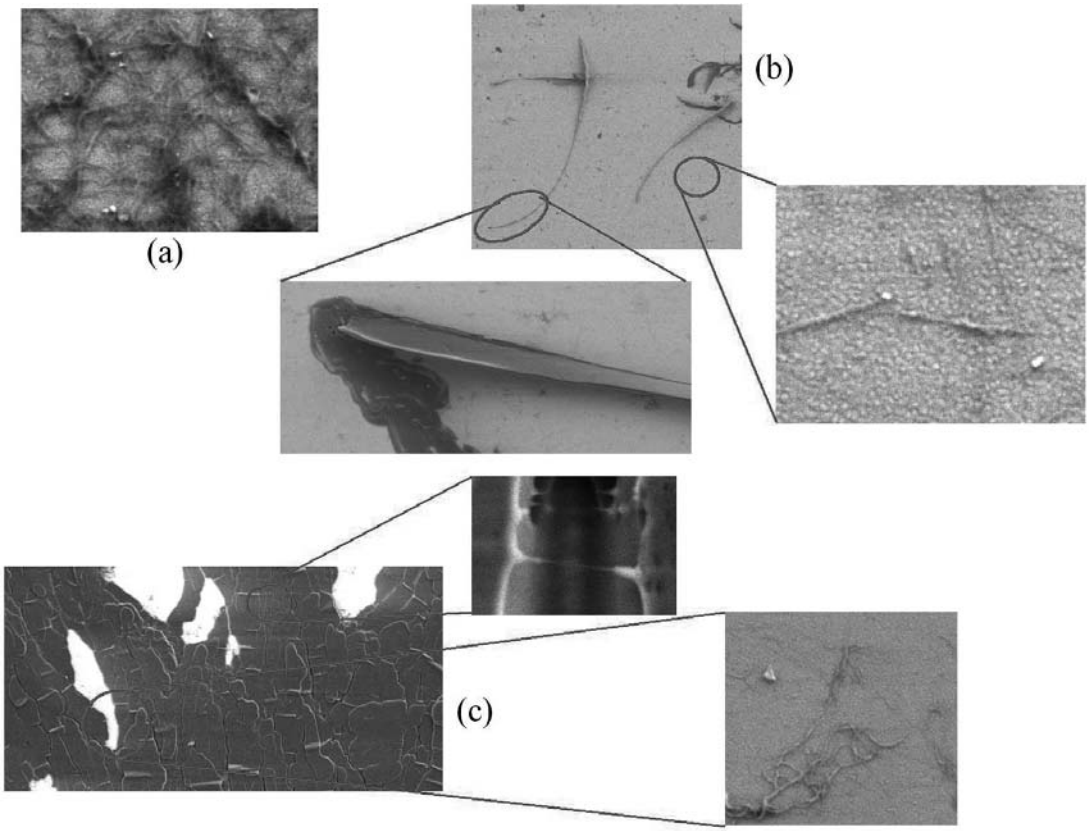

Figure 4.5: Images of the various regions formed on a Au substrate during vertical slow drying of SDS. In **(a)** the region contains densely packed nanotubes. In **(b)** sparse nanotubes and odd half cylindrical structures are found and in **(c)** thick SDS with cracks containing carbon nanotubes and open regions with sparse nanotubes are seen.

which then form larger and larger bundles that sedimentate.

The effect of DI water on a droplet of SDS with dispersed carbon nanotubes was first studied in [114] and seems to strengthen our own explanation of why the solution sedimentates after water is added to it. Droplets of SDS solution were placed on a silicon substrate consisting of numbered square regions for easy identification. The droplets were left to dry for 2 days. Half the substrate was then slowly immersed in water with a velocity of roughly 1 mm/sec and then pulled out with the same velocity. Once the water evaporated from the surface the droplet of the SDS was no longer visible in the area where the substrate had been immersed in water. SEM inspection revealed that the nanotubes were still on the substrate. The droplet not exposed to the water was left unchanged.

4.1.3 DCB solutions of SWCNTs

DCB is a liquid substance that has a low evaporation rate at room temperature. This property makes it ideal for the experiments and for imaging. As with all carbon nanotube solutions also this one contains bundles of single walled carbon nanotubes. The diameter and length of the nanotubes were measured at several

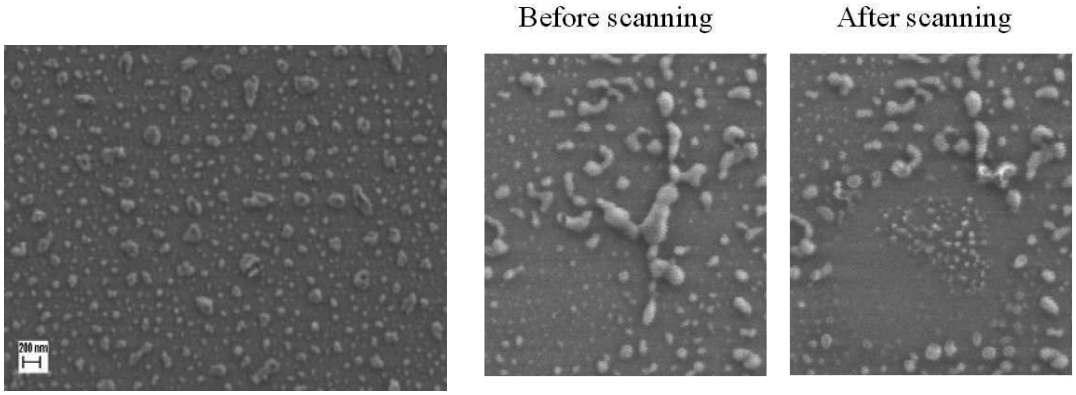

(a) Effect of heating (b) Effect of ion beam

Figure 4.6: The effects of heating the SDS solution can be seen in **(a)** and the effect of scanning the sample with an ion beam can be seen in **(b)**. The process that destroys the particles is the same that creates the cracks in Figure 4.5.

different locations and histograms showing their distribution were made. These are shown in figure 4.7. It is evident that the longer the ultrasonication time the smaller the bundles get. As we are interested in achieving small diameter bundles while at the same time keeping the length to about 1 μm it is evident from the figures that 3 hours of ultrasonication in DCB is the best time for this solution.

4.2 Test structures

As it was shown in chapter 2 the result of dielectrophoresis on carbon nanotubes depends on a number of parameters. In order to study the dielectrophoretic assembly of carbon nanotubes on microsized electrodes it is necessary to create some appropriate test structures. In this section the various test structures used in the study will be presented. These can be divided into three categories: the cantilever probes, the planar surface electrodes and the wafer-scale assembly structure.

4.2.1 Cantilever probes

Since the goal of this research is to place nanotubes at the tip of a cantilever it is important to show that such thing is possible using dielectrophoresis. For this purpose we have designed a number of free-standing electrodes at the tip of a cantilever probe. The general sketches of these are shown in figure 4.8.

The starting design is the four-point probe (4PP shown in 4.8(a)), a cantilever with 4 free-standing electrodes, developed at MIC[1] by C.L. Petersen [116] and T.M. Hansen [117]. The pitch varies from 1.5 to 16 μm. The probe is fabricated in silicon oxide (SiO_2) and the fingers are released using a backside KOH etch. The process

[1]MIC is now known as DTU Nanotech, Department of Micro- and Nanotechnology

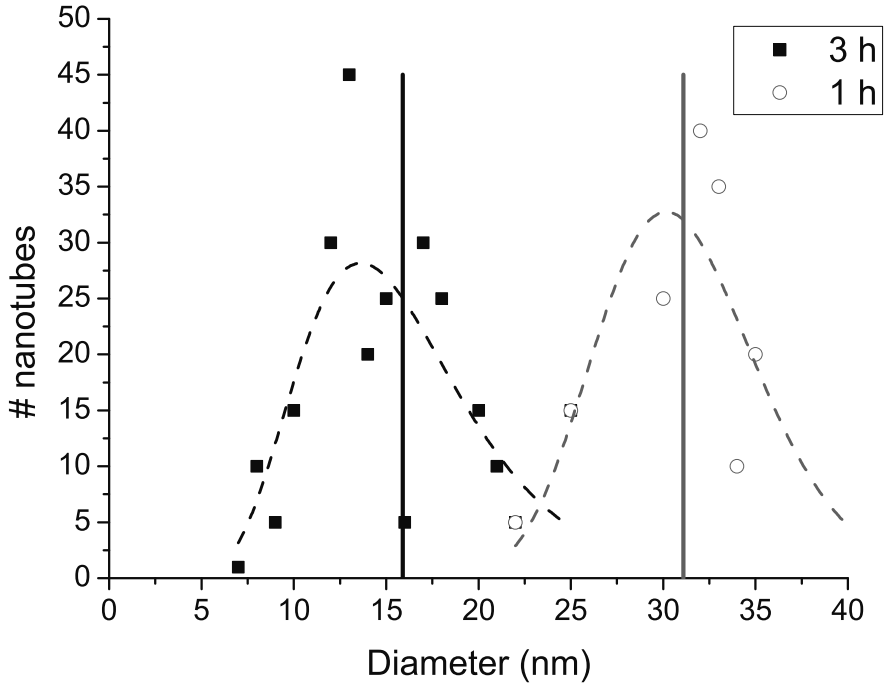

Figure 4.7: Measured diameters for the single-walled carbon nanotubes dispersed in DCB after 1 and 3 hours of ultrasonication. The thick lines correspond to the mean values and the dashed lines to the fit with the log normal distribution

is described in detail in [117] and repeated in appendix D for convenience. Due to an isotropic etch during the fabrication, evaporating gold on the entire structure does not short-circuit the fingers and therefore a 4PP is created. Experiments done with these probes showed two disadvantages: 1) The parallel structure of the fingers was essentially forming a capillary through which the solution was pulled towards the main body of the probe due to surface tension forces. That led to wetting of the probe surface and therefore unwanted contamination. By contamination we mean the deposition of nanotubes in a random way on the main probe surface. 2) The entire surface of the probe was covered in gold. Ideally the main surface of the probe should be made of a material on which nanotubes do not like to be. These problems were solved by changing the structure of the fingers and the experimental setup.

The above described problems led to the designs of figures 4.8(b), 4.8(c) and 4.8(d). In figure 4.8(b) the process is changed so that the substrate onto which the fingers and transmission lines are placed is not gold but silicon nitride (Si_3N_4). Moreover, the fingers are now bending at their ends creating a smaller gap. The fabrication process for these probes was developed by Ramona Mateiu and is described in appendix D. The increase of the surface area of the gap would in principle reduce the capillary effect and thus the contamination of the probe. It was also noted that the nanotubes would rather not deposit on the nitride so it was hoped that the change of substrate would also assist in reducing the

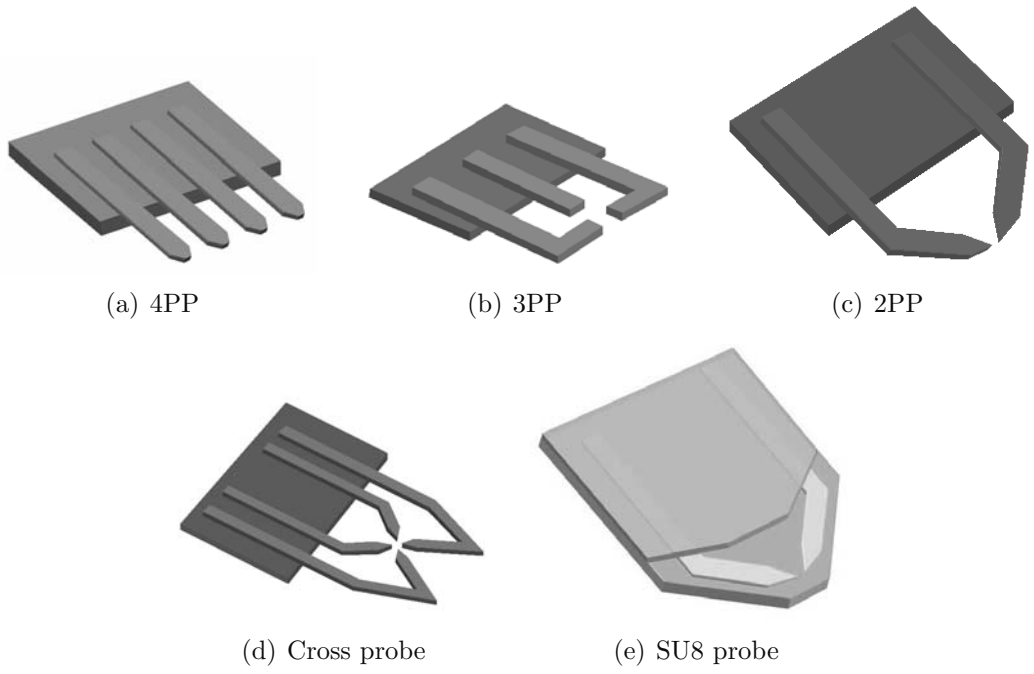

(a) 4PP (b) 3PP (c) 2PP

(d) Cross probe (e) SU8 probe

Figure 4.8: Schematics of the cantilever probes used in these experiments. The smallest spacing between the fingers is $1 - 3$ μm. See text for explanations.

contamination. This was indeed the case, however due to the small length of the free-standing fingers of these probes the capillary effect was still strong enough to cause contamination. We did notice however much fewer nanotubes on the nitride substrate than on the gold substrate.

In figures 4.8(c) and 4.8(d) the fabrication process of the 4PP was followed in order to produce longer structures and this time with a gradual change in the gap size and effectively the surface area of the induced capillary. The extra two electrodes in figure 4.8(d) where added in order to acquire two samples on the same chip. These structures functioned very well with solutions of MWCNTs in IPA using one of the experimental setups, and no capillary effect was observed. However, when an SDS solution of SWCNTs was used, the structures did not function properly.

Finally, a chip was designed with the purpose of avoiding the short-circuiting of the structure in case the solution was to move over the main body of the probe. This is shown in Figure 4.8(e) and was developed and fabricated by Alicia Johansson [118]. The probe is made entirely in the polymer SU-8 and has two cantilevers with gold electrodes, which are completely covered with an SU-8 layer except for the tips. Due to fabrication difficulties and further problems with contacting the electrodes externally, only few of these chips were tested.

4.2.2 Planar electrodes

In order to work with SWCNTs it was necessary to change both our experimental

setup and method as well as the structure of the electrodes used. Planar electrodes rather than cantilevers were chosen since they were easier and faster to fabricate. The fabrication process for these planar microstructures is described in section 4.3. Figure 4.9 shows the various planar structures used in the course of this project. A variety of other designs were also fabricated but are not shown here due to the similarity with those already presented.

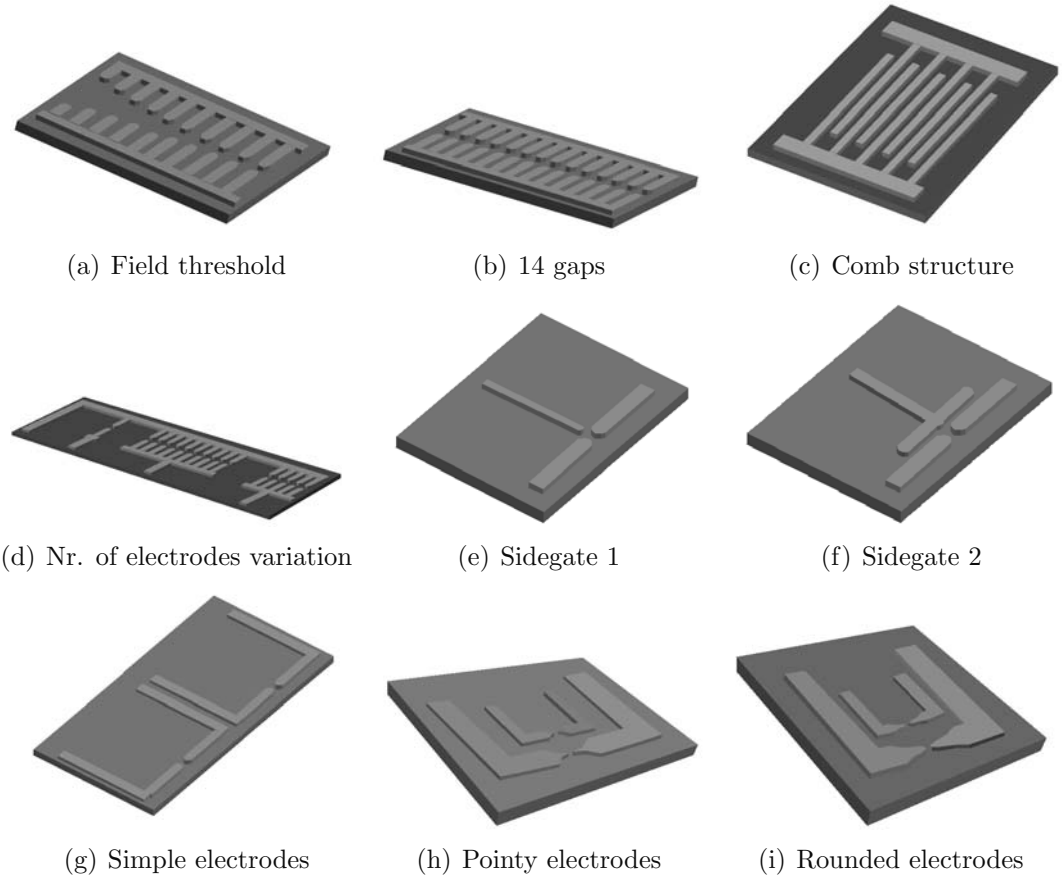

(a) Field threshold (b) 14 gaps (c) Comb structure

(d) Nr. of electrodes variation (e) Sidegate 1 (f) Sidegate 2

(g) Simple electrodes (h) Pointy electrodes (i) Rounded electrodes

Figure 4.9: Schematics of the planar probes used in the experiments. The smallest spacing between the fingers varies but is usually around 1.5 μm. See text for explanations.

In figure 4.9(a) a structure designed to investigate the required voltage for a successful assembly is shown. The structure comprises 10 identical electrode structures, each one containing 10 electrodes with varying spacing from 1 μm to 20 μm. When a voltage is applied between the electrodes, the field strength will vary depending on the electrode spacing. DEP is only possible when the field strength is large enough to overcome the random thermal forces and the forces on the liquid. With this structure we can get an idea about the field strength required for each solution of nanotubes. As there are 10 identical structures on each chip, relatively few chips are required for a statistical study. It should be noted that the results in part are geometry dependent.

Figure 4.9(b) shows a structure produced in order to obtain a large number of identical parallel networks addressed at the same time. This should ensure that measurements done on the networks will reflect an average behavior for the

particular assembly condition. On each chip there are 2 individually addressed structures each containing 14 identical electrodes with a spacing of about 3 mum.

Figure 4.9(c) shows a general sketch of a number of planar structures which were designed for investigating the alignment of carbon nanotubes at various frequencies as well as for investigating the effect of the frequency on the amount of metallic and semiconducting nanotubes on the chip. Several structures were produced with different spacing between the electrodes and different width of the electrodes. These chips were not tested extensively.

Figure 4.9(d) shows a structure designed in order to investigate whether the number of electrodes addressed simultaneously has an effect on the assembled networks resistance, after we have accounted for the number of electrodes present. Therefore this structure contains 3 groups of electrodes, one with 1, one with 5 and one with 10 electrodes. The spacing between the electrodes is 1.5 μm.

The structures shown in figures 4.9(e), 4.9(f), 4.9(g), 4.9(h) and 4.9(i) contain one or two assembly sites and were designed in order to obtain single nets or bundles of nanotubes and be able to individually characterise them. The structures of figures 4.9(e) and 4.9(f) contain an additional electrode to be used as a sidegate, however it was found that in most cases nanotubes assembled between that electrode and the actual source and drain electrodes, thus making it impossible to carry out any sort of sidegate measurements. The spacing between the electrodes was 1 μm and for the sidegate structures the third electrode was 1.5 μm away.

4.2.3 Wafer-scale assembly

One of the often encountered arguments for using the dielectrophoretic method for the assembly of carbon nanotube structures is that it is one of the few available assembly methods that is potentially scalable to wafer level. To investigate this potential we designed a wafer in such a way that all of the approximately 500 chips on the wafer were connected to two large and easily accessible electrodes on the wafer edge. Figure 4.10 shows a sketch of the concept while the actual mask design is shown in Figure 4.11. This design also uses the silicon wafer as a backgate electrode, contacted both on the wafer scale as well as on the individual chip scale. Moreover, each chip (see detail in Figure 4.10) has electrodes that can be contacted with a micro four-point probe so that post assembly testing of the structures can be done without needing to remove the chip and bond it to a substrate. The electrodes were designed with a spacing of 1.5 μm.

This design imposes some interesting restrictions on the fabrication, discussed in section 4.3.2.

4.3 Fabrication processes

The fabrication processes developed for this project are going to be described in this section. Appendix D contains the processes used in this project but developed

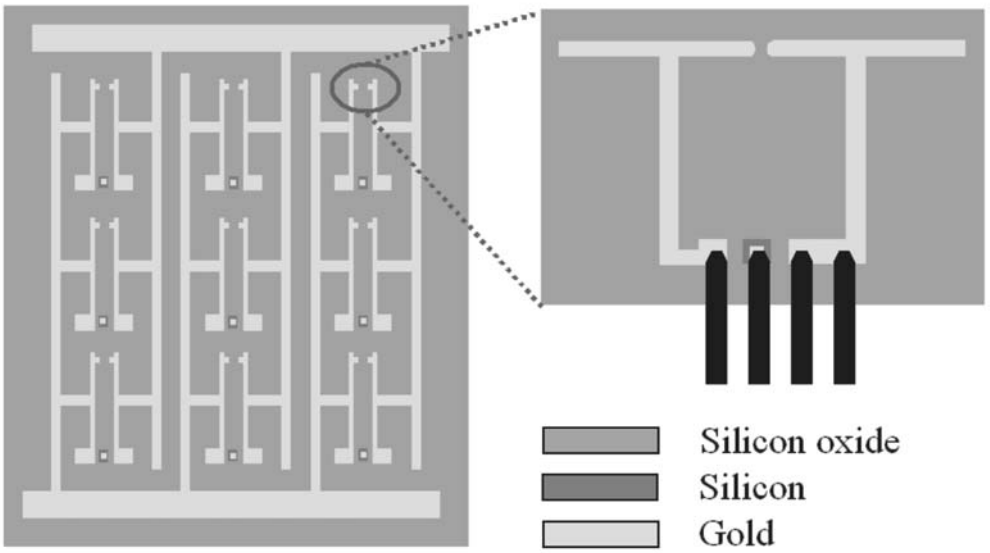

Figure 4.10: Schematic of the concept behind wafer scale DEP. The vertical bars connect all the chips together to large electrodes on the wafer. Each chip can also be taken out of the wafer after assembly and addressed through the bonding pads. The detail shows the electrodes along with pads suitable for contacting using a 16 μm pitch micro four-point probe. Each chips has a hole etched through the oxide so that contact to the silicon substrate acting as a backgate can be made.

previously.

4.3.1 Process 1: Planar structures

Regardless of their specific geometry, all planar test structures were developed using the same general 1-mask fabrication process, shown in figure 4.12.

A one-sided wafer with a nominal thickness of 500 μm was used and a silicon dioxide layer was thermally grown on it using a wet oxide oven process at 1000^{o}C. The thickness of the oxide varied from batch to batch but for most of the experiments described in this report the oxide was 500 nm thick. Subsequently, a 1.5 μm resist layer was spun on top of the oxide and a positive photolithography process was used in order to pattern the electrodes on the oxide. The resist is sensitive to the temperature and humidity conditions in the cleanroom and therefore a test to determine the optimal exposure time was used. The test involves dividing the wafer into 6 parts and exposing the resist on each part for different time intervals. Optical microscope evaluation of the developed structures determines the optimal time interval. For this resist thickness the exposure time varies between 3 and 10 sec. After patterning and development of the resist, 10 nm of titanium or chromium and 100-200 nm of gold were deposited on the wafer and a lift-off process was done to form the electrodes. The titanium or chromium layer was used in order to enhance the adhesion between the gold and the silicon oxide. With this method, submicron gaps were achieved with a yield very close to 100%.

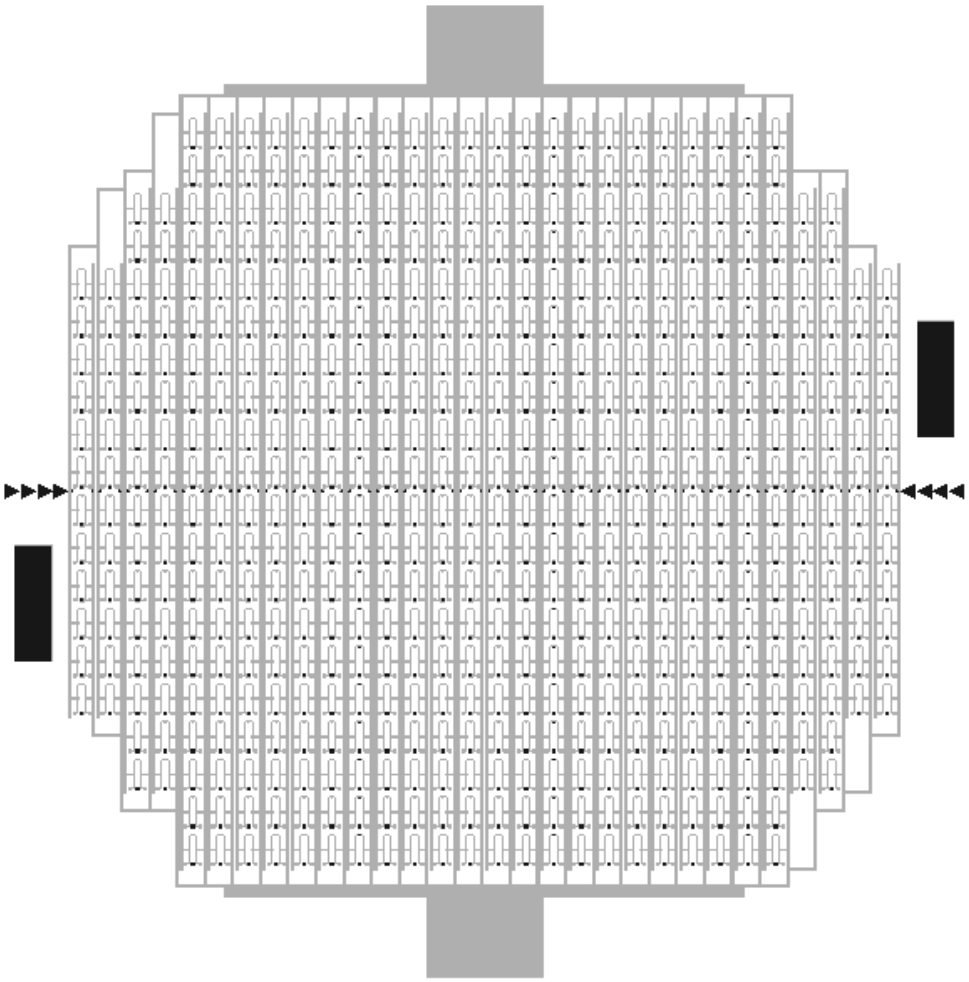

Figure 4.11: The mask design for the wafer scale DEP. The dark red areas are representing the contacts to the silicon substrate.

Since this process is relatively simple, in order to evaluate how it performs we basically only need to see how well the features from the mask are reproduced on the wafer. Taking into account the nature of the structures, this essentially means measuring the gap between the electrodes. Figure 4.13 shows a good and a bad reproduction of the gap for the structure of Figure 4.9(e). Generally the structures do not look smooth at the edges (roughness of 100-200 nm) but the gap is more or less reproduced. The irregular structure at the edges can be attributed to the use of the lift-off process. This involves placing the wafer in an acetone ultrasonic bath until the metal covered resist has been removed from the wafer leaving behind those metal pieces that were sitting on the silicon oxide itself. Because of the small gap sizes, inspection of the wafer under an optical microscope is required in order to confirm that the lift-off process is successful. This however can only be done if the wafer is dried first, something that should be avoided since during drying metal pieces tend to stick on the wafer and are therefore much harder to remove by further ultrasonication.

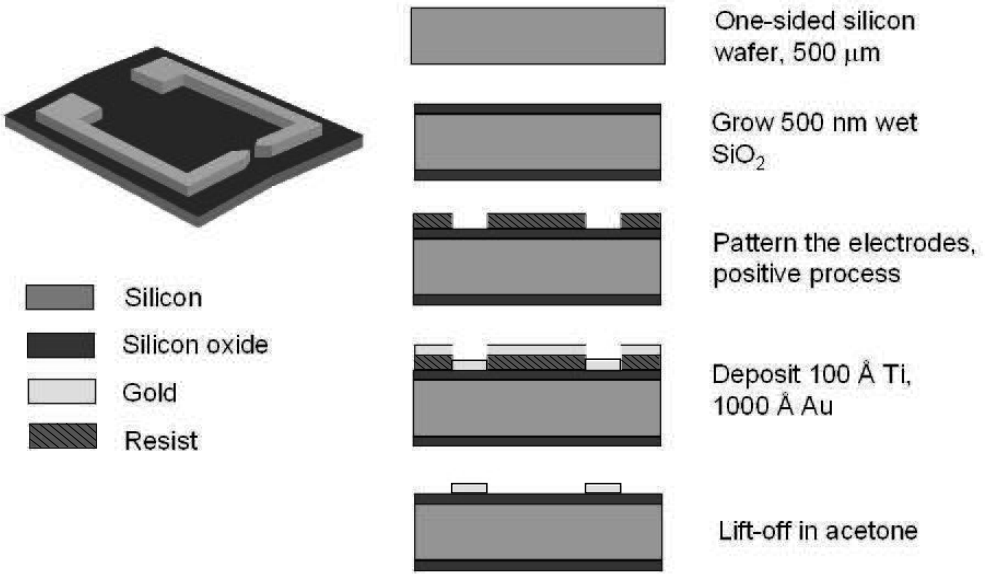

Figure 4.12: The fabrication process used to produce all planar test structures.

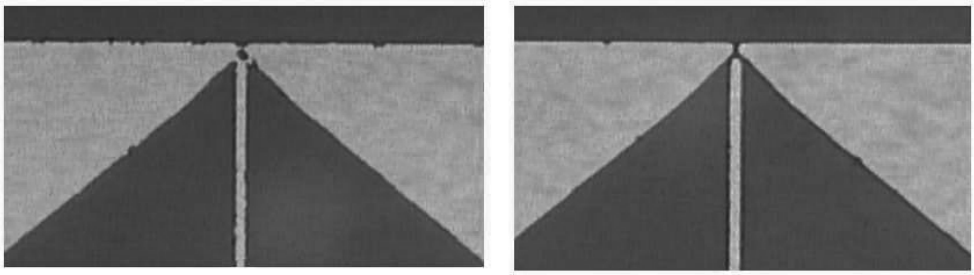

Figure 4.13: A bad and a good reproduction of the 1 μm gap in the structure of Figure 4.9(e). In the left figure the lift-off has not succeeded and gold is still bridging the gap. Moreover, the sidegate electrode has an irregular shape. In the right figure the gap is open and the sidegate electrode (1.5 μm wide) is well defined.

4.3.2 Process 2: Wafer scale assembly

A 2-mask process was used for these structures. We started with a one-sided wafer of nominal thickness of 500 μm (type ON 91) onto which 150 nm of thermal silicon oxide were grown in an wet oxide oven process at 1000 ^{o}C. 1.5 μm of photoresist were spun onto the wafer, which was then exposed for 5.3 seconds through the first mask, which was to pattern the contacts to the silicon wafer under the oxide. A positive photolithography step was used. The wafers were baked for 2 minutes at 120 ^{o}C in order to harden the resist, which was used as a mask for etching the silicon oxide at the contacts using a HF wet etch for about 3 minutes, to connect to the backgate.

After the etching the resist was stripped in acetone. It was judged that the wafer was clean enough so that further cleaning using a 7-up solution (a hot solution

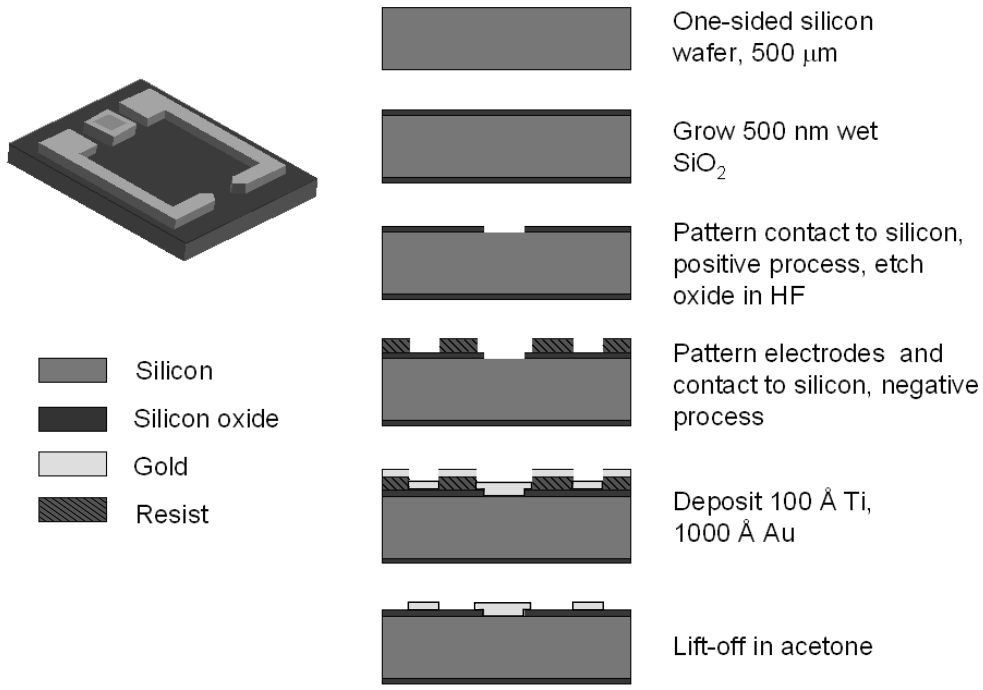

Figure 4.14: The fabrication process used to produce the wafer scale assembly wafers.

of H_2SO_4 and $(NH_4)_2S_2O_6$) was not necessary. After spinning 1.5 μm the resist was exposed to light again, but this time using a negative photolithography step. This means that the wafer has to be exposed through the mask first but for half the time used for a positive step, then baked for 100 seconds at 120 ^{o}C and then exposed again but without a mask for 30 sec (flood exposure). After development 10 nm of titanium and 100 nm of gold were evaporated on the wafer and a lift-off process was carried out.

There were two reasons for the choice of photolithography steps: 1) Since the existence of particles cannot be ignored in the cleanroom the first mask would have to be a dark field one, so that a possible particle contamination of the surface would not lead to unwanted holes on the resist layer and subsequent unwanted etched holes on the oxide. A dark field mask makes the areas which we want to etch transparent, so a positive process needs to be implemented (if the resist is to be used as an etch mask as in this case). 2) In order to align the second mask with the patterned surface of the wafer from the first mask we need to be able to see the wafer surface through the second mask. Therefore the second mask has to be a bright field one, forcing us to use a negative process for our electrode deposition. The process is shown in Figure 4.14.

In this 2-mask process one of the most critical parameters is the alignment. Any misalignment of more than 7 μm can cause a short circuit between one of the electrodes and the backgate due to the proximity of the features at the 4PP test pads (s. Figure 4.10). As it can be seen from Figure 4.15 the alignment is very good, though not perfect.

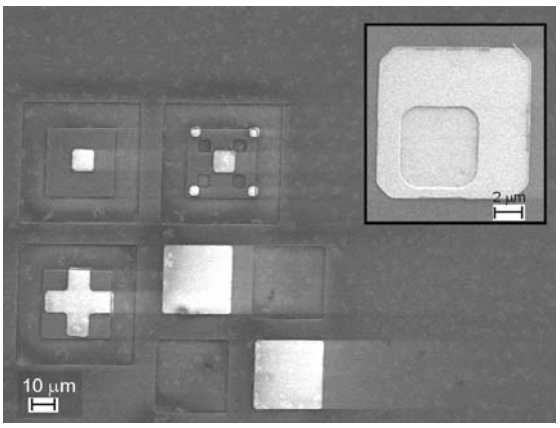

Figure 4.15: SEM image of the alignment marks after the process was finished. The second mask seems to be shifted about 1 μm towards the top right, and also slighly rotated in relation to the first mask but this is within the tolerance limits. The inset shows the backgate contact at the small 4PP pad.

The contacts were designed to be perfect rectangles. However, the reproduction clearly shows that the rectangles have circular edges, and even approach a circular shape in some cases. This is usually a sign of overexposing or underexposing the resist, but since the shape plays no role in this case, this error is not important. In this particular case, based on the dimensions of the obtained rectangles we can deduce that during the first exposure the resist was underexposed and during the second exposure it was overexposed.

A second critical parameter is the electrode gap. Due to the second mask being a bright field mask, the gap on the mask was 2 μm, i.e. 0.5 μm bigger than the actual design. Moreover, after lithography the final gap size became about 3 μm. This increase could be attributed to variations of the humidity in the cleanroom during the fabrication process or simply due to overexposure. The increased gap size could be a problem since small gaps are required for dielectrophoresis in order to keep the voltage small.

The third critical parameter is the electrical insulation between the backgate and the electrodes. Measuring the resistance between the two electrodes and between each electrode and the backgate after fabrication it was found that on all wafers there was contact between the bottom electrode and the backgate. The non-random nature of this unwanted contact led to the conclusion that the contact was established as part of the fabrication process and was not for example the result of some metal remains left on the wafer after the lift-off process. Indeed, upon examining the wafers, two regions were found where a hole had been etched in the oxide at a place where gold electrodes were deposited afterwards. Inspection of the mask at the same places showed the structures of Figure 4.16. These were planar structures on the mask and looked like breaks in the chromium layer covering the mask. Light was able to pass through these breaks, that were several micrometers in diameter, and expose the underlying resist, which was in turn removed during development, producing a hole in the silicon dioxide layer.

The flawed mask unfortunately made the wafers useless for wafer scale assembly

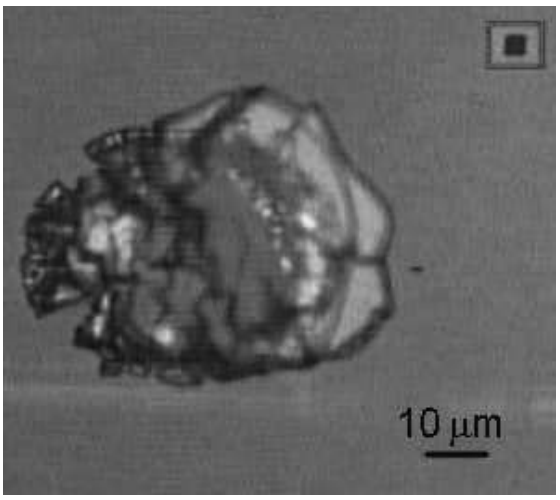

Figure 4.16: Optical microscope image of one of the error areas on the first mask, defining the holes to the silicon substrate. The small rectangle on the top corner shows one of the correct holes.

unless the affected chips were identified and removed. This is because the connection to the backgate introduces a large capacitor into the circuit (between the electrode and the backgate with the oxide acting as the dielectric), which at the frequencies we operate basically acts as a small resistor, which forces the voltage to appear across the internal resistance of the generator. Indeed, when 10 V are applied between the electrodes, the actual voltage measured across the gap amounts to a few mV only. We measured the capacitance between the top and bottom electrodes to be 86 nF, which for a frequency of 10 MHz corresponds to a resistance of 0.2 Ω. Such a big capacitance cannot be attributed to the parallel wires connecting all chips to the top and bottom electrodes, since these are 200 μm apart, but fits well with assuming a parallel plate capacitor between one of the big electrodes and the silicon substrate with the oxide acting as the dielectric. It is therefore quite probable that the wafers would function as intended if the connection to the backgate was not present.

A new mask was sent by the manufacturer without this error and will be used to do the experiment in the future[2].

4.4 Experimental setup

Two experimental setups have been used depending on the nature of the test structure.

[2]We were indeed able to perform wafer-scale dielectrophoresis after acquisition of the new mask. The results were published in the journal Physica Status Solidi (a), volume 203, No. 6, p. 1088 (2006)

4.4.1 The chip holder

In order to use the structures presented above we need to interface them with the external environment. A special ceramic chip is used for this purpose. The chip structures are glued to the ceramic using ultra high vacuum (UHV) glue and the electrodes are connected to the gold electrodes on the ceramic by aluminium bonding wires. A special holder was fabricated in PMMA using a CO_2 laser. The holder has tungsten wires contacting the golden pads on the ceramic chip and providing an interface to the electrical setup (Figure 4.17).

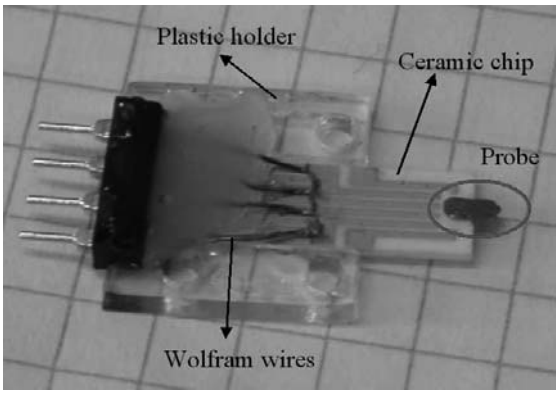

Figure 4.17: A plastic holder designed to hold a ceramic chip interfaces the chip to the rest of the setup. The chip is glued on a ceramic and bonded to it using aluminium wires 20 μm in diameter.

4.4.2 Cantilever-probe setup

A schematic of the basic experimental setup used with the cantilever structures is shown in figure 4.18. A tube, connected to a syringe containing the solution, is brought into contact with a cantilever structure attached on the ceramic. The whole process takes place under an optical microscope. Both the chip and the tube can be at an arbitrary angle with each other.

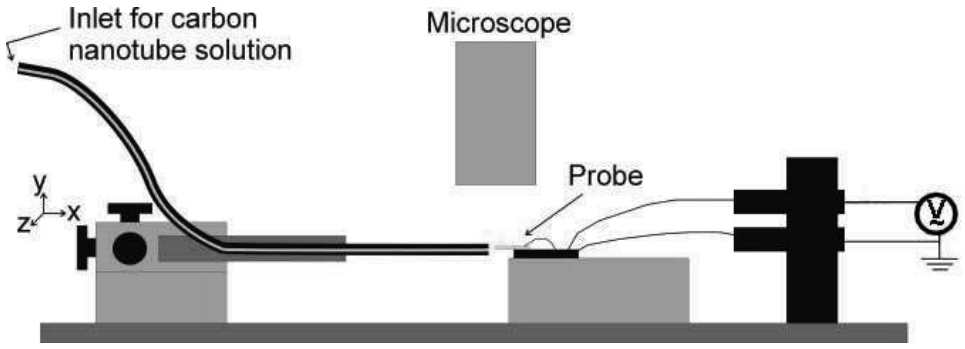

Figure 4.18: The setup sketched here for the case where both the chip and the tube are horizontal.

The original experiments were conducted using a tube of a diameter of 1.5 mm at an angle of 30-45 degrees with the horizontal plane and the chip at a similar

angle. It was observed that the liquid was crawling up the cantilevers onto the main body of the chip. The effect was the same when the tube containing the solution was placed at a zero angle to the horizontal plane but the chip was still at an angle. When both the tube and the chip were horizontal and the tube diameter was reduced to about 0.5 mm the wetting of the main body of the chip could be well controlled and even for cantilevers of 10 μm in length the solution would in most cases not wet the main body of the probe. An exception was when working with SDS solutions of single-walled carbon nanotubes. Although no wetting was observed while the voltage between the electrodes was turned off, upon application of the electric field the solution would immediately make its way up the electrodes and wet the main body of the probe. Based on the discussion of chapter 2, this can be attributed to the large electrothermal flow observed with high conductivity liquids such as aqueous SDS solutions.

Figure 4.19 shows a series of images recorded while the tube with a droplet of solution extending from the apex is approaching one of the cantilever probes. Great care should be taken so that the probe and the center of the droplet in 3D are on the same plane. This is achieved by using the microscope in order to focus the probe and the z control of the xyz micromanipulator in order to focus the middle of the droplet. In this way when the droplet touches the probe, it is energetically more favorable for it to stay in its spherical form rather than climb up the fingers.

When using isopropanol solutions the liquid at the apex of the tube tends to evaporate rapidly. Since the time scale for a DEP assembly experiment is rather short, this does not constitute a big problem, but compensation for the evaporation can be provided either manually, by applying a small pressure on the syringe while observing the droplet with the optical microscope, or by using a syringe pump calibrated to provide a liquid velocity in the tubing, which will keep the droplet size constant.

Although this experimental procedure can be rather well controlled, there are two problems associated with it. One could choose to end the experiment either by letting the droplet evaporate in which case the droplet will retreat back into the tube or by pulling the tube away from the probe. In both cases there will be a force exerted on the nanotubes on the cantilever by the liquid movement, which could destroy an already assembled bridge. A second problem is the surface forces at the droplet's air/liquid interface. When there are impurities or large bundles of nanotubes present in the solution it is possible to see their movement with an optical microscope. One can observe that these large objects are approaching the edge of the droplet with a rather large velocity and bounce back and forth in all three dimensions. Although we have no way of knowing whether this type of motion at the interface is also present for the smaller bundles or individual nanotubes, we can only assume that this is probably the case. This motion is therefore also a source of error in the dielectrophoretic assembly and could account for the rather irregular assemblies and the low yield rate observed with this method.

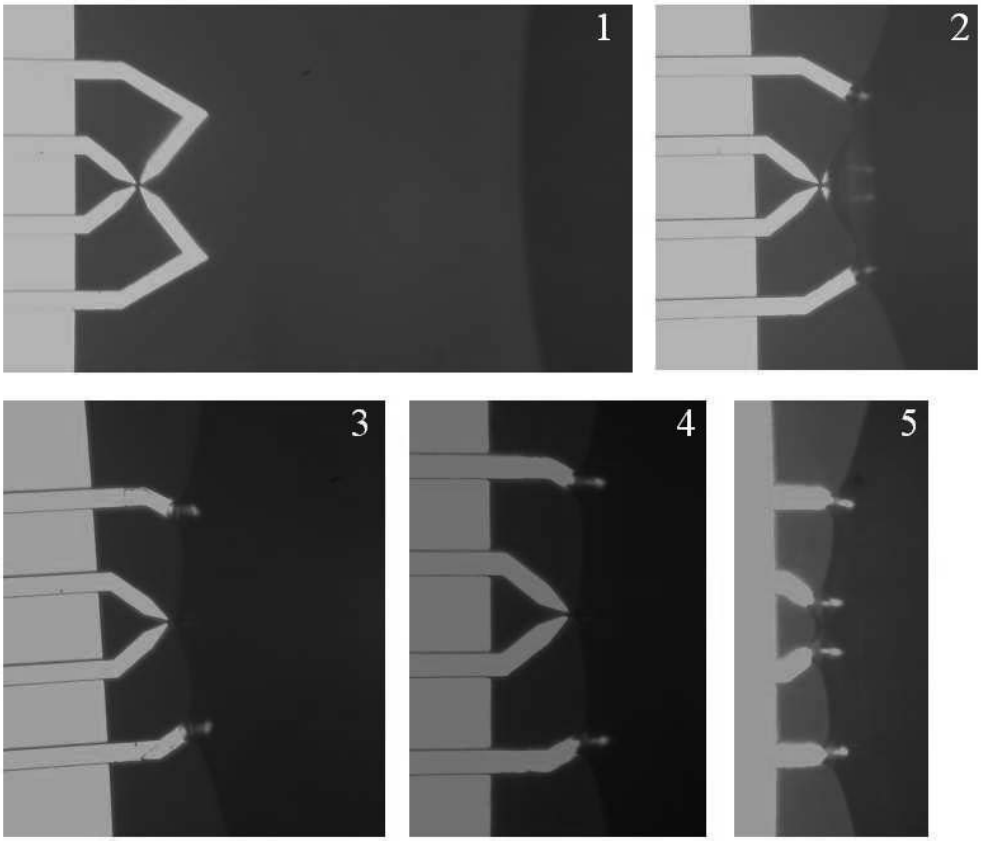

Figure 4.19: A series of images showing how it is possible to control the wetting of the probe using the horizontal setup and the inlined cantilevers. In 3 only the outer electrodes are in the droplet, in 4 the solution is just beginning to wet the inner two electrodes and in 5 both sets are inside the droplet.

4.4.3 Planar probe setup

The procedure used for the planar structures is much more simple and gives more reproducible results (Figure 4.20). The chip is placed in the chip holder and connected to the electrical circuit. A small droplet of the solution, usually between 2 and 10 μl is placed on top of the probe and the voltage is turned on. After a certain amount of time the voltage is turned off and the droplet is gently blown of the chip with a nitrogen stream.

Though there still exists an air/liquid interface, which could be the source of error, this interface is at least 0.5 mm away from each one of the assembly areas in the xy plane and more than 1.5 mm in the z direction. Since the DEP forces cannot be expected to be significant at a distance more than 100 μm away from the electrodes (see Figure 3.23), the forces at the interface and the nanotubes exposed to them probably do not affect the assembly process, but could be responsible for a continuous supply of nanotubes close to the assembly areas where DEP is strong.

However, this method has its disadvantages. As a stream of nitrogen is used for removing the solution from the probe surface the assembled networks are often carried away by the retreating solution and although they remain connected

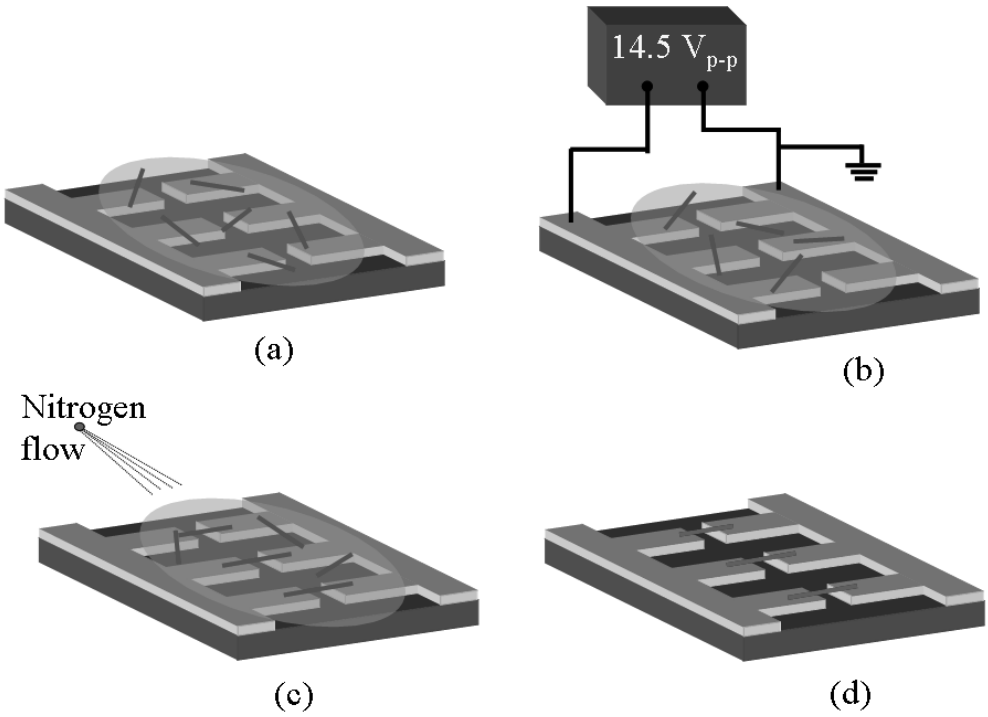

Figure 4.20: The experimental setup and method. **(a)** A droplet of solution containing carbon nanotubes is placed on the chip. **(b)** The voltage is applied on the electrodes. **(c)** Some of the nanotubes have assembled between the electrodes. The voltage is turned off and a stream of nitrogen is used in order to blow the remaining solution off the chip. **(d)** The chip is now free of solution containing assembled networks.

to the electrodes their alignment is destroyed. It was often observed that the nanotubes assembled on one side of the electrodes rather on both sides as would be expected due to symmetry (see Figure 4.21). The preference towards one side of the electrodes can be explained by the nitrogen flow being targeted towards that direction.

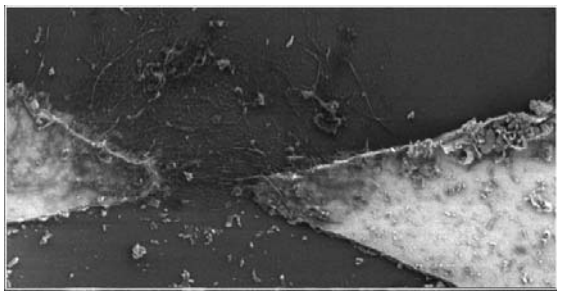

Figure 4.21: Though the electrodes are symmetrical, nanotubes are deposited mainly on the top part, the direction towards which the cleaning nitrogen stream is blown.

Finally, although not completely free of contamination, the method does protect electrode areas with no voltage applied on them. Several experiments were done on two-assembly-sites probes, where only one of the assembly sites was connected to an alternating voltage. In all cases nanotubes assembled only on the site where the field was turned on. We can therefore conclude that the field dominates the

nanotube motion near the electrodes and that this experimental method does not cause unwanted depositions.

4.5 Summary

The various solutions used during this project were presented and evaluated. The effect of ultrasonication time was demonstrated for two of the solutions and the effect of heating, SEM imaging and water rinsing for the most commonly used solution in this project was studied.

The various microstructures used in the project were presented along with the fabrication processes and an evaluation of the experimental setups developed was made.

Chapter 5

Parameter investigation

This chapter presents the assembly experiments performed on the test structures described in chapter 4. Single-walled nanotubes were used and the assemblies were examined both structurally, using a SEM operating at 2 kV, and electrically, by measurements of the resistance.

There are several parameters controlling the DEP assembly process:

- Nanotube solution
- Electrode geometry
- Frequency of applied electric field
- Voltage of applied electric field
- Nanotube dimensions
- Field application time

Though control of the dimensions of the nanotubes used in the experiments is not possible, the remaining parameters can be varied in order to determine the optimal conditions for dielectrophoresis. In each experiment only one of the parameters was varied while the rest were kept constant.

We also investigated the dependence of the resistance of the assembled nanotubes on the number of parallel electrodes on the assembly sites, since most of our structures contain multiple electrodes.

Furthermore the effects of heating at low temperatures and SEM imaging as well as the current carrying capacity of the assembled networks have been investigated.

5.1 Voltage dependence

These tests were carried out in two ways: 1) The structure of Figure 4.9(a) was used in order to evaluate the smallest field strength required for DEP. The

result was evaluated in a SEM. 2) The structure of Figure 4.9(g) was used with different voltages in order to evaluate the voltage required for DEP as well as the dependence of the resistance of the assembled networks on voltage.

5.1.1 Experiment 1: Field strength

A voltage of 10 V p-p amplitude and a frequency of 5 MHz was applied on four chips containing in total 25 active test sites. Two solutions were tested, the SDS solution (15 test sites) and the DCB solution (10 test sites). In both cases the voltage was turned on for 1.5 minutes, and after that the solution was blown off the chip with a stream of nitrogen. For each electrode spacing an order of magnitude estimate of the field strength can be made by using the equation $E = V/d$, where V is the applied voltage and d is the electrode spacing. The actual field strength will be higher than this estimate because of the sharp geometry of the electrodes.

Figure 5.1 shows the percentage of the test sites that still have visible nanotube connections for each field strength on the bottom x-axis and each electrode spacing on the top x-axis. It is seen that nanotubes dispersed in SDS are able to assemble on the electrodes even when the spacing is 10 μm, while the nanotubes dispersed in DCB assemble at distances up to 5 μm. If we define the threshold for DEP to be when 50% of the test sites have assembled nanotubes on them, then for this particular electrode shape the minimum field strength required for DEP is 1.11 MV/m and 1.54 MV/m (maximum electrode spacing of 9.1 μm and 6.7 μm) for SDS and DCB solutions respectively, when the applied voltage is 10 V p-p and the frequency is 5 MHz. This is illustrated in Figure 5.1. This difference could be attributed to nanotube bundle size differences between the SDS and the DCB solutions and/or differences in the viscosity and dielectric properties of the solutions.

Some images of the assembled networks are shown in Figure 5.2. Distinct differences can be seen in the way that SDS dispersed nanotubes and DCB dispersed nanotubes are assembling. While the SDS dispersed nanotube bundles deposit in a dense matrix in the majority of the experiments conducted, the DCB dispersed nanotube bundles deposit at more or less regular intervals across the length of the electrodes. This has been observed also in [43] for MWCNT deposition, where the authors attribute the effect to flow patterns developing due to the distortion of the electric field by the already deposited MWCNTs.

5.1.2 Experiment 2: Applied Voltage - Network Resistance relation

This investigation was performed twice and only on the SDS solutions. The first time the experiment consisted of 6 measurements at 6 different voltages, using a frequency of 10 MHz and an application time of 5 seconds. The second time the experiment consisted of 28 measurements at 7 different voltages, using a frequency of 10 MHz and an application time of 15 seconds.

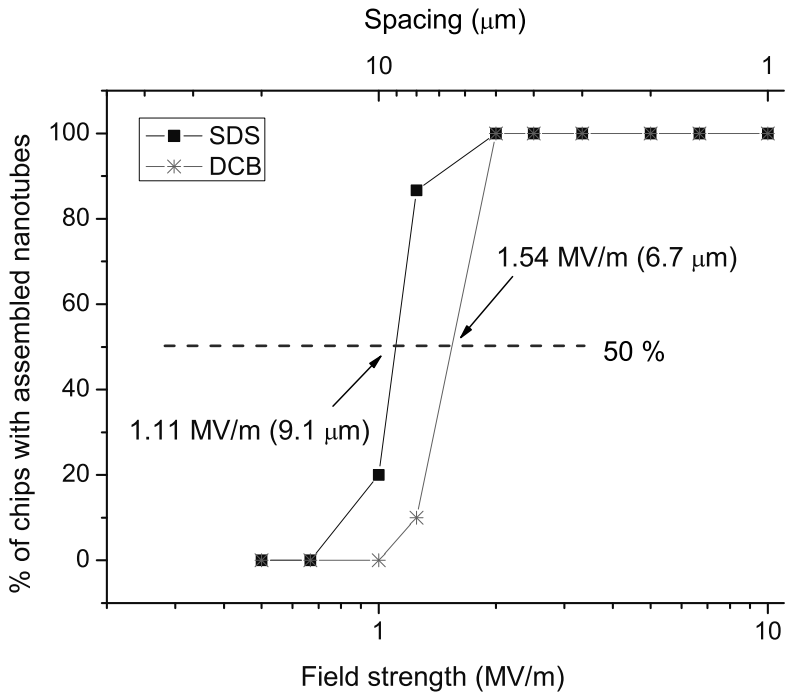

Figure 5.1: The percentage of chips that have assembled nanotubes between electrodes of a certain spacing for an SDS and a DCB solution of SWCNTs.

The result of the first experiment is shown in Figure 5.3 with the open circle markers. There is a tendency that the resistance of the assemblies generally decreases with increasing voltage up to about 10 Volts, at which point it increases again. We repeated this experiment using at least 4 measurements per voltage. The result of this experiment is plotted in Figure 5.3 (filled circle markers). It is clearly seen that the tendency of the first experiment is reproduced. Moreover, the values for the resistance are consistent in the two experiments despite the difference in field application time. From Figure 5.3 we can see that for voltages smaller than 5 Volts the resistance is rapidly increasing.

We define a successful assembly as one for which there is a measurable resistance in the kΩ range (<600 kΩ) for the networks. When the percentage of successful assemblies amongst all the measurements is plotted against the voltage we get the graph of Figure 5.4. The experimental points are fitted to an asymptotic model approaching 100% yield for voltages greater than 10 Volts. At voltages lower than 5 Volts the yield of the assemblies is drastically reduced. Moreover, the voltage at which the yield is 50% is 3.5 Volts. Therefore, for this particular electrode geometry and field application time and for a frequency of 10 MHz the threshold voltage for DEP is 3.5 Volts. Since the electrode spacing for these structures was 1 μm, the threshold field is 3.5 MV/m.

Comparing with the results of section 5.1.1 this threshold field strength is higher, but on the other hand the electrodes used in the experiment of section 5.1.1 are

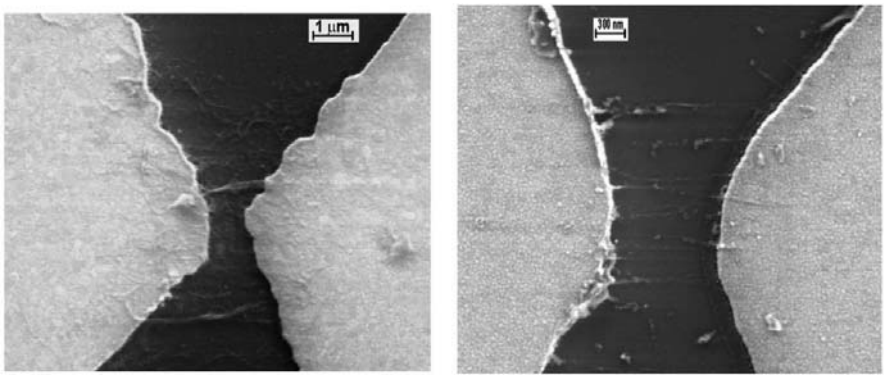

Figure 5.2: A typical assembled network from SDS dispersed nanotubes is shown on the left. The nanotubes are densely packed between the electrodes, in contrast to the sparse DCB dispersed nanotubes assembled on the electrodes to the right.

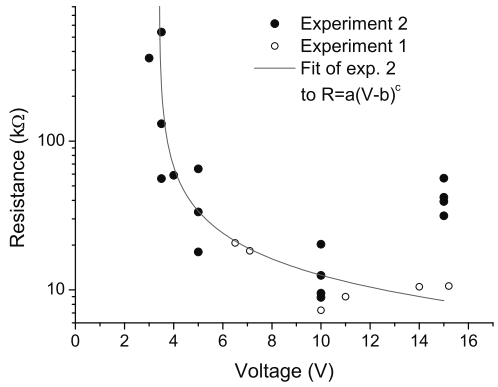

Figure 5.3: The resistance of the nanotube networks as a function of the voltage across the electrode gap for the two experiments conducted with an SDS solution.

much sharper, giving a higher electric field gradient close to the gap and thus a greater attractive DEP force. Moreover, the field application time is much smaller, meaning that fewer nanotubes would be able to reach the electrodes. Based on the various calculations presented in chapter 3.2 the frequency difference between the two experiments should not greatly affect the dielectrophoretic force.

In chapter 3 simulations on a system similar to this one were presented for various values of the frequency dependent factor K_f. The dielectrophoretic force is proportional to K_f and also proportional to the square of the voltage. When K_f changes from 1 to 100 the force changes the same as if K_f was 1 and the voltage had changed from 1 to 10 V. We can therefore use these simulations to find a relationship between the number of nanotubes caught and the voltage. It can easily be calculated that the number of nanotubes caught is proportional to $V^{0.7}$.

The resistance of the nanotube networks is a measure of how many nanotubes are assembled between the electrodes but also of the contact properties. If the contact resistances are negligible we would expect that the resistance is inversely proportional to the number of nanotubes assembled. This would mean that the

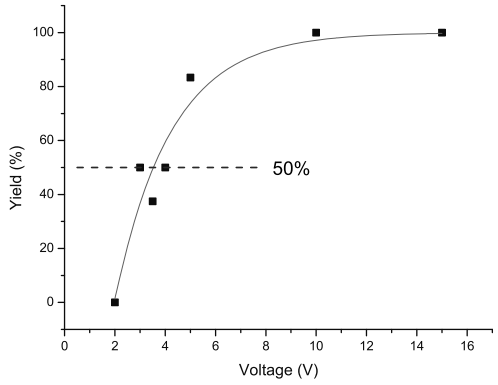

Figure 5.4: The percentage of successful assemblies for each voltage. The data has been fitted with an asymptotic curve and shows that for a success percentage of 50% a voltage of at least 3.5 V p-p needs to be applied.

resistance measured should be inversely proportional to $V^{0.7}$. If we disregard the data points recorded for DEP voltages over 10 V and try to fit the results using the relation $R = a(V - b)^c$, where $c = -0.7$, the fit is good when $b = 3.4$ for experiment 2. The value of a is of the order of 50. The fitted curve is also shown in Figure 5.3. It should be noted that good fits to the data are also observed for values of c ranging between -0.5 and -0.9.

The increase in the assembled network resistance for voltages over 15 V p-p cannot be explained easily. A possible explanation could be that the application of such a high voltage over a gap of 1 μm damages the electrodes and thus increases the contact resistance of the system. Another possible reason is that the nanotubes in the network that obtain a small contact resistance carry more of the current and are therefore damaged.

5.2 Assembly Time Dependence

Five series were done in order to investigate the dependency on assembly time, for different geometries (Figures 4.9(h) and 4.9(g)), solutions (SDS, SDS+Chloroform and DCB) and frequencies (5 MHz and 10 MHz):

- Using the structures of Figure 4.9(h) with an SDS solution at 10 MHz and 15 V p-p (Exp 1a)
- Using the structures of Figure 4.9(h) with an SDS with Chloroform solution at 10 MHz and 15 V p-p
- Using the structures of Figure 4.9(g) with a DCB solution at 10 MHz and 15 V p-p
- Using the structures of Figure 4.9(g) with a DCB solution at 5 MHz and 15 V p-p

- Using the structures of Figure 4.9(g) with an SDS solution at 10 MHz and 15 V p-p (Exp 1b).

Figure 5.5 shows the resistance as a function of time for the above experiments.

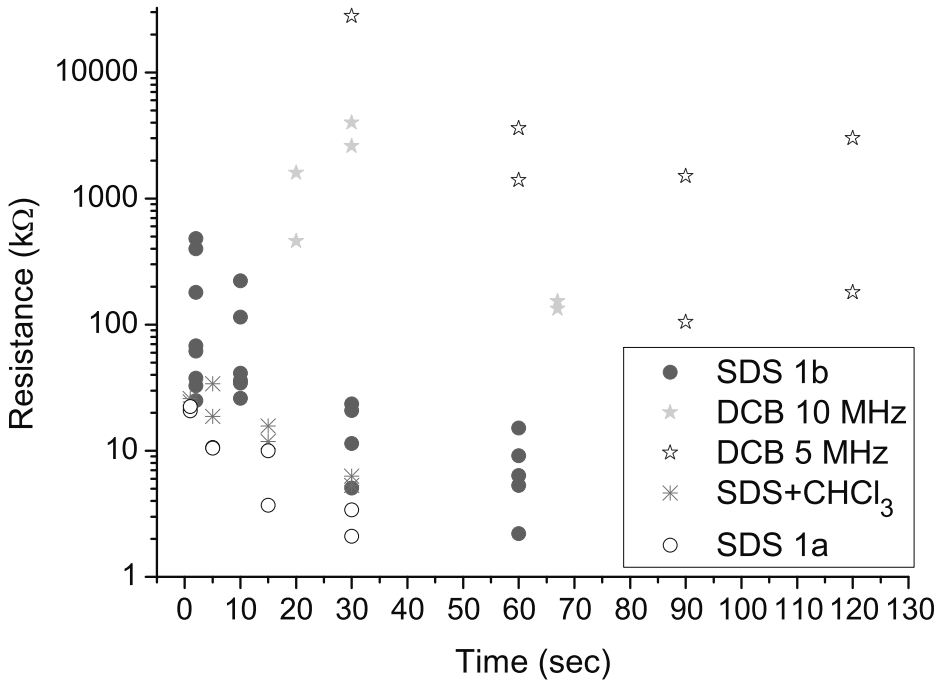

Figure 5.5: The resistance of the assembled nanotube networks as a function of the application time of a voltage of 15 V p-p across the electrodes.

There is a distinct difference in the resistance of the networks in the two SDS experiments. This can be attributed to the differences in the electrode geometry. Experiment 1a was done with sharper electrodes than those used in experiment 1b, so that the field strength was larger for experiment 1a. Therefore more nanotubes assemble between these electrodes for the same field application time, so that the resistance measured is lower. The results of experiment 1b show that the resistance of the assemblies is quite unpredictable for times smaller than 15 seconds but on average has a tendency to increase as the field application time decreases. Experiment 1a shows no instabilities in the resistance and the same tendency of an increasing resistance with decreasing field application time.

Similar to the SDS experiments, the nanotubes dispersed in the SDS/Chloroform mixture also show the tendency of a larger resistance for smaller field application times. Moreover, by comparing these results with those of experiment 1a, it is seen that the resistances recorded for this SDS/Chloroform solution are consistently higher than the resistances for the pure SDS solution. Since all other parameters are the same a possible explanation for this is that by adding chloroform (which with its 3 chlorium atoms forms a strong dipole) in the SDS solution and ultrasonicating it, the size of the nanotube bundles can further be reduced, so

that more force is required to move them to the electrodes, or equivalently, more time is needed in order to achieve the same resistance.

Characteristic for experiments done with DCB solutions of carbon nanotubes is the large value of the resistance of the assembled networks, mostly in the MΩ range. A tendency of decreasing resistance with increasing time of field application is also apparent.

The resistance of DCB dispersed nanotubes could be large for a number of reasons. The SEM images of these assembled networks generally show very few bundles deposited across the electrodes, as opposed to the assemblies from the SDS solutions. So, the measured resistance should be larger for these assemblies compared to those coming from SDS solutions. Another explanation could be that a monolayer of DCB is separating the nanotubes from the supporting contacts. The current would then need to tunnel through that layer from the electrode to the nanotube, i.e. the resistance measured would be large.

5.3 Number of electrodes dependence

In many of the probes used in these experiments there often is a large number of electrodes addressed at the same time. To investigate how the presence of one or more electrodes on a chip affects the assembly, the structure of Figure 4.9(d) was used with an SDS solution. Twelve assembly experiments were conducted with an applied voltage of 15 V p-p, a frequency of 1 MHz and a field application time of 10 seconds. The results are shown in Figure 5.6. In order to compare the values of the resistance it is assumed that each electrode in a multi-electrode group has the same resistance, R_0. Consequently the measured resistance is $R_m = \frac{R_0}{N}$ or $R_0 = N \cdot R_m$, where N is the number of electrodes in a group. The value R_0 has been plotted in the figures.

Figure 5.6 shows a plot of the mean value and the standard error of the mean value ($SE = SD/\sqrt{n}$) of the resistance per electrode, R_0. Of the 36 measurements one single electrode sample exhibited much larger resistances than the average and was disregarded. Measurements were done right after each experiment, two hours after and 100 hours after.

Several interesting observations can be made from Figure 5.6. First, the resistance per electrode is not the same for every N at any point in time after the experiment. The resistance is clearly larger for decreasing values of N, with the exception of the data for $t = 0$. Moreover, both the resistance and the standard error of the mean seem to be increasing with time. This is further investigated in chapter 6. The 10-electrode structure is the most stable of the three investigated values of N.

For this analysis we have assumed that all the N electrode pairs are equivalent, i.e. the resistance of the networks assembled between each pair is the same. That cannot expected to be the case, mainly due to the experimental method, something that has been verified by SEM observations. Having a large number

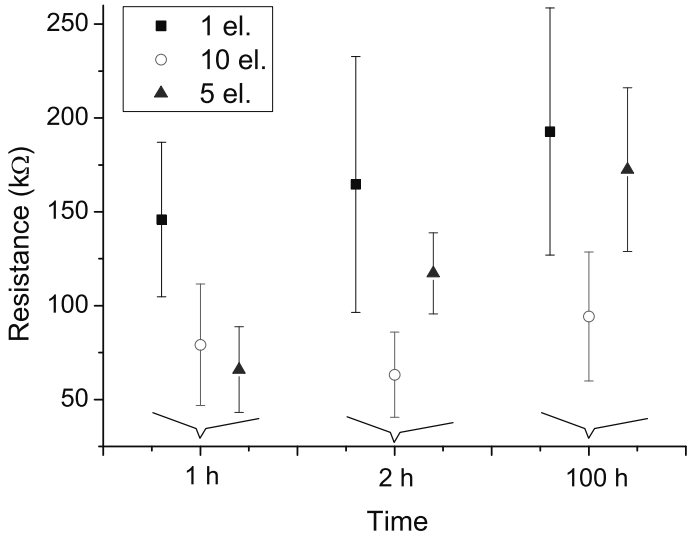

Figure 5.6: The resistance of the assembled nanotube networks from an SDS solution for chips containing different numbers of electrodes addressed at the same time.

of parallel electrode pairs implies that the pairs with small contact resistances dominated over the pairs with high contact resistance.

5.4 Frequency dependence

Perhaps the most interesting parameter to investigate is the frequency. From the simulations we see that the dielectrophoretic force is ultimately connected to the choice of model parameters. Since the resistance measured after an experiment is to a certain degree related to the dielectrophoretic force, measurements of the resistance as a function of frequency could give an idea of how the factor Kf is dependent on the frequency, thus allowing the determination of the dielectric properties of the nanotubes.

For these experiments 20 identical structures of the type shown in Figure 4.9(b) were used, each containing 2 identical 14-electrode assembly sites. Four different frequencies were investigated: 10 kHz, 100 kHz, 1 MHz and 10 MHz. For these frequencies, depending on the conductivity of the nanotube used, the models predict either no change in the dielectrophoretic force or a small decrease in the force for the 10 MHz frequency (see Figures 3.7 and 3.14), which could result in an increase of the measured resistance.

For each of the four investigated frequencies 10 measurements were made. The voltage amplitude was 14.5 V p-p and the field application time was 2 minutes, which according to Figure 5.5 should be sufficient to ensure a high yield of low resistance networks. Of the 40 samples, 2 samples assembled at 1 MHz and one sample assembled at 100 kHz were not successful.

Table 5.1: The various samples and the treatment they were exposed to after assembly

Treatment	10 kHz	100 kHz	1 MHz	10 MHz
R.T.	B8F12	A6F12	A11F12	B3F12
R.T.+ SEM	B8F34	A6F34	A11F34	B3F34
50	A2F12	A7F12	A12F12	B4F12
50	A2F34	A7F34	A12F34	B4F34
50	A3F12	A8F12	A13F12	B5F12
50	A3F34	A8F34	A13F34	B5F34
80	A4F12	A9F12	B1F12	B5F12
80	A4F34	A9F34	B1F34	B5F34
80	A5F12	A10F12	B2F12	B6F12
80	A5F34	A10F34	B2F34	B6F34

5.4.1 Overview of measurements

The resistance of the 37 networks was measured on 6 instances:

- 1: Immediately after the assembly experiment ($t = 0$)
- 2: 1.5 hours after the experiment ($t = 90$ min). At this point 29 of the samples were placed in a low temperature oven for 1 hour.
- 3: 3.5 hours after the assembly experiment ($t = 210$ min)
- 4: 20.5 hours minutes after the assembly experiment ($t = 1230$ min). At this point samples not previously heated were taken to a SEM for imaging.
- 5: 24.5 hours after the experiment ($t = 1470$ min) and right after the samples were taken out of the SEM.
- 6: 3 days after the assembly experiment ($t = 4320$ min).

The results of this investigation are shown in Figure 5.7 for each sample at each frequency. These graphs are explained further in this section. Table 5.1 shows the names of the samples, the frequencies they were assembled with and the treatment they were subjected to after assembly.

5.4.2 Resistance monitoring

Monitoring of the resistance was done in two ways over a 90 minute interval: 1) Two single measurements were taken at the beginning and end of the interval and 2) The resistance was monitored continuously during the 90 minute interval.

A plot of the frequency distribution of the resistance at $t = 0$ and $t = 90$ minutes is shown in Figure 5.8. The Figure shows that as the frequency increases the

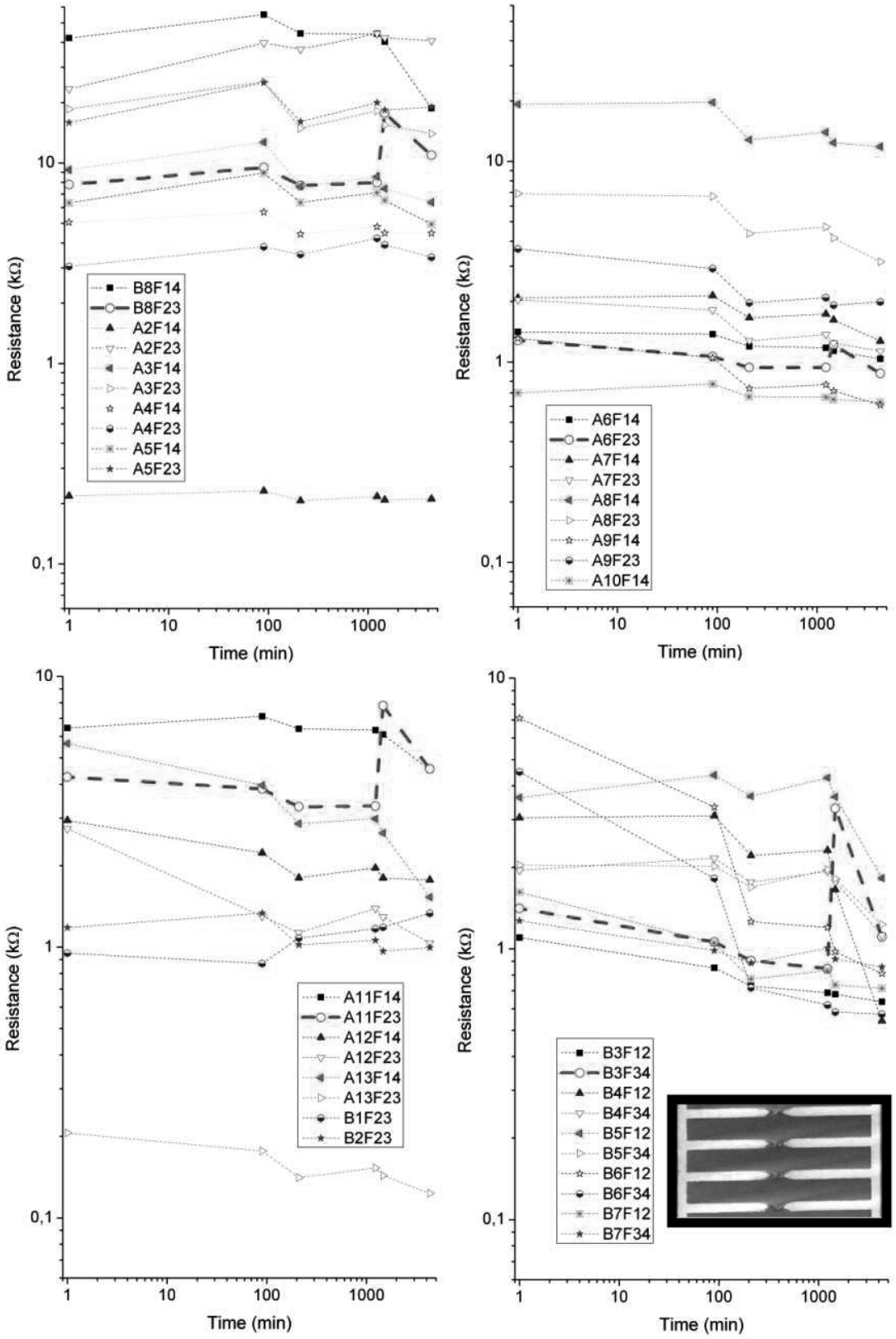

Figure 5.7: Measurements of the resistance of the assembled networks in a period of 24 hours, where the samples were exposed to different treatments. The dashed lines are for samples imaged in the SEM.

resistance of the assembled networks is decreasing. Moreover, the resistance is less spread at the higher frequencies. The figure also shows that with the exception of the 10 kHz samples, the mean value of the resistance for each frequency decreases in the 90 minutes between the measurements. This is expected as any water left on the samples after the assembly will be evaporating during this time, thus improving the contact resistance (in [66] the resistance of networks increases with increasing water content in the environment). The increase in the resistance mean value for the 10 kHz samples is observed for all samples of this frequency and can therefore not be explained by a statistical error. It is possible that the nature of the assemblies for this frequency prevents water evaporation or worsens the contacts.

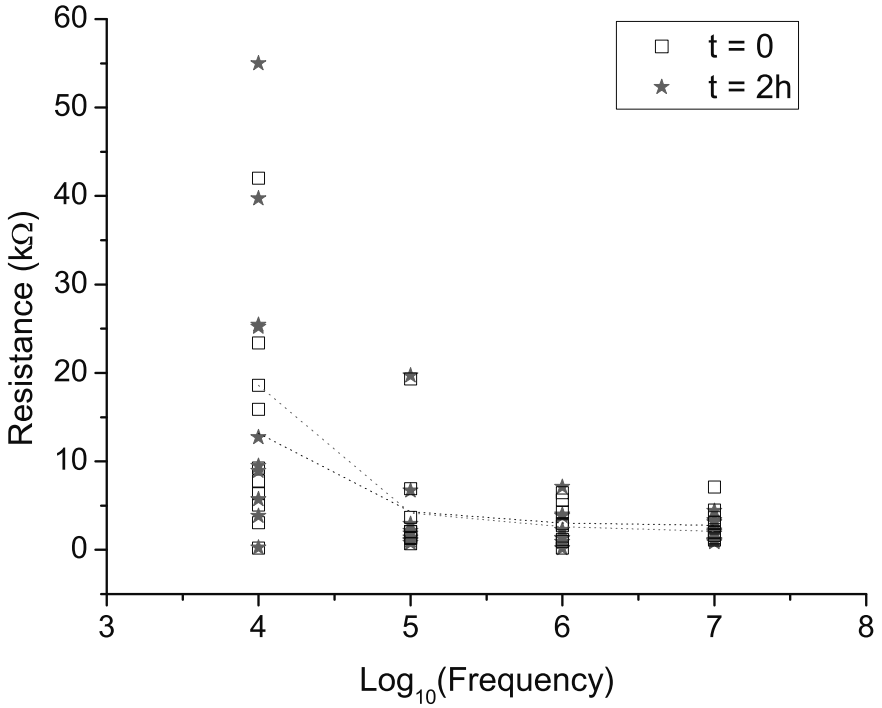

Figure 5.8: The resistance of the assembled networks as a function of the assembly frequency measured immediately after and 2 hours after the experiment.

It is also interesting to note that the mean values of the resistance can almost be fitted perfectly by curves following roughly a $\frac{1}{f}$ relation.

The second set of measurements was done using a Keithley 2400 sourcemeter driven by a Labview program in order to perform a current sweep and measure the voltage across the network. The program would then do a linear fit of the data and plot the resistance of the network real-time as well as each IV curve. The error of the fit was returned also, so that data points obtained when the divergence from the linear fit was large ($> 10^{-8}$) were not taken into account. By using a small current for the sweep (typically $0.1 - 1$ μA) such errors were never present. Constant monitoring of the resistance allows the characterisation of the

short term stability of the networks.

Figure 5.9(a) shows some typical curves measured during this experiment. The resistance of all samples decreased and the curves fit well with double exponential decay curves with a short first time constant and a much longer second one. To make certain that the measurement itself was not causing this behaviour, we stopped the measurement on the 10 kHz R.T. sample, as shown in Figure 5.9(a), and restarted it after an hour. As can be seen in the figure, the curve continued the exponential decay, where it would be expected if the measurement had continued.

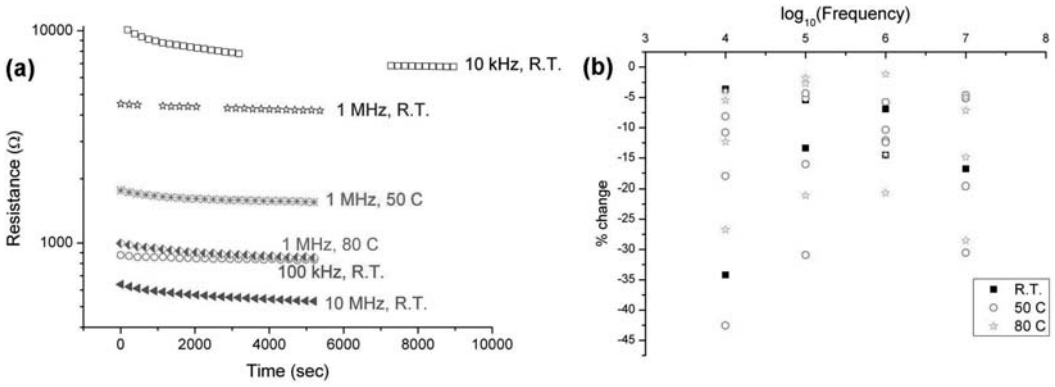

Figure 5.9: (a) Resistance as a function of time for some of the samples. The curves compare the room temperature samples for all frequencies and the heated samples to the room temperature ones for 1 MHz.**(b)** The relative change in the resistance value within about 1.7 hours under constant measurements for all the samples.

The relative change of the resistance during the monitoring for all samples has been plotted in figure 5.9(b). The resistance changes by 1-43% and it seems like the decrease becomes smaller for increasing frequencies from 10 kHz to 1 MHz. A slight increase for the 10 MHz samples compared to the 1 MHz samples is also observed. There is no apparent dependence of the resistance change on the previous heat treatment (described in section 5.4.3).

5.4.3 Low temperature heating

Figure 5.10 shows how the resistance was affected during the low temperature heating. The figure plots the percent change of the resistance as a function of frequency for the 3 different heating treatments. Of the 10 samples assembled at each frequency: 1) 2 were left at room temperature 2) 4 were heated to $50\,^oC$ for 1 hour and 3) 4 were heated to $80\,^oC$ for 1 hour.

Although the results are quite different from sample to sample, some observations can be made. With a single exception, all samples, regardless temperature treatment and assembly frequency, exhibit a decreased resistance right after the oven treatment (step 2 to step 3). Samples left at room temperature have reduced their resistance on average by 15%. No clear difference between the two heating temperatures can be seen.

After the samples were taken out of the oven and before the SEM imaging (step 3

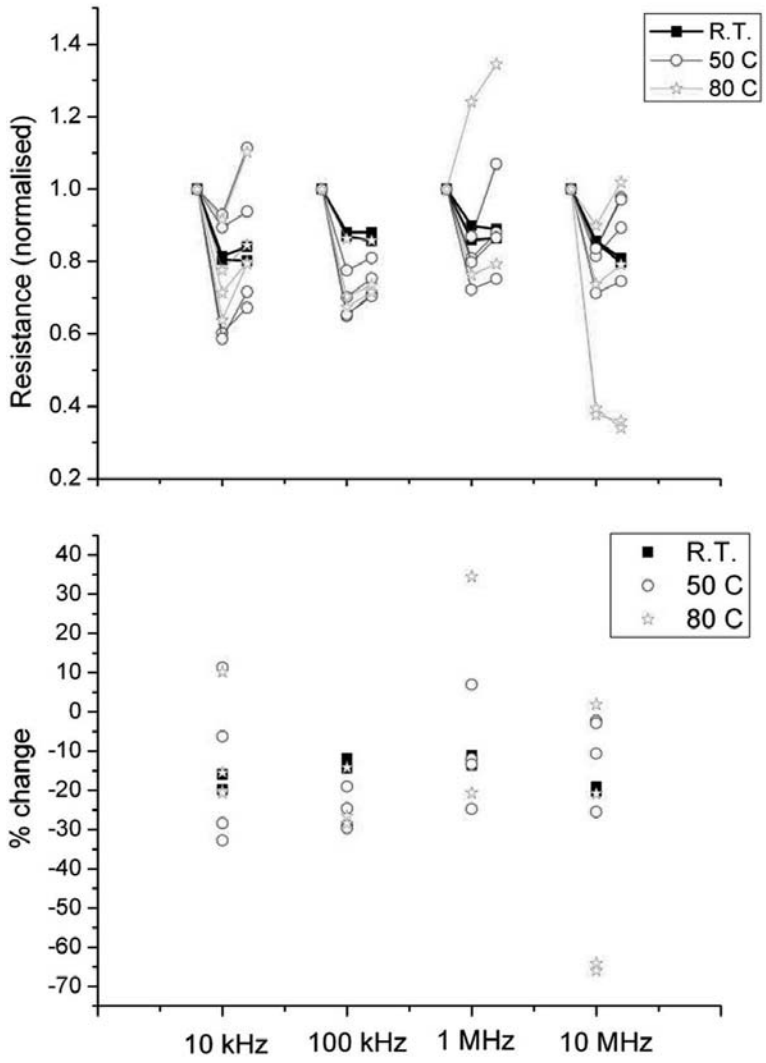

Figure 5.10: The relative change in the resistance values between steps 2 and 4. On the top graph the time series of the resistance between steps 2 and 4 can be seen for all samples and all frequencies.

to step 4) the behaviour is again changing. Now the resistance of most samples is increasing again. The few samples whose resistance decreases further are in fact 75% of those that were left at room temperature in the previous step, though a few of the probes previously heated ($\sim 10\%$) also reduced their resistance. There seems to be a slight tendency that the higher the frequency the smaller the increase in the resistance. Samples previously heated have changed their resistance the most in this step.

The bottom graph in Figure 5.10 shows the relative change of all samples in this time interval of about 20 hours, while the top graph shows the normalised resistance of all samples for the three steps (2, 3 and 4). As the figure shows only 5 of the 37 samples ended up having a resistance higher than the one they had before the heating step. However, 29 out of the 31 samples that were heated exhibit an increase in their resistance after they are taken out of the oven. The samples that were not heated do not show this resistance increase at any time

during these steps.

5.4.4 SEM imaging

The electrical measurements show that there is a small difference between the resistance of networks assembled at different frequencies. Using the SEM some structural differences were also observed. Figure 5.11 shows representative images of networks assembled at the four investigated frequencies, 10 kHz - 10 MHz. The figure shows that the degree of nanotube alignment increases with frequency and becomes largest for the 1 MHz and 10 MHz assembled networks. Moreover, on the 10 kHz samples, and to a smaller degree also in the 100 kHz, large disordered deposits of nanotubes and other material, perhaps carbon soot, are seen. These largely disappear as the frequency increases. A simulation of the field is also shown in the Figure in order to confirm that the nanotubes are indeed aligned with the field lines for the frequency of 10 MHz.

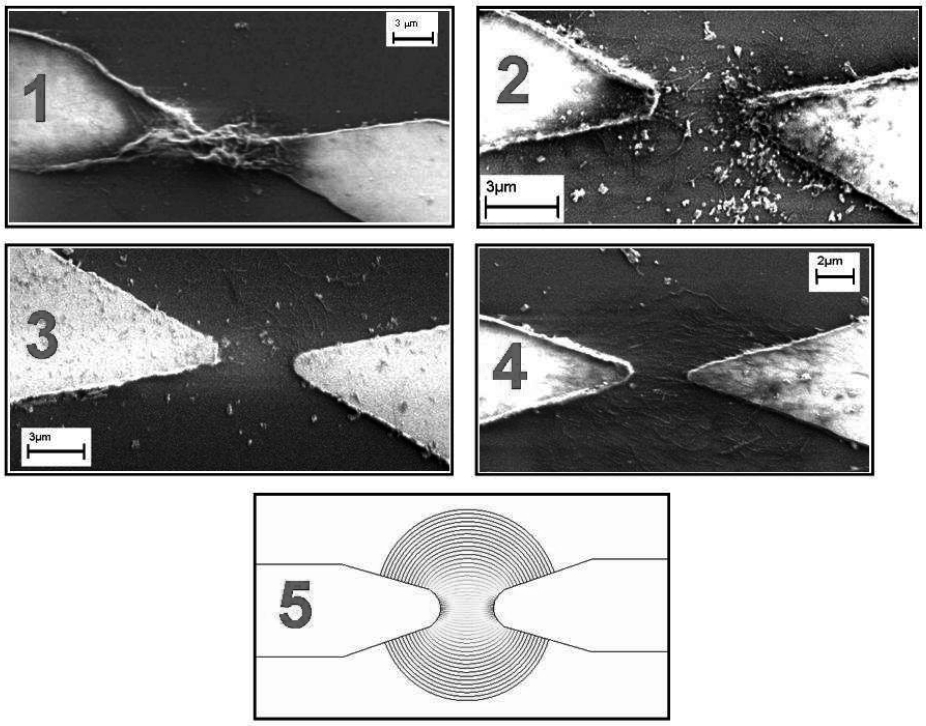

Figure 5.11: **(1)** Close-up of an assembly at 10 kHz. **(2)** Close-up of an assembly site at 100 kHz. **(3)** Close-up of an assembled gap at 1 MHz. **(4)** Close-up of an assembled gap at 10 MHz. **(5)** The simulated electric field showing the expected electric field lines for electrodes of this geometry.

In order to investigate how much the SEM affects the networks, only those probes that hadn't previously been heated were placed into the SEM and only one of the two samples on each probe were imaged. Figure 5.12 shows the relative change of the sample resistance during the course of the SEM imaging and up to step 6. Those samples that were imaged with the SEM clearly exhibit an increase in their resistance during the SEM imaging, while those that were in the SEM but

not imaged behave the same as those samples left at room temperature. The resistance rise generally increases with assembly frequency, but since the data come from only one sample, the only statistically valid observation is that the resistance increases when the samples are imaged with the SEM. The Figure also shows that amongst the samples that were not placed in the SEM there seems to be a tendency that the higher the frequency the larger the resistance decrease.

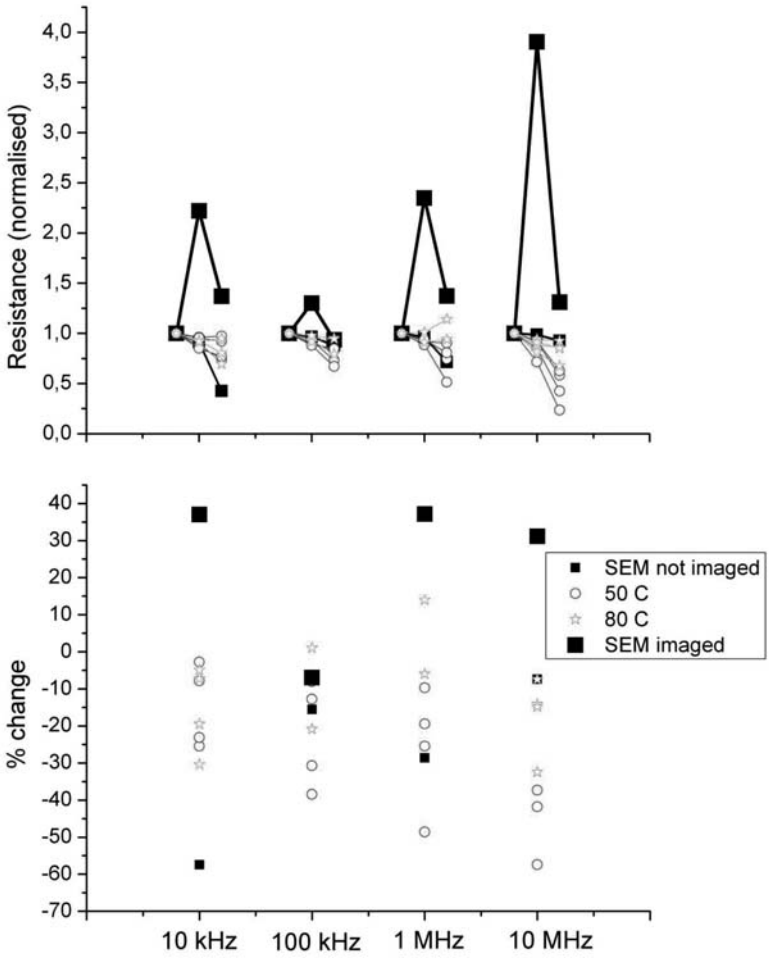

Figure 5.12: The change in the resistance values between steps 4 and 6. The top graph shows the time sequence for steps 4, 5 and 6. It is clear that samples left at room temperature or not imaged do not change their resistance. With a single exception, the samples that were imaged closely in the SEM have a resistance about 30-40 % higher than the one they had before the SEM imaging.

It has previously been shown [119] that SEM imaging at high magnification and even moderate voltages destroys the nanotubes. An explanation of the resistance increase could therefore be that some of the nanotubes in the network are destroyed. And indeed, with the exception of the 100 kHz sample, whose resistance had not been affected a lot by the SEM, after 3 days the imaged samples had reduced their resistance but not to the levels they were before the SEM imaging[1].

[1]The effect of SEM imaging was further investigated and the results can be found in Physica Status Solidi (a), volume 203, No. 6, p. 1088 (2006).

Table 5.2: The various samples and the parameters used for the DEP assembly.

Name	Frequency	Solution	Max. current (mA)
P1F14	5 MHz	original	3
P1F23	5 MHz	original	1.5
P2F14	5 MHz	diluted	2.6
P2F23	5 MHz	diluted	2
P3F14	500 kHz	diluted	1.7
P3F23	500 kHz	diluted	0.3
P4F14	1 MHz	original	3.5

However, it is also clear from Figure 5.12 that the samples that were imaged with the SEM were those whose resistance changed most compared to the average (large black squares) in the three days after the SEM imaging. The samples that were in the SEM but not imaged (small black squares on the top graph) generally displayed the average behaviour.

5.5 Current carrying properties

Whereas DEP appears to be a convenient method for fast integration of nanotube networks in nanosystems, the issue of reliability, and in particular the properties of the contacts, is important. Since networks involve multiple contacts between carbon nanotubes that are perhaps not bonded or fixed in any way other than by the van der Waals and capillary forces, it is important to investigate the current carrying properties of the networks, as well as the IV-characteristics.

Both multi-walled and single-walled carbon nanotubes were investigated. A Labview program was used in order to sweep the current between two values and measure the voltage across the network. After each IV curve was recorded the current would be set at a higher level and the process repeated until a jump in the IV curve was observed, indicating a structural change in the network, such as broken nanotube connections. The current would then be reduced and the process repeated again until all nanotube connections were broken.

The results for the multi-walled carbon nanotubes are presented in chapter 7.

A total of 7 networks were assembled on the structures shown in Figures 4.9(h) and 4.9(i) at various frequencies and subsequently destroyed in order to measure the current carrying capacity. An SDS solution of single-walled nanotubes was used. The solution had a concentration of about 35 μg/ml but was subsequently centrifuged at 20000G for 10 minutes. For two of the chips a 10 times diluted version of this solution was used. 8 μl of the solution were placed on top of the chips for 2 minutes and the voltage was turned on at 10 V p-p. Table 5.2 shows an overview of the chips used along with the DEP parameters and the maximum current they could carry.

As was the case for the multi-walled nanotubes, the largest current without any permanent network damage was of the order of 1.5 - 3.5 mA, with the exception of one network, which was destroyed already by a current of 300 μA. The particular network came from sample P3F23, assembled using a diluted solution. Figure 5.13 plots the maximum current able to flow through the network without destroying it as a function of the resistance of the networks at low bias at the beginning of the measurements. The figure shows that the larger the resistance of the network, the smaller the current needed to destroy it. The result is not surprising, as a high resistance usually indicates a bad contact, where large voltage drops are concentrated.

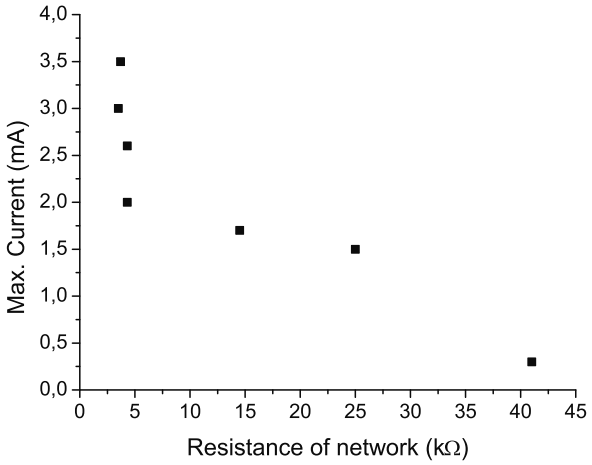

Figure 5.13: The maximum current able to flow through the network without destroying it as a function of the resistance of the networks at low bias at the beginning of the measurements.

Generally, the behaviour of all 7 samples was similar: By increasing the current step-wise the zero-bias resistance of the samples decreased until a permanent damage of the network was done. At this point the resistance increased and on several occasions measurements could continue but at lower currents.

In Figure 5.14 some of the IV curves recorded for two of the samples (probes p1f14 and p3f14) are shown. The legend also shows the order with which they were recorded. The curves are not linear but seem to experience a voltage saturation for large currents. This has previously been observed in similar experiments but at much lower temperatures. In [120] the authors attribute the non-linearity to the formation of barriers between the connection points of the nanotubes that participate in the grid as well as non-metallic segments of otherwise metallic tubes formed by defects. This explanation can be equally valid for the multi-walled nanotube networks presented in a following chapter, due to the presence of defects in these tubes.

Figure 5.15 plots the zero-bias resistance of all samples as a function of the maximum current used in the measurement, until the point, where a large increase in the resistance occurs, indicating a connection break. Two trends arise from this

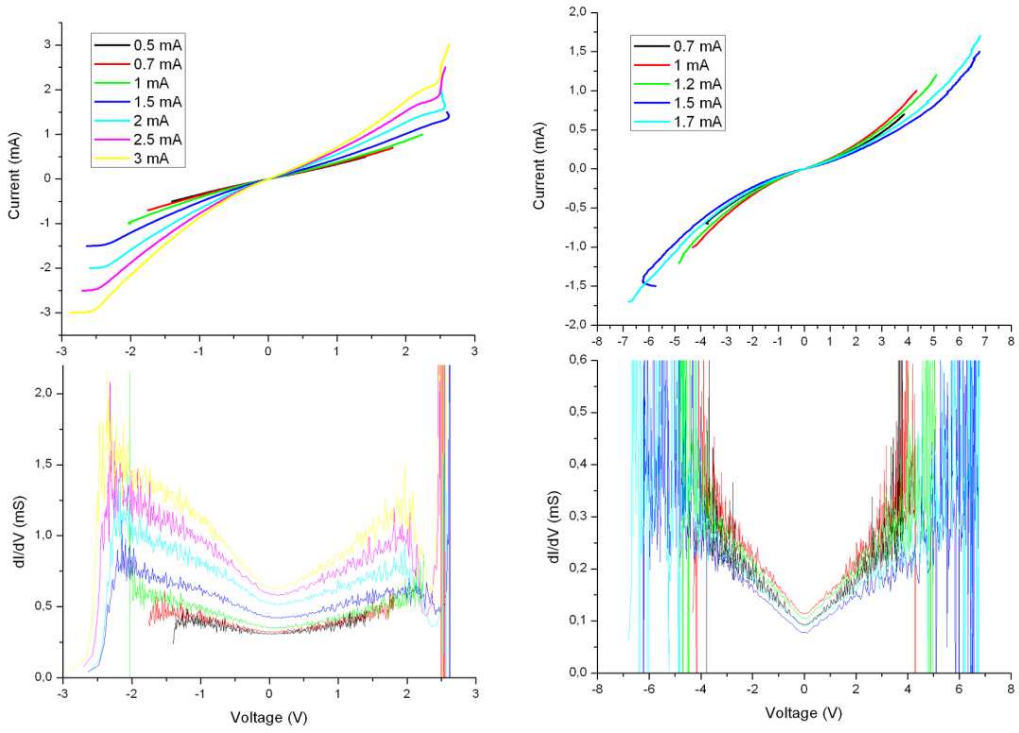

(a) P1F14 (b) P3F14

Figure 5.14: The current and differential conductance as a function of the voltage over the probe for probes P1F14 (a) and P3F14 (b).

figure: Either the resistance starts increasing slowly until the break occurs, like in samples P1F23, P3F14 and P4F14, or the break occurs suddenly, like in the remaining samples.

5.6 Discussion and summary

The dependence of the resistance of the assembled networks on the electrode geometry, the solution used, the number of electrodes addressed simultaneously, as well as the voltage amplitude, the field application time and frequency was investigated in this section. The results are in good agreement with theory, with the exception of the number of electrodes and frequency dependence, where interesting observations were made.

Some interesting phenomena were observed from the nanotubes during continuous monitoring of the resistance, namely that the resistance decreased with time as an exponential or a double exponential. This is in accordance with oxygen adsorption measurements on carbon nanotubes (e.g. in [121]). The two distinct time constants in the case of the double exponential decays could be explained by an "abnormal" diffusion process. The first part is characterised by an enhanced diffusion with a fast time constant. Enhanced diffusion is observed in porous layered systems [122] and our nanotube bundles can be regarded as porous

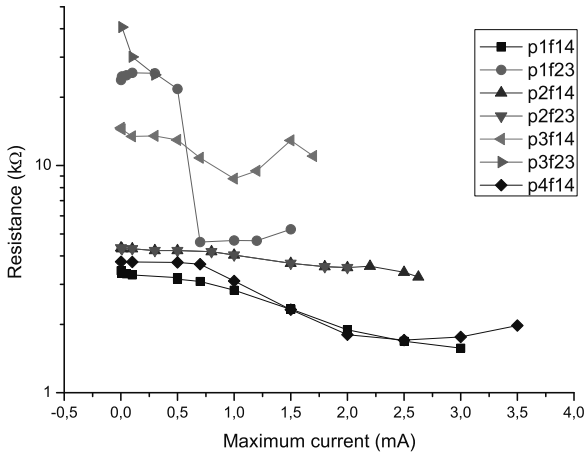

Figure 5.15: The zero bias resistance as a function of the maximum applied current through the network for all the examined SWCNT networks.

in several respects: between the tubes in the bundles, between the bundles themselves and between aggregates of bundles. The second slower diffusion has to do with the adsorption of the oxygen on nanotubes inside a bundle [123]. Whether or not that is the case for these samples is impossible to say. However, based on how SDS reacts to an electron beam, it is possible that the IV sweep starts a "chain reaction" of SDS micelle destruction, so that the nanotubes are exposed to atmospheric air and oxygen starts adsorbing on their surfaces, reducing the resistance. In that sense, the measurement itself **is** indeed the reason for this behaviour, however, the result (exposing the nanotubes to the environment) is an advantage, if these networks are to be used for sensor purposes.

It was also observed that the rate of resistance reduction with time was larger for samples previously imaged with a SEM. Based on the observations made when SDS solutions were imaged with the SEM, as described in section 4.1.2, as well as from [114], it is possible that the imaging of the nanotubes with the SEM destroys the micelles around the nanotube so that the nanotube surface is exposed to first the vacuum and then to air. The resistance increase could be a result of the desorption of oxygen from the newly exposed surfaces in the SEM vacuum chamber. After exposure to atmospheric air oxygen will start adsorbing on the SDS stripped nanotube surface much easier than on nanotubes that still have SDS on them. This could explain the higher relative change of the resistance for the SEM-imaged nanotube networks.

Also the current carrying capacity of carbon nanotube networks was tested. We found that the maximum current that a network can endure before a large change in the resistance, depends on the initial resistance of the sample and is generally in the mA range.

It was observed that the resistance was reduced after each measurement (see Figure 5.15). The resistance drop could be attributed to heating of the nanotube. During the measurements a power up to a few mW is dissipated in the network.

In [124] it was shown that an input power of 22 μW is enough to increase the temperature in the middle of a MWCNT by 40 K. Given that the network is a parallel collection of nanotubes, the power dissipation in each of them will be smaller, so the temperature increase for each nanotube could be smaller than 40 K. According to [124] for metallic single-walled carbon nanotubes the power dissipation is at the contacts at low bias and in the intermediate regions at high bias while for semiconducting SWCNTs the power dissipation is uniform along the length of the tube. Heating at the contacts could result in contact improvement and explain the resistance decrease.

The continuous resistance decrease with time as observed in section 5.4 could be another reason for the observed decrease in the zero bias resistance. For each chip the IV curves were taken during the course of 10-20 minutes. We showed that during IV measurements the resistance of the networks drops, possibly due to oxygen absorption on free from SDS nanotube surfaces. The same could be happening on these probes, however, as the decrease is also seen for multi-walled nanotubes that are dispersed in isopropanol, this alone cannot explain the resistance drop.

Generally, the experiments described in this section show that the assembled devices are unstable, with the resistance changing constantly even when the networks are left at room temperature. This indicates that the nanotube networks do indeed react to the environment humidity, oxygen concentration and temperature. This means that the nanotube networks could be used for sensing applications, if care is taken to isolate the nanotubes from the sources of this resistance drift. The dependence on these environmental parameters is further investigated in the following chapter.

Chapter 6

Response to environmental conditions

So far we have shown that dielectrophoretic assembly of nanotubes on micro-electrodes is possible and that the resistance of the assembled networks is quite unstable, possibly due to changes in their immediate environment in terms of temperature, humidity and oxygen concentration.

In this chapter the electrical response of the single-walled nanotube networks to changes in common environmental conditions such as temperature, humidity and light intensity, in a nitrogen and an air atmosphere has been investigated. This has been compared to the response of a single multi-walled nanotube that has been manually placed on electrodes and more reliably contacted, as well as with relevant literature.

6.1 Response to temperature

Literature shows that traditional sensors work better at high temperatures and that carbon nanotubes are extremely sensitive to oxygen concentration, since oxygen effectively acts like a dopant. We would therefore like to see how the assembled carbon nanotube networks behave at elevated temperature, where the oxygen concentration in their immediate environment could be changing due to desorption phenomena.

Six different samples were used to investigate the resistance of the networks as a function of temperature. Four of these were previously used for the frequency dependency experiments (see chapter 5), two for each of the frequencies 10 kHz and 10 MHz. The behaviour of these was investigated during heating in air and one of the samples was also tested in a nitrogen atmosphere. The fifth sample was assembled at a frequency of 10 MHz and a voltage amplitude of 14.5 V p-p on the structure of Figure 4.9(h). The behaviour of this sample was tested in air. Finally, the sixth sample had a single multi-walled nanotube on it contacted by a shadow-masking technique. The method and sample are illustrated in Figure 6.1. The response of this sample was measured in air.

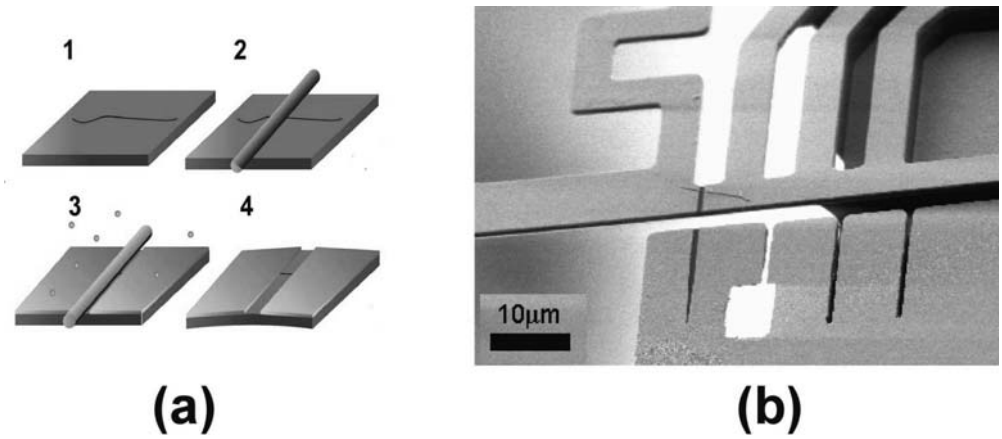

Figure 6.1: **(a)** The shadow masking technique: 1) A nanotube (CNT) is placed on a substrate. 2) A silicon nanowire (SN) is placed on top, dividing the CNT in two parts. 3) Metal (Au) is evaporated on the sample. 4) The SN is removed creating two electrodes. **(b)** The nanotube used in the comparison experiment, placed across the first slot on the cantilever.

6.1.1 Experiments in atmospheric air

For these experiments the setup of Figure 6.2 was used. A 10 Ω resistor was attached to a small aluminum box, where the sample was placed. By applying a voltage across the resistor, the box was heated to a temperature and at a rate depending on the applied voltage. An NTC resistor was used to measure the temperature inside the box close to the sample position. The NTC resistor was calibrated so that the resistor values correspond to a certain temperature. A Keithley 2400 Sourcemeter was used in order to monitor the resistance of the sample while the resistance of the NTC element was monitored with a Keithley 2000 Multimeter; both instruments were controlled by LabView. The program was also controlling a DC voltage generator for applying a voltage on the 10 Ω resistor.

The resistance of the samples was monitored continuously for the duration of the experiment. The voltage was turned on for 25 minutes each time, to allow the temperature inside the box to reach a steady state. Then the voltage was turned off and the box started cooling down to room temperature. That usually took 2-3 hours and it was at this time that the next experiment could begin. Therefore, due to these setup limitations, the rate of cooling and heating were not constant and the results could therefore also be depending on time.

Table 6.1 shows an overview of the samples used for reference.

The general response of a nanotube network to a change in temperature is shown in Figure 6.3.

The Figure shows that once the heating starts the resistance of the nanotubes starts decreasing until at some temperature it starts increasing again. When the cooling starts the resistance continues to increase but with a different rate until it reaches a maximum, which is higher than the starting point in all cases, at a

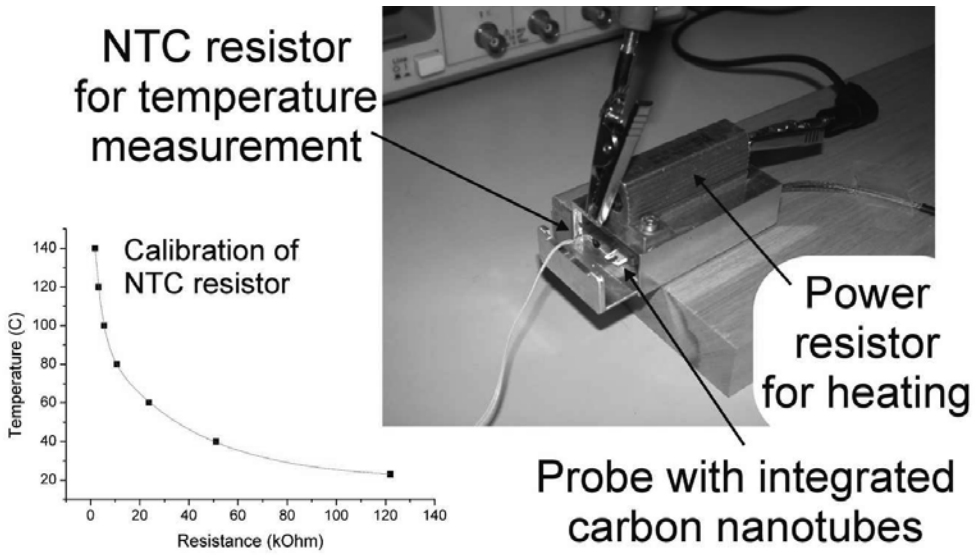

Figure 6.2: The oven setup used for the temperature response of the networks. The calibration of the thermal element is also shown.

Table 6.1: The probes used for the response during heating in air.

Name	Frequency	Type
B8	10 kHz	multi-electrode
A3m	10 kHz	multi-electrode
B3	10 MHz	multi-electrode
B5	10 MHz	multi-electrode
A3s	10 MHz	single-electrode
MW	shadow masking	single-electrode

temperature of $25 - 30\,^oC$. After that the resistance decreases with different rates depending on the sample.

We have heated the samples to 5 different temperatures starting from 38 degrees and up to 145 degrees. Due to the limitations of our setup the measured temperature is different from sample to sample, but the difference for all but one case is smaller than 4 degrees.

For most samples 2 or 3 measurements per heating and cooling cycle to a certain temperature were taken, with the exception of probes A3s and MW, where only 1 measurement per cycle was taken. Finally due to setup problems, usually only 1 measurement per cycle up to the highest temperature of 145 degrees was taken. The problem was in the holder housing the ceramic chip, which was made of plastic with tungsten wires glued on it. At these high temperatures the glue was becoming soft and the wires were able to move thus losing the contact to the ceramic chip.

Each sample was measured upon continuously for time periods ranging from 8 hours to 240 hours. This was necessary since every heating and cooling cycle alone

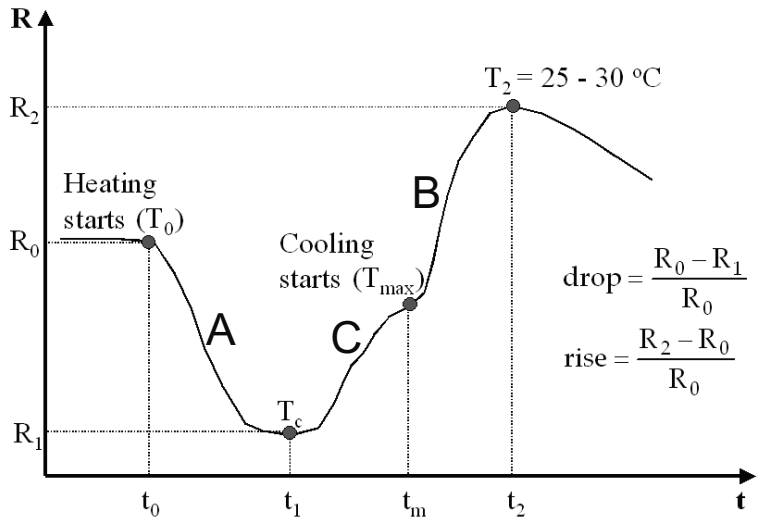

Figure 6.3: Schematic of the monitored behaviour of nanotube networks and the multi-walled carbon nanotube. The response curves are characterised by the drop ($\frac{(R_0-R_1)}{R_0}$) and the subsequent rise ($\frac{(R_2-R_0)}{R_0}$) compared to the initial level R_0.

needed about 2 hours to be completed. Figure 6.4 shows a typical measurement on a sample as it would appear on the LabView program screen at the end of the experiment.

In Figure 6.5 representative measurements from two single-walled network samples heated up to three different temperatures are presented and compared to each other as well as with the multi-walled carbon nanotube sample. Each column plots the normalised resistance, the temperature and the rate of resistance change as a function of time. In the following each of the graphs is presented in detail.

Figure 6.5(a) shows the response of 3 samples to heating up to 65 ^{o}C. For comparison purposes the resistance has been normalised to the initial value and the derivative is that of the normalised resistance. While the single-walled carbon nanotube networks were heated for 25 minutes the multi-walled nanotube was heated for 35 minutes, but the results are still comparable.

One first observation is the reproducibility of the temperature curve on the three samples. Moreover, one can note that the resistance of the single-walled carbon nanotube networks increases relatively more than the resistance of the multi-walled nanotube. This behaviour is generic for all multi-electrode samples.

The derivative curves plotted in Figure 6.5(a) have been filtered using an FFT low pass filter with a cut-off frequency of 0.005 Hz in order to remove the high frequency noise associated with the measurements. The scientific graphing and analysis software OriginPro 7.5 was used for the purpose. The plots show that for all samples the maximum resistance decrease rate (point A in Figure 6.3) is almost identical for all samples. The networks show this maximum at a temperature of 28.5 ^{o}C, after 138 seconds of heating, while the multi-walled nanotube shows the maximum at a temperature of 33 ^{o}C, after 224 seconds of heating. The maximum resistance increasing rate (point B in Figure 6.3) during the cooling cycle for the

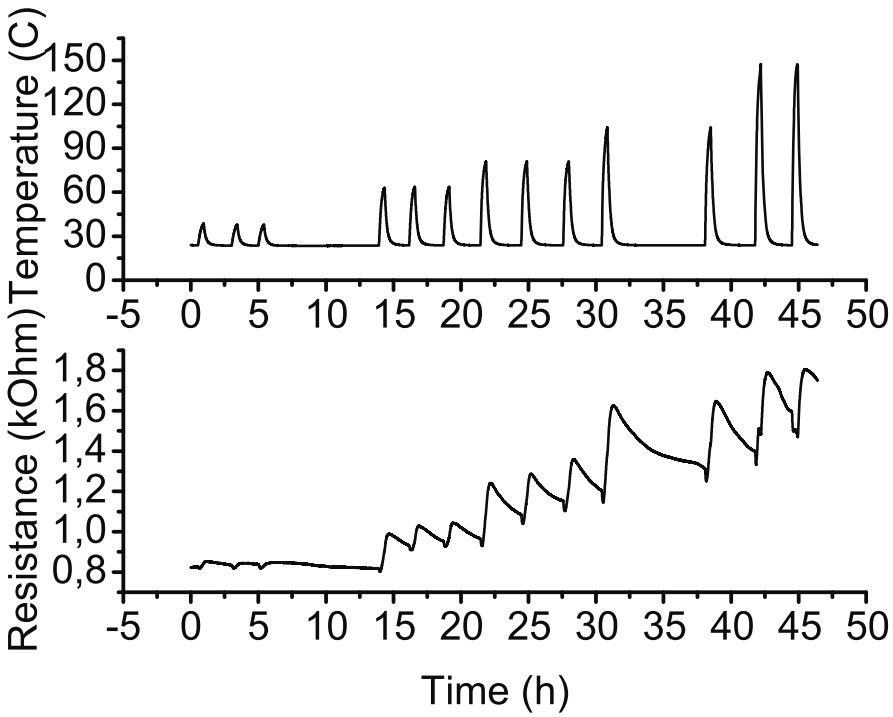

Figure 6.4: An entire experimental series as it would appear on the computer screen after the end of the experiment.

single-walled CNT networks occurs at a temperature of 52 ^{o}C and after 1714 seconds from the start.

In Figure 6.5(b) the same plots as in Figure 6.5(a) are shown but for heating to 104 ^{o}C. Characteristic for this high temperature heating is an obvious "kink" in the increasing resistance curve close to the cooling starting point (T_{max} in Figure 6.3). This is more evident in the derivative plot, where it appears as a double peak. Also, the change in the resistance is larger here.

The maximum decreasing rate (point A) is now not the same for all samples, however, it occurs at a temperature of 37 ^{o}C, after 134 seconds of heating, for the single-walled CNT networks and at a temperature of 50 ^{o}C, after 222 seconds of heating, for the multi-walled nanotube. We note that the times for the maximum decreasing rate occurrence are the same as for the low temperature heating.

During the cooling there is a maximum resistance increasing rate (point B - second positive maximum) as before. This occurs at a temperature of 80 ^{o}C, after 1734 seconds, for the single-walled CNT networks. This time is also the same as for the low temperature heating. The position of the first maximum (point C in Figure 6.3), which occurs during heating, is the same for both networks. Moreover, the local minimum in the derivative occurs exactly at the point where the heating resistance is turned off (point T_{max}), few seconds before the observed "kink" in the resistance-time plots.

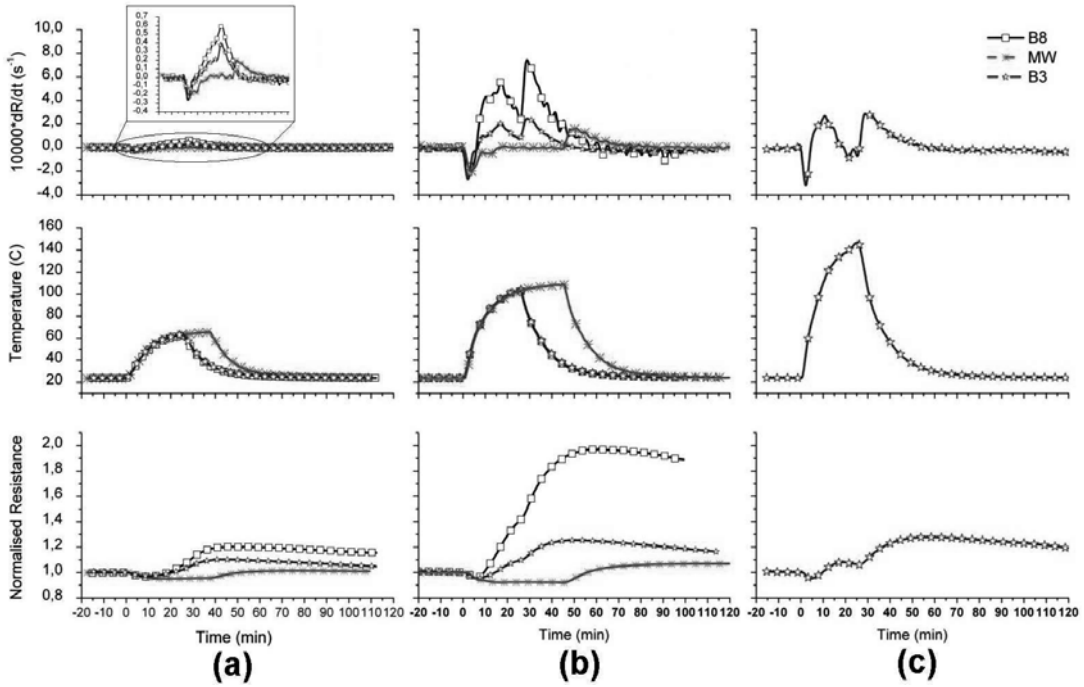

Figure 6.5: **(a)** The response of 3 different samples to heating up to 65 ^{o} C. **(b)** The response of 3 different samples to heating up to 104 ^{o} C. **(c)** The response of one sample to heating up to 147 ^{o} C

This double peak in the derivative can be even more pronounced at higher temperatures and even turn the increase in the resistance to a decrease, as it can be seen in Figure 6.5(c).

Figure 6.6 shows two consecutive measurements on sample B3, while heating it to 147 ^{o}C. In the first measurement the resistance behaves as expected but a bit before point T_{max} the resistance starts dropping again. In the second measurement the drop occurs much sooner, so that the first resistance increase rate maximum (point C) is actually very small. Although this was the only sample where the resistance started decreasing again, all samples showed a significant decrease in the increasing rate at this temperature, that is, the value of the local minimum between the two maxima was smaller for higher temperatures.

6.1.1.1 Comparison

Figure 6.7 shows the relative drop and increase of the resistance for all samples, calculated as shown in Figure 6.3, as a function of the temperature rise during heating. The figure shows that as far as the rise in resistance is concerned the differences between the various samples are very small at low temperatures but become very pronounced at high temperatures. One other interesting observation is that as far as the resistance rise is concerned, the multi-walled nanotube and the single-electrode network increase their resistance the least, with almost all values for the other samples lying over the line fitting the multi-walled nanotube data with an exponential curve ($R_{mwnt} = e^{0.02\Delta T}$, where ΔT is the temperature increase

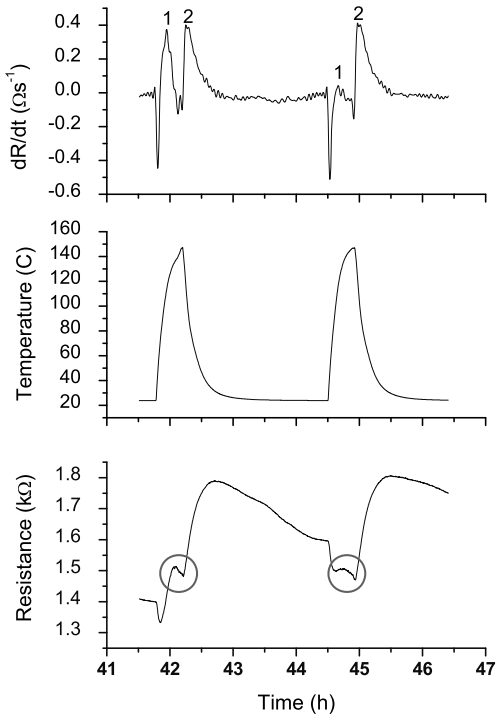

Figure 6.6: The response of sample B3 to heating up to 147 ^{o}C. The graphs plot the resistance, the temperature and the rate of resistance change as a function of time.

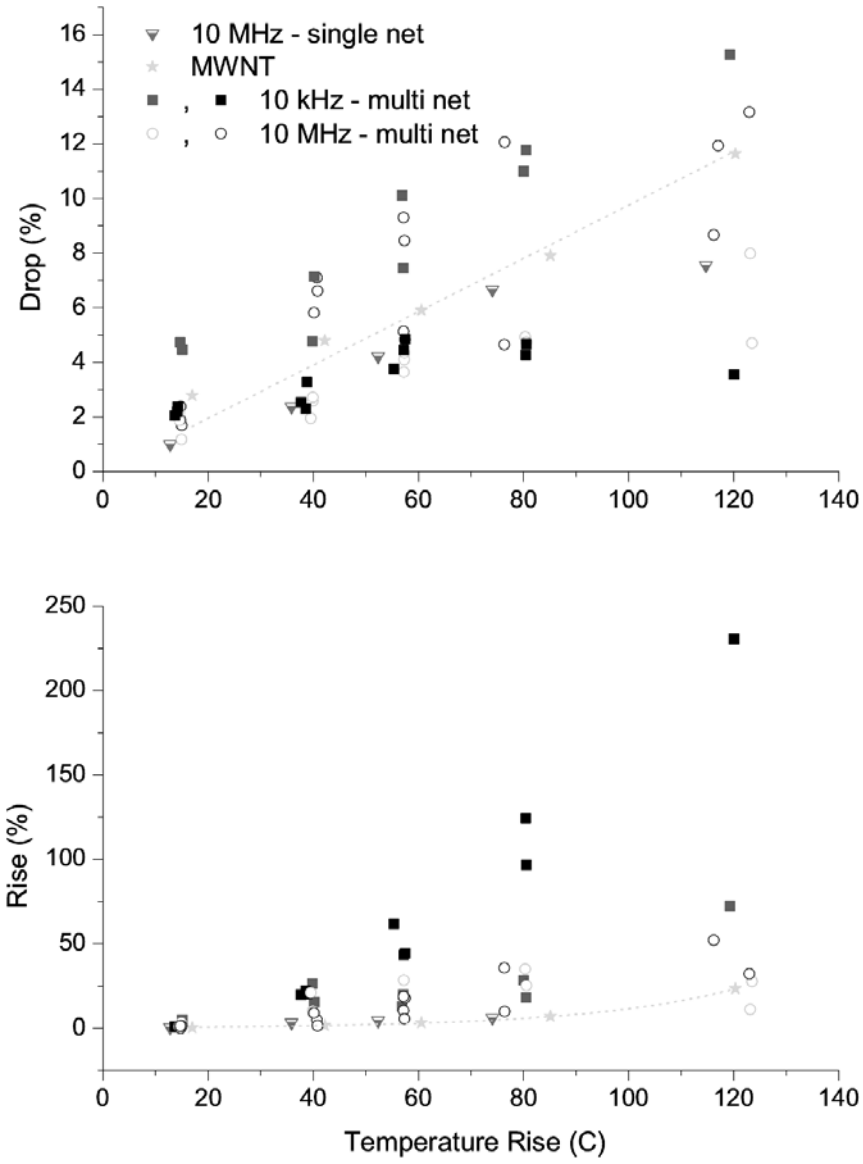

Figure 6.7: The relative resistance drop and rise during each heating and cooling cycle for all tested samples. The terms drop and rise refer to the definitions given in Figure 6.3.

in degrees Celcius). The situation is more unclear for the resistance drop, where the samples lie on both sides of a linear fit ($R_{mwnt} = 0.098\Delta T$) to the multi-walled data.

If one ignores the high temperature data (for 147 ^{o}C), where the double peak effect is very pronounced, all data show a linear resistance drop with temperature, while the resistance rise shows an exponential behaviour. In [35] the authors measure the resistance of bundles of multi-walled nanotubes as a function of temperature up to 60 degrees and fit their data with a linear curve. In [64], temperature measurements on a mat of SWCNTs show the same behaviour of the resistance during heating as it was observed in our own experiments.

In Figure 6.8(a) the temperature at which the resistance starts increasing during the heating cycle (temperature T_c in Figure 6.3) is plotted, while in Figure 6.8(b) the time from the cycle start relative to the total heating time (from Figure 6.3 this is $\frac{(t_1-t_0)}{(t_m-t_0)}$), at which this change occurs (referred to as "t_{htc}" from now on) is plotted.

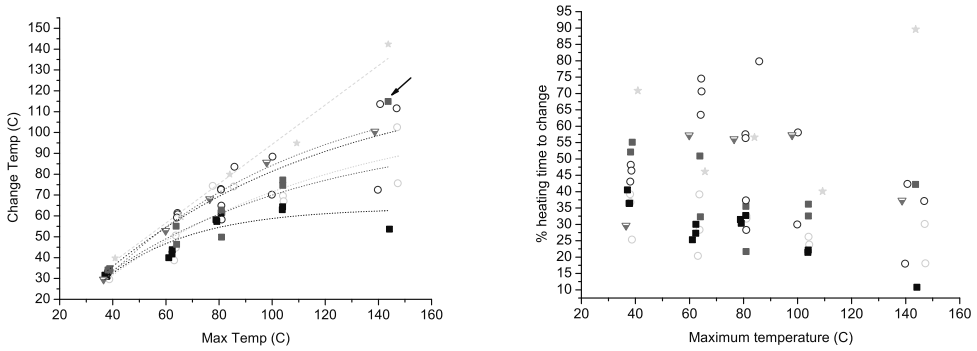

(a) (b)

Figure 6.8: (a) The time to resistance increase as a function of the maximum temperature. **(b)** Heating time to change (t_{htc}) as a function of the maximum temperature. The marker definition is the same as for Figure 6.7

In Figure 6.8(a) most points are below the line $T_{change} = T_{max}$ as expected. Moreover, the multi-walled carbon nanotube data points are placed on a line with a slope of 0.94 ± 0.03 and all other data points for the network probes lie below that line. For these networks the relationship between the change temperature and the maximum temperature is not linear but follows asymptotic curves. The fits are plotted with dashed lines in Figure 6.8(a).

When plotting t_{htc} as a function of the maximum temperature (which can be seen as a measure of the heating rate) we would normally expect a clear decrease with increasing temperature, since the high temperatures are reached much faster when we heat with a faster heating rate. Figure 6.8(b) shows that this is not quite the case. Although a slight tendency towards our expectations is observed, there are a great number of cases where the exact opposite is observed, particularly in the $60 - 100$ ^{o}C region.

Since these measurements are sequential, there exists a possibility that the result of a measurement greatly depends on the time elapsed since the last measurement. In Figure 6.9 we have plotted t_{htc} as a function of the time that has passed since the last measurement was done. The starting measurements have been placed at $t = 600000$ sec. The color coding corresponds to the maximum temperature while the different symbols of the points correspond to the different probes. The Figure shows that for each temperature the t_{htc} values are not in any obvious way related to the time from the previous measurement.

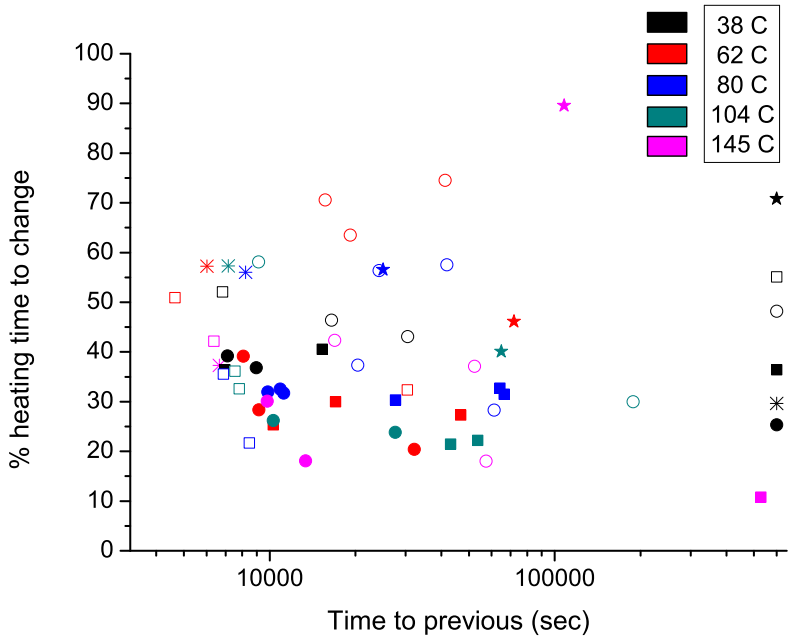

Figure 6.9: The heating time to change (t_{htc}) as a function of the time since the last measurement. The measurements have been color coded for the heating temperature they correspond to and the different samples are represented with different symbols.

6.1.1.2 Fast heating

In all previous experiments the heating time is 25 minutes, or in the case of the multi-walled nanotube even longer. In order to check if the behaviour of the nanotubes is different if the heating happens faster we used probe B3 again, where now the heating time was between 3 and 5 minutes. The cooling was also done faster, so that the entire cycle came to take 12-15 minutes instead of the 100 minutes in the previous experiments. Figure 6.10 shows the recorded data as well as the rate of resistance change for a slow and a fast measurement of the same sample at roughly the same temperature.

Despite the fact that we heated the sample up to 90 degrees there was no sign of the double peak effect in the derivative curve. The resistance only just barely started increasing again before the cooling started. The plateau in the derivative

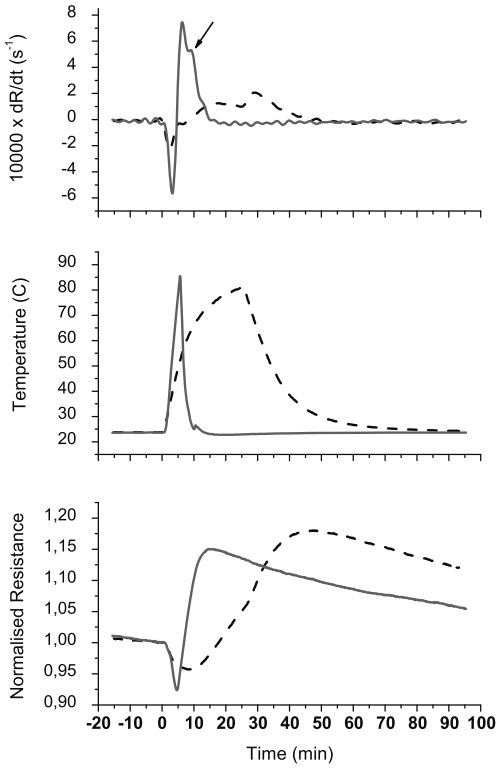

Figure 6.10: The resistance of probe B3 during fast heating along with temperature and rate of change as a function of time. Despite the high temperature the double peak effect is not observed.

curve indicated by the arrow is an artifact due to a slight irregularity in the cooling rate close to room temperature. We note that the initial slope is the same for both measurements.

Figure 6.11 plots the drop and rise of the resistance as described in Figure 6.3. The results of the slow heating are also given for comparison. It can be seen that the new data are quite different. The drop of the resistance is larger and the rise smaller. It also seems like the new data are lying on lines parallel to those formed by the previous data, although due to the small number of points this is to be taken with caution.

One could argue that due to the method we use to measure the temperature, the measured temperature is higher than the actual temperature on the chip. Although this could explain the differences in the rise data, it cannot explain why the resistance drop is larger. We therefore think that the differences arise from the heating rate. This will be discussed further in section 6.1.3.

6.1.2 Experiments in a nitrogen atmosphere

Probe B3 was also characterised in a nitrogen atmosphere. This measurement was done in a sealed chamber where the pressure, heating and cooling rate and

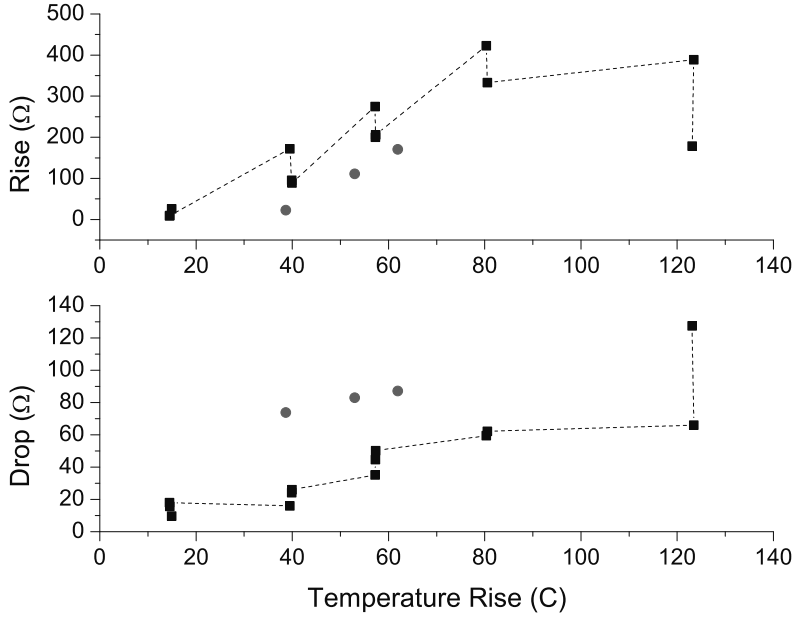

Figure 6.11: The absolute resistance drop and rise during each heating and cooling cycle for sample B3, both for slow (squares) and for fast (circles) heating. The relative data follow the same pattern.

atmosphere could be controlled. The probe was placed inside the chamber and the chamber was pumped down and flushed with nitrogen three times before it was filled with nitrogen at a pressure of 1 atm. This was done in order to ensure that the concentration of atmospheric oxygen in the chamber was as little as possible.

In order to protect the wiring in the chamber from overheating we conducted the experiment as follows: first the chamber was heated to 50 ^{o}C with a rate of 100 ^{o}C/h, then the temperature was kept constant at 50 ^{o}C for 10 minutes and then the heating continued to 70 ^{o}C with a slower rate of 50 ^{o}C/h. After that the chamber was cooled down as fast as possible. Since every chip contains two assembly sites, we were able to monitor both of them at the same time and the results showed that both sites reacted exactly the same way. This is shown in Figure 6.12, where the temperature, resistance of both assembly sites and the pressure are plotted as a function of time.

The response of the probe is actually the same as obtained from the simple oven experiments with the obvious change that the curves are more linear now that the heating rate is controlled. If one calculates the drop and rise of the resistance (3.7 % and 11% respectively) they are comparable with those results obtained in the open oven, keeping in mind that the rise was not completed when the experiment was interrupted.

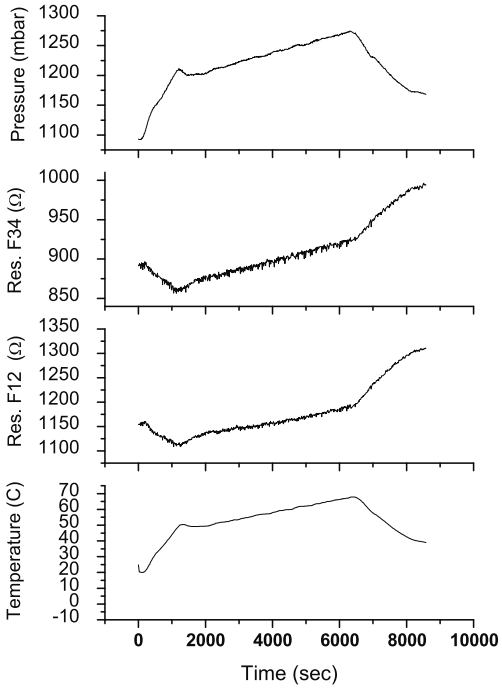

Figure 6.12: The recorded data during a heating and cooling cycle in a nitrogen atmosphere. In this system the heating and cooling rate can be controlled accurately.

6.1.3 Conclusion

In the previous sections the behaviour of carbon nanotube networks as well as that of a single multi-walled carbon nanotube has been monitored under heating and cooling cycles. When heated the nanotubes reduce their resistance in a roughly linear way with temperature (see Figure 6.13(a)). However, at some point during the heating the curve flattens out and even changes direction before the cooling starts. In this case the rate of resistance increase with temperature is different than the rate of resistance decrease, something previously reported in [122] for SWNT mats. Figure 6.13(a) also shows that as the measurements progress with time the resistance level at the maximum temperature is always higher than that of the previous cycle. The same effect is observed in a N_2 atmosphere (shown in Figure 6.13(b)), where it is also evident that the resistance changes linearly with temperature.

This behaviour cannot readily be explained by a single mechanism. We believe there are several phenomena going on at the same time. When a system is heated, oxygen desorption starts taking place with a rate depended on temperature, initial concentration and time. At low temperatures the rate of desorption is low but as the temperature increases so does the desorption of oxygen. Nanotubes are p-doped due to oxygen sitting on their surface. As oxygen is removed their resistance increases. The initial decrease in the resistance could be related to the nanotubes themselves, or to the contacts between the nanotubes and the electrodes or between the nanotubes themselves. At high temperatures the oxygen

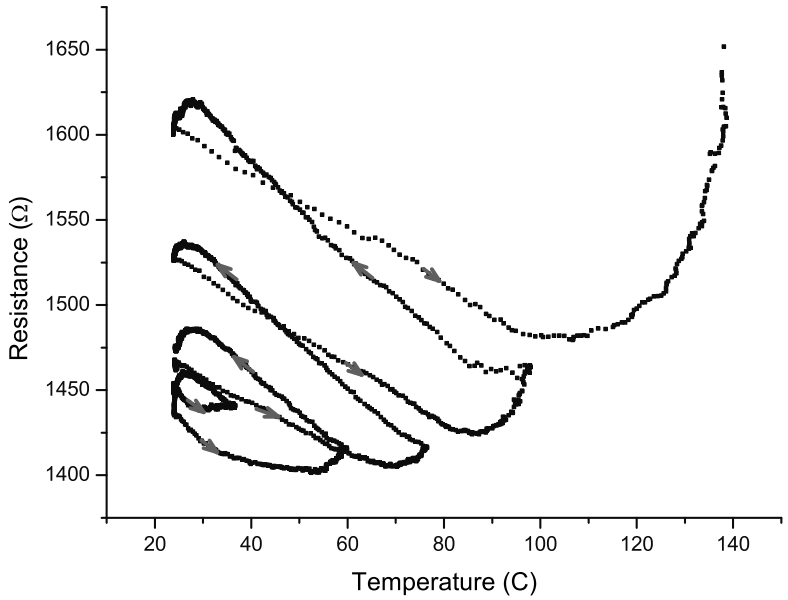

(a) A3s - in air

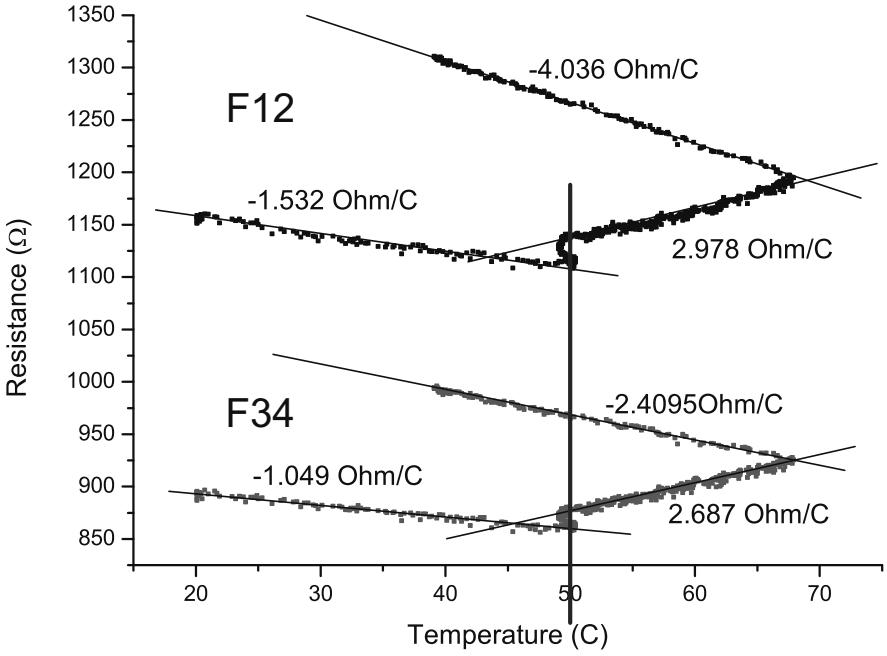

(b) B3 - in N_2

Figure 6.13: The resistance as a function of temperature for **(a)** sample A3s in air and **(b)** sample B3 in N_2. The figure shows that the resistance changes linearly with temperature except at the start and end of each cycle.

desorption takes over and the resistance starts increasing despite the fact that we are still heating the system.

Nanotube networks are a complex system often consisting of several layers of nanotubes in bundles. Oxygen from the core layers or from internal nanotubes in a bundle has to diffuse through the outer layers or the surrounding nanotubes in order to be released. That is more difficult and takes longer time and greater energy. That together with the fact that there cannot be infinite amounts of oxygen on the nanotubes causes the double peak effect at the higher temperatures: The adsorption rate decreases again and the curve starts flattening, or equivalently, the rate of increase becomes smaller and smaller. In the case of probe B3 the mechanism that causes the resistance decrease even takes over again as was shown in Figure 6.6.

When the cooling starts dR/dt changes again becoming maximum a little after the cooling starts, since now both mechanisms (oxygen desorption and resistance dependence on temperature) are causing the resistance to increase. Towards the end of the cooling cycle the curve has flattened again since now the temperature is low enough so that oxygen can start adsorbing on the nanotubes again. This causes the resistance to decrease in a exponential way in between the various measurements and this has been observed in every sample.

Figure 6.14 plots the initial resistance decreasing rates (dR/dt) after the experimental cycles (decrease rate after t_2 in Figure 6.3), as a function of the maximum temperature during the cycle. The rates have been normalised in relation to the minimum value, so that a comparison could be possible.

The Figure shows that the rates increase with temperature, which is in accordance with our assumptions that oxygen desorption and adsorption is part of the explanation for this behaviour. The higher the temperature the more oxygen will desorb. However, for the higher temperatures the rate is stabilised to a maximum, since for these temperatures all the oxygen that could desorb has done so and therefore the re-absorption rate is the same.

This decrease was also observed during constant monitoring of the resistance of the networks after assembly, described in chapter 5. The nature of the resistance decrease is precisely the same in these heating experiments: a double exponential can be fitted to the data, showing an initial fast and a subsequent slow adsorption process, in accordance with the multi-layer structure of the nanotube networks, reported in [122, 123, 125]. In chapter 5 we attributed the decrease to the current destroying the SDS micelles protecting the networks, thus exposing the surface to atmospheric oxygen, which then adsorbed on the nanotubes causing the resistance to decrease. In light of the results of this chapter, this assumption seems to be valid.

Since oxygen desorption also is a time-dependent process, when the samples are heated and cooled very fast, oxygen does not have enough time to desorb and re-adsorb. Therefore, only one mechanism, namely the one responsible for the resistance drop, is dominant during most of the heating time and thus the resistance drop is larger for the fast-heated samples.

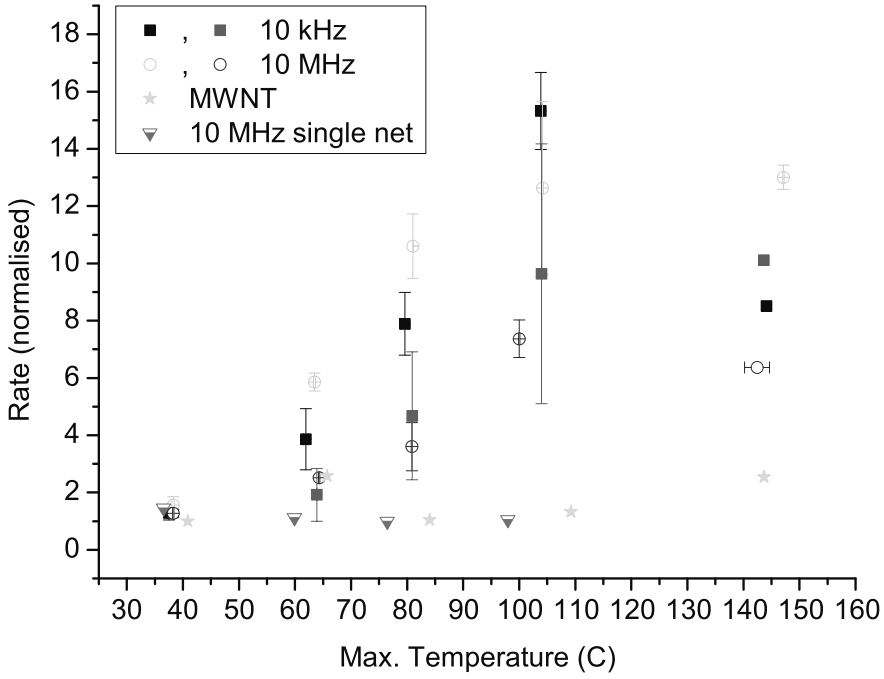

Figure 6.14: The normalised decay rates after each heating and cooling cycle as a function of the maximum temperature. Note the flattening of the data at the high temperatures.

Finally, the experiments conducted in a nitrogen atmosphere do not speak against our assumption. Although there is no atmospheric oxygen present, there is still oxygen trapped on the nanotubes which can desorb. A way to support our assumption would be to continue the resistance monitoring in nitrogen until after the cooling finishes. If the resistance of the nanotube remains constant or even increases instead of dropping exponentially, then our hypothesis holds. This experiment has not yet been conducted. However, an indication of the validity of our assumption is presented in the following section during another experiment, where oxygen desorption is suspected.

6.2 Response to light

It has previously been observed [126, 121, 127] that when a carbon nanotube forest, grown between two electrodes, is illuminated the resistance increases and when the light is switched off the resistance drops after a certain time back to the original levels. The resistance increase was also observed on an individual SWCNT in [121] and depended greatly on the wavelength of the light used. The purpose of our experiments was to see if the same happens with somewhat more ordered carbon nanotube networks and a plain white light source.

The response of 3 SWCNT networks to illumination using the focused light beam (maximum illumination 4000 lux, corresponding to 1600000 lux at scale 10 of the

Table 6.2: The samples used for the response during illumination.

Name	Time
C8	10 sec
D5	15 sec
C3	60 sec

lamp after a 20x magnification) from an optical microscope was measured. The response of a multi-walled nanotube was also measured for comparison purposes. The three networks used were assembled a few days before these experiments but had not been submitted to any other treatment (e.g. SEM imaging, heating or resistance monitoring) apart from measuring their resistance 3 times using a multimeter.

It was shown in chapter 5 that when the SWCNT networks are monitored constantly, they experience an exponential decay in their resistance value. Since these networks have not been subjected to constant monitoring prior to these experiments, an exponential decay on top of any other response should be expected. Indeed, Figure 6.15 shows the recorded data for one of the three networks with an exponential baseline. In the following discussion this baseline has been removed from the data, unless otherwise stated.

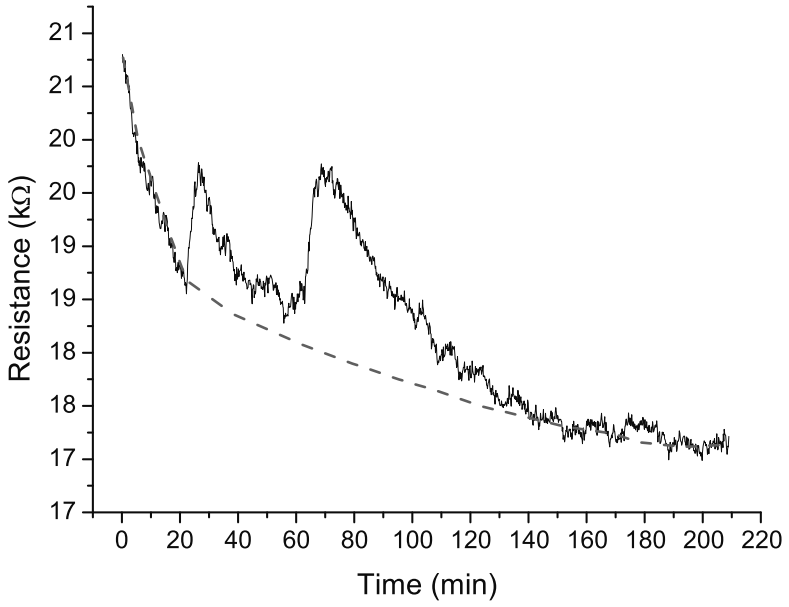

Figure 6.15: Recorded data for probe C8, fitted to an exponential baseline (dashed line).

All experiments were done on samples assembled on the structures of Figure 4.9(g) with a voltage of 15 V p-p at a frequency of 10 MHz. Table 6.2 shows the samples used along with the field application time for the assembly.

Since we were using the microscope light source to do these experiments, we were also able to test the response of the nanotubes to different intensity of the light, as well as the response when the light was on but not focused on the network.

Figure 6.16 shows the change in the resistance for the three nanotube networks tested during illumination. In the figure the light is switched on at $t = 0$. It is clear that the resistance of the networks increases immediately when the light is switched on and starts decreasing once the light is switched off. Moreover, the change in the resistance depends on the light intensity, as can be seen for sample C3, where the light is first switched on to scale 1 (at $t = 0$) and then to scale 4 (at $t = 206$ sec) with an obvious change in the resistance. By fitting exponential curves to the data, we found the time constant for the decay after the light is switched off to be between 500 and 800 seconds for the various samples.

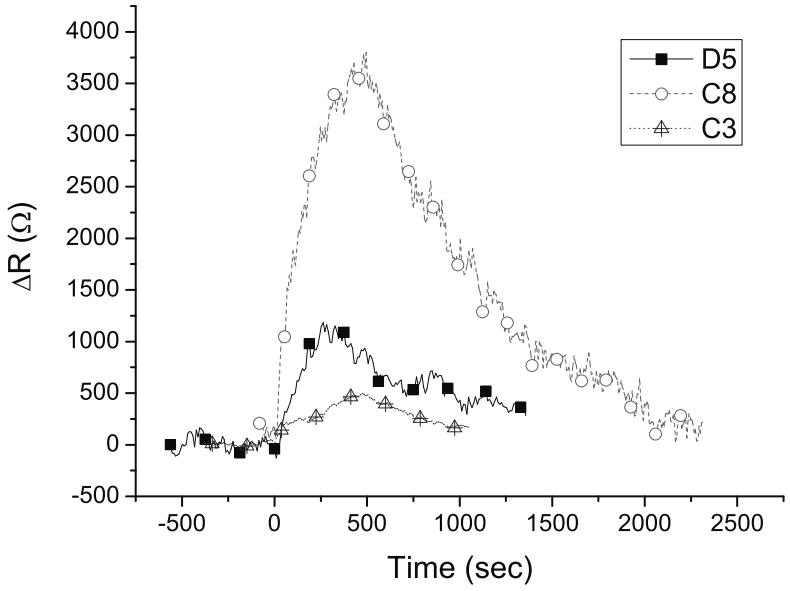

Figure 6.16: Resistance change during illumination for three nanotube networks. The light is switched on at $t = 0$. The baseline has been removed from these data.

An interesting observation is that the rate of resistance increase for the three samples shown in Figure 6.16 appears to be inversely proportional to the field application time for the assembly of these samples, so essentially, inversely proportional to the number of assembled nanotubes.

In [126] the authors attribute the change in the resistance to oxygen desorption when the nanotubes are illuminated. In order to confirm that, they performed the same experiment but in a nitrogen atmosphere, and indeed, they saw that the resistance did not return to its original value once the light was switched off.

In our setup we have the ability to locally change the environment around the nanotube networks by blowing nitrogen (or any other gas) through a tube placed close to the sample holder. The nitrogen is blown indirectly onto the sample, in order to avoid any mechanical forces on the nanotubes. Since the chamber is

rather big, a few minutes are usually necessary before the atmosphere around the sample has changed significantly.

This was tried on two of the samples. In the first one (sample C3) the nitrogen was turned on for 6 minutes starting when the light was switched off, while in the second one (sample C8), the nitrogen was turned on 2.5 minutes before the light was switched on and turned off 5 minutes after the light was switched off. The results are shown in Figure 6.17 for both samples, where the light is switched on at $t = 0$.

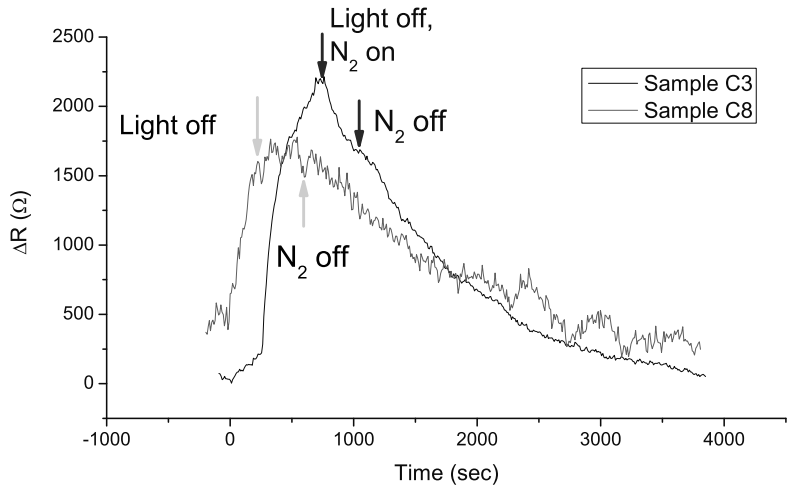

Figure 6.17: Effect of nitrogen for the behaviour of nanotube networks after illumination. The nitrogen delays the resistance decrease.

For sample C3 the decay starts immediately after the light is switched off, but as the environment around the sample is changing towards a higher nitrogen concentration the rate of the decay is decreasing. When the nitrogen is switched off and the oxygen concentration goes back to normal, the rate of the decay returns to the original values. For sample C8, where the entire experiment is taking place in a higher concentration of nitrogen than normal, the value of the resistance after the light is switched off remains at the high levels until the nitrogen is switched off and the oxygen concentration around the sample returns to normal.

The exponential decay constants for these two decays were 940 and 1644 seconds respectively. Though for sample C3 the higher (almost double) decay constant could be attributed to the fact that the light intensity for this second experiment was much higher than in the first experiment (in Figure 6.16), the same does not apply for sample C8. The time constant for this second experiment was also double as much as it was in the first experiment, but the light intensity was the same for both of them.

Based on the above described experiments it seems quite probable that the light causes oxygen desorption from the surface of the carbon nanotubes, which in turn causes the resistance of the networks to increase. When the light is switched off

and there is oxygen in the vicinity of the nanotubes, the oxygen re-adsorbs on the carbon nanotube surface causing their resistance to decrease again. In a nitrogen rich/oxygen poor atmosphere, the re-adsorption is much slower.

When the light was switched off but was not focused on the network under monitoring there was no observable change in the resistance even at the maximum light intensity. This was tested 3 times giving the same results. We can therefore conclude that the light needs to be strongly focused on the nanotube network in order to cause a change.

A single multi-walled nanotube contacted by the shadow-masking technique was also measured. The results are shown in Figure 6.18, where the light was always turned on at the same intensity and for two minutes several times, but every 950 seconds. The behaviour of the probe was the same as the single-walled networks, although some odd curves were also recorded. The main difference between the two, was that the single MWCNT was changing its resistance value immediately, while the SWCNT networks had a time constant associated with the resistance increase, which varied between 1 and 4 minutes. Figure 6.19 plots the time constants fitted to the decays recorded for the MWCNT. For the first 9 experiments the time constant for the decay is around 1000 seconds, however, for the last three decays it is more than 3 times higher. This increase coincides with the recording of an "odd" curve, namely an increase in the resistance of the MWCNT both when the light was switched on and when it was switched off again. It is possible that the system changed somehow at this point.

6.3 Response to humidity and nitrogen exposure

The following experiments have only been conducted on 1 to 2 samples and should therefore be considered as an indication of a certain behaviour.

The humidity control in the chamber is only capable of changing the humidity from indoor humidity to 100%. This is achieved by having nitrogen blown in the chamber through a water filled container. The nitrogen exposure has been described in the previous section.

Figure 6.20 shows the recorded curve for one nanotube network. As expected, the probe shows the same exponential decay as all examined networks in this project during continuous monitoring. However, here the environmental conditions are changed during the decay.

At point 2 the nitrogen is switched on. It does not seem like any change in the decay rate of the resistance is taking place. However, when the humidity is quickly increased at point 3 the rate of decay is clearly decreased and once the humidity is returned to normal the decay rate increases again, between points 4 and 5. The same now seems to happen during the nitrogen exposure between steps 5 and 6, with the rate of decay increasing after step 6, where the nitrogen is switched off.

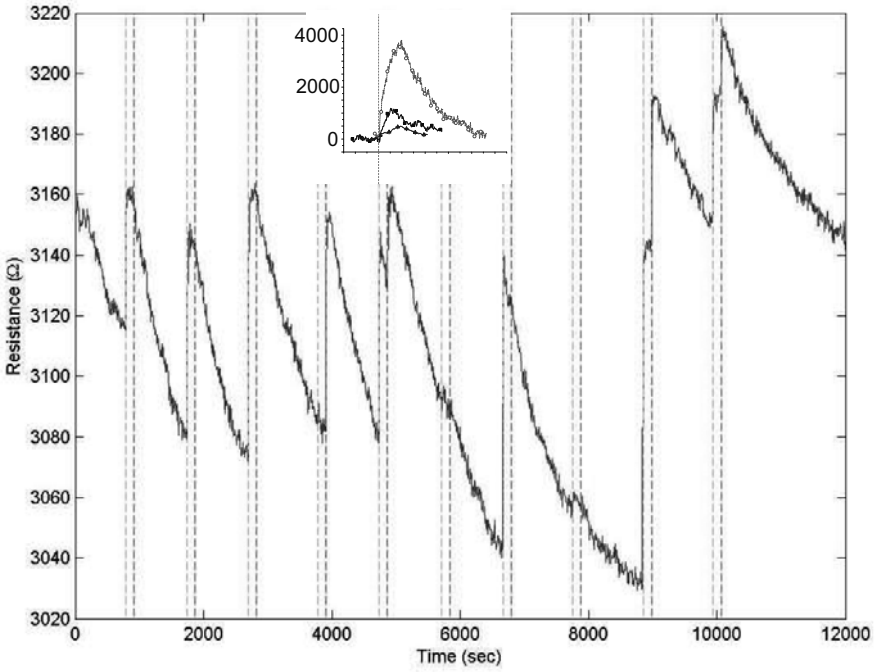

Figure 6.18: Some of the recorded response of the multi-walled carbon nanotube during illumination. The resistance increases immediately and remains constant while the light is on, but drops exponentially when the light is turned off. Shown also is the response from the SWCNT networks on the same time axes. The networks respond much slower but also much more upon illumination.

This curve alone would not tell us much about the way nitrogen affects the decay rate of the networks, however, given the previously described light experiments, it seems quite probable that exposure to nitrogen halts oxygen adsorption on the networks.

The humidity seems to have the same effect. This is supported by a second experiment on a different probe, shown in Figure 6.21. Here when the humidity is increased, the resistance stabilises and even increases and when the humidity is reduced back to normal levels and the chamber opened, the resistance starts decreasing again. The changes are however fairly small.

The nitrogen exposure and the humidity could in fact be the same effect considering that the humidity increase inside the chamber is caused by blowing nitrogen through the water container. More experiments with better humidity control need to be done in order to evaluate whether the humidity alone could be causing resistance increase[1].

In [122] the authors exposed a SWCNT mat to water vapor and noted an initial increase in the resistance of the mat for the first few minutes of exposure before the

[1]More experiments were conducted after the completion of this PhD thesis on the effect of humidity on CNT networks. The results are consistent with those described in this section and are published in Journal of Physics: Conference Series 61 (2007) p. 247

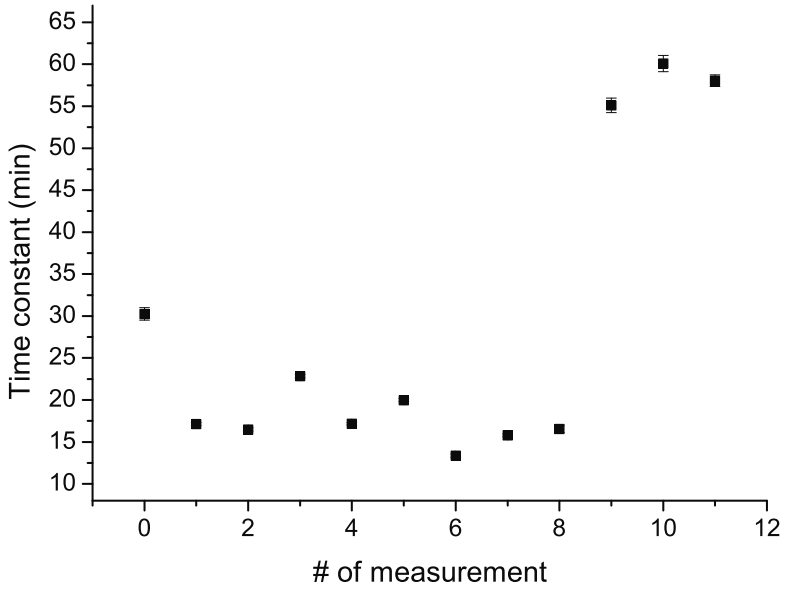

Figure 6.19: The time constant of the exponential decays for the multi-walled experiments. The constants lie at around 100 seconds for most of the measurements but become 3 times higher after a possible change in the system.

resistance started increasing. It is possible that our results are in agreement with this experiment, since the humidity exposure only took place for a few minutes.

Moreover, in [66] a network of multi-walled nanotubes was exposed to various degrees of humidity and the resistance showed an increasing behaviour with increasing humidity. This is also in agreement with our observations.

6.4 Response to nitrogen flow

The direct exposure of a nitrogen flow onto a carbon nanotube network has been investigated. The probes were placed on the holder and connected to the Keithley Sourcemeter which was monitoring their resistance. Then at $t = 0$ a stream of nitrogen was blown on the SWCNT networks at a distance of roughly 0.5 cm. Several probes were tested and the results from two of them are presented in Figure 6.22.

The Figure shows that the resistance immediately starts increasing until it reaches a stable value. When the nitrogen is removed the resistance goes back to the base value.

This result and those of section 6.3 neither agree or contradict each other. The direct nitrogen flow on the networks could simply have a mechanical effect on the nanotubes, changing the structure configuration and possibly the contact resistances. However, it could also mean that the nitrogen atoms knock some of

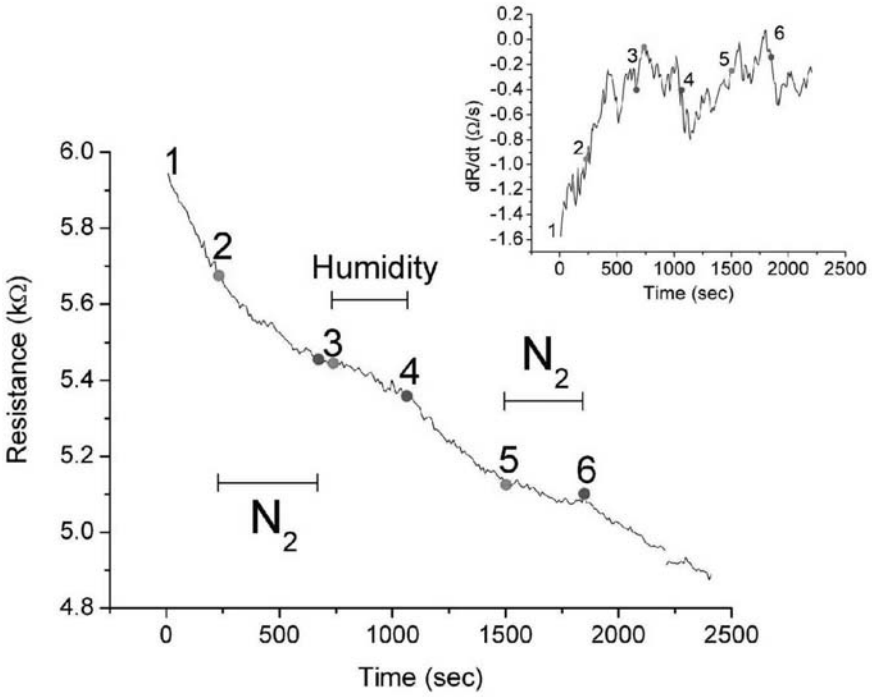

Figure 6.20: The recorded curve for probe C3 when it is exposed to nitrogen and 100% humidity. The regions where this happens are marked on the graph and the numbers are for reference in the text. The original data are presented in this figure. The derivative data are also plotted in the inset, in order to illustrate the change in the decay rate.

the physisorbed oxygen on the nanotube surface off, in which case the resistance would increase also. In section 6.3 the nitrogen was only able to delay the decay of the resistance, but the opening of the tube was placed more than 2 cm away from the sample and was not blowing nitrogen directly on it but at an angle. The result could still be attributed to a mechanical effect, under the assumption that the resistance decay rate is larger than the resistance growth rate due to the nitrogen. In [35] the authors demonstrate that by blowing air onto a nanotube network at varying distances the resistance of the nanotube changes with the largest change happening when the air gun is closest to the network. This agrees with our own data.

In experiments done in a vacuum chamber, where controlled amounts of nitrogen were let in through a valve placed far away from the sample and not directly opposite to it to reduce the mechanical effects arising from opening and closing the valve, no response was observed to the nitrogen exposure, apart from a clearly mechanical response when the valve and the pump were turned on. This was in agreement with [63].

From the above it is not possible to make a conclusion regarding the effects of nitrogen on the nanotubes, though our data points towards a response to the lack of oxygen rather than the presence of nitrogen.

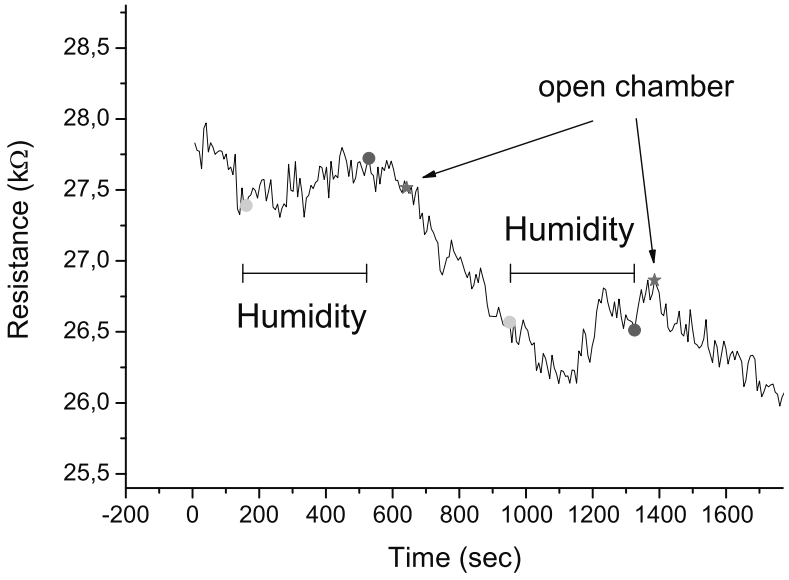

Figure 6.21: Effect of humidity on probe B5. The resistance stabilises or even increases in this experiment when the humidity is 100%. The original data has been plotted in this figure.

6.5 Summary

In this section the response of nanotubes to various environmental conditions was presented. Nanotubes were exposed to humidity, nitrogen, illumination and heating. For the two latter ones the observed behaviour is consistent with oxygen desorption and adsorption processes, while a nitrogen atmosphere seems to delay or suppress the oxygen adsorption process. Increased humidity may cause a similar behaviour but more studies are needed for this investigation.

A resistance increase from a direct nitrogen flow on the samples was also observed and attributed to mechanical effects.

We also noted that the response to light is faster for samples with fewer assembled nanotubes, with the single multi-walled nanotube responding immediately upon illumination. This can also be well explained with the idea of an abnormal diffusion, with oxygen from networks containing a large number of nanotubes needing more time to desorb than in the case of networks with fewer nanotubes.

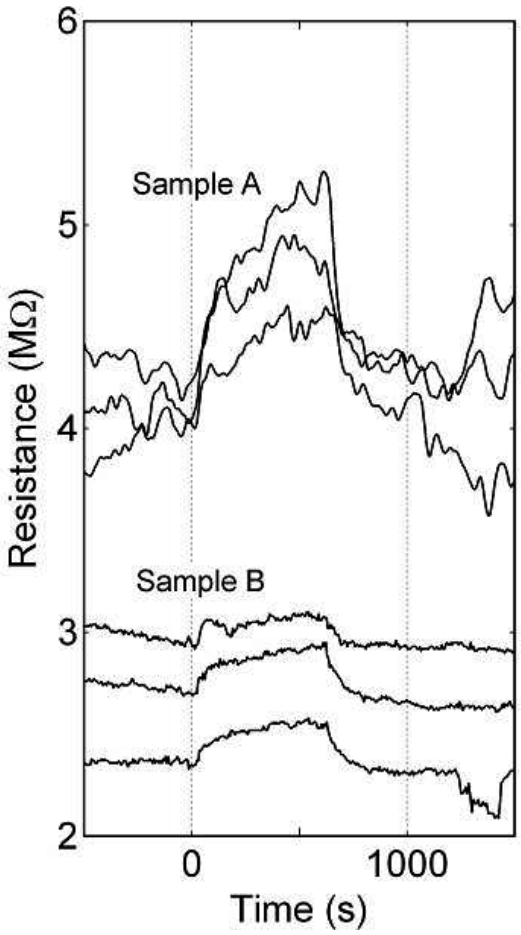

Figure 6.22: Change in the resistance of the SWCNT networks during exposure to a direct nitrogen flow. Three measurements for each sample are presented.

Chapter 7

Cantilever microprobe

In order to approach a sensor to a region with local concentration variations, such as near a cell surface, the sensor should be located on a pointed structure, such as a cantilever. In this chapter we investigate free hanging electrodes as well as electrodes on a mono-cantilever system with respect to their ability to assemble and support multi- and single-walled carbon nanotube networks. Through these experiments knowledge is gained that leads to a cantilever probe specially designed for dielectrophoretic assembly of carbon nanotubes. The design, fabrication, characterisation and application of this probe are going to be presented in this chapter.

7.1 Early cantilever designs

In this section the results obtained with the various cantilever structures of Figure 4.8 are going to be described and compared. Multi-walled carbon nanotubes were used for these experiments because they were long and relatively thick, easy to disperse in simple organic solvents, like isopropanol, and easy to view in the SEM.

7.1.1 4PP

4PP were used at the start of this project to assemble multi-walled nanotubes between the fingers. In the following experiments, the setup described in section 4.4.2 was used.

Several assembly experiments were done using 4PP with a pitch ranging from 1.5 μm to 16 μm. Some typical results are shown in Figure 7.1. Common characteristic is that the probes are either completely covered with tubes and dirt or have a number of formed bridges or networks between the fingers comprised from a large amount of nanotubes. The position of these bridges suggests that they were formed during drying of the solution rather than because of DEP.

The 4PP are not the optimal DEP electrodes for a number of reasons. They are parallel electrodes and therefore form a somewhat homogeneous field that is

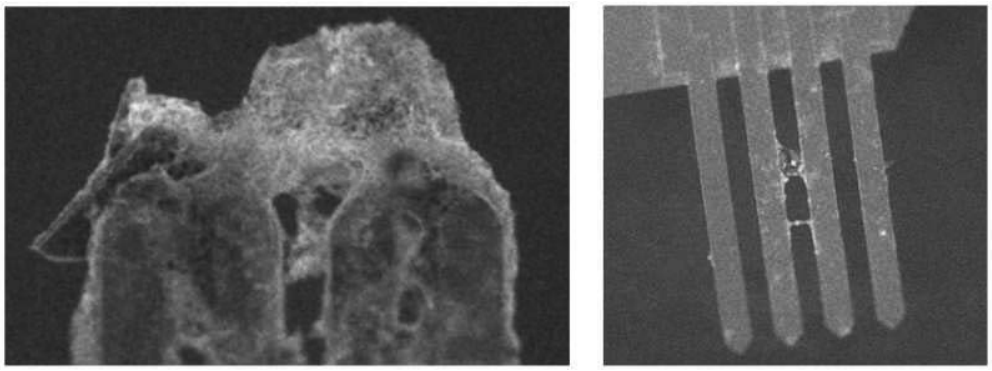

Figure 7.1: Typical results using the original cantilever setup with the 4PP. The depositions varied randomly between total coverage of the probe to nicely assembled bridges and nets.

not optimal for DEP. The field is the most inhomogeneous at the very edge of the probes, which is also the part of the probe, where the spacing between the electrode edges is the largest. The fingers extending the probe edge are quite long (around 100 μm), and although they are quite flexible, they can break rather easily. Given the fine manipulation needed in order to bring the probe into the tube, it was quite often that the fingers broke because they were pushed on some part of the tube. Moreover, the parallel fingers worked as a capillary tube and the solution was pulled towards the probe causing depositions over the entire length of the electrodes.

A second problem associated with these probes is the rather uncontrolled way that the bridges or networks are formed. The case shown on the right image of Figure 7.1, where a bridge and a network have formed on the electrodes were the voltage was applied is the exception rather than the rule. Normally one could find depositions on all four fingers, despite the fact that the voltage was only applied between two of the electrodes.

These probes were also used with the horizontal version of the cantilever setup. The size of the droplet being much smaller and the fingers being so long, the solution was now wetting only approximately half the finger length, so that nanotube depositions on the probe body were completely avoided. Figure 7.2 shows a nanotube bridge formed using this setup, while the inset shows a low-bias IV curve. A diluted solution was used for this experiment with a concentration estimated to be around 2 μg/ml. The thickness of the bundle is between 50 nm in the middle, and 150 nm at the left contacting point. Several MWNT can be seen in the bundle, which could contain anything from a few nanotubes to tens of nanotubes.

7.1.2 Silicon nitride substrate

Probes such as those shown in Figure 4.8(b) showed practically the same problems as the 4PP, despite the different geometry and the change of the substrate from gold to silicon nitride. An example of an experiment with such a probe is shown in Figure 7.3(a). The figure shows that most of the nanotube deposits are between

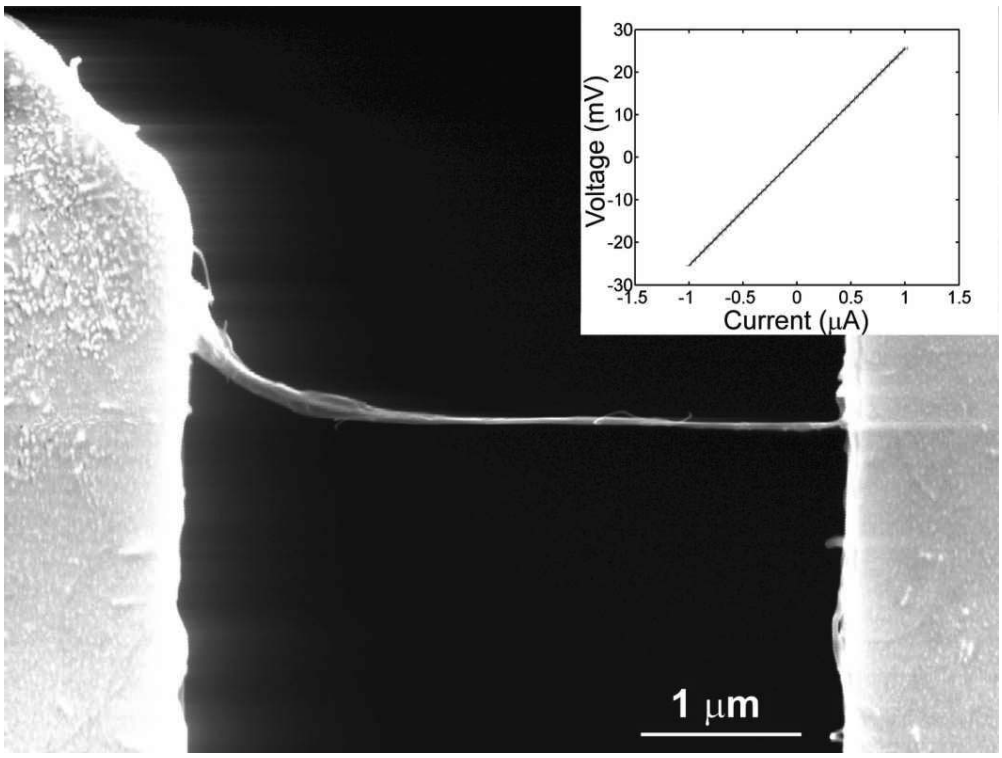

Figure 7.2: An isolated bridge formed using the horizontal cantilever setup with a narrow tube carrying the solution. The inset shows a low-bias IV curve of the bundle.

the two fingers where the voltage was applied, however, the entire probe surface is covered with nanotubes, appearing in this image as thick dark lines with a lighter line around them due to charging effects in the SEM.

Another example is shown in Figure 7.3(b), where the deposition occurs between the two fingers where the voltage is applied and not elsewhere. It should be noted however that such examples were not usual and that deposition, even with these probes occurred everywhere. Because of the short length of these fingers (about 10 μm) the horizontal setup did not improve the experiments.

7.1.3 Inclined fingers

The structures of Figures 4.8(c) and 4.8(d) were much better in terms of controlled deposition and reduced contamination. As was shown in Figure 4.19 it is possible to control the capillary effect so that the solution only stays at the top of the fingers. Figure 7.4 shows an example of an assembled bridge using structure 4.8(c). The inset shows a close up of the bridge, where it becomes clear that there are about 2 nanotubes bridging the gap, but also that the nanotubes seem to be going under the left electrode.

7.1.4 SU-8 cantilever structure

Despite the fact that the converging electrode probes seem to deal well with the

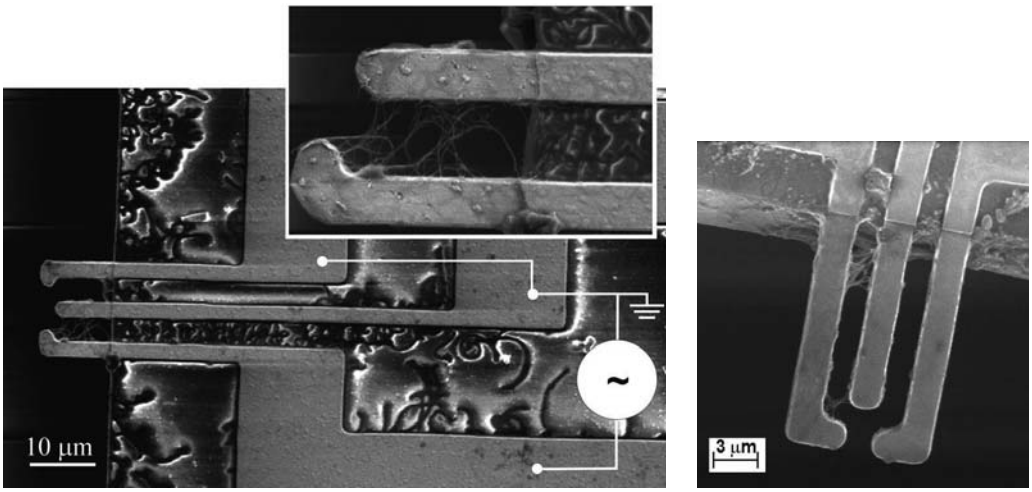

(a) 5 kHz, 5 V p-p (b) 100 kHz, 5 V p-p

Figure 7.3: Two networks assembled on the structures of Figure 4.8(b). Deposition occurs not only between the electrodes where the voltage is applied, though it is more pronounced between these.

problems of capillary effects and controlled assembly, there are still a few other issues associated with freestanding fingers. On several occasions we were able to measure a connection between the electrodes right after the experiment, but the SEM image showed that the nanotubes were just a few nanometers away from the electrodes and not in contact with one of them. One of the reasons for this could be that when handling the probes, the fingers tend to move and the nanotube bridges break due to stress.

Figure 7.5 shows a fine demonstration of yet another problem associated with free-standing fingers, namely that of assembling a "thread" at the sharp edges of the electrodes such as at the tips of a 4PP probe or the outer electrode corners of the structures of Figure 4.8(d). These threads seem to assemble themselves at the sharp edges of the probes with applied voltage on and extend in some cases several hundreds of micrometers. Since at the end of the assembly experiment the solution moves out of the probe fingers, it is likely that these nanotubes attach to the probe edges by DEP (since the field is greatest at the tip of the electrodes) but the liquid forces them to orientate with the solution movement thus creating these structures. While depositions like these can have other uses, like for example making very sharp Atomic Force Microscope (AFM) or Scanning Tunneling Microscope (STM) tips, they are unwanted when controlled assembly of nanotube bridges is the goal.

The SU-8 cantilever structure contains essentially planar electrodes but at the tip of a cantilever (see Figure 4.8(e)). It is therefore this cantilever that now comes in contact with the solution in the tube and although contamination of the surface cannot be avoided in this case, the polymer cover of the probe protects it from random nanotube depositions. Moreover, using a pipette capable of dispensing pl volumes, the planar setup method can be applied locally on the cantilevers, thus eliminating the problems that arise from capillary effects.

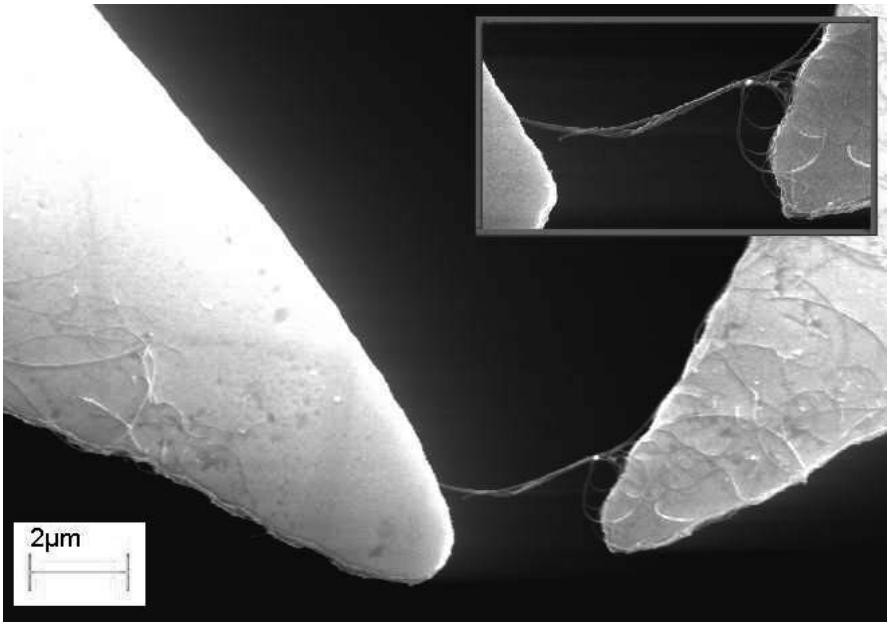

Figure 7.4: A bridge formed on an inclined structure. There are a lot of nanotubes on the electrodes but only two are bridging the gap.

Although very few probes were tested, we were able to both assemble multi-walled nanotubes between the electrodes and perform measurements on them. Figure 7.6 shows one of the assembled nanotube networks as well as the recorded low-bias IV curve. The resistance of the network was 19.5 kΩ, a typical value measured for MWCNT networks.

This design solves a number of problems associated with the cantilever structures described previously. As a consequence this cantilever structure was chosen for further development. This will be described in section 7.2.

7.1.5 Yield and parameter investigation

Experiments with multi-walled carbon nanotubes were done for several frequencies, voltages and chip geometries. Generally, the yield of the experiments (percentage of successful assemblies) was about 70 %, which is actually quite good considering the various problems associated with the cantilever probe setup. We were able to observe a tendency of fewer nanotube depositions between the fingers with increasing frequency. These experiments were done twice with two different probe geometries for frequencies ranging from 5 kHz to 1 MHz and the results were evaluated with the SEM. The decreasing efficiency of DEP with increasing frequency is in accordance with the theory (see chapter 3).

Although experiments with different voltages were conducted, we were not able to conclude anything on the voltage dependence of DEP using multi-walled nanotubes. However, we could get depositions even when using a 2.5 V p-p voltage across a 7.7 μm gap.

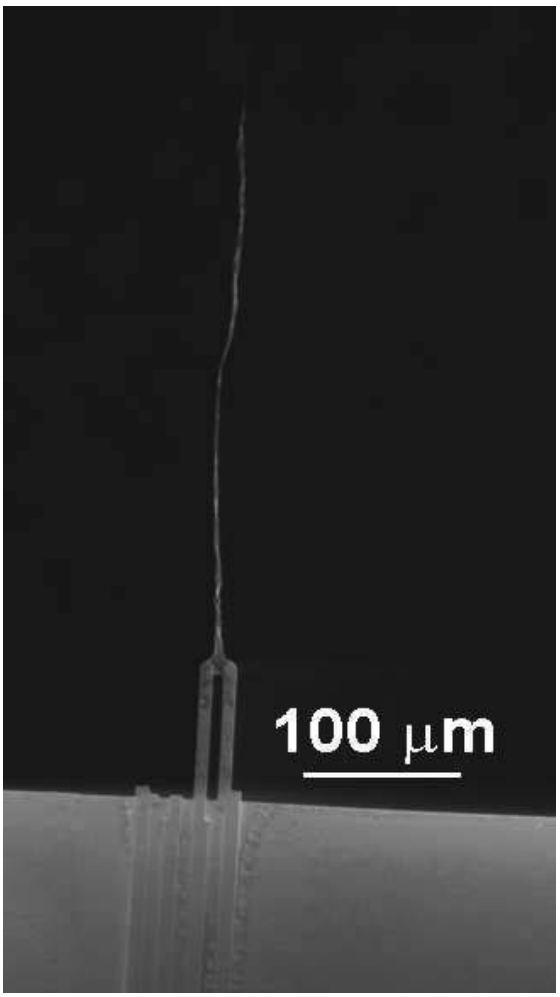

Figure 7.5: A long rope of carbon nanotubes ($\sim$ 350 μm) assembled at the sharp tip of the 4PP. Such ropes were present in almost every experiment with the 4PPs and the structures of Figure 4.8(d).

7.1.6 Current carrying capacity

The current carrying capacity of a suspended multi-walled nanotube network was measured. The obtained results agree well with similar measurements on several single-walled nanotube networks.

A probe similar to that of Figure 4.8(b), was assembled using an isopropanol solution of multi-walled carbon nanotubes, diluted to a concentration of about 5 μg/ml, with a 10 V p-p voltage applied between the middle and the outer electrodes at a frequency of 10 kHz. Figure 7.7(A) shows a SEM image of the assembled network.

After SEM imaging of the probe, a series of I-V curves were measured, while increasing the current range at every sweep. A current of 2 mA could be passed through the network before observing a permanent increase in the resistance of the network. Figure 7.7(C) shows the corresponding I-V curves. After 2 mA was applied, the resistance was increased from 2 kΩ to 30 kΩ. The resistance remained

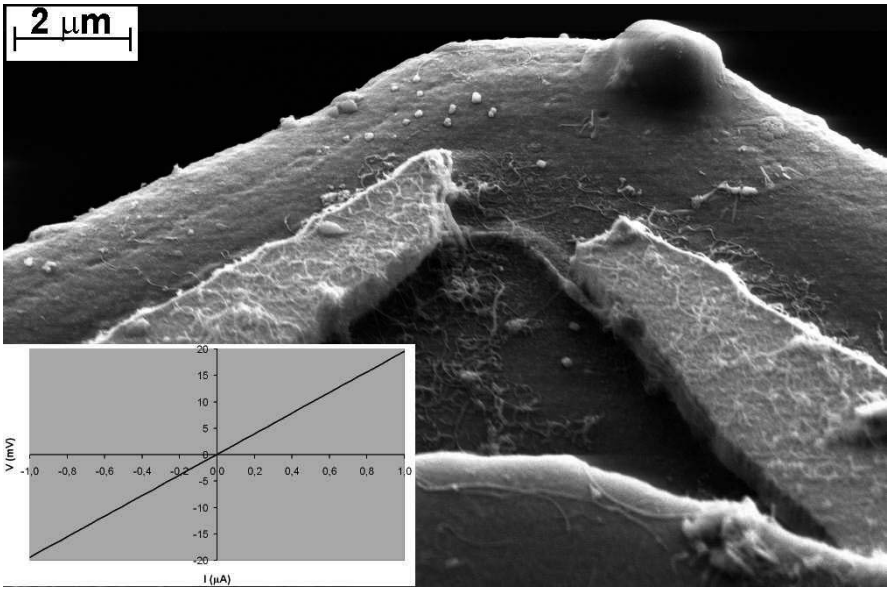

Figure 7.6: A MWCNT network assembled on an SU8 probe. The inset shows the low bias IV curve. The image was taken by depositing a thin Au layer on the SU8 chip.

at this level until all connection was lost at a current of 750 - 800 μA. It should be noted that the resistance of the bundle did not change significantly during the initial measurements; only a slight decrease was observed in the resistance for all current ranges prior to the 2 mA sweep (s. Figure 7.7(E)). We also note that the curve flattens at high bias.

Inspection of the sample in a SEM after loss of contact revealed that all nanotube connections were broken. Figure 7.7(B) shows that the failures of the individual MWCNTs occurred in the gap between the electrodes, rather than at the contacts to the electrodes. A dotted line is drawn through all gaps observed in the MWCNT. A blow-up of the region is shown in Figure 7.7(D) for clarity.

According to [124], when current flows through a MWCNT the temperature of the nanotube increases. The temperature rise is higher in the middle of the MWCNTs, further away from the electrodes, which act as heat sinks. Hence the nanotubes fail in the center.

7.1.7 Single-walled nanotubes

The cantilever structures were tested with single-walled nanotubes, but it was noted that it was impossible to avoid contamination of the surface as was the case with the multi-walled nanotubes: when the voltage was turned on the solution was pulled towards the main probe surface following the electrode lines. This can be attributed to a large electrothermal flow, because of the high conductivity of the SDS solution. In all cases the end result was a complex network of nanotubes in dried SDS. Even after washing with ethanol or water the contamination was still present (see Figure 7.8). It was impossible to use these cantilever probes with a highly conducting medium such as SDS and they were therefore not examined

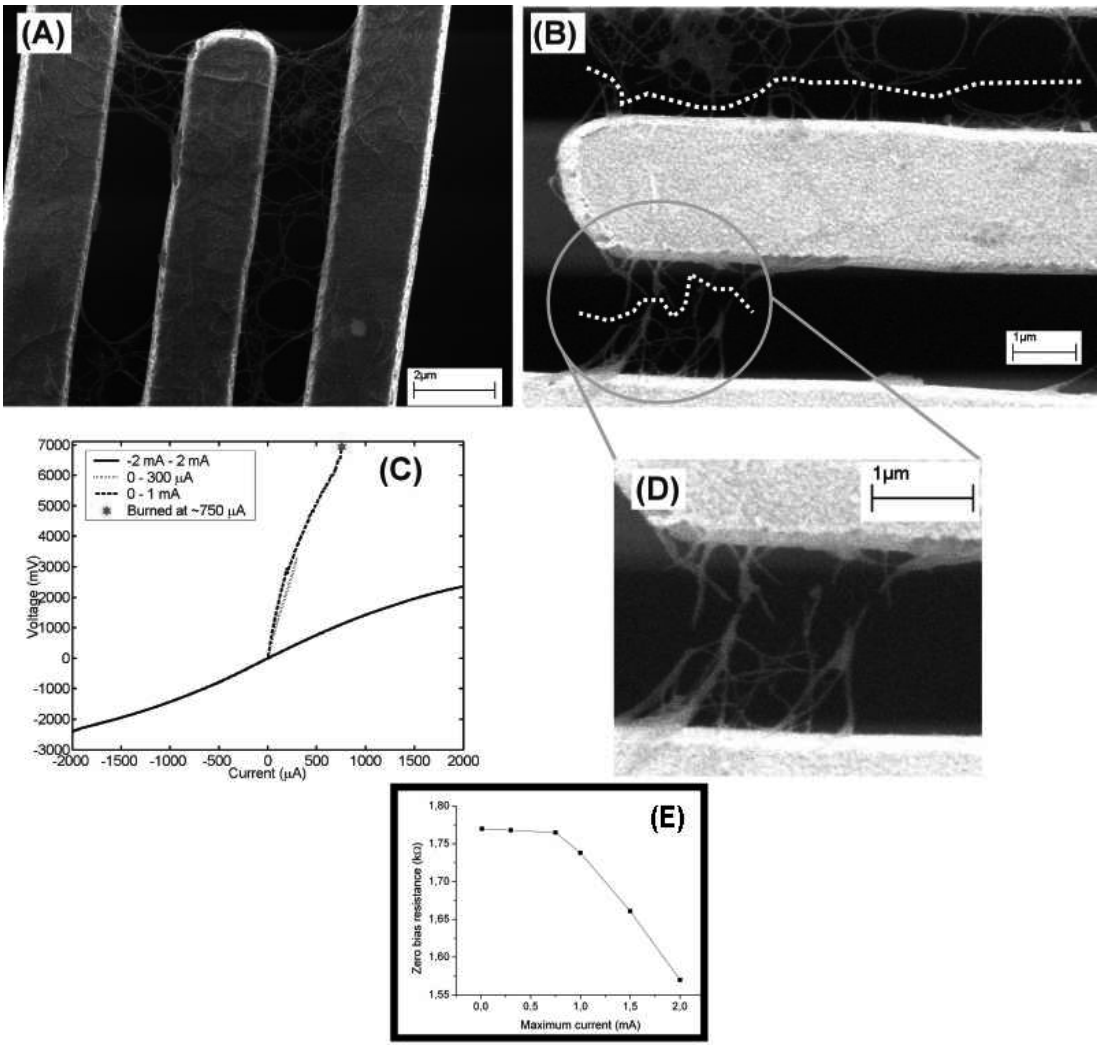

Figure 7.7: **(A)** A SEM image of the probe recorded after the assembly of nanotubes but before measuring the I-V curves. The probe spacing is about 2 μm. **(B)** An image of the probe after a 2 mA current was passed through the net. Note that all the nanotube connections are broken in the free space between the electrodes, shown with the dotted line. **(C)** The I-V curves as they were taken chronologically (in the legend from top to bottom). A dramatic change in the resistance is recorded only after the tubes have withstood 2 mA of current. **(D)** A close up of the bottom region of **(B)** without the dotted line, provided for clarity. **(E)** The zero bias resistance for the multi-walled nanotube networks as a function of maximum current until the first resistance increase.

further. Instead, the planar structures were used for the experiments mentioned in chapter 5. We should note that DCB solutions of carbon nanotubes could be used with the cantilever structures, however, because of the poisonous nature of DCB the tests were conducted with SDS solutions.

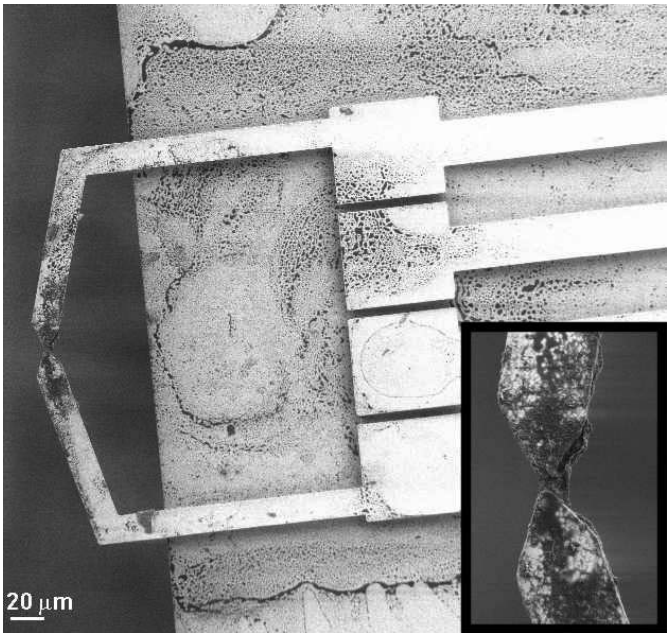

Figure 7.8: When the SDS SWCNT solution is used on the cantilever structures, contamination is inevitable. Despite extensive washing with ethanol the result is a complex structure of nanotubes and dried SDS.

7.2 The new cantilever microprobe

Though a cantilever probe is more convenient for measurement and mapping of local properties, it is the planar structures that have yields close to 100%. The SU8 probe (s. Figure 4.8(e)) is a good compromise between the cantilever and planar structures, as was mentioned in section 7.1.4. We therefore chose to develop a better design of this chip with more functionality.

The purpose of this new chip is to assemble nanotubes reliably on a cantilever structure using dielectrophoresis for sensing purposes. The design requirements for such a probe are the following:

- The cantilever should be small but robust so that stress is not an issue.
- The electrodes should be designed in such a way so that the field is highly localised and strong even for small applied potentials. They should be placed at the tip of the cantilever.
- The probe should be encapsulated in a protective layer at all regions but the tips of the cantilever where the tips of the electrodes are.

- The chip should have an embedded backgate electrode so that tuning of the nanotubes after the assembly is possible.

7.2.1 Design considerations

For a structure to become a cantilever, a releasing process is required, usually an etching step. To release the cantilever we chose etching using the Advanced Silicon Etcher, which meant that the cantilever should be fabricated in silicon oxide, since the selectivity of silicon to oxide etching is about 250:1. Cantilevers of two different sizes were fabricated.

The backgate layer can either be placed all over the chip, or at a specific location under the electrodes. The latter requires an extra masking step that defines the backgate shape and it was decided for simplicity to use a backgate under the entire chip, which is compatible to most structures used in the literature for investigating gating of nanotubes. Two materials were tried, amorphous silicon and polysilicon. The insulation of the backgate from the electrodes was done by deposition of a silicon oxide layer on top of the backgate. Deposition instead of growing preserves the underlying polysilicon or silicon layer from being oxidised.

The electrodes were designed so that the field was the strongest in the gap between the electrodes. All corners of the electrodes were rounded to reduce the field gradients there as much as possible. A simulation of the field from the electrodes in 3D space was done in FEMLAB. Figure 7.9 shows the calculated gradient for one of the electrode geometries used on the probes when a voltage of 10 V p-p is applied across the electrodes.

Three electrode layouts were designed (shown in Figure 7.10) with two different gap sizes, 1 and 2 μm, the final mask design, however, contains gaps up to 3 μm. This was due to the limitations imposed by the mask producer. Since the sizes are still large enough for nanotube DEP to work, there was no need to redesign the masks. The rounded ends of the electrodes are for alignment purposes.

Instead of putting a layer of a material on top of the probe as the encapsulation layer, which would increase the stress on the cantilever, we connected the electrodes to the bonding pads using titanium lines, the surface of which will oxidise and thus create the necessary protection of the electrodes on the bulk of the probe. The thickness of this native oxide layer was increased by exposing the titanium to a flow of O_2.

Electrical connection to the chip was to be done by bonding, so bonding pads were made of titanium with gold deposited on top. Figure 7.11 shows the various layers of the chip as they were described above and as they were fabricated.

7.2.2 Fabrication process

An overview of the fabrication process is shown in Figure 7.12. This final process was the result of extensive investigation done as part of an M.Sc. project and

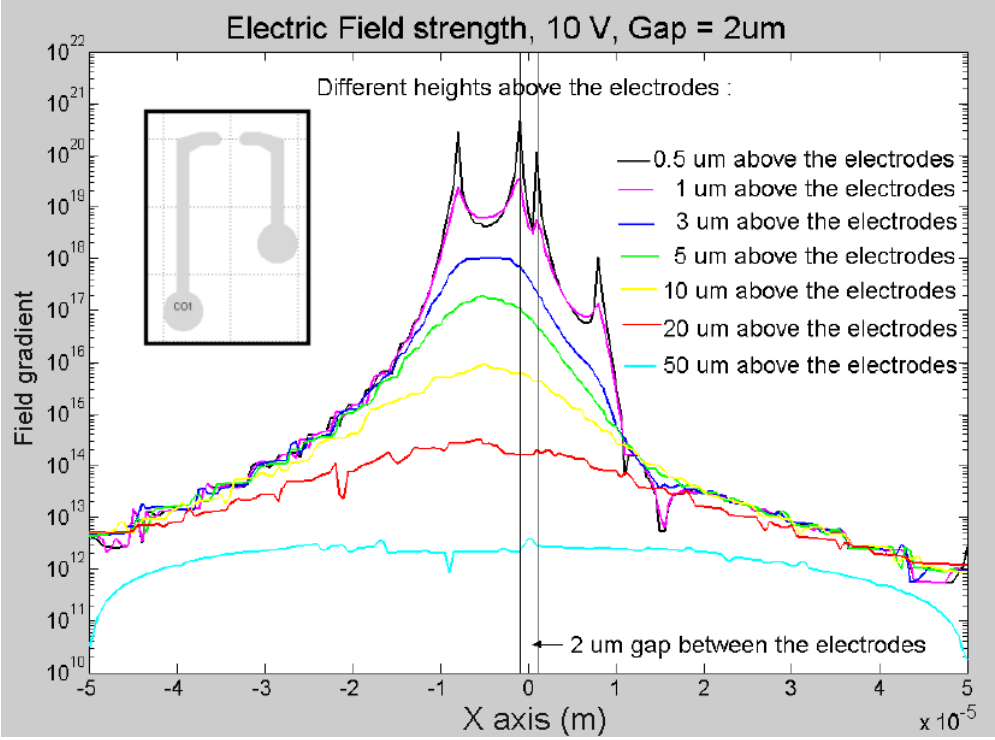

Figure 7.9: The calculated electric field gradient for various heights above the electrode plane. The peaks correspond to the electrode edges. The inset shows one of the electrode geometries found on the probes. The gap between the electrodes is 2 μm.

presented in [128].

A double polished silicon wafer of nominal thickness of 350 μm was used and a 500 nm thermal oxide was grown on top. Then 200 nm of polysilicon were deposited in an LPCVD system and on top of these a 150 nm TEOS oxide was deposited. This was further annealed at 1150 ^oC for 2 hours in order to reduce the stress of the layers and improve the surface smoothness and the quality of the oxide.

Then a positive photolithography step was used in order to define the chip structure. The chips were defined by etching the TEOS oxide, the polysilicon and the thermal oxide using BHF (Buffer HF), RIE (Reactive Ion Etch) dry etching and BHF respectively.

A negative photolithography process was then used in order to etch a hole in the backgate oxide with BHF so that contact to the backgate was achieved. The 3rd mask was also a negative photolithography step for defining the titanium wires and bonding pads. Before deposition of Ti a 15 sec BHF etch was done in order to enhance the adhesion of the Ti to the oxide. Then 200 nm of Ti were deposited using the Alcatel and the Ti wires were formed using lift-off.

Next the electrodes were deposited using a negative photolithography process. 20 nm of Ti and 180 nm of Au were deposited and a lift-off process was done after the metal deposition.

Before patterning and etching the backside the remaining polysilicon and oxide layers on the backside had to be etched. This was done by first protecting the

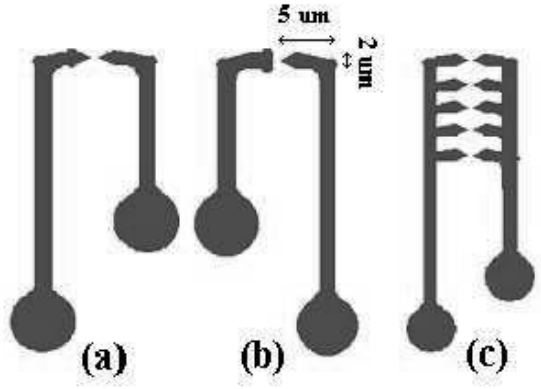

Figure 7.10: The three electrode geometries used on the cantilever probes. In **(a)** the electrodes are both sharp creating a very strong inhomogeneous electric field at the corners. In **(b)** one of the electrodes is flat and the other sharp, in order to enhance the electric field on the sharp electrode. In **(c)** a multi-electrode structure is shown for simultaneous deposition of nanotubes in more than one gap, which would increase the surface area. The electrode spacing on the mask is 1 μm.

front side of the wafer with a 9.5 μm thick resist baked at 120 ^{o}C for 5 minutes, then etching the polysilicon in a HNO_3-HF-H_2O bath and finally etching the oxide in BHF. The resist was removed in acetone from the front side.

For releasing the chip the backside was etched using the ASE. For reasons described with great detail in [128] a 900 nm aluminium layer was deposited on the frontside to act as a stop layer and a negative photolithography process was used on the backside in order to define the etch mask, which was a 500 nm thick layer of aluminium. The etch was done in two steps. The first 330 μm of the silicon wafer were etched using a deep etch recipe etching at a rate of 4.75 μm/s and the last 20 μm were etched using a shallow etch process etching at a rate of 1.7 μm/s.

After the etch the aluminium layers were removed in an aluminium etch bath. Figure 7.13 shows images of the chips taken at various stages during the fabrication process.

7.2.3 Characterisation of chip

The fabricated probes were examined both structurally and electrically in order to evaluate the success of the process. Structurally the chips were quite well defined, no stress was observed in the cantilever and the dimensions generally agreed with the design. The only problem was found in the dimensions of the gaps between the electrodes. These were larger than the designed 1 and 2 μm, mostly around 3 μm. Other dimensions on the chip were quite well reproduced, apart from the underetched and overetched polysilicon and oxide layers as shown in Figure 7.13(c). We note that this seemed to happen randomly around the wafer.

While the probes looked perfect, there seemed to be electrical contact between the electrodes and the backgate on the majority of the chips. From 100 examined

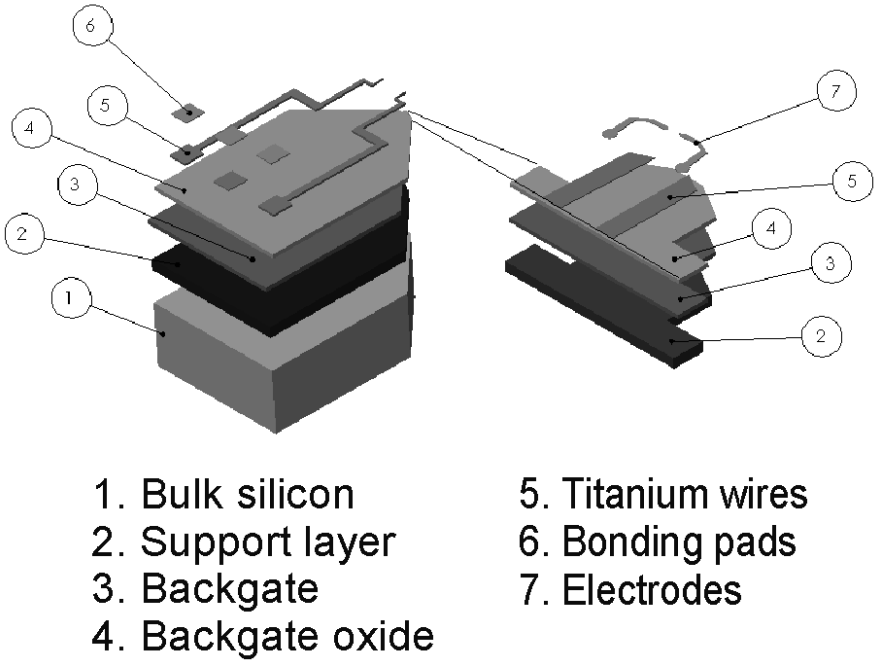

Figure 7.11: A schematic of the probe showing the various layers.

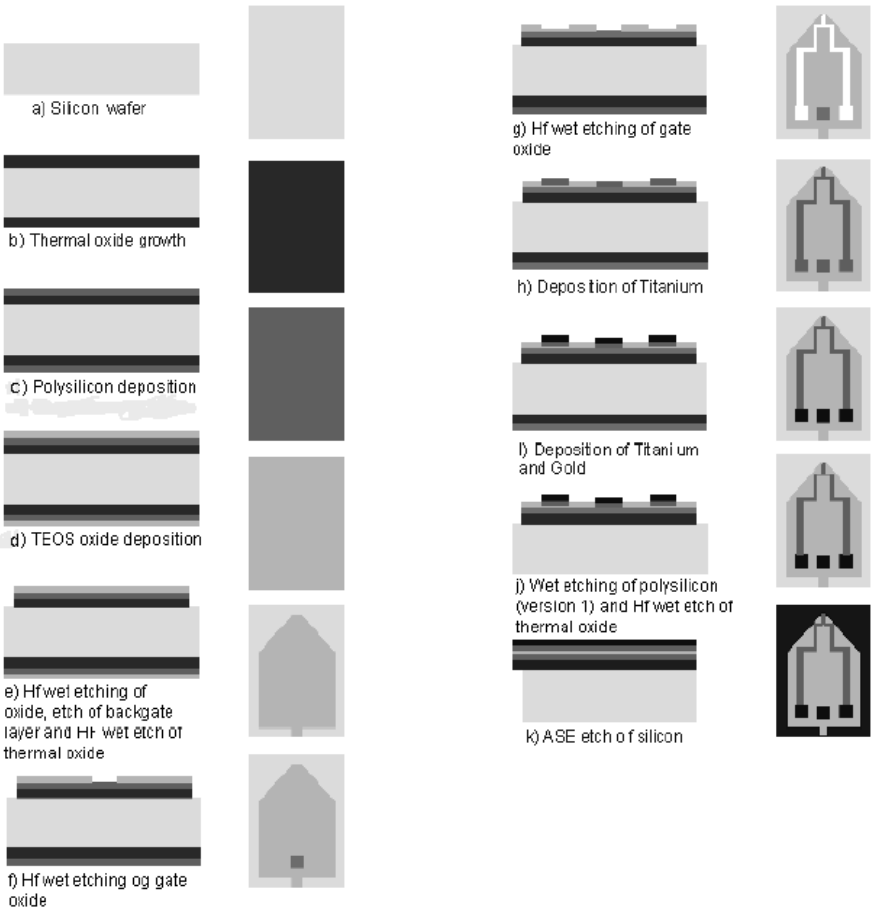

Figure 7.12: The fabrication process for the probes.

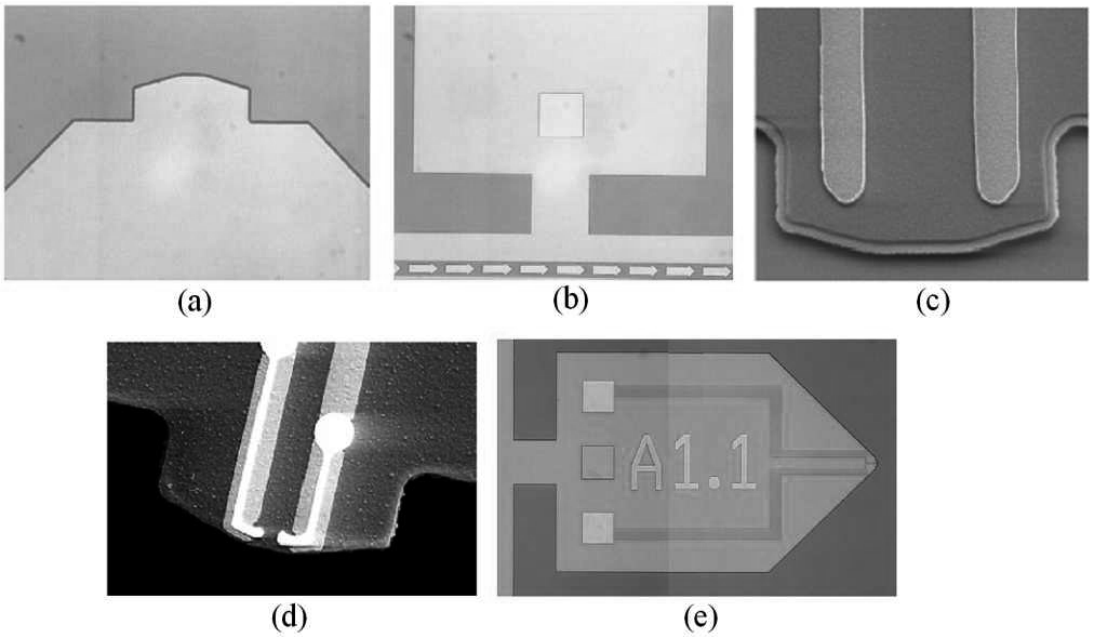

Figure 7.13: Images taken during the fabrication process: **(a)** Optical image of the short cantilever. **(b)** Optical image of the hole to the backgate. **(c)** SEM image of the titanium wires on a cantilever. The image also shows that the etching steps during chip definition are not anisotropic. The polysilicon layer is underetched and the backgate oxide is overetched. **(d)** SEM image of the deposited electrodes on the cantilever. **(e)** The finished chip after the ASE etch.

chips only 10 did not show this problem, which points to a design error. It is quite probable that placing the electrodes very close to the cantilever edge (2 μm) is the reason for the short-circuit, as the cantilevers are sometimes smaller than specified, so that the titanium wires make contact to the polysilicon.

We measured the current flowing between the backgate and one of the electrodes while sweeping the voltage from 0 to 5 Volts. The result is shown in Figure 7.14, where there clearly is a considerable leakage current through the backgate oxide of nA order, even at relatively low voltages.

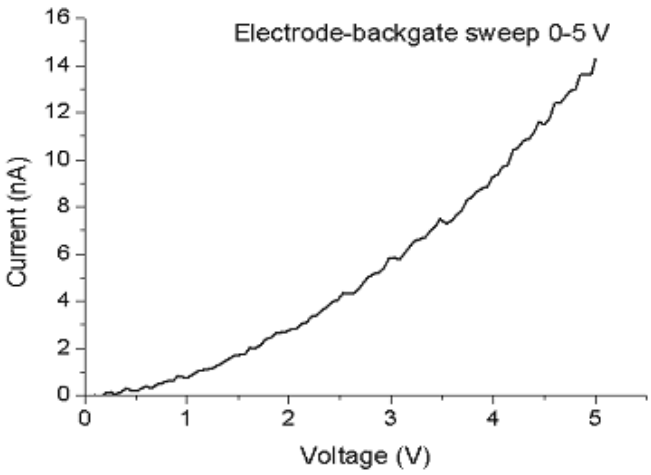

Figure 7.14: The leakage current through the backgate oxide as a function of voltage across the backgate and the electrodes.

A possible reason for the high leakage current could be that the surface roughness of the polysilicon layer underneath is actually quite big, measured at $30 - 80$ nm. With the oxide thickness being 150 nm there are regions under the electrodes, where the oxide thickness is only half of what we expected. Indeed, when replacing the polysilicon layer with amorphous silicon, which has a surface roughness of only 2 nm, the leakage current was very small in 3 out of the 4 chips tested, under the sensitivity of the Keithley sourcemeter.

When the current between the two electrodes was measured, without any nanotubes bridging the gap, the curves of Figure 7.15 were recorded. The leakage current was half that between the backgate and one electrode, which leads us to believe that the current simply flows from one electrode through the backgate oxide to the backgate and then through the oxide again to the other electrode. Again, when the backgate layer was replaced with amorphous silicon there was no measurable current flowing between the fingers, also when a voltage was applied to the backgate.

7.2.4 Nanotube assembly

Using the cantilever probe setup described in section 4.4.2 three assembly experiments using the four chips that survived the electrical characterisation

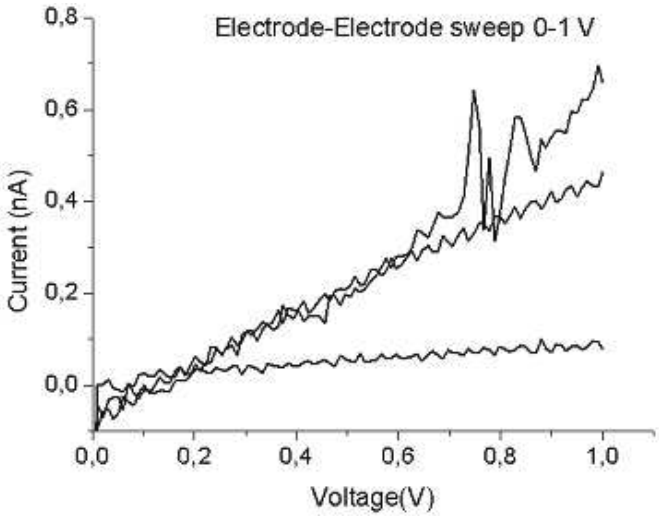

Figure 7.15: The leakage current when a potential is applied between the two unconnected electrodes.

experiments and a DCB solution of carbon nanotubes were performed. From tests on planar structures it was found that the best results were obtained for a frequency of 1 MHz and a voltage of 10-20 V p-p and therefore these values were used on the four cantilever chips. Figure 7.16 shows a picture of a cantilever with an assembled network of nanotubes. The nanotubes are deposited not only between the gold electrode but also between the titanium wires. Moreover, the nanotubes are remarkably aligned with the field lines. Finally, nanotubes seem to originate on the electrodes and come to the cantilever edge at almost perfect right angles.

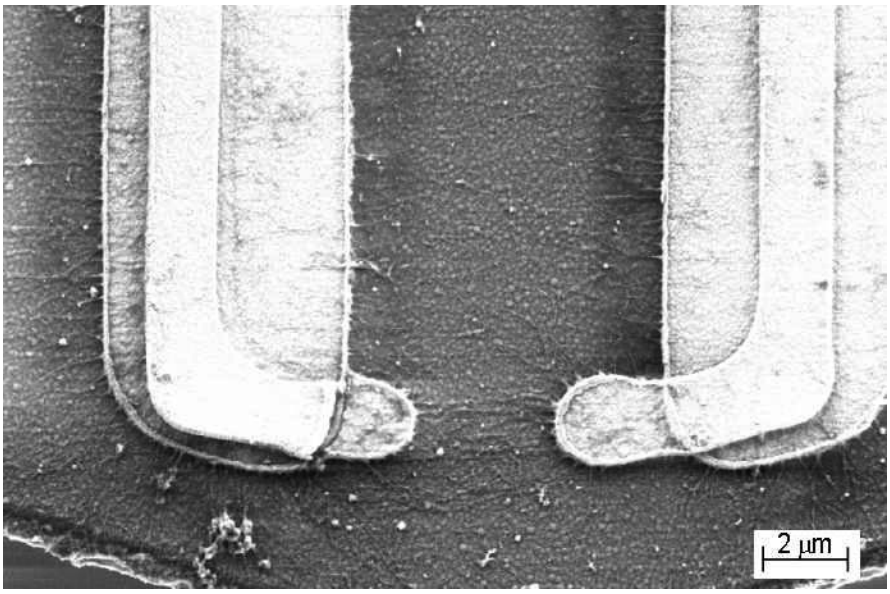

Figure 7.16: One of the assembled networks on the fabricated cantilever probes. Nanotubes have been deposited all over the areas where the solution had been in contact to the probe.

Given the fact that current leaks through the backgate oxide already at 1 V

and that we are using a 10 V p-p voltage for the assembly experiments, it is almost certain that this voltage is applied not only between the electrodes but also between the electrodes and the backgate. DEP assembly experiments, where the voltage was applied between the backgate and one electrode have been done in the past [41] for creating planar nanotube networks with success. The SEM image of Figure 7.16 points to the existence of an electric field towards the boundary of the cantilever, a place, where the polysilicon backgate is exposed from the backgate oxide.

The resistance of the assemblies on these chips was in the MΩ range, which agrees with the experiments with the DCB solution presented in section 5.2.

7.2.5 Preliminary results

It was shown in [75] that it is possible to selectively burn metallic nanotubes contained in a bundle of nanotubes by passing a high current through them while the semiconducting nanotubes have been depleted using the backgate. Similarly, we tried to destroy the metallic nanotubes assembled on the fabricated cantilever structures. First the resistance of the nanotube network at low bias (voltage sweep from -100 mV to 100 mV) was measured for gate potentials from 0 to 5 V with a step of 1 V. Then a positive potential of 30 V was applied on the backgate to deplete the semiconducting nanotubes and a voltage of 20 V was applied between the electrodes for 10 seconds. Afterwards the gate potential was changed again from 0 to 5 V and the resistance of the network was measured in the same way as before. Figure 7.17 shows the results. It is clear that after this process the resistance of the nanotube network has both increased and responds more strongly to backgate voltage variations.

This experiment was repeated with the same results on two more probes. Even so, it is questionable whether or not this has anything to do with the nanotubes. In Figure 7.14 it can be seen that the current through the backgate oxide increases in an exponential way. By applying the 30 V onto the backgate, a breakdown of the oxide could have occured, which would increase the leakage current. As both curves of Figure 7.17 are exponential, it is likely that this is the cause of the different behaviour and not the increase of the percentage of semiconducting nanotubes in the network. This assumption is strengthened by the fact that application of a 20 V voltage on a 3MΩ resistor would result in a current of 7 μA, which is smaller than the observed current breakdown of 12 μA [129, 130] or the saturation current of 25 μA in [131] for a single metallic nanotube. Given that we have a network of nanotubes and not a single one, the current through each one will be even smaller.

The final test involved the exposure of the probe to a nitrogen flow while the backgate potential was changed from 0 to -4 Volts at steps of 1 V. The resistance was determined by monitoring the current through the electrodes while sweeping the voltage from -100 mV to +100 mV. The same experiment was done in atmospheric air and the results are shown in Figure 7.18.

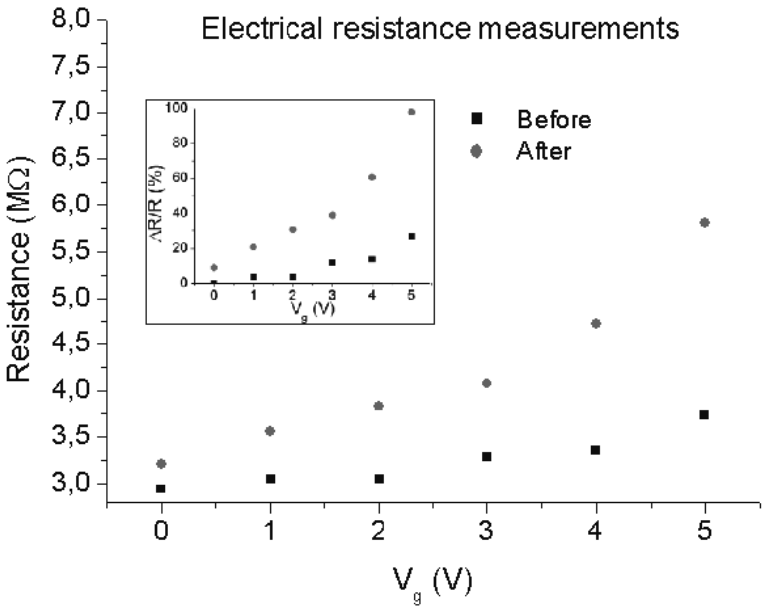

Figure 7.17: The resistance of the probe before and after the destructive process. The increased sensitivity of the network to the backgate indicates that the percentage of semiconducting nanotubes in the network is larger after the burning.

The probe is apparently more sensitive to the backgate voltage when it is in air, with a nitrogen concentration of 80%, than when the oxygen concentration in the immediate environment is smaller. Although such behaviour would not be wanted in a sensor, the results can be misleading. In section 6.4 it was observed that when the nanotubes were exposed to a direct nitrogen flow, their resistance increased. This behaviour was attributed to mechanical effects, the nitrogen flow disturbing the fragile contact between the nanotubes and the electrodes, and thus increasing the contact resistance. According to [53] the saturation value of the current in current vs gate voltage plot is a measure of the contact resistance between the nanotube and the electrodes. It can be shown that the two curves corresponding to air and nitrogen fit curves with the same growth constant but different saturation values for large negative gate voltages. If we interpret this result according to the observation in [53], it would mean that during the nitrogen exposure the contact resistance is larger than what it is in air, something that could indeed be the case due to the experimental method.

Another explanation lies in the cause of the p-type behaviour of the semiconducting SWCNTs. There are several explanations as to why a semiconducting nanotube is a p-type semiconductor [55], such as adsorption of oxygen from the atmospheric air on the surface of the nanotube. Under direct nitrogen flow oxygen could be removed from the nanotube, making it less doped and therefore less sensitive to changes in the backgate.

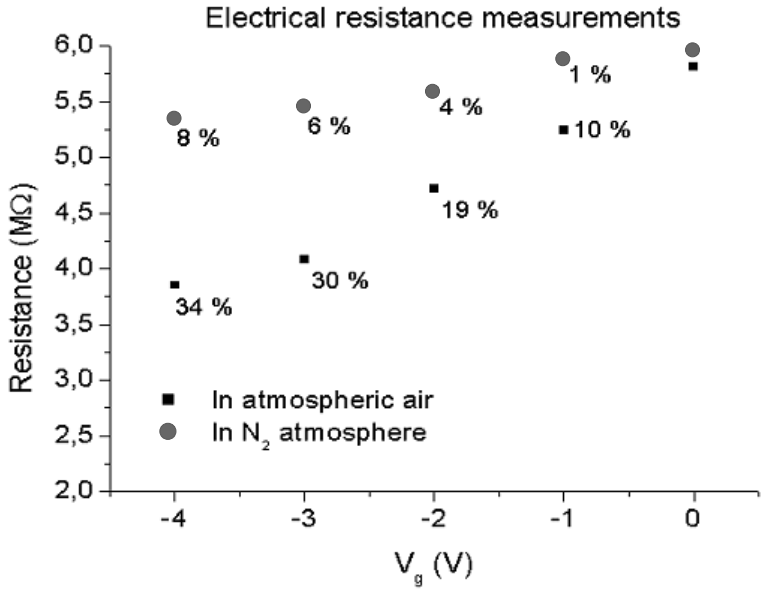

Figure 7.18: The resistance of the probe during exposure to a nitrogen flow and in air during gating. The probe is more sensitive to gating when in air.

7.3 Summary

We have shown that the fabrication of a cantilever probe specially designed for dielectrophoretic assembly, characterisation and tuning of carbon nanotube networks for sensing purposes is possible, although the yield of the probes due to processing and design errors was very low.

Selective burning of the metallic nanotubes present in the assembled nanotube networks was tried and although the results show a greater sensitivity to gating after the burning process, they can also be explained in terms of an increased leakage current due to backgate oxide breakdown.

Finally, it was attempted to measure the sensitivity of the sensor under nitrogen exposure. Though a change in the sensitivity of the sensor to gating was observed, it is unclear whether it originates from the nanotubes themselves or from the contact resistance. More experiments under better controlled conditions need to be done.

Chapter 8

Microfluidics and Nanotube sorting

In this chapter our efforts to build a microfluidic channel that would allow for better assembly and even sorting of metallic and semiconducting nanotubes are described. Several fabrication technologies were tried but all of our devices were unusable. However, Raman spectroscopy was used on several DEP assembled chips of planar structures that indicated that sorting could be difficult in the frequencies of up to 10 MHz, in contrast with the results of simulation 1 (section 3.2.2) and previously published experimental results ([73, 99]), but in agreement with the results of simulation 2 (section 3.2.3).

8.1 Why Microfluidics?

Although most of our experiments were done on planar structures, cantilever structures are still preferable for applications where proximity to a surface is needed. A cantilever structure can come close to a surface and with a nanotube at the tip acting as a sensor element be used as a surface property mapper, for instance to locally monitor byproducts of chemical reactions. A planar structure would be more difficult to handle when it comes to surface mapping, however is useful in for example gas sensing applications. With nanotubes suspended between cantilevers, the exposed surface of the nanotubes is larger, and interference from the substrate is avoided.

Our current cantilever probe setup has a number of disadvantages. The solution at the edge of the tube is exposed to air and thus evaporating continuously inducing liquid flow in the droplet that under all likelihood interferes with the DEP forces. Moreover, when the conductivity of the liquid is high, a large flow is developed towards the main probe surface, leading to surface contamination. In order to solve the first of these problems, a closed channel structure, where evaporation is not taking place, is wanted. Moreover, a fluid flow in the channel could align the tubes with the flow (as shown for nanowires in [18]) and perhaps aid the dielectrophoretic process if the electrodes are placed in such a way in the channel

so that the field lines fit with the flow lines.

A requirement on such a setup is that there is an access point for the cantilever probe to come in contact with the liquid. The hole would have to be as small as possible so that no leakage of the liquid through it occurs. An illustration of a possible setup is shown in Figure 8.1.

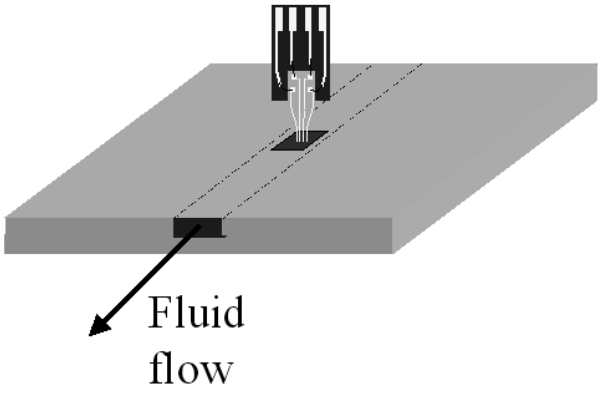

Figure 8.1: Schematic of a microfluidics setup with a small hole on the top, where the probe enters the channel.

We fabricated four different microfluidic devices using three fabrication technologies. These are described below.

8.1.1 PMMA chips using a CO_2 laser

The structure of Figure 8.1 was realised on PMMA chips patterned using a CO_2 laser ablation system. Two designs were made, one where the entry point to the channel was on the top of the device and one where it was on the side. These are shown in Figure 8.2. There are two inlets and one outlet. The two inlets were designed in order to allow for flushing the chip without the need of changing the tubing. It was also planned to use the second inlet as a means of diluting the solution while doing the experiment. Mixing is not possible in these small channels, since the flow is laminar, however, it can occur through diffusion. The meander structure was made in order to increase the channel length so that diffusion can occur.

In the design of Figure 8.2(a) the hole for the probe should be about 50 μm in diameter. Making such a small hole in a thick plastic piece is difficult, therefore a membrane of very small thickness should be fabricated around it, so that the laser only has to break through that. This turned out to be impossible to do with the CO_2 laser. Therefore in some subsequent designs a layer of aluminium or teflon tape were used to make the hole and these were placed in between the two plastic pieces during the bonding. However, no matter how small the flow velocity was, the liquid would in all cases flow through the small hole. In the case of the teflon layer, it was observed that it would inflate until a point, where the pressure under it became too big and the liquid would burst out of the hole.

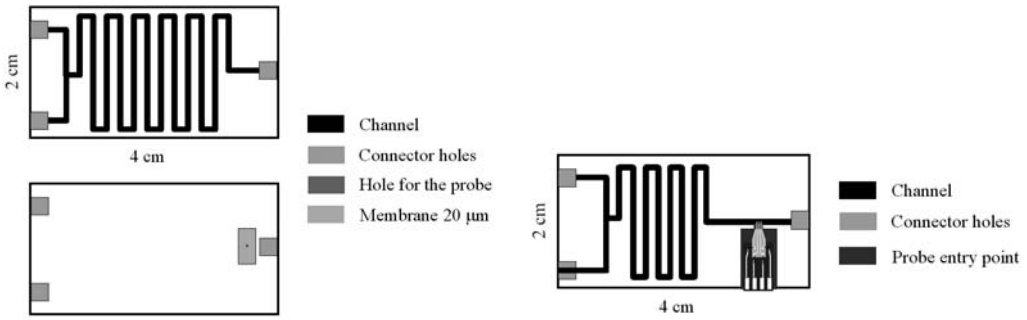

(a) Top access (b) Side access

Figure 8.2: (a) PMMA channel with top access for the probe. The two plastic pieces are bonded together in an oven. **(b)** PMMA chip with a side access for the chip.

Other problems included alignment difficulties of the two plastic pieces as well as insertion of the probe through the small hole. This setup was therefore abandoned.

Figure 8.2(b) shows a second variant of the PMMA design, where the entire laser cutting happens on one plastic piece. The probe enters the channel from the side of the chip. Holes are etched through the plastic chip so that the dimensions of the hole and the ceramic fit. Bonding to a cover PMMA chip is needed in order to seal the channel. This is done using the bonding oven. The problems of this structure arose mainly during the bonding. The probe holder hole would change dimensions during this process and the chip could then not fit in the hole.

8.1.2 Fabrication in silicon

As it was the small hole for the probe access that was posing the most problems for the PMMA chips, we decided to do the same process but this time in silicon, where etching of deep holes with controlled dimensions is possible.

The fabrication process of Figure 8.3 was used. We used transparency masks, which are inexpensive and quite accurate for structures bigger than 10 μm. That meant that alignment was possible but not very precise and that the whole process would have to be done on one side of the wafer.

Etching through the wafer in the first step is possible using the Advanced Silicon Etcher (ASE), a machine able to etch silicon with almost vertical walls at a rate of about 5.5 μm/s. However, a carrier wafer is necessary, so that the ASE chamber is not damaged. The bonding of the carrier wafer is achieved by pressing the two wafers together with a resist layer in between.

Although we were able to both reproduce our structures by using the transparency masks and create holes much smaller than those achieved with the CO_2 laser cutter, the process never produced finished chips. It was the carrier wafer bonding process that caused the problems. Usually, after the first 50 μm of the wafer were etched, the resist mask of 9.5 μm thickness had disappeared and the process continued by thinning the entire wafer. The disappearance of the resist was due to overheating of the wafer because of inefficient cooling. This in turn can be

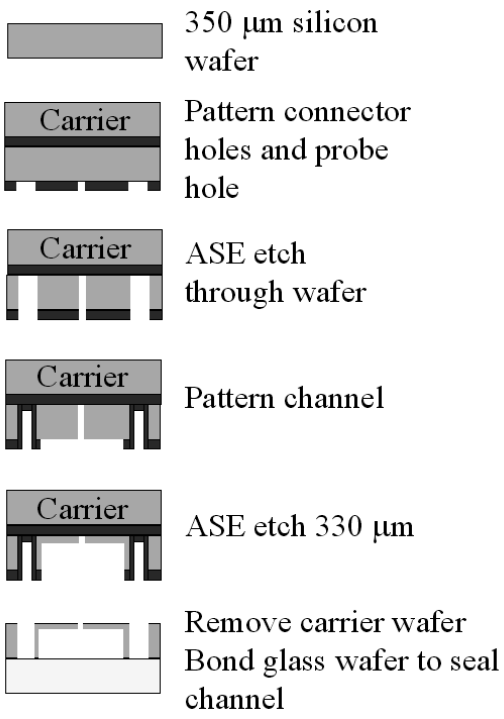

Figure 8.3: The fabrication process used to produce a silicon microfluidics chip with a hole for probe entry.

traced back to the bonding and perhaps the poor heat conducting properties of the resist.

Structures similar to ours were later successfully fabricated using a slightly modified process, as is described in [132]. This shows that fabrication of our chip in silicon is in fact possible.

8.1.3 PEEK setup

One of the problems of the top access approach is the precise positioning of the probe in the top hole without breaking the cantilevers. In order to control this positioning a setup previously developed in [133] was used. An image of the setup is shown in Figure 8.4 and it is made using the polymer material PEEK, chemically inert and creep resistant at high temperatures.

The setup is divided in three parts. A plug, a box lid and a box as shown in Figure 8.5. A straight channel runs through the box with access to the probe in a chamber in the middle of the box. To fasten the plug in the box a box lid is slid on. The plug can hold a probe with glue. By gluing the probe into the plug it is easy to insert the probe into the box in a controlled way. When the plug is inserted into the box, the box lid is slid on and the setup is ready for experiments.

The problem with the setup lies in gluing the probe to the plug. Although there is a slit for the bonding wires on the probe, it can be difficult to avoid bending or breaking of the bonding wires, resulting in either short circuits between the

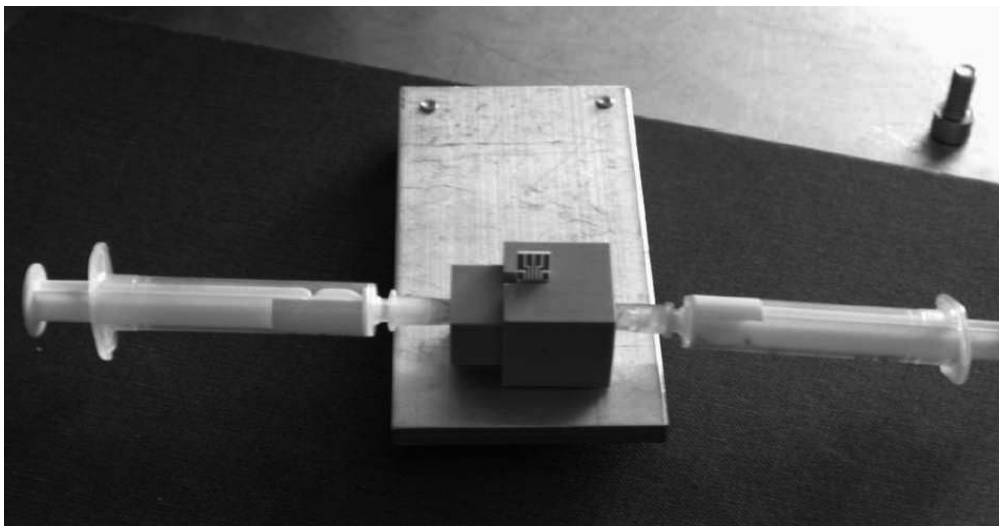

Figure 8.4: The PEEK setup with syringes placed at the inlet and outlet and a probe inserted on the top.

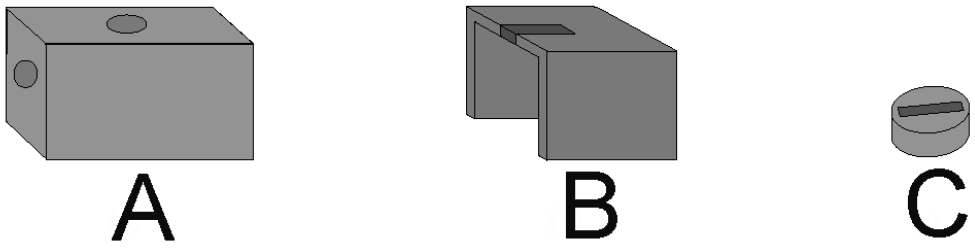

Figure 8.5: Schematics of the three components of the PEEK setup. The box containing the channel and the hole for the plug is shown in A, the box lid that keeps the plug in place is shown in B and the plug, where the probe is glued on is shown in C.

fingers, or no electrical connection to the probe, which prevented the setup from being used.

8.2 Nanotube sorting

In a recent experiment [73] the authors reported that separation of semiconducting from metallic nanotubes is possible by dielectrophoresis. They used a structure with an electrode spacing of 50 μm onto which a voltage of 10 V p-p at a frequency of 10 MHz was applied for 10 minutes while a droplet of SDS dispersed nanotubes was on top. Using Raman spectroscopy they showed that after their experiment the metallic to semiconducting nanotube ratio on the electrodes was 4:1, as opposed to 1:2 in the reference sample.

We tried to repeat this experiment using 3 different frequencies on a total of 12 chips, with 4 chips per frequency and each chip containing 2 assembly sites. The chips were those of Figure 4.9(b) and the frequencies used were 10 kHz, 1 MHz and 10 MHz. A droplet of 8 μl of solution was placed on top of each chip for

5 minutes and was subsequently blown off the chip using a stream of nitrogen. Raman spectra of the electrode gaps were taken at Cambridge University at a laser wavelength of 514 nm, 633 nm and 785 nm. Figure 8.6 shows the results obtained, where the various spectra have been averaged both from spectra from several sites on each chip and from 3 chips at each frequency. In general there is little difference between the various chips at each frequency.

A close up of the radial breathing mode and the G-mode region is shown in Figure 8.6. Based on section 2.1.6 we can easily calculate that for the 514 nm wavelength the metallic nanotubes should have peaks at 215.7 - 275 cm^{-1}, while the semiconducting nanotubes appear at 142.5 - 206.9 cm^{-1}. For the 633 nm excitation wavelength the metallic nanotubes appear at 172 - 219 cm^{-1}, while the semiconducting nanotubes at 261 - 323 cm^{-1}. The spectra at 785 nm excitation wavelength only show semiconducting nanotubes. Moreover, an enhancement of the metallic nanotubes would lead in the suppression of the G+ mode and the broadening and shifting of the G- band to lower energies.

Our samples do not show any of the behaviour typical to metallic nanotube enhancement. On the contrary, if one calculated the area ratio of metallic to semiconducting nanotubes (based on the Raman intensity) for the reference sample and the assembled samples, then a clear enhancement of the semiconducting nanotubes is observed for frequencies up to 1 MHz. Moreover,no suppression of the G+ band nor broadening or shift of the G- band is observed, although the G- band is enhanced in the assembled samples. We note that for the 514 and 633 nm laser wavelengths the enhancement of the G- band is largest for the 10 kHz samples and approaches the levels of the reference sample as the frequency increases. As we have seen in chapter 5, the networks become increasingly aligned with the field lines and free of impurities with increasing frequency, with the 10 MHz samples resembling the reference sample the most.

The situation is slightly different for the 785 nm wavelength that only probes the semiconducting carbon nanotubes. One interesting observation is that for all investigated frequencies enhancement of the peak at 270 cm^{-1} with respect to the reference solution is observed. A second observation is that for 10 kHz and 1 MHz the area under the curve is clearly smaller compared to the reference solution, while for the 10 MHz samples the area under the curve is larger compared to the reference solution. While it is tempting to conclude that we have observed enhancement of the metallic nanotubes at 10 kHz and 1 MHz, one should note that the difference in intensities could simply be attributed to decreased or increased alignment and to the presence of more or less nanotubes in the sample. For the 514 nm and 633 nm spectra comparison was possible by means of the ratio between metallic and semiconducting nanotubes, as both were probed by Raman. This is not the case for the 785 nm, since only one kind of nanotubes can be probed.

Based on the Raman spectra we conclude that our experiments do not agree with those described in [73]. Recently it was shown [134] that the apparent change in the Raman spectra found in [73] could be an effect of the choice of reference sample, particularly by its morphology. The authors found that the Raman spectra of their DEP assembled sample showed an area ratio enhancement

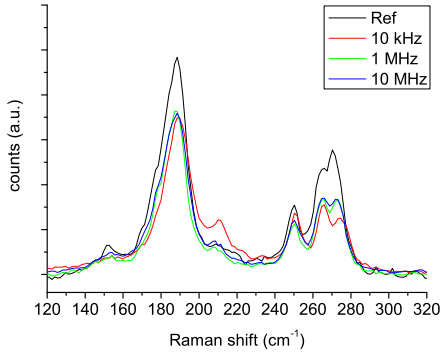

(a) Radial Breathing mode - 514 nm

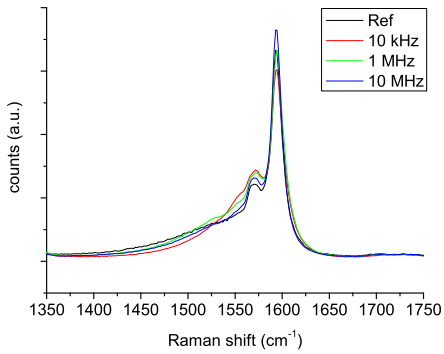

(b) High energy mode - 514 nm

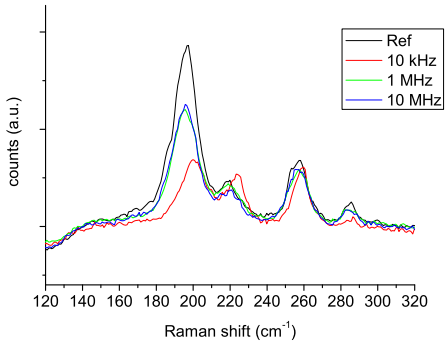

(c) Radial Breathing mode - 633 nm

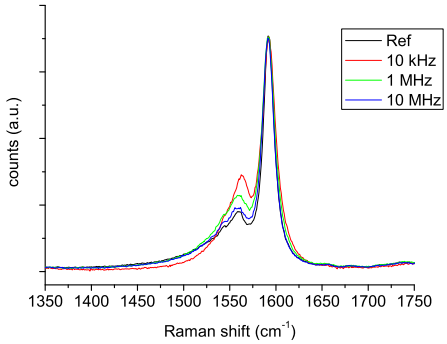

(d) High energy mode - 633 nm

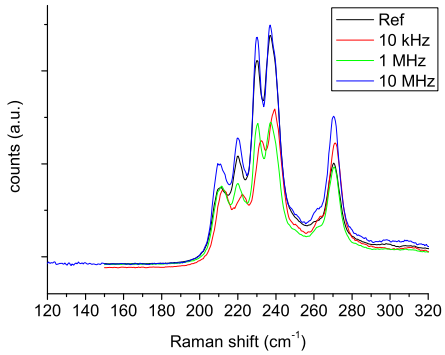

(e) Radial Breathing mode - 785 nm

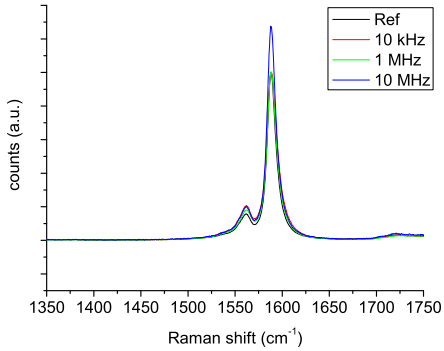

(f) High energy mode - 785 nm

Figure 8.6: **(a)** A close up of the radial breathing mode (RBM) for an excitation wavelength of 514 nm. **(b)** A close up of the high energy modes for an excitation wavelength of 514 nm. **(c)** A close up of the radial breathing mode (RBM) for an excitation wavelength of 633 nm.**(d)** A close up of the high energy modes for an excitation wavelength of 633 nm. **(e)** A close up of the radial breathing mode (RBM) for an excitation wavelength of 785 nm.**(f)** A close up of the high energy modes for an excitation wavelength of 785 nm.

of metallic over semiconducting nanotubes of about 40%, when the control was made by drying an SDS solution droplet on a substrate. However, the same enhancement was observed on a control sample made by precipitating the SDS solution using acetone and drying it. While the first control contains ropes of about 100 nm in diameter, the second contains ropes of 5 - 20 nm in diameter. They therefore conclude that there is no evidence of metallic nanotube enrichment under the conditions of the experiment described in [73].

Our control sample involved drying a droplet of the SDS solution on a gold substrate. When we examine the control sample under a SEM we generally do not see any differences in the diameter distribution on the control and on the DEP assembled chip. This could also explain the lack of any differences between the reference sample and the DEP samples.

8.3 Sorting in a microfluidic channel

The aim of this experiment was to experimentally evaluate the simulations described in chapter 3. Gold electrodes fabricated on a glass wafer and embedded in an channel made of SU8 were used. The structures were originally designed for dielectrophoretic sorting of cells but since the electrode spacing was 10 μm they could also be used for dielectrophoresis of carbon nanotubes.

The process was developed by Anders Wolff and the chips were fabricated in the Danchip cleanroom by lab technicians. The process is described in [135].

The chip was placed on a plastic holder and a lid made of a PDMS layer on a piece of plastic was pressed on top of the chip in order to seal it. This lid also contained the connector tubes to the chips. A schematic of the chip is shown in Figure 8.7.

The use of a PDMS lid on a PMMA plastic piece was the source of extensive leaking. The PDMS layer has to be very homogeneous for the seal to be tight and in our case it was not. Alignment of the seal to the SU8 channel was also difficult, and in most cases resulted in the placement of the connector tubes on the SU8 wall instead of inside the round inlets and outlets. Leaking was observed even at extremely low fluid velocities in the channel.

Another problem was making certain that there was a voltage drop across the electrodes. The POGO pins were difficult to use in the sense that they were often fixed loosely in their holes. They contain a spring, whose purpose is to keep them tight in contact with the electrodes, but unfortunately in our case it was functioning mostly as an ejection mechanism out of the holes.

Due to all the above-mentioned problems only one experiment using a carbon nanotube solution was conducted with these chips. A SEM image (see Figure 8.8) of the electrodes showed that nanotubes had indeed deposited mostly at the corners of the electrodes, which are the sites of the highest electric field.

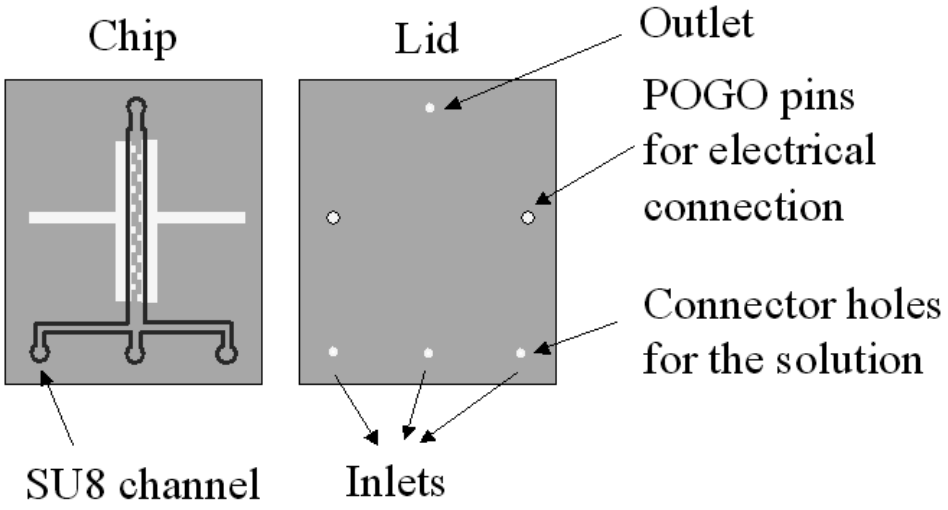

Figure 8.7: Schematic of the chip used for the microfluidic sorting experiments. The chip is fabricated on a glass wafer and the lid is made of a PDMS onto PMMA. The connectors are golden tubes of 1 mm diameter and are placed on the lid.

8.4 Comparison with theory

Although the theory was performed while the solution was flowing through a channel with a certain velocity, we can still at least qualitatively evaluate the static experimental results of the sorting with the theoretical predictions. Based on the Raman spectra from 12 probes, a total of 24 assembly sites, there is little difference between the reference sample and the deposited material on the probes for all examined frequencies up to 10 MHz. The results of the second simulation (Figure 3.19) show that at a frequency of 1 MHz and a fluid velocity of just 1 μm/s the concentration of metallic nanotubes on the electrodes is never larger than 33 %, so the same as that of the reference solution. The results of the first simulation are not confirmed by this experiment, though they are confirmed by the results of the experiments described in [73, 99].

One should though be careful with claiming that the model is absolutely correct. The results in Figure 3.19 are plotted as a function of the number of passes N through the electrodes. For a high N the number of metallic nanotubes on the electrodes will always approach the 33% of the reference. In a real system N could correspond to the number of electrode pairs available in the structure. In the case of the structure used in the experiments there were 14 electrode pairs, so one could argue that $N = 14$. Moreover there is the issue of the time that the solution was left in contact with the electrodes. The simulation predicts that for an SDS solution it could take anything from 40 sec to 160 sec for the nanotubes to reach the electrodes depending on their entry position in the channel. The next cycle through the channel does not begin until the last of the first batch of the nanotubes has left the channel. The situation is of course completely different in the real system, since nanotubes continuously enter into the region around the electrodes due to a heat developed flow as well as forces developed during the

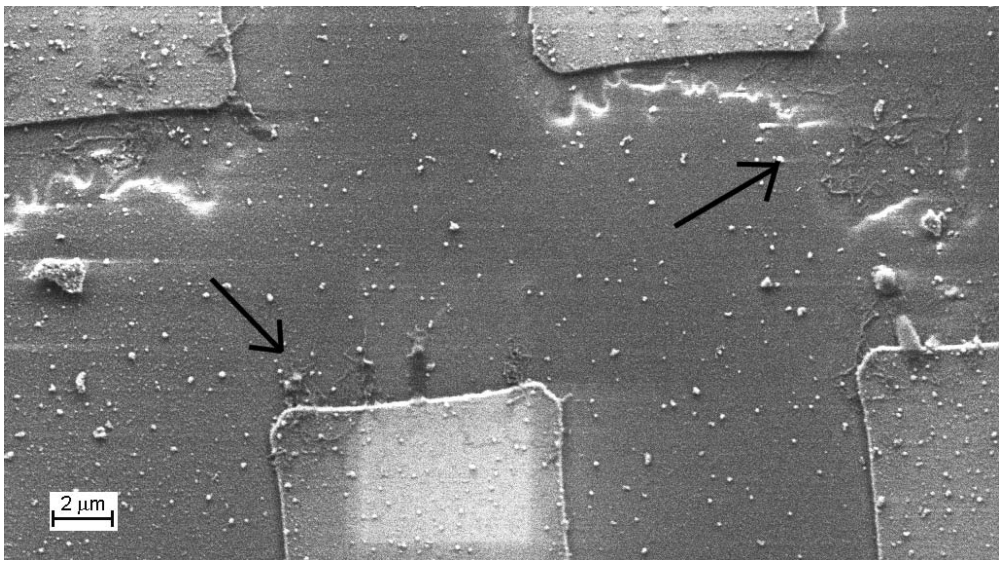

Figure 8.8: A SEM image of the electrodes of the sorting chip after use. There are nanotubes deposited in the gaps between the electrodes, mostly around the corners.

evaporation of the solution. Therefore time plays a crucial role. If nanotubes starting at a certain point in space take 30 seconds to reach the electrodes and the total experiment lasts 5 minutes then this is equivalent to $N = 10$ in the simulation space.

We have derived a simple method in order to take the time into account. We can group the nanotubes according to how much time they need to get to the electrodes based on the results of the simulation. Then we can calculate an equivalent N for each group of nanotubes based on the total experiment time, calculate the relative concentration of metallic and semiconducting nanotubes on the electrodes for each group and then add them together to get the collective result as a function of the time that the solution is in contact with the electrodes.

Figure 8.9 plots the metallic to semiconducting ratio on the electrodes relative to that on the reference sample as a function of the time of the experiment for the results of the second simulation for the SDS solution at 1 MHz. It is seen that the ratio is in fact dependent on the time of the experiment, however, for the 5 minutes that our experiment lasted, we should not expect any enrichment of the metallic tubes with respect to their normal concentration, at least not at this frequency and as far as the parameters of simulation 2 are correct. For a frequency of 100 MHz the ratio is slightly enhanced but still very close to 1.

8.5 Summary

Attempts to build a microfluidic assembly setup have been presented. Use of a laser cutter may be a cheap and easy method for fabricating microfluidic channels, however, our demands on the dimensions of the system are out of the laser's capabilities. Fabrication in silicon was more successful though the chip was never

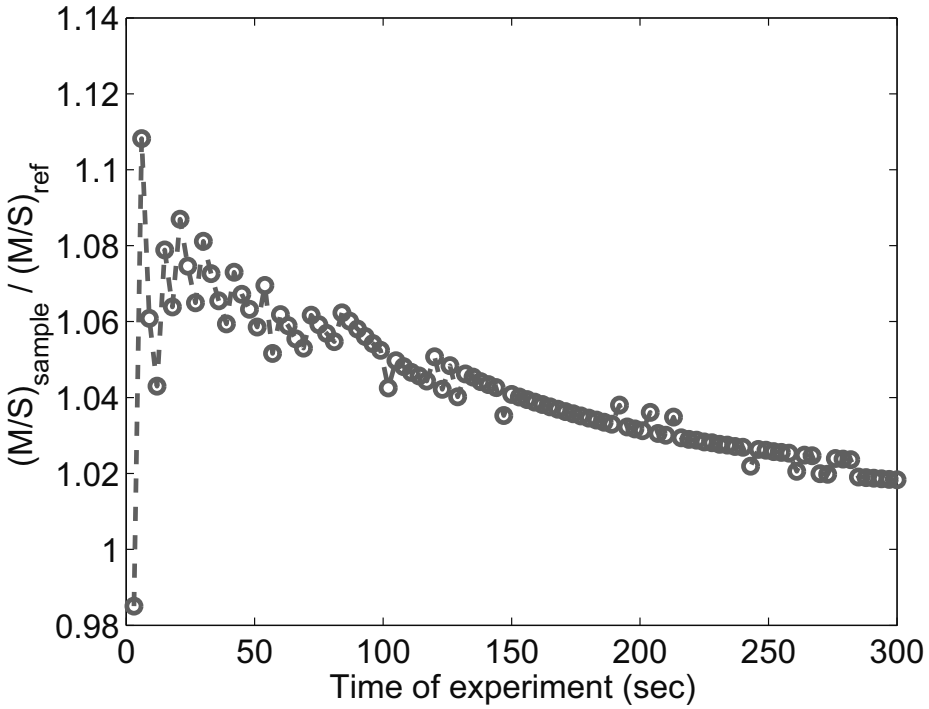

Figure 8.9: A plot of the metallic to semiconducting nanotube ratio on the electrodes relative to that of the reference solution as a function of the time that the solution is in contact with the electrodes. The calculation is based on the results of simulation 2 of chapter 3.2 and is done here for an SDS solution at 1 MHz.

realised due to equipment problems in the cleanroom.

Our results of Raman spectroscopy on samples assembled at different frequencies were also presented. The results show the opposite of what was expected based on the calculations and on work previously published [73, 99], that is, that the semiconducting nanotube concentration is enhanced on the electrodes.

Finally a more realistic calculation of the sorting efficiency of the dielectrophoretic process was presented, showing that the sorting efficiency also depends on the time of application of the electric field.

Chapter 9

Summary and perspectives

In this chapter the various results described in the previous chapters will be summarised and evaluated. Future work and perspectives for the method are going to be presented and discussed.

9.1 Simulation evaluation

A model for the dielectrophoretic assembly of carbon nanotubes on microelectrodes was developed. The nanotube is treated like a stiff cylinder moving in the fluid with its major axis always aligned with the field lines. Due to the high conductivity of nanotubes compared to the conductivity of the liquid in which they are dispersed, the depolarising factor of equation 2.39 plays an important role in the magnitude of the frequency dependent factor in the dielectrophoretic force term, as it was shown in the two microfluidics simulations described in chapter 3.

The most difficult parameters to estimate for the model are the permittivity and conductivity of the nanotubes. In the frequency range of interest for experiments the permittivity does not play a significant role. The conductivity, however, is very important for the results of the simulations. From measurements of the resistance/conductance of single-walled carbon nanotubes we deduced some values for the conductivity of metallic and semiconducting carbon nanotubes. The use of these values with the more elaborate second simulation showed that sorting between metallic and semiconducting nanotubes is not feasible at frequencies under 100 MHz. The result is confirmed by our own experiments described in section 8.2, however, it is in direct disagreement with experiments done first in [73] and later in [99], where separation between metallic and semiconducting nanotubes dispersed in a sodium dodecylbenzene sulfonate solution (SDBS) was demonstrated at frequencies of a few MHz.

In the before-mentioned papers the authors use Raman spectroscopy to compare spectra taken from nanotubes assembled between electrodes with a reference solution and attribute the differences in the spectra to an abundance of metallic relative to semiconducting nanotubes in the DEP assembled networks. However,

it was shown in [134] that differences in the spectra similar to those observed in [73] can occur just from the choice of reference sample. The various contradicting results and interpretations of the Raman data leads us to the conclusion that this method alone is not enough to clarify the dielectrophoretic behaviour of semiconducting nanotubes.

Although the model gives a variety of different results depending on the parameters used, it is a useful instrument for estimating the dielectrophoretic assembly of nanotubes as long as a realistic estimation of their permittivity and conductivity is available.

9.2 Assembly of nanotubes on microelectrodes

In chapters 5 and 7 the assembly of carbon nanotubes on microelectrodes has been described and an investigation of the parameter space for dielectrophoresis has been made. Though one of the goals of the project was to assemble a single or at least few semiconducting carbon nanotubes at the tip of a cantilever and use it to study cells, the majority of the work was done on planar structures because of the easier fabrication process and experimental protocol.

The result of DEP on nanotubes depends on a great number of parameters: the electrode geometry, frequency and amplitude of the electric field, the liquid in which the nanotubes are dispersed and the time of application of the electric field. For most experiments a 1% SDS solution of carbon nanotubes was used, although solutions of DCB were also tested. Each one of the above-mentioned parameters was investigated one by one while the others were constant. Evaluation of the results was done visually in a SEM and by electrical measurements of the two terminal resistance of the assembled nanotube networks. It was shown that the resistance of the assembled networks is inversely proportional to both the applied voltage amplitude to the power of 0.7 and the frequency of the electric field, as well as to the time of application of the voltage. As the resistance is also inversely proportional to the number of nanotubes deposited across the electrodes, the voltage and time experiments agree well with what we would expect from the theory.

The situation is more complicated when it comes to the frequency dependence. Even when we assume a conductivity of 0.1 S/m for the semiconducting nanotubes, a rather pessimistic estimate based on the literature, the results should be practically independent of the frequency up to 1 MHz, as it can be seen from Figure 3.25. Then we would expect a small increase in the resistance as the number of semiconducting nanotubes is decreasing while the number of metallic nanotubes remains unchanged. We observed quite the opposite. Our experiments described in section 5.4 show that the resistance decreases significantly for frequencies from 10 kHz to 1 MHz and then remains practically unchanged, though a slight tendency of an increase at 10 MHz is observed. Given the structural differences of the networks between the frequencies of 10 kHz and 10 MHz, it is quite probable that this behaviour is the direct result of other effects in the low frequencies, such

as soot deposition on the electrodes.

Our results regarding the dependence on the number of electrodes of the resistance show that more reliable networks can be made when a large number of electrodes are addressed in parallel. The reason could be the smaller current passing through each set of electrodes when contact is made, so that burning of the nanotubes can be avoided.

The choice of dispersing medium is also critical. Though single bundle depositions were achieved with an SDS solution, these were rare and mostly large networks of nanotubes were deposited. When the dispersing medium was DCB the depositions were normally consisting of very few nanotube bundles, which were also assembled at regular intervals between the electrodes, as was shown in Figure 5.2. Also, the resistance of DCB dispersed nanotubes was always much larger than that of the SDS dispersed nanotubes. The difference could be attributed to larger contact resistances between the nanotubes and the electrodes, or simply a smaller amount of nanotubes.

9.3 Nanotubes as sensors

The stability of the nanotube networks from an SDS solution was evaluated by measuring the resistance variation over time. In all cases it was observed that the resistance of the nanotube does not remain the same and can drop by as much as 40% within a couple of hours during constant monitoring. It is possible that the measurement itself causes this behaviour by destroying the SDS micelles. This phenomenon is interesting in itself, since SDS is generally quite difficult to remove from the nanotube surface.

The resistance of the nanotube networks is also very sensitive to SEM imaging. Although destruction of some nanotubes during the imaging cannot be excluded from our considerations, it is quite unlikely since eventually, though after a significant time interval, the resistance returns to its original value. Having observed that the SEM destroys the SDS micelles, it is also possible that the increase is related to oxygen desorption in vacuum and adsorption once the samples are out of the SEM again.

We also showed that the resistance of the nanotube network increases dramatically and rapidly during illumination from a common microscope light. As soon as the light is switched off, the resistance slowly drops again in an exponential manner. When the experiment was done in a nitrogen atmosphere the resistance did not drop significantly after the light was switched off. This behaviour is consistent with the mechanism of oxygen desorption and adsorption from the nanotube networks.

A complex behaviour of the nanotube networks during heating was observed. After an initial decrease in the resistance of the network a significant increase is observed even while the heating still takes place. After cooling, the network resistance is almost always larger than what it was before the cooling cycle but

decreases again in an exponential manner, pointing to oxygen desorption and adsorption effects. This is observed to a small degree also for low temperature heating, up to 40 ^{o}C. Understanding these phenomena is very important if nanotubes are to be used in commercial electronics.

From the above it can be seen that almost every recorded behaviour in our experiments has something to do with oxygen influence on the electrical properties of nanotubes, in agreement with [63]. We also note that the observed effects could be the result of the surfactant used to disperse the nanotubes, as investigated in [136], where nanotubes treated so that no sodium contamination was present did not react to oxygen exposure.

9.4 Cantilever microprobe evaluation

In chapter 7 the fabrication, characterisation and usage of a specially designed cantilever microprobe for the dielectrophoretic assembly of carbon nanotubes was presented. The present design was very difficult to fabricate due to a number of critical etch steps that were probably responsible for the observed high leakage current between the electrodes and the backgate. Replacing the polysilicon backgate with an amorphous silicon layer resulted in a significantly lower leakage current.

The yield of the fabrication process was also very low. Only 10% of the examined probes were functional and the reasons are unknown but could be related to the aluminium protection layer in the front side of the wafer for the ASE etch release of the cantilever.

A number of improvements reducing the risk of short circuits can be proposed. The backgate electrode could be reduced in size so that it covers only the part of the cantilever which is under the electrodes. Although this requires an extra masking step, it will reduce the problems associated with a conducting layer at the edge of the cantilever with which the electrodes (placed only 2 μm away from the edge) can come in contact, thus short circuiting the chip.

The titanium wires were used in order to protect the electrodes from contamination, as they would oxidise so that no electrical contact to any overlying nanotubes could be detected. Fabrication of the titanium lines required a brief etching step into the oxide for better adhesion onto the substrate. This was needed because the following deposition and subsequent stripping of the masking aluminium layer caused the titanium lines to lift if the etching had not taken place. Taking this into account, a better solution would be to cover the entire probe apart from the tip and the bonding pads with an insulating substance, such as silicon oxide, silicon nitride, SU8 or even common resist, which is much easier to handle.

Finally, the release of the cantilever in ASE is not optimal because of the problems related to finding a proper masking material capable of both protecting the chamber from the underlying gold layer and efficiently carrying the heat away from the wafer onto the ASE chuck. Wet etching of the silicon with KOH, though

slower, could solve these problems, although some issues remain, such as the protection of the front side during etching. LPCVD silicon nitride is normally deposited for KOH etching for the protection, however, the presence of Au on the frontside forbids the use of the LPCVD oven at DANCHIP. Other methods exist, such as KOH etch compatible resists, or mechanical front side protection. The use of titanium silicide electrodes instead of gold electrodes could also be a solution, since the material is allowed in the LPCVD oven, along with many other silicides [137].

The experiments conducted with these cantilever probes were few and inconclusive, due to the small number of chips that survived the fabrication process and the high leakage current they experienced. The apparent modulation of the nanotube assemblies with backgate voltage can be explained by the leakage current changes with voltage and the differences in the modulation during exposure to nitrogen and atmospheric air can be explained by an increase in the contact resistance due to mechanical effects. Experiments on probes with much lower leakage currents are needed in order to evaluate the performance of these probes and their potential usage as a dielectrophoretic assembly platform for carbon nanotube sensors.

9.5 Fluid assisted assembly and nanotube sorting

In chapter 8 our efforts to build a microfluidic device capable of accepting a cantilever probe for the assembly of nanotubes with dielectrophoresis were described. The most promising method is that of the silicon chip, since the dimensions of the channel and the hole for the probe can be very accurately controlled. The advantage of using such chips as opposed to fabrication of simpler structures with integrated electrodes is that the probe can then be removed from the channel and used for sensor purposes afterwards.

Raman spectroscopy was used to evaluate the possible separation of metallic from semiconducting carbon nanotubes by dielectrophoresis. Our experiments showed a small separation between metallic and semiconducting nanotubes at the investigated frequencies in favor of the semiconducting nanotubes, in contrast to the results of another group [73, 99]. This was covered in section 9.1. As the Raman spectra intensities are greatly influenced by the alignment of the nanotubes relative to the light polarisation, and since our sharp electrodes are not capable of offering large areas where the field lines are all aligned in one direction, some more suitable electrode structures, such as those of Figure 4.9(c), should be used for these experiments. Moreover, a better solution, containing smaller bundles or even individual carbon nanotubes should be realised, so that the results do not depend on the random nature of the amount of semiconducting nanotubes present in a metallic bundle, which will essentially behave as a metallic nanotube and result in misleading Raman spectra.

9.6 Conclusion and perspectives

Nanotubes are an extraordinary material with properties that could one day make them a worthy replacement of the silicon electronic devices. Working with nanotubes is challenging as new interesting behaviour is constantly reported.

Dielectrophoresis is a nanotube manipulation method that has received a lot of attention in the last few years because of the existing potential of being scaled-up to wafer level. Simultaneous deposition of networks or single nanotube bundles onto several microelectrodes has been demonstrated by several groups, though a wafer-scale assembly has not yet been achieved. Similarly no groups have reported the dielectrophoretic deposition of a single SWCNT. Theoretically such should be possible with the method, but good separation of the nanotubes in a solution is needed.

A thorough investigation of the various parameters controlling the dielectrophoretic deposition of nanotubes has been carried out in this project and we have been able to find those parameters that yield the best results in terms of reproducible resistance over several chips and nice structure, meaning few and aligned carbon nanotubes. The application of this knowledge to cantilever structures remains to be done. Initial experiments using an SDS solution showed incompatibility of the currently used experimental setup with the solution due to a large flow developing towards the probe body. A better setup incorporating a fluid flow for better alignment needs to be fabricated.

The wafer-scale assembly was not completed due to a mask fabrication error[1]. For the commercialisation of CNTs as sensors and transistors it is of great importance to demonstrate that dielectrophoresis can in fact be scaled up to wafer level. We note that the same connected network of chips presented in 4.2.3 on the wafer can be utilised for any microstructures, even on the cantilever structures of chapter 7.

Though DCB solutions of SWCNT showed a better assembled nanotube structure than the SDS solutions in terms of bundle diameter achieved in the solution and number of nanotube bundles deposited in the gaps, good electrical contacts with the nanotube networks were difficult to obtain. A difference of 2-3 orders of magnitude of the resistance was seen between DCB and SDS dispersed nanotube networks. If DCB is to be used for dielectrophoresis a new method for contacting the nanotubes needs to be developed. A solution could be the use of e-beam lithography for definition and deposition of contacts on top of the nanotubes.

We demonstrated that phenomena previously observed on single bundles or on thin films of carbon nanotubes can also be observed on large networks of nanotubes. Many observations made in this project can be attributed to oxygen desorption and adsorption, though more experiments are needed in order to verify this assumption particularly for the current induced change in the resistance.

Finally dielectrophoresis of carbon nanotubes can be used for other applications,

[1]This was later achieved and reported in Physica Status Solidi (a), volume 203, No. 6, p. 1088 (2006)

such as the formation of nanochannels by use of the nanotubes as an anisotropic etch mask. A proof of principle was shown in [138] using MWCNTs, although the placement of the nanotubes on the substrate was not controlled and the channels were made on arbitrary positions on the substrate. Dielectrophoresis could provide the necessary positioning control for this application.

Going back to the introduction we can see that with the exception of measuring in a liquid, the goals set for this project have been reached. We have managed to establish and control the dielectrophoretic process so that networks of carbon nanotubes with good contact properties and structure can assemble on either planar or cantilever structures with high yield. Moreover, we have shown that the assembled networks are very sensitive to various environmental conditions as well as mechanical stimuli. We have also investigated the possibility of separating the wanted semiconducting nanotubes from the unwanted metallic ones, either by dielectrophoresis or by selective burning using a special cantilever probe with an in-built backgate.

If measurements in liquids are possible using the new cantilever probe or an improved version of it, then measuring on cells will also be possible. Even if those show that the nanotube is not the proper sensing element for such measurements, the knowledge gained in the course of the project will not go to waste, as a vast number of other applications are available, not only with carbon nanotubes, but also with non-carbon based nanostructures.

Although nanotubes can make very sensitive sensors, they are highly non-specific and quite difficult to functionalise. Other 3D nanostructures, such as peptides, self assemble into cylinders and can be used for various applications, such as casting metallic nanowires [139]. For the characterisation of such structures, dielectrophoresis as the method and the new cantilever probe as the tool could play an important role. An EU application is currently prepared with these peptide nanotubes in mind.

Bibliography

[1] S. Iijima. Helical microtubules of graphitic carbon. *Nature*, 354(6348):56–58, 1991.

[2] S. Iijima and T. Ichihashi. Single-shell carbon nanotubes of 1-nm diameter. *Nature*, 363(6430):603–605, 1993.

[3] D.S. Bethune, C.H. Kiang, M.S. de Vries, G. Gorman, R. Savoy, and J. Vasquez amd R. Beyers. Cobalt-catalysed growth of carbon nanotubes with single-atomic-layer walls. *Nature*, 363(6430):605–607, 1993.

[4] www.nanoelectronics.jp. http://www.nanoelectronics.jp/freestuff.htm.

[5] R. Saito, G. Dresselhaus, and M.S. Dresselhaus. *Physical Properties of Carbon Nanotubes*. Imperial College Press, 1998.

[6] Pavel Nikolaev, Michael J. Bronikowski, R. Kelley Bradley, Frank Rohmund, Daniel T. Colbert, K.A. Smith, and Richard E. Smalley. Gas-phase catalytic growth of single-walled carbon nanotubes from carbon monoxide. *Chemical Physics Letters*, 313:91–97, 1999.

[7] T.W. Ebbesen and P.M. Ajayan. Large-scale synthesis of carbon nanotubes. *Nature*, 358(6383):220–222, 1992.

[8] C. Journet, W. K. Maser, P. Bernier, A. Loiseau, M. Lamyde la Chapelle, S. Lefrant, P. Deniard, R. Lee, and J. E. Fischer. Large-scale production of single-walled carbon nanotubes by the electric-arc technique. *Nature*, 388:756–758, 1997.

[9] A. Thess, R. Lee, P. Nikolaev, H. Dai, P. Petit, J. Robert, C. Xu, Y.H. Lee, S.G. Kim, A.G. Rinzler, D.T. Colbert, G.E. Scuseria, D. Tomanek, J.E. Fischer, and R.E. Smalley. Crystalline ropes of metallic carbon nanotubes. *Science*, 273(5274):483–487, 1996.

[10] Hongjie Dai. Carbon nanotubes: Synthesis, integration, and properties. *Accounts of Chemical Research*, 35(12):1035–1044, 2002.

[11] Seamus Curran, David L. Carroll, Pulickel M. Ajayan, Philipp Redlich, Siegmar Roth, Manfred Rühle, and Werner Blau. Picking needles from nano-haystacks. *Advanced Materials*, 3(4):311–313, 1998.

[12] Tobias Hertel, Richard Martel, and Phaedon Avouris. Manipulation of individual carbon nanotubes and their interaction with surfaces. *Journal of Physical Chemistry B*, 102:910–915, 1998.

[13] M. Yu, M.J. Dyer, G.D. Skidmore, H.W. Rohrs, X. Lu, K.D. Ausman, J.R. Von Ehr, and R.S. Ruoff. Three-dimensional manipulation of carbon nanotubes under a scanning electron microscope. *Nanotechnology - Proceedings of the 1998 6th Foresight Conference on Molecular Nanotechnology*, 10(3):244–252, 1998.

[14] Claes Thelander and Lars Samuelson. Afm manipulation of carbon nanotubes: realization of ultra-fine nanoelectrodes. *Nanotechnology*, 13(1):108–113, 2002.

[15] Michael R. Falvo and Richard Superfine. Mechanics and friction at the nanometer scale. *Journal of Nanoparticle Research*, 2:237248, 2000.

[16] M.R. Falvo, J. Steele, R.M. Taylor II, and R. Superfine. Evidence of commensurate contact and rolling motion: Afm manipulation studies of carbon nanotubes on hopg. *Tribology Letters*, 9:7376, 2000.

[17] Ziyong Shen, Saijin Liu, Shimin Hou, Zhennan Gu, and Zengquan Xue. In situ splitting of carbon nanotube bundles with atomic force microscopy. *Journal of Physics D: Applied Physics*, 36(17):2050–2053, 2003.

[18] Yu Huang, Xiangfeng Duan, Qingqiao Wei, and Charles M. Lieber. Directed assembly of one-dimensional nanostructures into functional networks. *Science*, 291(5504):630–633, 2001.

[19] Marko Burghard, Georg Duesberg, Guenther Philipp, Joerg Muster, and Siegmar Roth. Controlled adsorption of carbon nanotubes on chemically modified electrode arrays. *Advanced Materials*, 10(8):584–588, 1998.

[20] Jie Liu, Michael J. Casavant, Michael Cox, D.A. Walters, P. Boul, Wei Lu, A.J. Rimberg, K.A. Smith, Daniel T. Colbert, and Richard E. Smalley. Controlled deposition of individual single-walled carbon nanotubes on chemically functionalized templates. *Chemical Physics Letters*, 303:125–129, 1999.

[21] K.H. Choi, J.P. Bourgoin, S. Auvray, D. Esteve, G.S. Duesberg, S. Roth, and M. Burghard. Controlled deposition of carbon nanotubes on a patterned substrate. *Surface Science*, 462:195–202, 2000.

[22] Emmanuel Valentin, Stephane Auvray, Julie Goethals, Justin Lewenstein, Laurence Capes, Arianna Filoramo, Aline Ribayrol, Ray Tsui, Jean-Philippe Bourgoin, and Jean-Noel Patillon. High-density selective placement methods for carbon nanotubes. *Microelectronic Engineering*, 61-62:491–496, 2002.

[23] Emmanuel Valentin, Stephane Auvray, Arianna Filoramo, Aline Ribayrol, Marcelo Goffman, Laurence Capes, Jean-Philippe Bourgoin, and Jean-Noel Patillon. Self-assembly fabrication of high performance carbon nanotubes based fets. *Materials Research Society Symposium Proceedings: Nanotube-Based Devices*, 772:201–207, 2003.

[24] M. Mauger, Vu Thien Binh, A. Levesque, and D. Guillot. Freestanding vertically aligned arrays of individual carbon nanotubes on metallic substrates for field emission cathodes. *Applied Physics Letters*, 85(2):305–307, 2004.

[25] Shaoming Huang, Liming Dai, and Albert Mau. Controlled fabrication of aligned carbon nanotube patterns. *Physica B*, 323:333–335, 2002.

[26] Shoushan Fan, Michael G. Chapline, Nathan R. Franklin, Thomas W. Tombler, Alan M. Cassell, and Hongjie Dai. Self-oriented regular arrays of carbon nanotubes and their field emission properties. *Science*, 283:512–514, 1999.

[27] Daisuke Takagi, Yoshikazu Homma, and Yoshihiro Kobayashi. Selective growth of individual single-walled carbon nanotubes suspended between pillar structures. *Physica E*, 24:1–5, 2004.

[28] J. Kong, C. Zhou, A. Morpurgo, H.T. Soh, C.F.Quate, C.Marcus, and H. Dai. Synthesis, integration, and electrical properties of individual single-walled carbon nanotubes. *Appl. Phys. A*, 69:305–308, 1999.

[29] Nathan R. Franklin and Hongjie Dai. An enhanced cvd approach to extensive nanotube networks with directionality. *Advanced Materials*, 12(12):890–894, 2000.

[30] Nathan R. Franklin, Yiming Li, Robert J. Chen, Ali Javey, and Hongjie Dai. Patterned growth of single-walled carbon nanotubes on full 4-inch wafers. *Applied Physics Letters*, 79(27):4571–4573, 2001.

[31] Yuegang Zhang, Aileen Chang, Jien Cao, Qian Wang, Woong Kim, Yiming Li, Nathan Morris, Erhan Yenilmez, Jing Kong, and Hongjie Dai. Electric-field-directed growth of aligned single-walled carbon nanotubes. *Applied Physics Letters*, 79(19):3155–3157, 2001.

[32] A. Bezryadin and C. Dekker. Nanofabrication of electrodes with sub-5 nm spacing for transport experiments on single molecules and metal clusters. *J. Vac. Sci. Technol. B*, 15(4):793–799, 1997.

[33] Kunitoshi Yamamoto, Seiji Akita, and Yoshikazu Nakayama. Orientation and purification of carbon nanotubes using ac electrophoresis. *J. Phys. D: Appl. Phys.*, 31(8):L34–6, 1998.

[34] X. Q. Chen, T. Saito, H. Yamada, and K. Matsushige. Aligning single-wall carbon nanotubes with an alternating-current electric field. *Applied Physics Letters*, 78(23):3714–3716, 2001.

[35] Victor T.S. Wong and Wen J. Li. Bundled carbon nanotubes as electronic circuit and sensing elements. *Proceedings of the 2003 IEEE International Conference on Robotics and Automation, Taipei, Taiwan*, pages 3648–3653, September 2003.

[36] Carmen K. M. Fung, Victor T. S. Wong, Rosa H. M. Chan, and Wen J. Li. Dielectrophoretic batch fabrication of bundled carbon nanotube thermal sensors. *IEEE Transactions on Nanotechnology*, 3(3):395–403, 2004.

[37] Rosa H M Chan, Carmen K M Fung, and Wen J Li. Rapid assembly of carbon nanotubes for nanosensing by dielectrophoretic force. *Nanotechnology*, 15:S672–S677, 2004.

[38] Fujio Wakaya, Takayoshi Nagai, and Kenji Gamo. Position control of carbon nanotube using patterned electrode and electric field. *Microelectronic Engineering*, 63:27–31, 2002.

[39] X. Liu, J.L. Spencer, A.B. Kaiser, and W.M. Arnold. Electric-field-induced accummulation and alignment of carbon nanotubes. In *Annual Report Conference on Electrical Insulation and Dielectric Phenomena*, pages 31–33, 2002.

[40] R. Krupke, F. Hennrich, H.B. Weber, D. Beckmann, O. Hampe, S. Malik, M.M. Kappes, and H.V. Löhneysen. Contacting single bundles of carbon nanotubes with alternating electric fields. *Appl. Phys. A*, 76:397–400, 2003.

[41] R. Krupke, F. Hennrich, H. B. Weber, M. M. Kappes, and H. v. Löhneysen. Simultaneous deposition of metallic bundles of single-walled carbon nanotubes using ac-dielectrophoresis. *Nano Letters*, 3(8):1019–1023, 2003.

[42] Jaehyun Chung and Junghoon Lee. Nanoscale gap fabrication and integration of carbon nanotubes by micromachining. *Sensors and Actuators A*, 104:229–235, 2003.

[43] Jaehyun Chung, Kyong-Hoon Lee, Junghoon Lee, and Rodney S. Ruoff. Toward large-scale integration of carbon nanotubes. *Langmuir*, 20:3011–3017, 2004.

[44] S.W. Lee, D.S. Lee, H.Y. Yu, E.E.B. Campbell, and Y.W. Park. Production of individual suspended single-walled carbon nanotubes using the ac electrophoresis technique. *Appl. Phys. A*, 78:283–286, 2004.

[45] Erik T. Thostenson, Zhifeng Ren, and Tsu-Wei Chou. Advances in the science and technology of carbon nanotubes and their composites: a review. *Composites Science and Technology 61 (2001) 18991912*, 61:1899–1912, 2001.

[46] M.J. Biercuk, M.C. Llaguno, M. Radosavljevic, J.K. Hyun, and A.T. Johnson. Carbon nanotube composites for thermal management. *Applied Physics Letters*, 80:2767, 2002.

[47] C.A. Grimes, C. Mungle, D. Kouzoudis, S. Fang, and P.C. Eklund. The 500 mhz to 5.50 ghz complex permittivity spectra of single-wall carbon nanotube-loaded polymer composites. *Chemical Physics Letters*, 319:460–464, 2000.

[48] Juthika Basak, Deepanjan Mitra, and Shashank Sinha. Carbon nanotubes (cnts): The next generation sensors. Final Project Report MAE 284 (Sensors and Actuators), 2002.

[49] Hongjie Dai, Jason H. Hafner, Andrew G. Rinzler, Daniel T. Colbert, and Richard E. Smalley. Nanotubes as nanoprobes in scanning probe microscopy. *Nature*, 384:147–151, 1996.

[50] Erhan Yenilmez, Qian Wang, Robert J. Chen, Dunwei Wang, and Hongjie Dai. Wafer scale production of carbon nanotube scanning probe tips for atomic force microscopy. *Applied Physics Letters*, 80(12):2225–2227, 2002.

[51] R. Stevens, C. Nguyen, A. Cassell, L. Delzeit, M. Meyyappan, and Jie Han. Improved fabrication approach for carbon nanotube probe devices. *Applied Physics Letters*, 77(21):3453–3455, 2000.

[52] Sander J. Tans, Alwin R. M. Verschueren, and Cees Dekker. Room-temperature transistor based on a single carbon nanotube. *Nature*, 393:49–52, 1998.

[53] R. Martel, T. Schmidt, H. R. Shea, T. Hertel, and Ph. Avouris). Single- and multi-wall carbon nanotube field-effect transistors. *Applied Physics Letters*, 73(17):2447–2449, October 1998.

[54] Henk W. Ch. Postma, Tijs Teepen, Zhen Yao, Milena Grifoni, and Cees Dekker. Carbon nanotube single-electron transistors at room temperature. *Science*, 293:76–79, 2001.

[55] R. Martel, V. Derycke, C. Lavoie, J. Appenzeller, K.K. Chan, J. Tersoff, and Ph. Avouris. Ambipolar electrical transport in semiconducting single-wall carbon nanotubes. *Physical Review Letters*, 87(25):256805–1 – 256805–4, December 2001.

[56] Ali Javey, Hyoungsub Kim, Markus Brink, Qian Wang, Ant Ural, Jing Guo, Paul McIntyre, Paul McEuen, Mark Lundstrom, and Hongjie Dai. High-κ dielectrics for advanced carbon nanotube transistors and logic gates. *Nature Materials*, 1(4):241–246, 2003.

[57] Ali Javey, Moonsub Shim, and Hongjie Dai. Electrical properties and devices of large-diameter single-walled carbon nanotubes. *Applied Physics Letters*, 80(6):1064–1066, 2002.

[58] T. Durkop, S. A. Getty, Enrique Cobas, and M. S. Fuhrer. Extraordinary mobility in semiconducting carbon nanotubes. *NanoLetters*, 4(1):35–39, 2004.

[59] Jingqi Li, Qing Zhang, Dajiang Yang, and Jingze Tian. Fabrication of carbon nanotube .eld e.ect transistors by ac dielectrophoresis method. *Carbon*, 42:22632267, 2004.

[60] V. Derycke, R. Martel, J. Appenzeller, and Ph. Avouris. Carbon nanotube inter- and intramolecular logic gates. *NanoLetters*, 1(9):453–456, 2001.

[61] Adrian Bachtold, Peter Hadley, Takeshi Nakanishi, and Cees Dekker. Logic circuits with carbon nanotube transistors. *Science*, 294:1317–1320, 2001.

[62] Jing Kong, Nathan R. Franklin, Chongwu Zhou, Michael G. Chapline, Shu Peng, Kyeongjae Cho, and Hongjie Dai. Nanotube molecular wires as chemical sensors. *Science*, 287:622–625, 2000.

[63] Philip G. Collins, Keith Bradley, Masa Ishigami, and A. Zettl. Extreme oxygen sensitivity of electronic properties of carbon nanotubes. *Science*, 287:1801–1804, March 2000.

[64] C. Cantalini, L. Valentini, I. Armentano, L. Lozzi, J.M. Kenny, and S. Santucci. Sensitivity to no2 and cross-sensitivity analysis to nh3, ethanol and humidity of carbon nanotubes thin film prepared by pecvd. *Sensors and Actuators B*, 95:195–202, 2003.

[65] L. Valentini, C. Cantalini, I. Armentano, J.M. Kenny, L. Lozzi, and S. Santucci. Highly sensitive and selective sensors based on carbon nanotubes thin films for molecular detection. *Diamond and Related Materials*, 13:1301–1305, 2004.

[66] O.K. Varghese, P.D. Kichambre, D. Gong, K.G. Ong, E.C. Dickey, and C.A. Grimes. Gas sensing characteristics of multi-wall carbon nanotubes. *Sensors and Actuators B*, 81:32–41, 2001.

[67] Prabhu Soundarrajan, Ajeeta Patil, , and Liming Dai. Surface modification of aligned carbon nanotube arrays for electrochemical sensing applications. *J. Vac. Sci. Technol. A*, 21(4):1198–1201, 2003.

[68] Robert J. Chen, Sarunya Bangsaruntip, Katerina A. Drouvalakis, Nadine Wong Shi Kam, Moonsub Shim, Yiming Li, Woong Kim, Paul J. Utz, , and Hongjie Dai. Noncovalent functionalization of carbon nanotubes for highly specific electronic biosensors. *PNAS*, 100(9):4984–4989, 2003.

[69] J. P. Novak, E. S. Snow, E. J. Houser, D. Park, J. L. Stepnowski, and R. A. McGill. Nerve agent detection using networks of single-walled carbon nanotubes. *Applied Physics Letters*, 83(19):4026–4028, 2003.

[70] M. Chhowalla, C. Ducati, N. L. Rupesinghe, K. B. K. Teo, and G. A. J. Amaratunga. Field emission from short and stubby vertically aligned carbon nanotubes. *Applied Physics Letters*, 79(13):2079–2081, 2001.

[71] Q. H. Wang, A. A. Setlur, J. M. Lauerhaas, J. Y. Dai, E. W. Seelig, and R. P. H. Chang. A nanotube-based field-emission flat panel display. *Applied Physics Letters*, 72(22):2912–2913, 1998.

[72] Phaedon Avouris. Carbon nanotube electronics. *Chemical Physics*, 281:429445, 2002.

[73] Ralph Krupke, Frank Hennrich, Hilbert v. Löhneysen, and Manfred M. Kappes. Separation of metallic from semiconducting single-walled carbon nanotubes. *Science*, 301(5631):344–347, 2003.

[74] Ming Zheng, Anand Jagota, Michael S. Strano, Adelina P. Santos, Paul Barone, S. Grace Chou, Bruce A. Diner, Mildred S. Dresselhaus, Robert S. Mclean, G. Bibiana Onoa, Georgii G. Samsonidze, Ellen D. Semke, Monica Usrey, and Dennis J. Walls. Structure-based carbon nanotube sorting by sequence-dependent dna assembly. *Science*, 302:1545–1548, 2003.

[75] Philip G. Collins, Michael S. Arnold, and Phaedon Avouris. Engineering carbon nanotubes and nanotube circuits using electrical breakdown. *Science*, 292:706–709, April 2001.

[76] M. Yudasaka, M. Zhang, and S. Iijima. Diameter-selective removal of single-wall carbon nanotubes through light-assisted oxidation. *Chemical Physics Letters*, 374:132–136, 2003.

[77] P. C. Garell, M. A. Granner, M. D. Noh, M. A. Howard III, I. O. Volkov, and G. T. Gillies. Introductory overview of research instruments for recording the electrical activity of neurons in the human brain. *Review of Scientific Instruments*, 69(1):4027–4037, 1998.

[78] A. Bruno Frazier, David P. O'Brien, and Mark G. Allen. Two dimensional metallic microelectrode arrays for extracellular stimulation and recording of neurons. *IEEE*, pages 195–200, 1993.

[79] Kenneth L. Drake, Kensall D. Wise, Jamille Farraye, David J. Anderson, and Spencer L. BeMent. Performance of planar multisite microprobes in recording extracellular single-unit intracortical activity. *IEEE Transactions on Biomedical Engineering*, 35(9):719–732, 1988.

[80] Jin Ji and Kensall D. Wise. An implantable cmos analog signal processor for multiplexed microelectrode recording arrays. *IEEE - Solid-State Sensor and Actuator Workshop, 4th Technical Digest*, pages 107–110, 1990.

[81] K. D. Wise, K. Najafi, J. Ji, J. F. Hetke, S.J. Tanghe, A. Hoogerwerf, D. J. Anderson, S. L. BeMent, M. Ghazzi, W. Baer, T. Hull, and Y. Yang. Micromachined silicon microprobes for cns recording and stimulation. *Annual International Conference of the IEEE Engineering in Medicine and Biology Society*, 12(5):2334–2335, 1990.

[82] Jin Ji and Kensall D. Wise. An implantable cmos circuit interface for multiplexed microelectrode recording arrays. *IEEE Journal of Solid State Circuits*, 23(3):433–443, 1992.

[83] A. Bragin, J. Hetke, C. L. Wilson, D. J. Anderson, J. Engel Jr, and G. Buzsaki. Multiple site silicon-based probes for chronic recordings in freely moving rats: implantation, recording and histological verification. *Journal of Neuroscience Methods*, 98:77–82, 2000.

[84] B. Bhushan, editor. *Handbook of Nanotechnology*. Springer, 2003.

[85] Phaedon Avouris. Molecular electronics with carbon nanotubes. *Accounts of Chemical Research*, 35(12):1026–1034, 2000.

[86] J W Ding, X H Yan, and J X Cao. Analytical relation of band gaps to both chirality and diameter of single-wall carbon nanotubes. *Phys. Rev. B*, 66:073401, 2002.

[87] L X Benedict, S G Louie, and M L Cohen. Static polarizabilities of single-wall carbon nanotubes. *Phys. Rev. B*, 52:8541–9, 1995.

[88] F Leonard and J Tersoff. Dielectric response of semiconducting carbon nanotubes. *Appl. Phys. Letters*, 81:4835–7, 2002.

[89] T. Pichler, M. Knupfer, M. S. Golden, J. Fink, A. Rinzler, and R. E. Smalley. Localized and delocalized electronic states in single-wall carbon nanotubes. *Physical Review Letters*, 80(21):4729–4732, 1998.

[90] H.C.F. Martens, J.A. Reedijk, H.B. Brown, D. M. de Leeuw, and R. Menon. Metallic state in disordered quasi-one-dimensional conductors. *Physical Review B*, 63(7):073203/1–4, 2001.

[91] J. Kong, H.T. Soh, A.M. Cassell, C.F. Quate, and H. Dai. Synthesis of individual single-walled carbon nanotubes on patterned silicon wafers. *Nature*, 395(6705):878–881, 1998.

[92] M. Krüger, I. Widmer, T. Nussbaumer, M. Buitellar, and C. Schönenberger. Sensitivity of single multiwalled carbon nanotubes to the environment. *New Journal of Physics*, 5:138.1–138.11, 2003.

[93] Jeroen W. G. Wildöer, Liesbeth C. Venema, Andrew G. Rinzler, Richard E. Smalley, and Cees Dekker. Electronic structure of atomically resolved carbon nanotubes. *Nature*, 391, January 1998.

[94] S. Reich, A. C. Ferrari, and J. Robertson. Raman scattering on carbon nanotubes. www-g.eng.cam.ac.uk/edm/research/nanotubes/CNT_raman.html.

[95] Shunji Bandow, S. Asaka, Y. Saito A. M. Rao, L. Grigorian, E. Richter, and P. C. Eklund. Effect of the growth temperature on the diameter distribution and chirality of single-wall carbon nanotubes. *Physical Review Letters*, 80(17):3779–3782, April 1998.

[96] Sergei M. Bachilo, Michael S. Strano, Carter Kittrell, Robert H. Hauge, Richard E. Smalley, and R. Bruce Weisman. Structure-assigned optical spectra of single-walled carbon nanotubes. *Science*, 298:2361–2366, December 2002.

[97] Laurent Alvarez, Ariete Righi, Tony Guillard, Stephane Rols, Eric Anglaret, Daniel Laplaze, and Jean-Louis Sauvajol. Resonant raman study of the structure and electronic properties of single-wall carbon nanotubes. *Chemical Physics Letters*, 316:186–190, January 2000.

[98] A. Jorio, A. G. Souza Filho, V. W. Brar, A. K. Swan, M. S. Ünlü, B. B. Goldberg, A. Righi, J. H. Hafner, C. M. Lieber, R. Saito, G. Dresselhaus, and M. S. Dresselhaus. Polarized resonant raman study of isolated single-wall carbon nanotubes: Symmetry selection rules, dipolar and multipolar antenna effects. *Physical Review B*, 65:121402–1 – 121402–4, 2002.

[99] Ralph Krupke, Frank Hennrich, Manfred M. Kappes, and Hilbert v. Löhneysen. Surface conductance induced dielectrophoresis of semiconducting single-walled carbon nanotubes. *Nano Letters*, 4(8):1395–1399, 2004.

[100] Sreeja B. Asokan, L. Jawerth, R. Lloyd Carroll, R. E. Cheney, S. Washburn, and R. Superfine. Two-dimensional manipulation and orientation of actin-myosin systems with dielectrophoresis. *Nanoletters*, 3(4):431–437, 2003.

[101] Hywel Morgan and Nicolas G. Green. *AC Electrokinetics: colloids and nanoparticles*. Research Studies Press Ltd., 2003.

[102] A. Bachtold, M. S. Fuhrer, S. Plyasunov, M. Forero, Erik H. Anderson, A. Zettl, and Paul L. McEuen. Scanned probe microscopy of electronic transport in carbon nanotubes. *Physical Review Letters*, 84(26):6082–6085, 2000.

[103] C.T. White and T.N. Todorov. Carbon nanotubes as long ballistic conductors. *Nature*, 393(6682):240–242, 1998.

[104] Chongwu Zhou, Jing Kong, and Hongjie Dai. Intrinsic electrical properties of individual single-walled carbon nanotubes with small band gaps. *Physical Review Letters*, 84(24):5604–5607, 2000.

[105] Ali Javey, Moonsub Shim, and Hongjie Dai. Electrical properties and devices of large-diameter single-walled carbon nanotubes. *Applied Physics Letters*, 80(6):1064–1066, 2002.

[106] Chongwu Zhou, Jing Kong, and Hongjie Dai. Electrical measurements of individual semiconducting single-walled carbon nanotubes of various diameters. *Applied Physics Letters*, 76(12):1597–1599, 2000.

[107] Ana Dominguez, Aurora Fernandez, Noemi Gonzalez, Emilia Iglesias, and Luis Montenegro. Determination of critical micelle concentration of some surfactants by three techniques. *Journal of Chemical Education*, 74(10):1227–1231, 1997.

[108] Yiming Li, Woong Kim, Yuegang Zhang, Marco Rolandi, Dunwei Wang, and Hongjie Dai. Growth of single-walled carbon nanotubes from discrete catalytic nanoparticles of various sizes. *Journal of Physical Chemistry B*, 105(46):11424–11431, 2001.

[109] M.S. Dresselhaus, G. Dresselhaus, and Ph. Avouris, editors. *Carbon Nanotubes: Synthesis, Structure, Properties and Applications*. Topics in Applied Physics. Springer-Verlag Berlin and Heidelberg GmbH and Co. K, 2001.

[110] A. Ramos, H. Morgan, N.G. Green, and A. Castellanos. Ac electrokinetics: a review of forces in microelectrode structures. *J. Phys. D: Appl. Phys.*, 31(18):2338–2353, 1998.

[111] A. Gonzalez, A. Ramos, N.G. Green, A. Castellanos, and H. Morgan. Fluid flow induced by nonuniform ac electric fields in electrolytes on microelectrodes. ii. a linear double-layer analysis. *Physical Review E*, 61(4):4019–4028, April 2000.

[112] M. Scott, K.V.I.S. Kaler, and R. Paul. Theoretical model of electrode polarization and ac electroosmotic fluid flow in planar electrode arrays. *Journal of Colloid and Interface Science*, 238:449–451, 2001.

[113] P.K. Wong, C. Chen, T. Wang, and C. Ho. An ac electroosmotic processor for biomolecules. Conference Paper: TRANSDUCERS 2003, 12th Innational Conference on Solid-State Sensors, Actuators and Microsystems, June 2003.

[114] Limin Huang, Xiaodong Cui, Gordana Dukovic, and Stephen P OBrien. Self-organizing high-density single-walled carbon nanotube arrays from surfactant suspensions. *Nanotechnology*, 15:1450–1454, 2004.

[115] Promega Corporation. Material safety datasheet. http://www.promega.com/msds/us

[116] C.L. Petersen. *Microscopic Four-Point Probes*. PhD thesis, MIC - Department of Micro and Nanotechnology, Technical University of Denmark, February 1999.

[117] Torben M. Hansen. *Tools for Nanoscale Conductivity Measurements*. PhD thesis, MIC - Technical University of Denmark, February 2003.

[118] Alicia Johansson, Montserrat Calleja, Maria I. Dimaki, Peter Rasmussen, Peter Bøggild, and Anja Boisen. Polymer cantilever platform for dielectrophoretic assembly of carbon nanotubes. *Sensor Letters*, 2(2):117–120, 2004.

[119] Kristian Mølhave. *Tools for In-situ Manipulation and Characterization of Nanostructures*. PhD thesis, MIC - Department of Micro and Nanotechnology, Technical University of Denmark, August 2004.

[120] A.B. Kaiser, K.J. Challis, G.C. MacIntosh, G.T. Kim, H.Y. Yu, J.G. Park, S.H. Jhang, and Y.W. Park. Frequency and field dependent conductivity of carbon nanotube networks. *Current Applied Physics*, 2:163–166, 2002.

[121] Robert J. Chen, Nathan R. Franklin, Jing Kong, Jien Cao, Thomas W. Tombler, Yuegang Zhang, and Hongjie Dai. Molecular photodesorption from single-walled carbon nanotubes. *Applied Physics Letters*, 79(14):2258–2260, October 2001.

[122] A. Zahab, L. Spina, P. Poncharal, and C. Marlière. Water-vapor effect on the electrical conductivity of a single-walled carbon nanotube mat. *Physical Review B*, 62(15):10000–10003, October 2000.

[123] Renju Zacharia. *Desorption of gases from graphitic and porous carbon surfaces*. PhD thesis, FU Berlin, May 2004.

[124] Shi L., Kim P., Plyasunov S., Bachtold A., McEuen P.L., and Majumdar A. Scanning thermal microscopy study of dissipation in current-carrying carbon nanotubes. *Proceedings of 2001 ASME International Mechanical Engineering Congress and Exposition*, 369(7):247–252, 2001.

[125] Hendrik Ulbricht, Gunnar Moos, and Tobias Hertel. Interaction of molecular oxygen with single-wall carbon nanotube bundles and graphite. *Surface Science*, 532535:852856, 2003.

[126] L. Valentini, I. Armentano, D. Puglia, L. Lozzi, S. Santucci, and J.M. Kenny. A deeper understanding of the photodesorption mechanism of aligned carbon nanotube thin films by impedance spectroscopy. *Thin Solid Films*, 449:105–112, 2004.

[127] Moonsub Shima and Giles P. Siddons. Photoinduced conductivity changes in carbon nanotube transistors. *Applied Physics Letters*, 83(17):3564–4566, October 2003.

[128] René B. Nyberg. Micro-cantilever probe with self-assembled carbon nanotube sensor. Master's thesis, Department of Micro and Nanotechnology, Technical University of Denmark, September 2004.

[129] M. Radosavljevic, J. Lefebvre, and A. T. Johnson. High-field electrical transport and breakdown in bundles of single-wall carbon nanotubes. *Physical Review B*, 64:241307–1 – 241307–4, 2001.

[130] Philip G. Collins, M. Hersam, M. Arnold, R. Martel, and Ph. Avouris. Current saturation and electrical breakdown in multiwalled carbon nanotubes. *Physical Review Letters*, 86(14):3128–3131, 2001.

[131] Zhen Yao, Charles L. Kane, and Cees Dekker. High-field electrical transport in single-wall carbon nanotubes. *Physical Review Letters*, 84(13):2941–2944, 2000.

[132] Søren Jensen. *Inductively Coupled Plasma Etching for Microsystems*. PhD thesis, MIC - Department of Micro and Nanotechnology, Technical University of Denmark, March 2004.

[133] Steen Christian Eriksen. Dna detection on cantilever-based sensors. Master's thesis, MIC - Technical University of Denmark, July 2002.

[134] Seunghyun Baik, Monica Usrey, Lolita Rotkina, and Michael Strano. Using the selective functionalization of metallic single-walled carbon nanotubes to contol dielectrophoretic mobility. *J. Phys. Chem. B*, 108:15560–15564, 2004.

[135] Z. Wang, J. El-Ali, M. Engelund, T. Gotsæd, I. R. Perch-Nielsen, K. B. Mogensen, D. Snakenborg, J. P. Kutter, and A. Wolff. Measurements of scattered light on a microchip flow cytometer with integrated polymer based optical elements. *Lab on a Chip*, 4:372–377, 2004.

[136] R. Larciprete, A. Goldoni, and S. Lizzit. Interaction of molecular oxygen with single wall nanotubes: Role of surfactant contamination. *Nuclear Instruments and Methods in Physics Research B*, 200:5–10, 2003.

[137] Peter Andreas Rasmussen. *Cantilever-based Sensors for Surface Stress Measurements*. PhD thesis, Department of Micro and Nanotechnology - Technical University of Denmark, August 2003.

[138] Michael Stenbæk Schmidt. Anisotropic reactive ion etching of carbon nanotube structured stamps for nanoimprint lithography. Master's thesis, Department of Micro and Nanotechnology - Technical University of Denmark, September 2004.

[139] Meital Reches and Ehud Gazit. Casting metal nanowires within discrete self-assembled peptide nanotubes. *Science*, 300:625–627, 2003.

Appendix A

Publications and conferences

A.1 Journal publications

This section contains the journal articles published, accepted or submitted up to the submission of this thesis in December 2004:

- Frequency dependence of structure and electrical behaviour of carbon nanotube networks assembled by dielectrophoresis, Maria Dimaki and Peter Bøggild, submitted to Nanotechnology[1]
- Single- and multi-walled carbon nanotube networks and bundles assembled on microelectrodes, Maria Dimaki, Peter Bøggild, accepted for publication in the Journal of Nanoengineering and Nanosystems[2]
- Polymer Cantilever Platform for Dielectrophoretic Assembly of Carbon Nanotubes, Alicia Johansson, Montserrat Calleja, Maria I. Dimaki, Peter Rasmussen, Peter Bøggild and Anja Boisen, Sensor Letters, Vol. 2, 117-120, 2004
- Dielectrophoresis of carbon nanotubes using microelectrodes: a numerical study, Maria Dimaki and Peter Bøggild, Nanotechnology 15 (2004), p. 1095-1102

A.2 Conference Proceedings

- Sorting and assembly of single-walled carbon nanotubes by dielectrophoresis in microliquid channels: a numerical study, Maria Dimaki, René Nyberg, Peter Bøggild, Proceedings of μTAS 2004, 8th International Conference on Miniaturized Systems in Chemistry and Life Sciences, September 26-30, Malmö, Sweden

[1]This article was accepted and published in Nanotechnology, Volume 16 (2005), p. 759
[2]Proc. IMechE Vol. 218 Part N: Journal of Nanoengineering and Nanosystems, p. 17 (2005)

- Design of Microfabricated Biocompatible Multi-electrode for single ion channel activity, Maria I. Dimaki, Helle Ruseng, René Fléron, Emmanuelle Boubour, Peter Bøggild, Proceedings of the 7th international conference on nanometer-scale science and technology, 24-28 June 2002, Malmö, Sweden

- Assembly of Carbon nanotubes on Microelectrodes by Nanomanipulation, Kristian Mølhave, Ramona Mateiu, Maria Dimaki, Torben Mikael Hansen, Dorte Nørgaard Madsen, Peter Bøggild, Proceedings of the 7th international conference on nanometer-scale science and technology, 24-28 June 2002, Malmö, Sweden

A.3 Conferences

- **MicroTAS 2004**, September 2004, Malmö, Sweden
  Poster contribution: Sorting and assembly of single-walled carbon nanotubes by dielectrophoresis in microliquid channels: a numerical study, Maria Dimaki, René Nyberg, Peter Bøggild

- **DFS Meeting 2004**
  Oral presentation: Dielectrophoretic assembly of carbon nanotubes on microelectrodes, characterisation and application, Maria Dimaki, Peter Bøggild
  Poster contribution: Fabrication and characterisation of specially designed cantilever probes for carbon nanotube dielectrophoresis, René Nyberg, Maria Dimaki, Peter Bøggild

- **Trends in Nanotechnology (TNT)**, September 2003, Salamanca, Spain
  Poster contribution: Electric field assisted assembly of carbon nanotubes between microfabricated electrodes, Maria Dimaki, Kristian Mølhave, Peter Bøggild

- **DFS Meeting 2003**
  Oral presentation: Self-integration of carbon nanotubes on microelectrodes under the influence of AC electric fields, Maria Dimaki, Kristian Mølhave, Peter Bøggild

- **Nano-7, Ecoss-21**, September 2002 in Malmö, Sweden
  Poster contributions:
  a) Design of Microfabricated Biocompatible Multi-electrode for single ion channel activity, Maria I. Dimaki, Helle Ruseng, René Fléron, Emmanuelle Boubour, Peter Bøggild
  b) Assembly of Carbon nanotubes on Microelectrodes by Nanomanipulation, Kristian Mølhave, Ramona Mateiu, Maria Dimaki, Torben Mikael Hansen, Dorte Nørgaard Madsen, Peter Bøggild

- **DFS Meeting 2002**
  Poster contribution: Self assembly of carbon nanotubes by AC dielectrophoresis, Maria Dimaki, Kristian Mølhave, Peter Bøggild

A.4 Upcoming publications

Three articles are expected to be submitted by the end of February based on results described in the thesis:

- Removal of adsorbed molecules from dielectrophoretically assembled nanotube networks using heat and light[3]
  Maria Dimaki, Jakob Kjelstrup-Hansen and Peter Bøggild
  Abstract
  Carbon nanotube networks have been assembled on microstructures with the use of dielectrophoresis, a method incorporating the use of an inhomogeneous alternating electric field to attract nanotubes towards the electrodes. The networks have been assembled at different frequencies and exposed to heating and cooling to temperatures up to 150 degrees Celcius. The same experiments have been conducted on a single multiwalled nanotube assembled on a cantilever structure by direct manipulation. The results obtained on both the singlewalled carbon nanotube networks and the multiwalled nanotube are similar and show that the behaviour of nanotubes in the 20-150 degrees is a complex response involving oxygen desorption and subsequent adsorption. The same effect is responsible for the response observed on the networks when they are illuminated by a white light source.

  This article is based on the results described in chapter 6.

- Raman spectra from dielectrophoretically assembled nanotube networks in the 10 kHz - 10 MHz frequency range[4]
  Maria Dimaki, Andrea Ferrari, Vittorio Scardaci and Peter Bøggild
  Abstract
  Carbon nanotube networks have been assembled on microelectrodes using dielectrophoresis at three different frequencies, 10 kHz, 1 MHz and 10 MHz. Raman spectra were taken on the samples at three different laser wavelengths (514, 633 and 785 nm) and compared to spectra from a reference sample. The results showed that differences in the spectra were not pronounced, though a tendency existed, that the relative concentration of semiconducting single-walled carbon nanotubes is higher in the dielectrophoretically assembled samples, which conflicts with the theory and previously published results.

  This article is based on the results described in section 8.2

- Parameters affecting the dielectrophoretic assembly of carbon nanotubes on

[3]More controlled experiments in a closed chamber with environmental control were performed. Therefore, this article was rewritten and published under a different title: Temperature response of carbon nanotubes networks, Maria Dimaki, Peter Bøggild and Winnie Svendsen, Journal of Physics: Conference Series 61, p. 247 (2007)

[4]It was judged that the results obtained were not sufficient for a publication, so this article was never submitted

microelectrodes[5]

Maria Dimaki and Peter Bøggild

Abstract

The dielectrophoretic assembly of carbon nanotubes on microelectrodes depends on a great number of parameters. We present here an investigation of the resulting electrical properties of the assembled networks as a function of voltage, frequency and time of application of the electric field, for two different electrode geometries and 2 different nanotube solutions and suggest optimal parameters for the assembly in terms of structural and electrical properties of the networks.

This article is based on the results described in chapter 5.

[5]This article was published as: Investigation of Parameters Controlling the Dielectrophoretic Assembly of Carbon Nanotubes on Microelectrodes, Maria Dimaki, Peter Bøggild, J. Nanosci. Nanotechnol. 8 (2008),p. 1973

Appendix B

Natural convection simulation

A simulation of the temperature gradient generated in a droplet of an SDS solution when 14.5 Vp-p are applied between all 14 electrode pairs of Figure 4.9(b) and the resulting fluid flow due to natural convection are presented in this section.

An order of magnitude estimate of the temperature rise was given in chapter 3. For a real electrode geometry, such as the geometry of Figure 4.9(b), which was thoroughly used throughout the experimental work described in this project, the temperature as a function of position can be more accurately calculated.

We have simulated the electric field produced by one half of one electrode since the remaining structure is symmetrical to this and can therefore be taken into account by the boundary conditions. A schematic of the geometry with the relevant dimensions is shown in Figure B.1. The half electrode is shown with the shaded area and the dimensions correspond precisely to those of the real geometry.

The electric field on three different planes of the simulated space is shown in Figure B.2. It can be seen that the maximum field on the $z = 0$ plane is on the electrode edges and particularly at the center of the electrodes (0,0,0). As we move upwards the variations in the field become smaller. For the $y = 0$ plane it is seen that the strongest field is again at the electrode center (0,0,0) and that the field drops exponentially higher up. A nanotube would move perpendicular to these contour lines and assemble at the electrode center.

Based on the simulation the average energy dissipation was calculated using equation 3.12 for an investigated volume of 2 mm $\times$ 2 mm $\times$ 1 mm, where the 14 electrode pairs were contained in the center. This energy was considered to be a heat source placed in the middle of the volume giving rise to a temperature gradient due to Joule heating in the volume, shown in Figure B.3 for the $x = 0$ plane, which is the plane passing through the middle of all the 14 gaps.

A temperature rise of 18 ^{o}C is calculated. This is rather a lot, however, in a real system, some if not most of the heat will actually be dissipated in the SiO_2 substrate onto which the electrodes are placed, so that the temperature increase will not be as high.

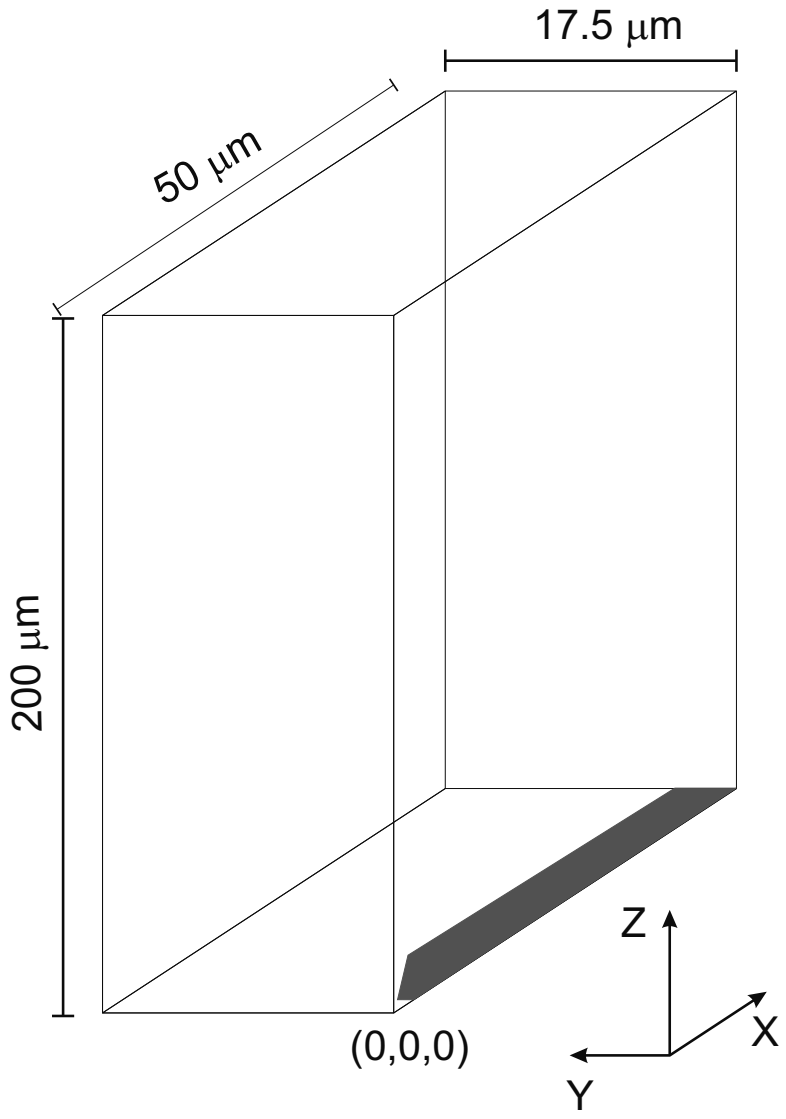

Figure B.1: The simulation space for the structures of Figure 4.9(b).

This temperature distribution will give rise to a fluid flow in the volume, which in turn will change the temperature distribution, etc. For microsystems the two problems are decoupled, however, in this investigation the coupled problem has been solved. The resulting fluid flow due to this temperature gradient is shown in Figure B.4 for the $x = 0$ plane.

A maximum velocity of 300 μm/s is calculated 500 μm above the electrode plane. Close to the electrodes and the substrate, where the dielectrophoretic forces are operating, the fluid velocity is smaller than 30 μm/s and they are carrying the fluid towards the electrode area and upwards. It is therefore expected that this effect will constantly be supplying the region close to the electrodes with new nanotubes, so that the region around the electrodes will never be cleared of nanotubes as was calculated in section 3.3. In the real case the fluid velocity will be lower, due to the lower temperature increase.

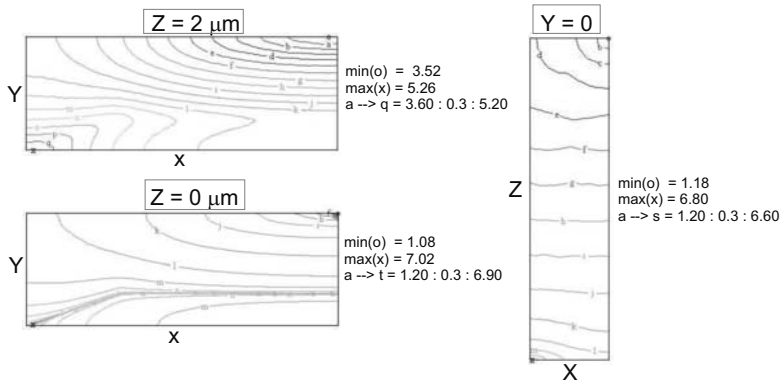

Figure B.2: Three views of the calculated magnitude of the electric field. The strongest field is at the electrode edges.

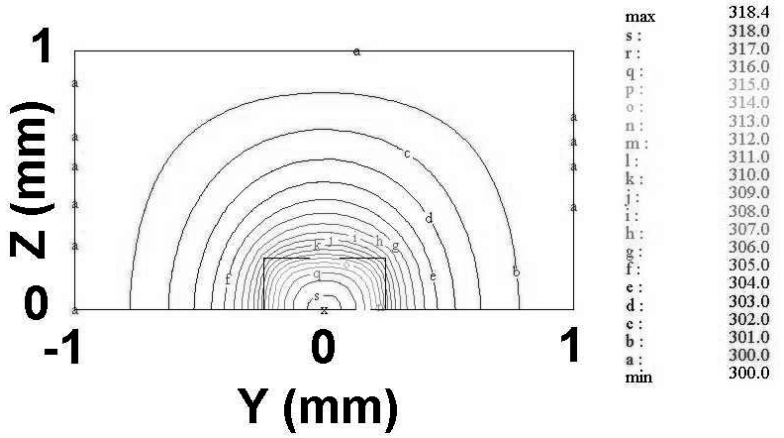

Figure B.3: The temperature distribution in the liquid by diffusion due to the heat source at the center of the volume (average energy dissipation from the 14 electrode pairs in SDS).

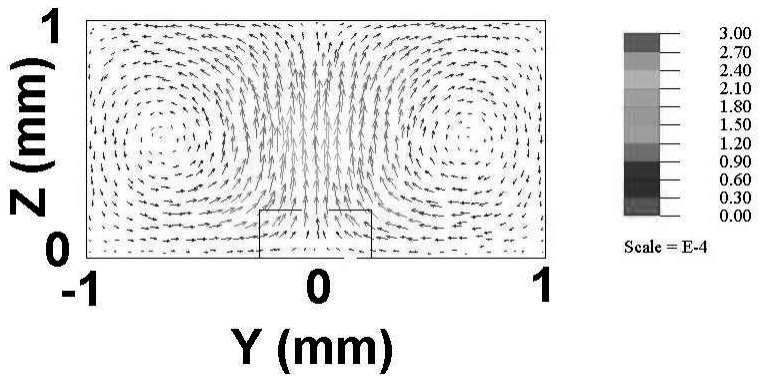

Figure B.4: The resulting fluid flow due to Joule heating for the structure of figure 4.9(b) operating at 14.5 V p-p.

Appendix C

Ideal solution calculation

A small amount of carbon nanotubes is added to a large amount of dispersing medium. This amount can roughly be calculated by setting a limit on how many nanotubes one would like to have in a given volume of solution with a certain probability. The number N of nanotubes in a volume V of solution with concentration C can be considered a random variable following the Poisson distribution with a parameter λ equal to:

$$\lambda = C \cdot V \tag{C.1}$$

a number that corresponds to the average number of tubes in volume V of solution with concentration C.

The probability that N will be equal to a given number M is given by the formula:

$$P(N = M) = e^{-\lambda} \cdot \frac{\lambda^M}{M!} \tag{C.2}$$

If the desired number of nanotubes in the volume V of the solution is M or less and the probability that "something will go wrong" is required to be p then

$$p = 1 - \sum_{i=1}^{M} P(N = i) \Rightarrow p = 1 - \sum_{i=1}^{M} e^{-CV} \frac{(CV)^i}{i!} \tag{C.3}$$

A recursive algorithm can be constructed from equation C.3 in order to calculate the desired concentration C given the volume V, the desirable number of tubes M in that volume and the probability p at the number of tubes will be larger than M. From equation C.3

$$e^{-CV} = \frac{1-p}{\sum_{i=1}^{M} \frac{(CV)^i}{i!}} \Rightarrow C = \frac{1}{V} \cdot \frac{\sum_{i=1}^{M} \frac{(CV)^i}{i!}}{1-p} \tag{C.4}$$

From equation C.4 it becomes clear that the recursive algorithm should be

$$C_m = \frac{1}{V} \cdot \frac{\sum_{i=1}^{M} \frac{(C_m V)^i}{i!}}{1-p}, m \geq 0 \tag{C.5}$$

where for $m = 0$ the concentration C_0 is set to some arbitrary value and the algorithm stops when the difference between two successive values for the concentration is smaller than a preset error value.

Equation C.5 will provide the concentration in tubes/ml. However, since making a solution requires knowledge of an amount in grams of nanotubes to be added to a certain volume of dispersing medium, conversion of the concentration to grams/ml is necessary. For this, we need to calculate the weight of a single tube. This can only be a very rough calculation, since tubes can be either single-walled or multi-walled and have a variety of diameters. For a single-walled nanotube with a radius around 1 nm it can be shown that the weight is of the order of 10^{-18} gr/μm. The calculation merely estimates the number of carbon atoms in a nanotube of radius 1 nm and length of 1 μm.

An example result for this algorithm tells us that if we wish to have no more than 20 tubes in a volume of 10 μl with a probability of 90% then the concentration of the nanotubes should be no more than 1538 tubes/ml or $7.6914 \cdot 10^{-14}$ gr/ml. This is a very small number indeed and such concentrations can be achieved by diluting an originally dense solution a number of times. One should mention at this point that for these calculations we have taken a "unit weight" equal to 5 times the previously calculated one because the solutions we are dealing with are multi-walled nanotube solutions and the lengths of the tubes are bigger than 1 μm.

Appendix D

Process sequences

The process sequences for the structures of Figures 4.8(a), 4.8(c), 4.8(d) and 4.8(b) are going to be given in this section.

D.1 Process: 4PP and inclined probes

Figure D.1 shows the process sequence for the fabrication of the 4PP.

- 1: A double polished wafer is thinned down to 340 ± 2 μm using KOH.
- 2: A 1 μm thick wet oxide is grown on the wafer and a chromium layer of 750 Åis patterned on top of the oxide using a negative process, metal deposition and lift-off.
- 3: The chromium is used as a mask for the RIE etching of the oxide, which forms the fingers of the 4PP. After the RIE etch the chromium is removed in a plasma asher (1000 W, O_2 for 10 min).
- 4: A low stress, silicon rich nitride layer (1000 Å) is deposited on the wafer.
- 5: The backside is patterned and RIE etching is used to etch through the nitride and HF to etch through the oxide.
- 6: KOH etch of the backside for the release of the 4PP fingers. RIE etch of the nitride layer on the frontside
- 7: Metal deposition on the frontside.

D.2 Process: Nitride substrate probes

The process sequence for the probes of Figure 4.8(c) is described in this section. This process was developed so that it was possible to do using wet etching at all steps.

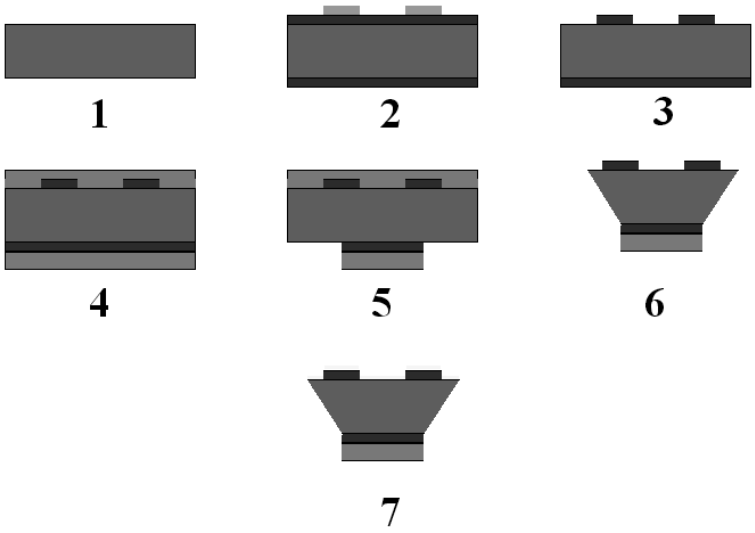

Figure D.1: The process sequence for the structures of the Figures 4.8(a), 4.8(c) and 4.8(d).

- 1: A double polished wafer is thinned down to 340 ± 2 μm using KOH.
- 2: LPCVD deposition of 2000 Åsilicon rich nitride.
- 3: LPCVD deposition of 2000 ÅTEOS silicon oxide.
- 4: Photolithography on the front side to pattern the oxide for chip definition. The backside is protected using blue tape and the oxide on the frontside is etched in BHF. The blue tape is removed from the backside.
- 5: Photolithography on the back side to pattern the oxide for the backside release process. The front side is protected with blue tape and the oxide on the back side is etched in BHF. The blue tape is removed.
- 6: The nitride on both sides is etched using H_3PO_4 at 180 degrees Celcius for 1 hour.)
- 7: The oxide is stipped in BHF.
- 8: Photolithography on the front side to pattern the electrodes. Metal deposition (Cr/Au: 50 Å/7500 Å) and lift off in acetone.
- 9: KOH etch of the backside using a front side protector.

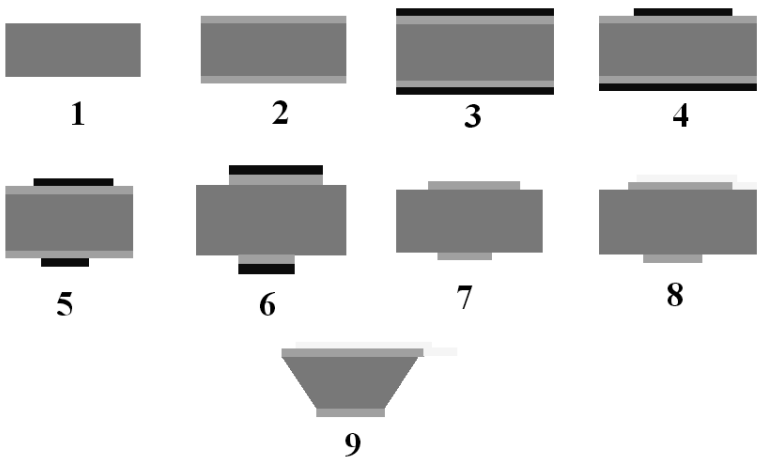

Figure D.2: The process sequence for the structures of the Figure 4.8(b)